Use of 0.7-in. Diameter Prestressing Strand in Bridge Girders: Bond Behavior and Girder Stability

by

Abdullah Abdulaziz Alabdulkarim

BEng, King Saud University, Riyadh, KSA 2012

MSCE, University of Dayton, Dayton, USA 2017

Submitted to the Graduate Faculty of

Swanson School of Engineering in partial fulfillment

of the requirements for the degree of

Doctor of Philosophy

University of Pittsburgh

2021

UNIVERSITY OF PITTSBURGH

SWANSON SCHOOL OF ENGINEERING

This dissertation was presented

by

Abdullah Abdulaziz Alabdulkarim

It was defended on

January 12, 2021

and approved by

Dr. Bahram M. Shahrooz, PhD, Professor, College of Engineering and Applied Science, University of Cincinnati

Dr. Lev Khazanovich, PhD, Professor, Department of Civil and Environmental Engineering

Dr. Jeen-Shang Lin, PhD, Associate Professor, Department of Civil and Environmental Engineering

Dissertation Director: Dr. Kent A. Harries, PhD, Professor, Department of Civil and Environmental Engineering

Use of 0.7-in. Diameter Prestressing Strand in Bridge Girders: Bond Behavior and Girder Stability

Abdullah Abdulaziz Alabdulkarim, PhD

University of Pittsburgh, 2021

In prestressed concrete bridge girders, the use of 0.7-in. diameter strand will allow 35% increase in prestressing force than 0.6-in. diameter strand and 92% increase than 0.5-in. diameter strand. This increase in prestressing force will theoretically permit longer span lengths, shallow girders or fewer girders across the width of a given bridge. AASHTO bridge design and construction specifications do not specify the use of 0.7-in. diameter strands for precast prestressed girders. Lack of data on the use, and particularly the bond behavior, of 0.7-in. diameter strand prevent its wide use in bridge construction. In this thesis the bond behavior of 0.7-in. diameter strand is evaluated. In addition to geometric and material characterization, five strands of each diameter (0.5, 0.6 and 0.7-in.) were tested to evaluate the Hoyer effect. Test results indicate that the dilation ratio of the strand exceeds that predicted by the Poison ratio alone. A parametric investigation using the finite element method was conducted to evaluate the effects of strand dilation over the expected transfer length of the strand. Single-strand models were used to illustrate the Hoyer effect and four-strands models to investigate the effect of strand spacing. Potential for local cracking resulting from the Hoyer effect is identified.

Thirty beam-end specimens having straight and 90^{o} hooked anchorages with different embedment lengths in different weight concretes were tested to evaluate the relative bond capacity of the strands. Test results indicate a predictable variation in bond behavior not attributed to the strand size. All tests exhibited shorter development lengths (i.e., better bond) than that prescribed

in design. The potential benefits of hooked anchorage are identified in resisting high longitudinal tensile forces related to beam-end shear effects.

With the potential for longer girders, stability is a concern during all the stages of girder construction and erection. A few previously designed girders that had been optimized for length are evaluated for stability following the PCI method. Analysis indicated that stability generally could be achieved. When necessary, increasing the width of the top flange since I_y/I_x has the pronounced effect on improving stability.

Table of Contents

List of Tables

List of Figures

List of Abbreviations

AASHTO	American Association of State Highway and Transportation Officials
ACI	American Concrete Institute
AE	Air Entraining Admixture
ASTM	American Society for Testing and Materials
BIV	Box-IV; girder cross section shape
BT	Bulb Tee; girder cross section shape
CGS	Center Gravity of Steel
CL	Center Line
COV	Coefficient of Variation
CTE	Coefficient of Thermal Expansion
DIC	Digital Image Correlations
DOT	Department of Transportation
FEM	Finite Element Method
FHWA	Federal Highway Administration
FIB	Florida I-Beam; girder cross section shape
FS	Factor of Safety
GGBFS	Ground-Granulated Blast-Furnace Slag

ID	Inner Diameter
LRFD	Load-and-Resistance Factor Design
LTB	Lateral Torsional Buckling
LVDT	Linear Variable Differential Transformer
LWC	Lightweight Concrete
NCHRP	National Cooperative Highway Research Program
NU	University of Nebraska I-girders; girder cross section shape
NWC	Normal Weight Concrete
OHWF	Ohio Wide Flange Girder; girder cross section shape
PCI	Precast/Prestressed Concrete Institute
RC	Reinforced Concrete
R-O	Ramberg-Osgoode
WF	Wide Flange Girder; girder cross section shape
WSDOT	Washington State Department of Transportation

List of Notations

A_{girder}	cross sectional area of girder (in^2)
A	length of the hook "tail" in the diaphragm (in)
a	lifting and/or dunnage location (in)
$A_{bottom\ flange}$	cross sectional area of bottom flange of girder (in^2)
a_{lift1}	lift connection locations from end of girder during lifting from bed stage (ft)
A_{ps}	area of prestressed steel (in^2)
A_r	a dimensionless constant taken as 1.0 for all rectangular shapes and 1.333 for an infinite strip
A_s	area of non-prestressed steel (in^2)
a_{seat2}	transverse seating tolerance from level (ft/ft)
$A_{top\ flange}$	cross sectional area of top flange of girder (in^2)
a_{trans}	superelevation (ft/ft)
b	distance from end-span to harp point (ft)
b_{fc}	compression-flange width between webs (in)
B_r	a dimensionless constant calculated in Eq. (6–19)
$b_{topflange}$	width of top flange (in)
c	radius of concrete cylinder (in)

d	nominal diameter of Strand (in)
d_b	nominal diameter of strand (in)
d_c	center wire diameter in a strand (in)
D_c	depth of the web in compression in the elastic range (in)
d_h	helical wire diameter in a strand (in)
d_i	sum of center and helical wires of a strand (in)
d_{ps}	nominal diameter of Strand (in)
d_v	effective shear depth (in)
E	modulus of elasticity for steel (ksi)
e'	eccentricity of harped or debonded tendon with center of gravity of girder (in)
e'_h	eccentricity of harped strands at end-span (in)
E_0	initial tangent modulus (ksi)
e_{brace}	imperfection (play) in each brace (in)
$e_{brg.seat1}$	bearing tolerance from CL girder to CL support during seated on dunnage (in)
$e_{brg.seat2}$	bearing tolerance from CL girder to CL support during seated on bearings (in)
$e_{brg.seat3}$	bearing tolerance from CL girder to CL support during inactive construction (in)
$e_{bunk.trans}$	bunking tolerance from CL girder to CL support during transportation (in)
E_c	young's modulus of concrete (ksi)
$E_{c.lift1}$	concrete modulus of elasticity during lifting from bed stage (ksi)

$e_{c,h}$	eccentricity of harped strands at mid-span (in)
$e_{c,sb}$	eccentricity of straight bottom strands at mid-span (in)
$e_{c,st}$	eccentricity of straight top strands at mid-span (in)
E_{ci}	modulus of elasticity of concrete at transfer (ksi)
e_{conn}	lateral tolerance of lift device from centerline of girder (in)
e_i	lateral eccentricity due to sweep and eccentricity due to lifting device from the center line (in)
$e_{i,bed}$	sweep eccentricity at initial lift from the prestressing bed (in)
$e_{i,trans}$	sweep eccentricity at transfer stage (in)
$e_{i.total}$	total sweep eccentricity at certain stage (in)
$e_{i.total.lift1}$	total sweep eccentricity at lifting from bed stage (in)
$e_{i.lift1}$	center of mass eccentricity due to lateral deflection (in)
E_p	young's modulus of prestressing strand (ksi)
e_{wind}	eccentricity of girder weight due to wind force (in)
$e_{wind.lift1}$	eccentricity of girder dead load to equilibrate wind load (in)
f_2	the ultimate biaxial compressive stress (ksi)
$f_{b.lift1.base}$	base concrete stresses at bottom girder before rotation and wind during lifting from bed stage (ksi)
$f_{b.lift2.base}$	base concrete stresses at bottom girder before rotation and wind during lift in field stage (ksi)

$f_{b.ck.lift1.wl}$ bottom flange tips stress - wind left during lifting from bed stage (ksi)

$f_{b.ck.lift2.wl}$ bottom flange tips stress - wind left during lift in field stage (ksi)

$f_{b.lift1.wl.left}$ left bottom flange tips stress - wind left during lifting from bed stage (ksi)

$f_{b.lift2.wl.left}$ left bottom flange tips stress - wind left during lift in field stage (ksi)

$f_{b.lift1.wl.right}$ right bottom flange tips stress - wind left during lifting from bed stage (ksi)

$f_{b.lift2.wl.right}$ right bottom flange tips stress - wind left during lift in filed stage (ksi)

$f_{b.ck.lift1.wr}$ bottom flange tips stress - wind right during lifting from bed stage (ksi)

$f_{b.lift1.wr.left}$ left bottom flange tips stress - wind right during lifting from bed stage (ksi)

$f_{b.lift2.wr.left}$ left bottom flange tips stress - wind right during lift in field stage (ksi)

$f_{b.lift1.wr.right}$ right bottom flange tips stress - wind right during lifting from bed stage (ksi)

$f_{b.lift2.wr.right}$ right bottom flange tips stress - wind right during lift in field stage (ksi)

$f_{b.seat1}$ bottom concrete stresses in girder during seated on dunnage stage (ksi)

$f_{b.seat2}$ bottom concrete stresses in girder during seated on bearings stage (ksi)

$f_{b.trans}$ bottom concrete stresses in girder during transportation stage (ksi)

f_c 56-day compressive strength concrete (ksi)

f_c' 28-day compressive strength of concrete (ksi)

$f_{c.lift1}$ concrete compressive strength during lifting from bed stage (ksi)

f_{ci} concrete strength at transfer (ksi)

f_{crack} strand stress of strand when first crack occurs (ksi)

f_{cz}	axial stress in concrete a distance z from the free end (ksi)
$f_{eq.t.trans}$	equivalent top concrete stresses in girder during transportation stage (ksi)
$f_{eq.t.seat1}$	equivalent top concrete stresses in girder during seated on dunnage stage (ksi)
$f_{eq.t.seat2}$	equivalent top concrete stresses in girder during seated on bearings stage (ksi)
$f_{eq.b.seat1}$	equivalent bottom concrete stresses in girder during seated on dunnage (ksi)
$f_{eq.b.seat2}$	equivalent bottom concrete stresses in girder during seated on bearings (ksi)
$f_{eq.b.trans}$	equivalent bottom concrete stresses in girder during transportation stage (ksi)
f_{hook}	constant stress that is attributed to the hook (ksi)
f_{max}	maximum stress in strand where beam-end specimen fails (ksi)
$F_{ot.seat1.brace}$	concurrent lateral force (service) during seated on dunnage (kip)
$F_{ot.seat2.brace}$	concurrent lateral force (service) during seated on bearings (kip)
f_p	strand stress (ksi)
f_{pe}	effective prestress force (ksi)
f_{peff}	the effective prestress after losses (ksi)
f_{pi}	initial prestress force (ksi)
f_{ps}	nominal resistance of the strand (ksi)
$f_{ps,straight}$	design stress in straight pretensioned strand at nominal flexural strength (ksi)
f_{pu}	ultimate tensile strength of prestressing strand (ksi)
f_{px}	strand design stress based on transfer length (ksi)

f_{pz}	axial stress in prestressing strand a distance z from the free end of the concrete embedment (ksi)
f_R	relative rib ratio
$f_{r.lift1}$	modulus of rupture during lifting from bed stage (ksi)
f_s	strand stress due to applied load (ksi)
FS'	factor of safety against lateral torsional buckling failure
FS_{cr}	factor of safety against girder cracking
$FS_{cr.lift1}$	factor of safety against cracking during lifting from bed
$FS_{cr.lift2}$	factor of safety against cracking during lift in field
$FS_{cr.lift1.wl}$	factor of safety against cracking during lifting from bed – wind left
$FS_{cr.lift2.wl}$	factor of safety against cracking during lift in field – wind left
$FS_{cr.lift1.wr}$	factor of safety against cracking during lifting from bed – wind right
$FS_{cr.lift2.wr}$	factor of safety against cracking during lift in field – wind right
$FS_{cr.seat1}$	factor of safety against cracking during seated on dunnage stage
$FS_{cr.seat2}$	factor of safety against cracking during seated on bearings stage
$FS_{cr.trans}$	factor of safety against cracking during transportation stage
f_{slip}	strand stress of strand when first slip occurs (ksi)
$FS_{ult.crit.lift1}$	critical factor of safety against failure during lifting from bed stage
$FS_{ult.crit.lift2}$	critical factor of safety against failure during lift in field stage

$FS_{ult.lift1}$	factor of safety against failure for critical case during lifting from bed stage
$FS_{ult.lift2}$	factor of safety against failure for critical case during lift in field stage
$FS_{ult.lift1.wl}$	factor of safety against failure - wind left during lifting from bed stage
$FS_{ult.lift2.wl}$	factor of safety against failure - wind left during lift in field stage
$FS_{ult.lift1.wr}$	factor of safety against failure - wind right during lifting from bed stage
$FS_{ult.lift2.wr}$	factor of safety against failure - wind right during lift in field stage
$FS_{ult.seat1}$	factor of safety against failure during seated on dunnage stage
$FS_{ult.seat2}$	factor of safety against failure during seated on bearings stage
$FS_{ult.trans}$	factor of safety against failure during transportation stage
FS_{roll}	factor of safety against girder rolling off supports
$FS_{roll.seat1}$	factor of safety against rollover (cracked) during seated on dunnage stage
$FS_{roll.seat2}$	factor of safety against rollover (cracked) during seated on bearings stage
$FS_{roll.trans}$	factor of safety against rollover (cracked) during transportation stage
f_{t0}	maximum tensile strength in modified tension stiffening model (ksi)
$f_{t.lift1.base}$	base concrete stresses in top girder before rotation and wind during lifting from bed stage (ksi)
$f_{t.lift2.base}$	base concrete stresses in top girder before rotation and wind during lift in field stage (ksi)
$f_{t.ck.lift1.wl}$	top flange tips stress – wind left during lifting from bed stage (ksi)

$f_{t.ck.lift2.wl}$ top flange tips stress – wind left during lift in field stage (ksi)

$f_{t.lift1.wl.left}$ left top flange tips stress – wind left during lifting from bed stage (ksi)

$f_{t.lift2.wl.left}$ left top flange tips stress – wind left during lift in field stage (ksi)

$f_{t.lift1.wl.right}$ right top flange tips stress – wind left during lifting from bed stage (ksi)

$f_{t.lift2.wl.right}$ right top flange tips stress – wind left during lift in field stage (ksi)

$f_{t.ck.lift1.wr}$ top flange tips stress – wind right during lifting from bed stage (ksi)

$f_{t.ck.lift2.wr}$ top flange tips stress – wind right during lift in field stage (ksi)

$f_{t.lift2.wr}$ base concrete stresses in girder with wind (left top tip) during lift in field (ksi)

$f_{t.lift1.wr.left}$ left top flange tips stress – wind right during lifting from bed stage (ksi)

$f_{t.lift2.wr.left}$ left top flange tips stress – wind right during lift in field stage (ksi)

$f_{t.lift1.wr.right}$ right top flange tips stress – wind right during lifting from bed stage (ksi)

$f_{t.lift2.wr.right}$ right top flange tips stress – wind right during lift in field stage (ksi)

$f_{t.seat1}$ top concrete stresses in girder during seated on dunnage stage (ksi)

$f_{t.seat2}$ top concrete stresses in girder during seated on bearings stage (ksi)

$f_{t.trans}$ top concrete stresses in girder during transportation stage (ksi)

f_y specified yield strength of reinforcement in non-prestressed steel (ksi)

F_{yc} specified minimum yield strength of a compression flange (ksi)

F_{yr} compression flange stress (ksi)

F_{yw}	specified minimum yield strength of a web (ksi)
G	shear modulus of bearing (ksi)
H	height of girder (in)
$h_{brg.seat2}$	height of bearing (in)
h_r	height of roll center about the roadway (in)
$h_{roll.seat1}$	height of roll center from bearing seat (in)
$h_{roll.seat2}$	height of roll center from bearing seat, $h_{roll.seat2} = y_{brg.seat2}$ (in)
$h_{roll.trans}$	height of roll center above roadway (in)
I_g	moment of inertia about the strong axis (in^4)
IM_{lift1}	vertical wind uplift considered negligible for lifting impact factor
I_x	moment of inertia about x-axis (in^4)
I_y	moment of inertial about y-axis (in^4)
$I_{y\ bottom\ flange}$	moment of inertia for bottom flange of girder about y-axis (in^4)
$I_{y\ top\ flange}$	moment of inertia for top flange of girder about y-axis (in^4)
$I_{y\ web}$	moment of inertia for web of girder about y-axis (in^4)
J_{girder}	torsional constant (in^4)
K	bulk modulus of bearing (ksi)
k	development length magnification factor
k	number of helical elements in a strand

K_1	correction factor for modulus of elasticity
$K_{g,trans}$	hauling rig stiffness during transportation stage (kip-in/rad)
$K_{q.seat2}$	bearing rotational stiffness during seated on bearings stage (kip-in/rad)
$K_{q.seat3}$	bearing rotational stiffness during inactive construction stage, $K_{q.seat3} = K_{q.seat2}$ (kip-in/rad)
K_{qseat1}	bearing rotational stiffness during seated on dunnage stage (kip-in/rad)
K_q	bearing rotational stiffness for all stages (kip-in/rad)
K_θ	rotational constant of the transport rig (kip-in/rad)
L	length of girder span (ft)
$L_{1.lift1}$	center of mass eccentricity reduction factor (ft)
L_b	unbraced length (in)
L_{brg}	plan dimension of the bearing perpendicular to the axis of rotation (length along beam) (in)
l_d	straight strand development length (in)
l_{dh}	hooked strand development length (in)
l_e	embedment length of a straight strand in a beam (in)
L_g	full girder length (ft)
l_h	embedment length of a hooked strand in a beam (in)
L_{harp}	distance from midspan to strand draping harp point
l_{hook}	embedment length of hooked strand into diaphragm (in)

L_p	limiting unbraced length to achieve the nominal flexural resistance (in)
l_{px}	distance from free end of pretensioned strand to section of member under consideration (in)
L_r	limiting unbraced length to achieve the onset of nominal yielding (in)
l_t	transfer length (in)
M_a	acting moment (kip-in)
$M_{g.lift1}$	moment due to gravity load during lifting from bed (kip-in)
$M_{g.lift2}$	moment due to gravity load during lifting in field (kip-in)
$M_{g.seat1}$	moment due to gravity load during seated on dunnage (kip-in)
$M_{g.seat2}$	moment due to gravity load during seated on bearings (kip-in)
$M_{lat.lift1.wl}$	lateral moment to cause cracking – wind left during lifting from bed (kip-in)
$M_{lat.lift2.wl}$	lateral moment to cause cracking – wind left during lift in field (kip-in)
$M_{lat.lift1.wr}$	lateral moment to cause cracking – wind right during lifting from bed (kip-in)
$M_{lat.lift2.wr}$	lateral moment to cause cracking – wind right during lift in field (kip-in)
$M_{lat.seat1}$	lateral moment to cause cracking during seated on dunnage (kip-in)
$M_{lat.seat2}$	lateral moment to cause cracking during seated on bearings (kip-in)
$M_{lat.trans}$	lateral moment to cause cracking during seated on dunnage (kip-ft)
$M_{ot.seat1}$	overturning moment due to wind during seated on dunnage stage (kip-in)
$M_{ot.seat2}$	overturning moment due to wind during seated on bearings stage (kip-in)

$M_{ot.seat1.brace}$ overturning moment to be resisted by bracing (service) during seated on dunnage stage (kip-ft)

$M_{ot.seat2.brace}$ overturning moment to be resisted by bracing (service) during seated on bearings stage (kip-ft)

$M_{ot.trans}$ overturning moment due to wind during transportation stage (kip-in)

M_r resisting moment (kip-in)

$M_{roll.seat1}$ overturning moment from wind during seated on dunnage stage (kip-in)

$M_{roll.seat2}$ overturning moment from wind during seated on bearings stage (kip-in)

$M_{roll.trans}$ overturning moment from wind during transportation stage (kip-in)

$M_{total.trans}$ total lateral moment during transportation stage (kip-in)

M_u factored moment (kip-in)

$M_{ult.y.lift1}$ lateral ultimate moment capacity required during lifting from bed (kip-ft)

$M_{ult.y.lift2}$ lateral ultimate moment capacity required during lift in field (kip-ft)

$M_{wind.lift1}$ lateral moment due to wind during lifting from bed (kip-in)

$M_{wind.lift2}$ lateral moment due to wind during lifting in field (kip-in)

$M_{wind.seat1}$ lateral moment due to wind during seated on dunnage (kip-in)

$M_{wind.seat2}$ lateral moment due to wind during seated on bearings (kip-in)

$M_{y,crack}$ lateral moment applied to the girder that causes tensile cracking in the most critical flange (kip-in)

M_z	gravity moment of the girder (kip-in)
n_{braces}	number of braces, including at end of girder
$n_{girders}$	number of Girders in Typical Section
N_u	factored axial force (kips)
P	applied load to the strand for beam-end tests (kips)
p	radial pressure at the interface (ksi)
P_{crack}	applied load to the strand for beam-end tests when first crack occurs (kips)
$P_{eff,h}$	effective prestress force for harped strands (kips)
$P_{eff,sb}$	effective prestress force for straight bottom strands (kips)
$P_{eff,st}$	effective prestress force for straight top strands (kips)
$P_{eff.lift1}$	effective prestress force at lifting during lifting from bed (kips)
P_{max}	maximum applied load to the strand when beam-end specimen fails (kips)
P_{slip}	applied load to the strand for beam-end tests when first slip occurs (kips)
R	radial distance to the inner boundary of the isotropic (uncracked) region (in)
r	radius or radial distance from center of strand (in)
r_0	initial radius of steel before prestressing (in)
$Radius_{trans}$	turn radius for adverse cross slope (ft)
r_s	radius of steel after prestressing (in)
r_t	effective radius of gyration of LTB (in)

r_x	radius of gyration about the x-axis (in)
$r_{y\ top\ flange}$	radius of gyration of top flange of girder about y-axis (in)
r_y	radius of gyration about the y-axis (in)
S	shape factor used to calculate bearing rotational stiffness
s	spacing between prestressed strands (in)
s_{girder}	spacing between girders (ft)
$S_{x.b}$	horizontal axis section modulus bottom flange
$S_{x.t}$	horizontal axis section modulus top flange
$S_{y.b}$	vertical axis section modulus bottom flange
$S_{y.t}$	vertical axis section modulus top flange
$\bar{s}$	length of pitch in a strand (in)
t	elastomer layer thickness (in)
T	tension force (kips)
t_{fc}	thickness of the compression flange (in)
t_w	web thickness (in)
u_0	initial displacement of steel (in)
u_c	displacement of concrete (in)
Vel_{trans}	hauling rig velocity in turn (mph)

V_p	component in the direction of the applied shear of the effective prestressing force (kips)
V_s	shear resistance provided by the transverse reinforcement (kips)
V_u	factored shear force at section (kips)
w	weight of girder per ft (kip/ft)
W	weight of the girder (kips)
W_{brg}	plan dimension of the bearing parallel to the axis of the rotation (width across beam section) (in)
$W_{brg.seat1}$	plan dimension of the bearing parallel to the axis of the rotation (in)
w_c	unit weight of concrete (kcf)
$w_{DC.girder}$	unit weight of girder (klf)
$w_{DC.girder.lift1}$	effective unit weight of girder during lifting from bed (klf)
w_{girder}	unit weight of girder with reinforcement (kcf)
$w_{lift.seat3}$	lateral wind uplift force during inactive construction (klf)
$w_{wind.lift1}$	lateral wind force at lifting from bed (klf)
$w_{wind.lift2}$	lateral wind force at lifting in field (klf)
$w_{wind.seat1}$	lateral wind force during seating on dunnage (ft/ft)
$w_{wind.seat2}$	lateral wind force during single girder on bearing stage (klf)
$w_{wind.seat3}$	lateral wind force during inactive construction stage (klf)

$w_{wind.trans}$	lateral wind force during transportation (klf)
y_b	distance from the bottom of the girder to neutral axis of girder (in)
$y_{brg.seat1}$	height from roll center to bottom of girder during seated on dunnage stage (in)
$y_{brg.seat2}$	height from roll center to bottom of girder during on bearings stage, $y_{brg.seat2} = h_{brg.seat2}/2$ (in)
$y_{brg.seat3}$	height from roll center to bottom of girder during inactive construction stage, $y_{brg.seat3} = y_{brg.seat2}$ (in)
$y_{cgs,mid}$	center of gravity of all prestressed strands at mid-span (in)
$y_{cgs.mid.lift1}$	cg of strands at midspan to bottom of girder cg of strands at midspan to bottom of girder during lifting from bed stage (in)
y_{lift}	rigid extension of lift device above top of girder (in)
y_r	distance of center of gravity from roll axis (in)
$y_{r.lift1}$	distance from the center of mass of the cambered girder below roll axis (in)
$y_{seat.trans}$	height from roll center to bottom of girder during transportation stage (in)
$y_{upper.yoke}$	the distance between upper yolk and lower lift connection (ft)
$y_{w.lift1}$	mid-height of the cambered arc below roll axis (in)
z	longitudinal distance from the free end of the strand/concrete interface (in)
z_0	theoretical lateral deflection of the center of gravity of the beam with full dead weight applied laterally (in)
$\bar{z_0}$	lateral deflection of centroid of the cross section (in)

$z_{0.lift1}$	center of mass eccentricity due to girder weight on weak axis (in)
$z_{0.p.seat1}$	corresponding center of mass eccentricity due to tilt angle during seated on dunnage stage (in)
$z_{0.p.seat2}$	corresponding center of mass eccentricity due to tilt angle during seated on bearings stage (in)
$z_{0.p.trans}$	corresponding center of mass eccentricity due to tilt angle during transportation stage (in)
z_{CE}	deflection of girder due to centrifugal force (in)
$z_{max.seat1}$	horizontal distance from roll axis to edge of girder (in)
$z_{max.seat2}$	horizontal distance from roll axis to edge of girder (in)
$z_{max.trans}$	horizontal distance from roll axis to center of tire group (in)
z_{wind}	lateral deflection due to wind force (in)
$z_{wind.lift1}$	center of mass eccentricity due to wind deflection during lifting from bed stage (in)
α	maximum roadway super elevation
α_s	thermal expansion of strand (m/m^{o}K)
β	helix or lay angle in a strand (rad)
$\bar{\beta}$	a parameter depends on the shape of the stress-strain diagram
Δ	camber/deflection (in)
$\Delta_{camb.lift1}$	camber during lifting from bed stage (in)

Δ_{ohang}	deflection resulting from the girder overhang beyond locations of support (in)
Δ_{ps}	deflection due to prestress (in)
$\Delta_{ps,harped}$	deflection due to prestress harped strands (in)
$\Delta_{(ps,straight\ bot)}$	deflection due to prestress bottom straight strands (in)
$\Delta_{(ps,straight\ top)}$	deflection due to prestress temporary top straight strands (in)
Δ_{self}	deflection due to girder self-weight calculated over the distance between supports (in)
ΔT	change in temperature (K^0)
ε	strain (in/in)
ε_0	strain at peak stress (in/in)
ε_c	strain oriented along the longitudinal axis of the strand (in/in)
ε_{cr}	strain that meets maximum tensile strength in modified tension stiffening model (in/in)
ε_h	strain measured along the axis of the helical wire (in/in)
ε_{pH}	dilation strain of a prestressing strand due to initial prestress force (in/in)
ε_t	diametric strain of a strand (in/in)
ε_{t0}	the uniaxial tensile strain at failure (in/in)
θ	angle of inclination of diagonal compressive stresses (rad)
θ	rotation angle of the girder from vertical (rad)
$\theta_{eq.lift1.wl}$	rotation angle during lifting from bed stage - wind left (rad)

$\theta_{eq.lift2.wl}$ rotation angle during lift in field stage - wind left (rad)

$\theta_{eq.lift1.wr}$ rotation angle during lifting from bed stage - wind right (rad)

$\theta_{eq.lift2.wr}$ rotation angle during lift in field stage - wind right (rad)

$\theta_{eq.seat1}$ rotation angle during seated on dunnage stage (rad)

$\theta_{eq.seat2}$ rotation angle during seated on bearings stage (rad)

$\theta_{eq.trans}$ rotation angle during transportation stage (rad)

$\theta_{cr.lift1.wl}$ tilt angle at cracking due to lateral deflection – wind left during lifting from bed stage (rad)

$\theta_{cr.lift2.wl}$ tilt angle at cracking due to lateral deflection – wind left during lift in field stage (rad)

$\theta_{cr.lift1.wr}$ tilt angle at cracking due to lateral deflection – wind right during lifting from bed stage (rad)

$\theta_{cr.lift2.wr}$ tilt angle at cracking due to lateral deflection – wind right during lift in field stage (rad)

$\theta_{cr.seat1}$ tilt angle at cracking due to lateral deflection during seated on dunnage (rad)

$\theta_{cr.seat2}$ tilt angle at cracking due to lateral deflection during seated on bearings (rad)

$\theta_{cr.trans}$ tilt angle at cracking due to lateral deflection during transportation (rad)

θ''_{max} rotation angle when rollover is respected (rad)

θ'_{max} maximum tilt angle for the cracked section (rad)

θ_{max}	the rotation at which a girder crack (rad)
$\theta_{max.p.seat1}$	tilt angle at maximum resisting moment arm during seated on dunnage (rad)
$\theta_{max.p.seat2}$	tilt angle at maximum resisting moment arm during seated on bearings (rad)
$\theta_{max.p.trans}$	tilt angle at maximum resisting moment arm during transportation (rad)
$\theta_{max.ult.lift1.wl}$	rotation at maximum factor of safety – wind left during lifting from bed (rad)
$\theta_{max.ult.lift2.wl}$	rotation at maximum factor of safety – wind left during lift in field (rad)
$\theta_{max.ult.lift1.wr}$	rotation at maximum factor of safety – wind right during lifting from bed (rad)
$\theta_{max.ult.lift2.wr}$	rotation at maximum factor of safety – wind right during lift in field (rad)
λ	concrete density modification factor
λ_{brg}	compressibility index
v_c	Poisson's ratio of concrete
v_p	dilation ratio of prestressing strand
v_s	Poisson's ratio of steel
σ	stress (ksi)
σ_{cu}	maximum compressive strength (ksi)
σ_r	radial stress (ksi)
σ_t	tensile strength in modified tension stiffening model (ksi)
σ_{t0}	maximum tensile strength in modified tension stiffening model (ksi)
σ_x	horizontally oriented stress (ksi)

σ_θ	circumferential stress (ksi)
τ	average bond stress of strand with concrete (ksi)
τ_{max}	maximum bond stress when the strand in pulled out the beam (ksi)
τ_{slip}	average bond stress when first slip occurs (ksi)
υ	Poisson's ratio
ϕ_c	resistance factor for axial force
ϕ_f	resistance factor for flexure
ϕ_v	resistance factor for shear and torsion

This dissertation is presented primarily in US standard units except where maintaining native SI units is consistent with cited source material or is considered critical to understanding or presentation. Conversion factors are as follows:

1 in. = 25.4 mm

1 kip = 4.448 kN

1 ksi = 6.895 MPa

Inconsistent dimensions are used in reference to concrete tensile properties given in terms $(f_c')^{0.5}$. Equivalent leading coefficients are as follows:

$(1/31.6)\ (f_c'$ in ksi$)^{0.5} = 1.0\ (f_c'$ in psi$)^{0.5} = (1/12)\ (f_c'$ in MPa$)^{0.5}$

Acknowledgement

I would like to acknowledge everyone who has contributed to my success to fulfill this dissertation. First, thanks to Almighty Allah for giving me the strength to understand and accomplish this mammoth task.

It is my genuine pleasure to express my sincere appreciation and gratitude to Dr. Kent Harries. Without his guidnese I would not have made it. His dedecation and eager to help was significant to me. I'm extremely thankful for the encouragement and positive attitude throughout all the meetings we had. Its my pleasure to also thanks my comittee members: Dr. Shahrooz, Dr. Khazanovich and Dr. Lin for their support to help me reach my goal.

A special thanks goes to my parents, who have been great mentors for me not only in this chapter of my life but my whole life. I'm grateful for all the utmost support and prayers they always give me. To my wife Amal, I'm deeply indebted for the patience and understanding as I sailed towards the end of this journey. To my family and friends: thank you for the encouragement and moral support which made my stay and studies in USA more comfortable.

Many thanks to my collegues in the labortary Charles Hager, Yusuf Akinbade, Christian Gauss, and Chase Rogers for their contribution in my work.

1.0 Introduction and Literature Review

1.1 Motivation

Prestressed concrete girder bridges are a common alternative for spans ranging from 50 to 200 feet (Chen and Duan, 2014). By prestressing the primary reinforcement prior to placing the concrete and transferring (releasing) this prestress into the concrete once it is cures, the concrete element is drawn into compression. Cracking due to subsequent application of service loads is therefore retarded or mitigated resulting in a more durable structure.

In U.S. practice, such girders are prestressed using ASTM A416 Grade 270 (f_{pu} = 270 ksi) seven-wire strand having diameters up to 0.6-in. Nonetheless, 0.7-in. diameter prestressing strand is available and is conventionally used in the underground mining industry as anchors or roof bolts. As shown in Table 1.1, 0.7-in. strand has 35.5% greater cross section area than 0.6-in. strand. Its use in prestressed concrete girders, therefore has the potential to provide greater prestressing forces than are presently available using 0.6-in. or 0.5-in. strand without adding additional strands which may require larger concrete cross sections to accommodate.

Table 1.1 Properties of ASTM A416 seven-wire prestressing strand.

Strand diameter, d_{ps}	3/8-in.	0.5-in.	0.6-in.	0.7-in.
Strand area, A_{ps}	0.085 in^2	0.153 in^2	0.217 in^2	0.294 in^2
Available prestress force: $0.75A_{ps}f_{pu}$	17.2 kips	31.0 kips	43.9 kips	59.5 kips

Greater prestress force has the potential to increase practically achievable span lengths of existing standard prestressed concrete bridge girder sections and to permit the use of higher strength concrete in bridge design. Ball (2019) reports the potential to increase span lengths is a function of the girder cross section. For AASHTO bulb tees (BT72), for instance, span increases

on the order of 20% can be achieved using 0.7-in. strand in place of 0.6-in. strand in girders having 10 ksi concrete. Marginally greater increases are observed using higher strength concrete. Other girder sections reported by Ball generally did not permit such large span increases. Increasing available prestressed concrete girder spans above 200 feet make it practical to span typical interstate right-of-ways without a central pier. This saves foundation cost, improves safety and may permit additional carriageways or alternate use of the central reservation. Several recent record-breaking spans up to 223 feet have been constructed using 0.6-in. strand (West 2019).

In addition to longer overall spans, a second potential advantage of providing greater prestress forces in a girder section is the ability to use shallower girders or fewer girders across the width of a given bridge. These may be particular advantages for bridge replacement, especially when abutments are being reused.

AASHTO bridge design (AASHTO 2017a) and construction specifications (AASHTO 2017b) do not specify the use of 0.7-in. diameter strands for prestressed girders. If 0.7-in. strand is to be adopted for prestressed concrete bridge elements, contractors, designers and fabricators require guidelines and specifications for their use. The objective of this study is to investigate the bond behavior of 0.7-in. diameter prestressing strand; that is, how the strand interacts with the surrounding concrete at all stages of construction and use. This study also addresses the concepts of transfer length, development length and the parameters affecting these relevant to the use of larger diameter 0.7-in. strands. Finally, the ability to construct longer spans requires investigation of aspects of stability of these girders during casting, handling, erection and in service.

1.2 Transfer and Development Length

Reinforcement in concrete – whether prestressed or not – provides tension capacity necessary for the structural performance of the member. Internal stresses are transferred between the steel and surrounding concrete by bond stresses (Section 1.3) built up over the length of steel embedment. For prestressing strand, bond is developed over two regions: the transfer and development lengths.

Transfer length, l_t, is the length of prestressed strand required to fully transfer the effective prestress force from the prestressed strand into the concrete. It is measured from the point at which force transfer begins; typically at end of concrete member but also be within the span when partially debonded strands are used (Shahrooz et al. 2017). Over the transfer length, the transferred force is assumed to increase linearly (therefore assuming a uniform bond stress over the transfer length) from zero at the initiation of bond to the effective prestress force, f_{pe}, at the end of the transfer length (see Figure 1.1).

Transfer length affects the available strand force near the girder end. A short transfer length may introduce the eccentric prestress force into the beam too rapidly resulting in bursting stresses near the strand end or cracking associated with the internal moment resulting from the eccentricity of the prestressing force (Girgis and Tuan, 2004). A long transfer length may result in insufficient primary reinforcing capacity to resist the horizontal component of shear stresses at the girder end (Shahrooz et al. 2017). Accurate estimation of transfer length in design is important and has implications: a “conservative” estimation, resulting in an assumed transfer length longer than is actually present may result in cracking of the section as force is transferred over a shorter distance

than assumed. A “non-conservative” estimation may result in inadequate section capacity at the girder end since the strand is not developed as rapidly as assumed.

The AASHTO-LRFD *Design Specifications* (2017a; §5.11.4.1) prescribe the transfer length, l_t, as:

$$l_t = 60 d_b \tag{1–1}$$

Where d_b = nominal strand diameter.

Development length, l_d, is the minimum distance of strand embedment in concrete required to achieve the nominal resistance of the strand, f_{ps}, without strand slip (see Figure 1.1). Therefore, the ultimate capacity of the strand can be achieved at the end of the development length without failure of bond between strand and concrete. The development length is important for design of the critical section for flexure. If the development length is underestimated in design, actual girder capacity is reduced along the entire development length and beyond, to the location at which the strand is eventually fully developed. If the development length is overestimated, no detrimental effect is likely although an uneconomical design may result.

The AASHTO-LRFD *Bridge Design Specifications* (Eq. 5.11.4.2-1) prescribe the development length, l_d, as:

$$l_d = \mathrm{k}\left(f_{ps} - \frac{2}{3} f_{pe}\right) d_b \tag{1–2}$$

Where, k = development length magnification factor; k = 1.0 for pretensioned panels, piling, and other pretensioned members with a depth less than or equal to 24 in. (610 mm); k = 1.6 otherwise. For partially debonded strands, k = 2.0; f_{ps} = average stress in prestressing steel to be developed; typically, $f_{ps} = f_{pu}$ = 270 ksi; f_{pe} = effectives prestress in prestressing steel; $f_{pe} \leq 0.72 f_{pu}$ and typically, $f_{pe} \approx 0.56 f_{pu}$.

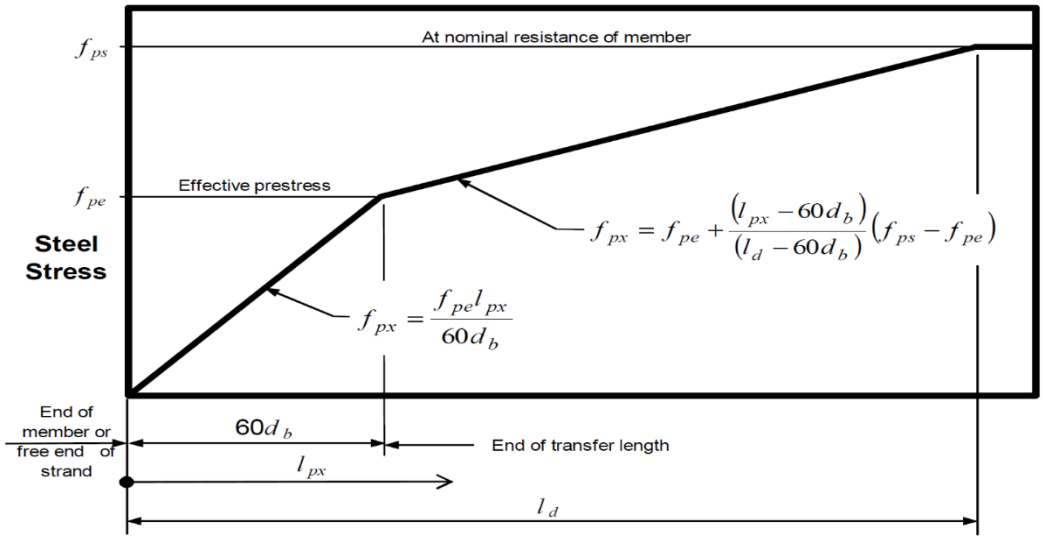

Figure 1.1 Transfer and development length (AASHTO 2017a)

In NCHRP *Report 603* (Ramirez and Russell, 2008) refinements to the AASHTO transfer and development length equations are proposed. *Report 603* proposed new requirements in order to account for the basic properties of bonding for prestressing strand. AASHTO requirements (Eqs (1–1) and (1–2)) only address the mechanical properties of the strand; i.e., strand size and strength. The recommendations of *Report 603* introduce the concrete strength at prestress release, f_{ci} – specifically a measure of the concrete tensile strength: $\sqrt{f_{ci}}$ (in ksi units) – to the transfer and development lengths equations. Additionally, *Report 603* permits a shorter lower limit on transfer length:

$$l_t = 120\, d_b f'_{ci} \geq 40 d_b \tag{1–3}$$

$$l_d = \left[\frac{120}{\sqrt{f'_{ci}}} + \frac{225}{\sqrt{f'_c}}\right] d_b \geq 100 d_b \tag{1–4}$$

Both Eqs (1–3), and (1–4) typically will result in shorter values of l_t and l_d than prescribed by Eqs (1–1) and (1–2).

1.3 Bond Characteristics

The bond between pretensioned strands and the surrounding concrete includes components of adhesion, friction and the wedge mechanism resulting from the "Hoyer effect", and mechanical interlock (Figure 1.2a) between deformed strands and the surrounding concrete (Briere et al. 2013). Adhesion is chemical action between the steel and the concrete. It effectively restrains the relative slip at the interface of concrete and steel until a critical stress is achieved; adhesion is overcome once slip occurs (Jiang 2013). Adhesion is rapidly overcome and conventionally not considered in reinforcing bar or prestressing strand bond capacity.

The Hoyer effect, described in detail in Section 1.5, is a function of the deformation of the strand resulting from initial prestress and the restraint provided by the surrounding concrete.

As with non-prestressed reinforcing, mechanical interlock is the dominate component of the bond mechanism of prestressing strand. Mechanical interlock in prestressing strands is similar in nature to that of reinforcing deformed bars but also engages a helical twisting action which generates an enhanced friction component coincident with mechanical interlock (Figure 1.2c). The shallow-angle helical deformations of prestressing strand (Figure 1.2b) result in a smaller radial component of bond stress than conventional deformed bars which typically have near-transverse-oriented deformations (Figure 1.2a). The kinematics of seven wire strand subject to tension is described by Machida and Durelli (1973) and Utting and Jones (1987). The resulting mechanism of mechanical interlock with concrete is described by Salmons and McCrate (1973) and shown schematically in (Figure 1.2b). (Figure 1.2d) shows the strand imprint in concrete illustrating well-defined helical deformations and identifying the need for excellent consolidation around the strand.

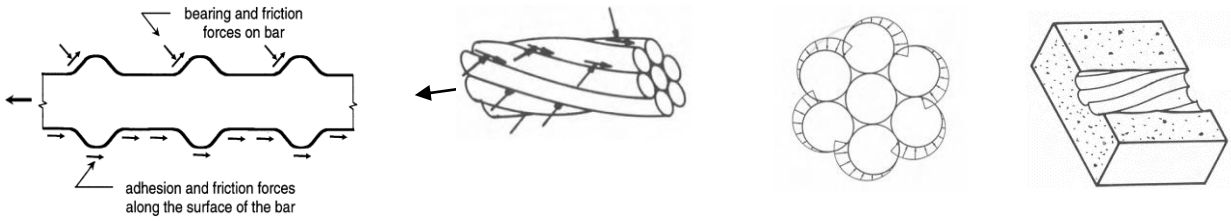

a) components of bond force acting on deformed reinforcing bar (ACI 408R-03 2012)

b) components of bond force acting on seven-wire strand (Salmons and McCrate 1973)

c) normal or shear stress distribution around strand resulting from helical twisting action (Salmons and McCrate 1973)

d) imprint of strand in concrete (Salmons and McCrate 1973)

Figure 1.2 Bond forces engaged in embedded deformed bars and strands.

Transferring the prestress forces into prestressed concrete members can lead to local concrete cracking due to excessive bursting stresses or splitting resulting from the radial component of the transfer of the strand force through bond. The bond behavior of 0.7-in. strand is largely unstudied. Although not anticipated to be significantly different in character from the behavior of smaller strands, the use larger strands and the presence of the resulting larger local forces raise concerns regarding increased local stresses and the requirements for spacing and confinement for 0.7-in. strands. The following sections address the current state of the art in terms of the bond behavior of seven wire prestressing strand.

1.4 Concrete Stresses Due to Strand Anchorage

Oh et al. (2006) describes the behavior of a prestressing strand embedded in concrete considering the strand as a solid cylinder and the concrete around it as a hollow cylinder. Compatibility is enforced at the steel-concrete interface. Right after releasing the prestressing

strand a radial stress develops affecting, and possibly cracking the surrounding concrete. Applying compatibility at the steel-concrete interface the following compatibility equation can be attained from Figure 1.3:

$$r_0 + u_0 = u_c + r_s \tag{1–5}$$

In which u_0 = displacement of steel; r_0 = initial radius of steel before prestressing; u_c = displacement of concrete; and r_s = radius of steel after prestressing due to initial prestress force f_{pi}.

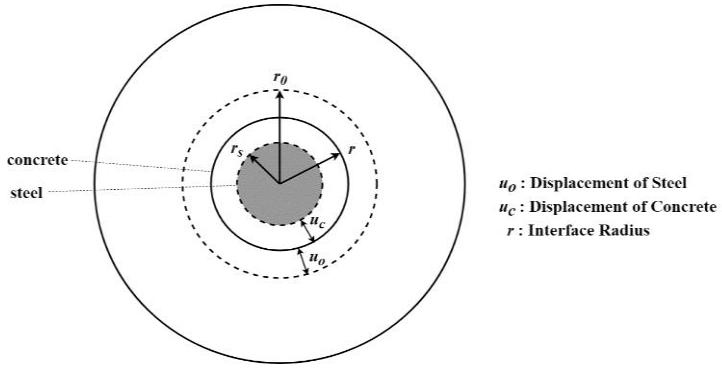

Figure 1.3 Schematic representation of Hoyer effect (Briere et al., 2013).

From the compatibility conditions of Eq.(1–5), an expression for the interface pressure, p, (see Figure 1.4a) can be obtained as follows (Oh et al. 2006):

$$p = \frac{r_0\left(1 - \upsilon_p f_{pz}/E_p\right) - r_s(1 - \upsilon_c f_{cz}/E_c)}{\left(1 - \upsilon_p\right)r_0/E_p \; + [\upsilon_c - (r_s^2 + c^2)/(r_s^2 - c^2)]r_s/E_c} \tag{1–6}$$

Where: v_p = dilation ratio of prestressing strand; E_p = Young's modulus of prestressing strand; f_{pz} = axial stress in prestressing strand a distance z from the free end of the concrete embedment (see Figure 1.4a); v_c = Poisson's ratio of concrete; E_c = Young's modulus of concrete; f_{cz} = axial stress in concrete a distance z from the free end; c = radius of concrete cylinder; c = clear cover + r_0 (see Figure 1.4b). r_s and f_{cz} can be expressed as follows:

$$r_s = r_0(1 - v_p f_{pi}/E_p)$$ (see Figure 1.5e) (1–7)

$$f_{cz} = f_{pz} r_o^2/c^2 \quad (1–8)$$

From the radial pressure at the interface, p, the radial and circumferential stresses, σ_r and σ_Θ, can be determined as follows:

$$\sigma_r = -p(1/c^2 – 1/r^2)/(1/c^2 – 1/R^2) \quad (1–9)$$

$$\sigma_\theta = -p(1/c^2 + 1/r^2)/(1/c^2 – 1/R^2) \quad (1–10)$$

Where R is the radial distance to the inner boundary of the isotropic (uncracked) region. For an isotropic concrete cylinder, $R = r_0$; this solution is shown schematically in Figure 1.4(b).

The stresses calculated at the strand-concrete interface and those near the free end of the embedment ($z = 0$) are very high and will result in radial cracking of the concrete, as shown schematically in Figure 1.4(b). The stress drops off very quickly with the radial distance from the strand, r. (Briere et al. 2013).

If the concrete cover is sufficient, this behavior results in a cross section having a cracked zone adjacent the strand and an uncracked annular region surrounding the cracked zone where the stresses are below the tensile capacity of the concrete, that is, anisotropic and isotropic material regions, respectively (Figure 1.4).

1.5 Hoyer Effect

Briere et al. (2013) provides a complete discussion of the "Hoyer effect". Much of the following discussion is adopted from this reference.

After releasing the prestressing force, the primary strand behavior affecting the transfer of prestressing force is called the Hoyer effect (Hoyer, 1939 and Hoyer and Friedrich, 1939). When a straight wire or "tendon" is placed under tension, the diameter of the strand decreases due to the Poisson effect (from $2r_0$ to $2r_s$ as shown in Figure 1.4). After the stress is released, the wire tries to return to its original diameter. If the wire is not encased by concrete, it returns to its original diameter ($2r_0$). Similarly, where the prestressing force has been fully developed (beyond the transfer length), the wire maintains its stressed diameter ($2r_s$; see Figure 1.4). In reality, the prestressing force does not develop linearly along the transfer length but varies as shown in Figure 1.4a). Thus, the diameter of the wire varies in a similar manner creating a wedge shape (Figure 1.4a). Radial forces will evolve along the concrete/wire interface (Figure 1.4). These restrain lateral expansion and provide friction to develop the bond strength in the interface thereby transferring the force from the wire to the concrete. This development in the bond strength between the wire and the concrete is called the "Hoyer effect".

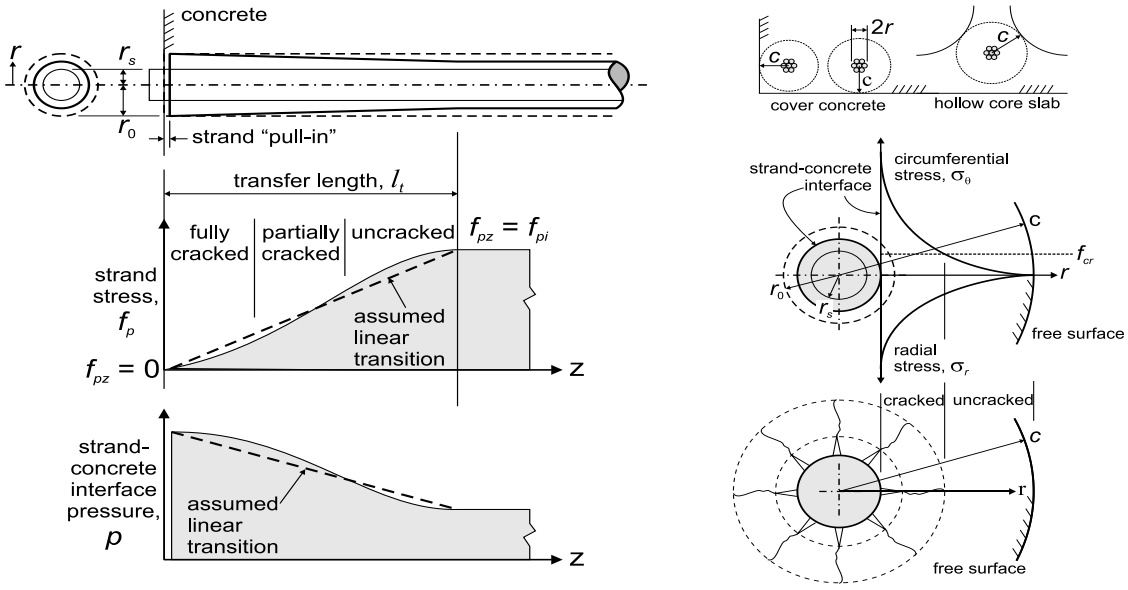

(a) Hoyer effect along transfer length

(b) Representations of stresses and cracking adjacent to embedded strand

Figure 1.4 Schematic representation of Hoyer effect (Briere et al., 2013).

In the case of multi-wire tendon, an additional "tightening" between the wires making up the strand also accompanies the application of prestress force (Figure 1.5). Comparable to the Poisson effect, the strand "unfurls" when the stress is relieved. This effect (also included in the Hoyer effect) helps to develop bond by producing radial forces and "locking" in mechanical bond correlated to the helical deformation of the strand.

In summary, the radial expansion of multi-wire strand enhances bond and therefore the transfer the prestress force to the concrete by (a) applying a force normal to the strand-concrete interface, increasing friction; and (b) evolving a wedge-like geometry (Figure 1.4a) which will increase the efficiency of this normal force. This evolution of these bond effects are a function of the surrounding concrete.

When the radial force is in compression, directed into the concrete, a perpendicular circumferential tension force is developed (Figure 1.4b). These forces can lead to radial cracking emanating from the strand (Figure 1.4b), which degrades the transfer mechanism. This issue can be more serious if strands are closely spaced; interaction between adjacent strands may lead to sever cracking and spalling, especially near the ends of girders where strand stresses are being transferred. The partial debonding of strands at the ends of girders can decrease the cumulative effect of transferring multiple strands at the same location (Shahrooz et al. 2017).

1.6 Dilation of Prestressing Strand

As described in 1.5, a force normal to the strand/concrete interface develops along with the transfer length. This normal force is increased by the wedge-like action as shown in Figure 1.4a. The Poisson's ratio of the prestressing steel does not completely characterize the dilation of seven-wire prestressing strand because dilation is not only resulting from tension in the strand. The strand is additionally experiencing some torsion and 'tightening' of the helical outer wires, starting with 'filling' any annular space in the strand (Figure 1.5a) and then interacting with each other at their points of contact; this progression is shown in Figure 1.5. The outer helical wires 'tighten' and bear on the straight center wire resulting in greater dilation of the center wire (Figure 1.5d).

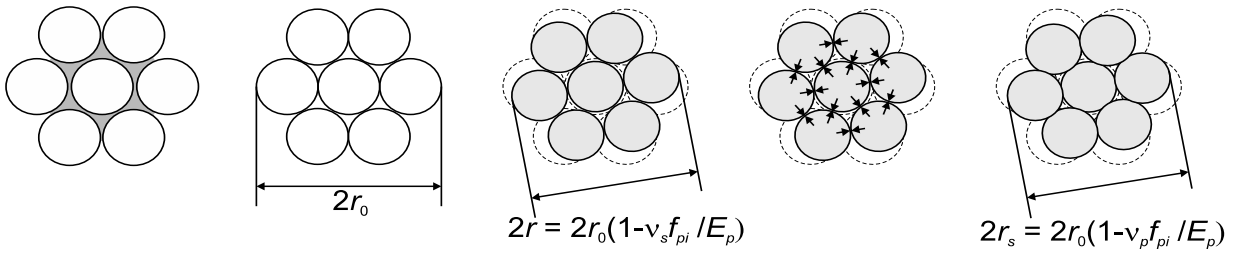

(a) Annular space (if any) between wires is first closed

(b) Unstressed, low-relaxation seven-wire strand

(c) Poisson effect results in contraction of wires and tightening of helical wires

(d) Contact stresses, particularly those compressing the center straight strand

(e) Stressed seven-wire strand

Figure 1.5 Contraction behavior of seven-wire prestressing strand (Briere et al., 2013)

Machida and Durelli (1973) describe the geometry of an unstressed prestressing strand as one in which the helical wires are "slightly elliptical", resulting in a small clearance between the center wire and the helical wires if the diameters of all wires are the same. It is not clear from Machida and Durelli whether this geometry, and the associated annular space, is applicable to both stress-relieved and low-relaxation strand. Briere et al. (2013) contend that the annular space is negligible in modern low-relaxation strand since this strand is tempered with the strand under tension and the central straight wire has a marginally larger diameter (ASTM A416).

As discussed in 1.5, the stressed radius of the strand, r_s is critical to the stress generated in the concrete. Thus, the combined effects of tightening, individual wire interaction and Poisson effect in each wire, results in strand dilation. When the prestress force is released, these effects are reversed, but in the presence of confining concrete. These effects can, nonetheless, be described using Eqs (1–6) and (1–7) with ν_p interpreted as the apparent dilation ratio of the strand, necessarily greater than the Poisson's ratio for steel.

In an attempt to quantify v_p, Briere et al. (2013) report an experimental procedure for determining the dilation of prestressing strand (shown in Chapter 3, Figure 3.1); they reported results of tests of 0.5-in. and 0.6-in. low-relaxation strand. Using the same methodology, a limited number of tests on 0.7-in. low-relaxation strands were conducted as part of the development of this project. The values of ν_p = 0.40, 0.34, and 0.32 were found for 0.5-in., 0.6-in., and 0.7-in. strand, respectively. Chapter 3 reports a more extensive investigation of 0.7-in. strand dilation. The inverse relationship between 7-wire strand diameter and apparent dilation is attributed to the tightening effect being proportionally greater for smaller helical wires having the same lay angle (Briere et al., 2013) confirming the theoretical geometric analysis of Machida and Durelli (1973).

1.7 Strand Spacing

Applying the approach described in Section 1.4, it is clear that the spacing between strands will affect behavior. By convention, prestressed concrete bridge girders have strands spaced at 2 in. on center. Based on previous studies, there is no guidance for the spacing requirements on the 0.7-in. prestressing strands.

The basis for strand spacing requirements requires context. ACI 318-63 states that "minimum clear spacing between pretensioning steel at each member end shall be…three times the diameter of strands…" This requirement corresponds to a required strand spacing of $4d_b$. Much of the basis for the 1963 requirement seems to come from Hanson and Kaar (1959) who reported 250 grade strand having diameters up to 0.5 in. There is no mention of strand spacing in the multi-strand specimens tested; one must assume that the 0.5-in. strand was tested with $4d_b = 2$ in. spacing (this assumption is consistent with specimen dimensions). It is unclear whether smaller 0.25-in. and 0.375-in. strand was tested with spacing of $4d_b$ or 2 in.

In 1988, the Federal Highway Administration (FHWA) issued a moratorium on the use of 0.6-in. strands and required a minimum spacing of $4d_b$ be applied. This was because the only available data at that time was for 0.5-in strands and critically, only for 250 grade stress-relieved strand. This encouraged Lane (1998) to investigate the issue of adequate strand spacing. Lane's study resulted in FHWA lifting its moratorium in 1996 and permitting the use of 0.6-in. strands with spacing less than $4d_b$. The permitted spacing was 2 in. ($3.33d_b$) for 0.6-in. strand and 1.75 in. ($3.5d_b$) for 0.5-in. strand. The reduced permitted spacing is based on satisfactory test results of sixteen AASHTO Type II girders having either 5 or 10 ksi concrete (Lane, 1998).

Another significant test program (Unay et al., 1991) considered 0.5 and 0.6-in. strand at spacing of 2 in. ($4d_b$ and $3.33d_b$, respectively) and 2.25 in. ($4.5d_b$ and $3.75d_b$, respectively). In this study, the edge distance for all strands was 2.5 in. No difference was seen in performance, and it was concluded that 2-in. spacing was adequate; the conclusion reads: "the 2.25 inch spacing of 0.6-inch strand had no effect on transfer length." Shahawy (1999) similarly concludes that "a spacing of 2 in. is acceptable, irrespective of strand size, up to 0.6-in. dia." The specimens reported in Shahawy were provided with 2-in. spacing for both 0.5-in. or 0.6-in. strands.

In summary, most studies have used 2-in. spacing for both 0.5-in. and 0.6-in. strand. Only one study can be found that (a) uses smaller, 1.75-in., spacing for 0.5-in. strands; and (b) uses larger, 2.25-in. spacing for 0.6-in. strands. The "conventional" 2-in. strand spacing appears to be a legacy of the $4d_b$ requirement prescribed in 1963.

Nonetheless, using 2 in. spacing for 0.7-in. strands remains a concern. There are limited studies on NU girders with 0.7-in. strands spaced at 2 in. which show adequate performance (Morcous, 2013; Morcous et al., 2014; Shahrooz et al., 2017). However, in Morcous (2013) and Morcous et al. (2014), the strands were only prestressed to an initial prestress of $0.64f_{pu}$, lower than the typically used $0.75f_{pu}$.

Based on the discussions of Sections 1.3 to 1.5, splitting resistance is partially a function of clear spacing. In this case, the ratios presented in Table 1.2 are obtained. The Hoyer dilation, v_p, represents a measure of the applied radial strain; values reported in Section 1.5 are adopted in the Table 1.2. The normalized splitting stress is a simple approximation (shown in Table 1.2) that indicates the expected radial splitting stress of a 0.7-in. strand at 2 in. is 30% greater than a 0.5-in. strand at 2 in. Increasing the spacing to 2.25 in. mitigates most of this increase. However, 0.7-in. strands at 2 in. results in similar stress as 0.5-in. strands at 1.75 in. Much of this comparison hinges on the Hoyer dilation which falls with increasing diameter and whose determination is an objective of this study (Chapter 3). The finite-element analyses presented in (Chapter 5) suggests the same trends shown in Table 1.2.

Table 1.2 Effect of spacing on splitting stress.

Strand d_b (in.)	Spacing s (in.)	Clear spacing $s - d_b$ (in.)	Hoyer dilation v_p	Normalized splitting stress $(v_p \times d_b)/(s - d_b)$	
0.5	1.75	1.25	0.40	0.160	+20%
0.5	2.0	1.50	0.40	0.133	baseline
0.6	1.75	1.15	0.34	0.186	+39%
0.6	2.0	1.40	0.34	0.146	+10%
0.6	2.25	1.65	0.34	0.124	-7%
0.7	1.75	1.05	0.32	0.213	+60%
0.7	2.0	1.30	0.32	0.173	+30%
0.7	2.25	1.55	0.32	0.143	+7%

1.8 Effects of Embedding Strand in Lightweight Concrete

The previous discussion is based on the behavior of conventional normal weight concrete (NWC). Lightweight [aggregate] concrete (LWC), however, is receiving greater attention for its ability to reduce the weight of long bridge girders. Although it is occasionally specified, the use of LWC in prestressed bridge girder elements remains relatively uncommon except for very long spans. From a design perspective, the gains made in reduced weight are offset by reductions in concrete strength (Ball, 2019).

There is comparatively little study of strand performance when used to prestress LWC. Greene and Graybeal (2019) assembled a dataset of 350 NWC and 250 LWC girders to study the effect on transfer length. An analysis of the database was used to develop potential revisions to provisions related to LWC and NWC within Section 5 of the AASHTO LRFD Bridge Design Specifications. Greene and Graybeal confirmed the existing AASHTO definition of LWC as "concrete containing lightweight aggregate conforming to AASHTO M195 and having an

equilibrium density not exceeding 0.135 kcf, as determined by ASTM C567." Thus 135 pcf is threshold between LWC and NWC. They also confirmed the applicability of AASHTO Eq. 5.4.2.4-1 for modulus of concrete, E_c, as appropriate for unit weights from 90 to 155 pcf:

$$E_c = 120{,}000K_1 w_c^{2.0} f'^{0.33}_c \quad (1\text{–}11)$$

Greene and Graybeal (2019) propose revisions to strand transfer length. They propose revising the existing NWC transfer length Eq. (1–1) to that proposed by Ramirez and Russell (2008): Eq. (1–3). For LWC, Greene and Graybeal propose:

$$l_t = 220{,}000 d_b / E_{ci} \geq 40 d_b \quad (1\text{–}12)$$

Figure 1.6 shows transfer lengths calculated for a range of unit weight, w_c, from 100 to 155 pcf and concrete strength, f_c', from 5 to 12 ksi. Eq.(1–3) is used for $w_c \geq 135$ pcf and Eq. (1–12) is applied for $w_c < 135$ pcf.

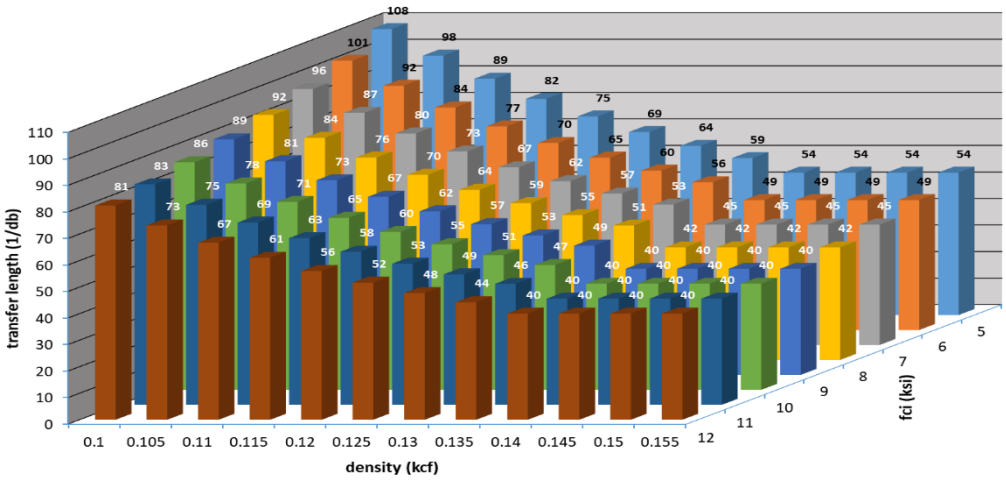

Figure 1.6 Effect of concrete on the prestressing strand transfer length (data based on Greene and Graybeal, 2019)

From Figure 1.6 it is observed that $l_t < 60d_b$ for all NWC shown ($w_c > 0.135$ kcf) and $l_t > 60d_b$ for LWC having lower density and lower strength. Realistically, for LWC, $l_t > 40d_b$ (at $w_c = 0.135$, $f_{ci} \geq 16$ ksi to achieve $l_t \leq 40d_b$). LWC has longer transfer length than NWC (which may

exceed $60d_b$ in some reasonable cases). The data reported by Greene and Graybeal is mostly 0.5 and 0.6-in. strand. There are some limited data for 0.62 and 0.75 in. strand in NWC. No data appears to suggest anything other than the linear correlation between transfer and development lengths and strand diameter implied by AASHTO (Eqs (1–1) and (1–2)).

1.9 Girder Stability

Prestressed concrete girders using 0.7-in. diameter strand may become longer and more slender than current beam types using smaller diameter strands (Ball 2019). Therefore, lateral stability should be checked during all project phases: handling, transportation, erection, and in service. Usually fabricators are responsible for stability checks. However, the designer should consider and assess lateral stability during design, particularly when a non-standard or more slender girder is selected. The designer should verify assumed support and stability parameters (including transport stiffness, elevation, height of center of gravity for girder, etc.) with local fabricators, contractors and other designers. Procedures for checking lateral stability are addressed in PCI (2015) and will be discussed in Chapter 6. Because of the intimate connection between parameters and their use in stability checks, and to avoid repetition, the literature review on this topic is integrated into the description of parameters in Chapter 6.

1.10 Objectives

The objectives of this research are to study the bond behavior of 0.7-in. diameter prestress strand. This will be accomplished in Chapter 2 through 5. The stability behavior associated with potentially longer girders resulting from the use of 0.7-in. strand is addressed in Chapter 6. This thesis is organized as follows:

Chapter 2 presents characterization of materials and geometric properties of 0.7-in., 0.6-in., 0.5-in. and 3/8-in. strands used in experimental studies reported in Chapters 3 and 4.

Chapters 3 presents characterization of dilation of 0.7-in., 0.6-in., 0.5-in. and 3/8-in. strands to determine Hoyer effect and confirm differences and trends identified by Briere et al. (2013) who considered only 0.6-in. and 0.5-in. strand.

Chapter 4 presents characterization of bond properties of 0.7-in., 0.6-in., 0.5-in. and 3/8-in. strands using beam end tests (adopted from ASTM A944 procedure) and the effect of providing 90-degree anchorage to unstressed strand. Based on the data collected the utility of providing 90-degree strand anchorages into cast-in-place end diaphragms is assessed.

Chapter 5 presents an analytic finite element-based study (using ABAQUS) to simulate local effects of strand diameter and dilation properties with the objective of assessing appropriate strand spacing requirements for 0.7-in. strand.

Chapter 6 presents a series of parametric studies to assess potential effects on girder stability and identify limitations that may arise from increased prestress forces in girder sections resulting from the use of 0.7-in. strands.

Chapter 7 summarizes findings of this study and integrates these to develop recommendations for the adoption of 0.7-in. prestressing strand in highway bridge girder design standards, focusing on aspects of bond, transfer and development lengths, and stability. Chapter 7 also identifies areas requiring further study.

2.0 Geometric and Material Characterization of Seven Wire Prestressing Strand

This Chapter presents characterization of materials and geometric properties of strands used in experimental studies reported in Chapters 3 and 4. Samples of four strand sizes – 0.7-in., 0.6-in., 0.5-in. and 3/8-in. – were received (Figure 2.1). Samples of the same 0.6 and 0.7-in. strand having 90-degree hooks were also received (Chapter 4). All strand samples of the same size come from the same spools; therefore, little variation in behavior is anticipated. All but the 0.7-in. samples were obtained from the same manufacturer.

top to bottom: 0.7-in., 0.6-in., 0.5 in. and 3/8 in.

0.7-in.

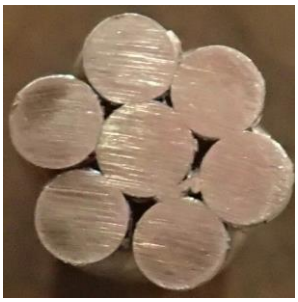

0.6-in.

0.5 in.

3/8 in.

Figure 2.1 Strands as received

2.1 Strand Geometry

Strand diameter (d_b) and individual wire (d_c and d_h; it is noted that in seven wire strand, the central straight wire is drawn slightly larger than the six helical wires) diameters (Figure 2.2a) were obtained using a digital caliper. Twist angle, β, as seen in Figure 2.2b was measured from photographs and confirmed with measurements of the wire pitch, $\bar{s}$:

$$\beta = tan^{-1}(\pi d_i/s) \approx tan^{-1}(2\pi d_b/3s) \quad (2–1)$$

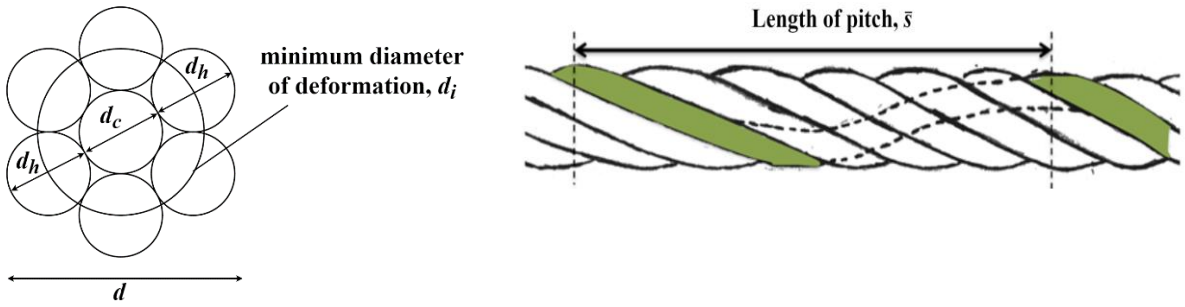

(a) diameters of strand and wires (b) length of pitch in a cable

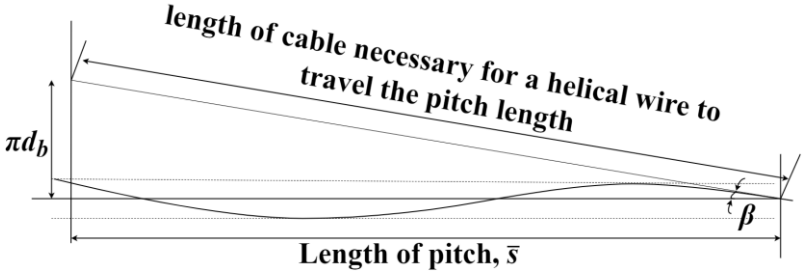

(c) pitch angle, β, for a helical wire

Figure 2.2 Helical deformation of strand (after Briere et al. 2013)

Seven-wire strand, regardless of its dimension, has helical deformations formed by the helical wires; these deformations are in proportion to the strand diameter and are the means of affecting mechanical interlock with the surrounding concrete. A measure of relative rib ratio, f_R,

proposed by Rehm (1961) is given by Eq.(2–2). This ratio specifically addresses helical deformation patterns and a variation of this ratio is given by EuroCode 2 (BSI 2014).

$$f_R = k(d^2 - d_i^2)sin\beta / 4d_i\bar{s} \quad (2–2)$$

In which k is the number of helical elements, $k = 6$ for seven wire strand; d and d_i are the outer and minimum diameter of the deformations, respectively; for strand: $d = d_b$ and $d_i = d_c + d_h$; β is the helix or lay angle; and s is the pitch. All parameters are shown in Figure 2.2.

The values of relative rib area calculated using Eq. (2–2) are given in Table 2.1. It is seen that the relative rib area for 0.6, 0.5 and 3/8 in. strands are quite similar and the value for the 0.7-in. strand is 90% of the value calculated for the smaller strands. This would suggest that the mechanical interlock of the 0.7-in. strand is marginally less efficient than that of the other strand sizes.

2.2 Material Properties

To determine the tension properties of the strands, three randomly selected strands of each diameter were used. Ultimate capacity, f_{pu}, was obtained (see Table 2.1) from direct tension tests (Figure 2.3). The tests were conducted based on ASTM A1061 except that strand chucks were used as anchors (not compliant with ASTM A1061). Load displacement curves are shown in Figure 2.3d; all show essentially identical behavior.

There were two types of failures observed: unraveling of the strand (Figure 2.3b) or the strand breaking at the chuck (Figure 2.3c). These failures – an artifact of using strand chucks – result in marginally lower strand capacities. Nonetheless, all strands met the minimum 270 ksi

breaking strength requirements of ASTM A416 although the 0.7-in. strands only barely meet the '$0.90f_{pu}$ = 243 ksi at 1% elongation' requirement (Table 2.1). Elongation and relaxation were not measured in the tension tests. Due to the need for appropriate instrumentation, tensile modulus (reported in Table 2.1) was determined in subsequent Hoyer effect tests reported in Chapter 3.

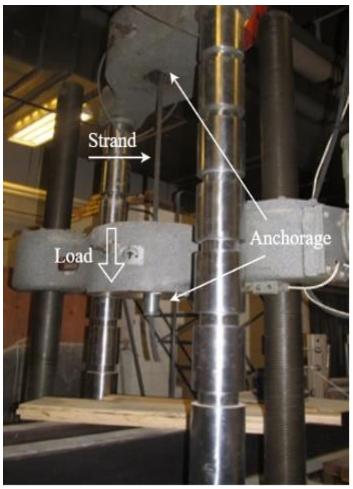

a) tension test set up

b) strand unravelling failure

c) wire fracture in strand chuck

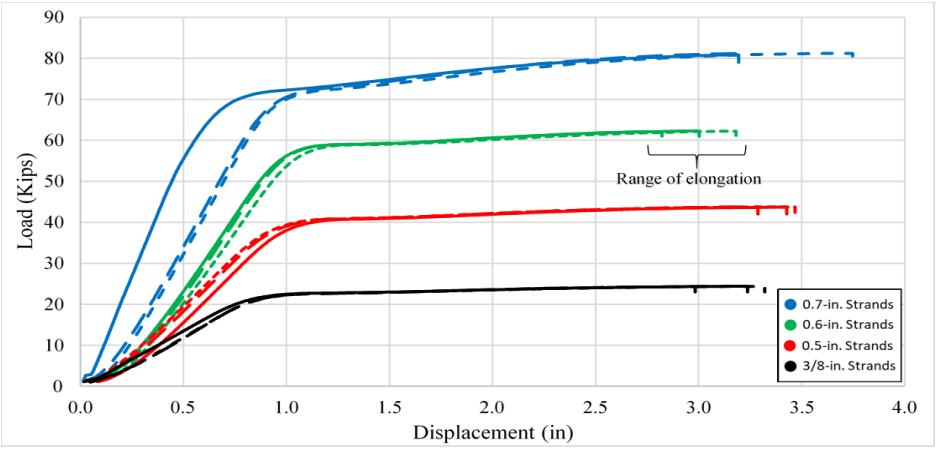

d) acquired load versus cross-head displacement curves

Figure 2.3 Tension test setup

Stress strain curves are shown in Figure 2.4. From these, best-fit Ramberg-Osgoode (R-O) parameters are fitted Eq.(2–3). R-O functions are used to describe strand behavior since these are continuous and more easily integrated into analytical studies than piece-wise functions.

$$f_p = E_p \varepsilon_p \left(A + \frac{1-A}{\left[1+\left(B\varepsilon_p\right)^C\right]^{1/C}} \right) \leq f_{pu} \tag{2–3}$$

Table 2.1 Strand dimensions and material properties (COV in brackets).

nominal strand diameter, d_b	in.	**0.7**	**0.6**	**0.5**	**3/8**
strand manufacturer		B	A	A	**A**
strand geometry					
nominal strand area, A_{ps}	in^2	0.294	0.217	0.153	0.085
diameter of center wire, d_c	in.	0.239	0.206	0.170	0.128
diameter of helical wire, d_h	in.	0.231	0.198	0.165	0.123
pitch, s	in.	9.93	8.02	6.76	5.07
twist angle, β	deg.	8.4	8.9	8.8	8.8
relative rib area, f_R, Eq.(2–2)		0.0085	0.0095	0.0093	0.0093
mechanical properties					
measured ultimate capacity, f_{pu}	ksi	276 (0.003)	287 (0.001)	286 (0.001)	287 (0.002)
measured capacity at 1% elongation	ksi	244 (0.016)	269 (0.000)	260 (0.004)	257 (0.023)
measured tensile modulus obtained during Hoyer tests, E (0.2-0.5f_{pu})	ksi	31206 (0.069)	31985 (0.019)	30415 (0.035)	30234 (0.036)
Ramberg-Osgoode E_p	ksi	30000	30000	30000	30000
Ramberg-Osgoode parameter A		0.060	0.030	0.035	0.030
Ramberg-Osgoode parameter B		124	111	114	113
Ramberg-Osgoode parameter C		12	15	11	10

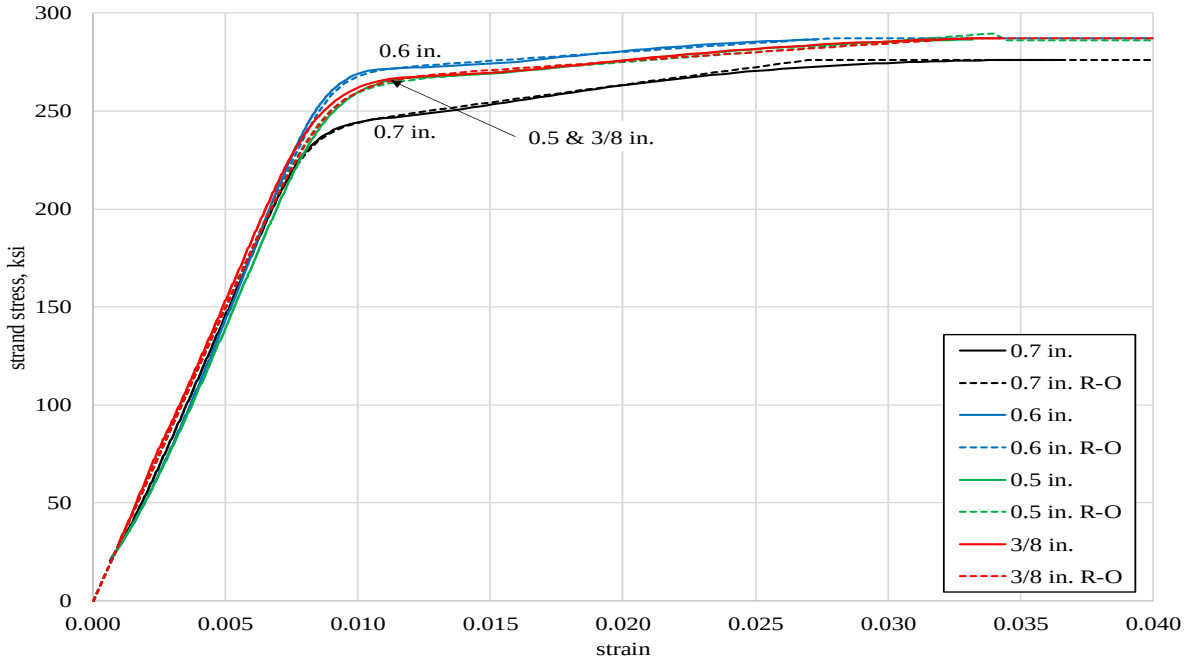

Figure 2.4 Representative stress-strain curves and fitted Ramberg-Osgoode functions for strands tested.

3.0 Characterization of Strand Dilation (Hoyer Effect)

The Hoyer effect is understood to improve transfer length behavior but is unlikely significant in terms of ultimate development length. In this study, the Hoyer effect is of more interest in terms of the radial forces generated at girder ends and the resulting likelihood of cracking. Accurate assessment of the Hoyer effect is required for modeling (Chapter 5). The assessment of dilation is not only affected by Poisson's ratio but also the 'tightening' of the helical wires and the effects of the bearings between these wires. The experimental approach developed by Briere et al. (2013) is adopted to assess the dilation behavior of all four strand sizes described in Chapter 2.

Limited Hoyer effect testing had been performed prior to this study; a summary of previous available data is given in Table 3.1 (none of this was determined using the strands reported in Chapter 2). The present study afforded the opportunity to retest a few strands from the earlier 2013 Briere et al. study. As seen in Table 3.1, the 0.6 strand behaved identically while there was some apparent reduction in dilation ratio of 0.5 in. strands. The differences are believed to be associated with improvements made to the clip gage assembly for the current study.

Table 3.1 Data from previous Hoyer tests.

nominal strand diameter, d_b	in.	**0.7[1]**	**0.6[2]**	**0.5[2]**
nominal strand area, A_{ps}	in^2	0.294	0.217	0.153
measured ultimate capacity, f_{pu}	ksi	282	278	306
measured tensile modulus, E	ksi	29800	29200	31100
twist angle, β	deg.	8.4	8.2	8.1
average dilation ratio		0.32	0.34	0.40
average dilation ratio of retested strands only[2]		-	0.34	0.37
retests of Briere[2] strands conducted during this study		-	0.34	0.32

[1] sample strands tested to support proposal for present study
[2] Briere et al. (2013)

In this study, tests identical to those described in Briere et al. (2013) were conducted (Figure 3.1). Five strands of each diameter were tested. Each strand was tested with five load repetitions, sufficient to establish a steady state load-strain-dilation response. Typically, for strand that has not been previously stressed, the initial stressing operation is a 'shakedown' and larger dilation ratios are obtained. Second and subsequent stress cycles approach a steady state behavior. Each strand is stressed to $0.8f_{pu}$ and released while measuring both axial strain (strain gauge) and transverse dilation (clip gage).

3.1 Test Set-up and Instrumentation

Strand samples are anchored using strand chucks and stressed using two 60 kip hydraulic cylinders in a self-reacting frame as shown in Figure 3.1. A clip gage is used to measure dilation and an electrical resistance strain gage is used to measure longitudinal strain. Load is determined directly from cylinder pressure. Since the test is determinate and self-reacting, the applied strand force is equal to the force in the cylinders.

The clip gage (Figure 3.1a and c) used does not measure dilation strain directly, but rather the change in dimension of the strand diameter. The diameter is measured with a precision of 0.000014 in.; this is equivalent to a strain resolution (in microstrain) of $14.3/d_b$. Therefore, the strain resolution is improved for larger strand diameter strands (20 με for 0.7-in. strand and 38 με for 3/8 in. strand).

A single longitudinal strain gage is aligned along the axis of a helical wire (Figure 3.1a). Therefore, a correction is necessary to transform the strain measured along the axis of the helical

wire, ε_h, to the strain oriented along the longitudinal axis of the strand, ε_c. (Machida and Durelli 1973):

$$\varepsilon_c = \varepsilon_h / \cos^2\beta \qquad (3\text{–}1)$$

The correction given by Eq.(3–1) is applied prior to calculating dilation ratio and offset strains reported in Table 3.2. The dilation ratio is calculated as the ratio of transverse (dilation) strain, ε_t to the longitudinal strain oriented along the strand axis, ε_c.

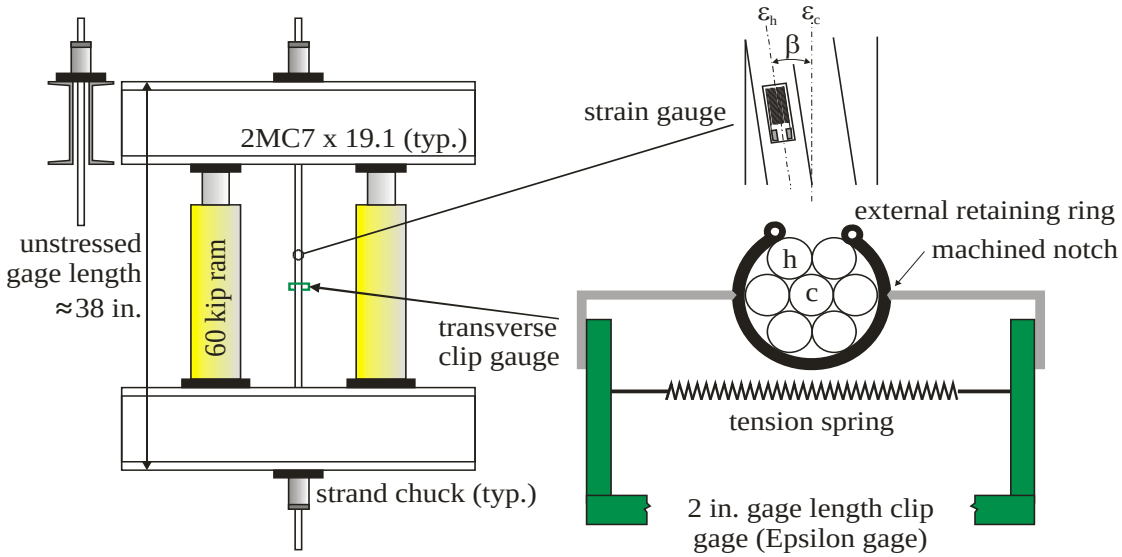

a) schematic diagram of test setup and instrumentation

b) test setup

c) clip gage

Figure 3.1 Hoyer effect test setup and instrumentation

3.2 Test Results

Dilation ratio from the first cycle (initial prestress) and the average ratio obtained over five cycles is given in Table 3.2. The average ratios are expected to be smaller due to the 'shakedown' effect. The longitudinal offset strain following the first cycle and after all five cycles are complete is also reported in Table 3.2; the majority of offset strain occurs in the first cycle. Complete data from all 20 tests is provided in Appendix A.

Table 3.2 Results from Hoyer testing (COV in brackets).

nominal strand diameter, d_b	in.	**0.7**	**0.6**	**0.5**	**3/8**
first cycle dilation ratio		0.373 (0.043)	0.312 (0.124)	0.346 (0.145)	0.301 (0.289)
average dilation ratio (5 cycles)		0.333 (0.180)	0.302 (0.169)	0.297 (0.229)	0.289 (0.198)
longitudinal strain offset following initial cycle	με	522 (0.142)	317 (0.182)	201 (0.417)	139 (0.382)
longitudinal strain offset following five cycles	με	805 (0.411)	311 (0.172)	223 (0.389)	201 (0.165)

3.3 Discussion of Hoyer Test Results

From the results reported in Table 3.2, it can be seen that the dilation ratio is not just affected by the Poisson effect. As explained in Section 1.5, the tightening and bearing between the wires will play a part in the dilation of the strand. The Poisson's ratio for steel is conventionally given as 0.27 to 0.30. From Table 3.2 and especially with bigger diameter strands such as 0.6-in. and 0.7-in., it is clear that the dilation ratio exceeds Poisson ratio. The effect of dilation on radial stresses will be simulated later in Chapter 5 using finite element method.

The trend of decreasing dilation ratio effect with increasing strand diameter reported by Briere et al. (2013) and seen in Table 3.1 is not evident in the present data. Indeed, dilation is relatively uniform in the present study with the 0.7-in. strand, if anything, exhibiting greater dilation. The reason for this divergence from previous data is unknown.

4.0 Characterization of Bond (Beam End Tests)

Beam end tests measure the force required to produce a specified slip of a strand (or bar) embedded in concrete. The test is a means of estimating average bond capacity over the embedded length and comparing bond performance across parameters. The ASTM A944 beam end test, or variations of this test has been used by many researchers to assess bond. The test is primarily an A-B comparison test and should not be interpreted as providing a definitive average bond stress value. The longer the embedment used in this test, the better understanding of the development of the strand being tested. Nonetheless, it is impractical to test entire development lengths and, conventionally, relatively short embedment lengths are provided.

4.1 Test Set-up and Instrumentation (Straight and 90^{o})

Thirty beam end tests were conducted: twelve straight strand arrangements (duplicated) with three development lengths ($20d_b$, $30d_b$, and $40d_b$) using normal (NWC) and light weight (LWC) concrete. and six 90^{o} hooked strand embedments. The test specimen and loading arrangement is shown in Figure 4.1 and the matrix of tests is given in Table 4.1. All dimensions and internal reinforcement are compliant with ASTM A944 except for five tests having longer embedment, for which 6 in. is added to the 25 in. standard specimen length (see Table 4.1 and Figure 4.1a). The longer specimens also contained an additional pair of #4 stirrups along their lengths (Figure 4.1a).

The 90-degree hooks were formed around a 3.5 in. diameter mandrel for both strand sizes, 0.6-in. and 0.7-in. This diameter is smaller than that required for standard reinforcing bar hooks which would require 3.75 in. and 4.5 in. for 0.6-in. and 0.7-in. strand, respectively. The length of the hook "tail", **A** in Figure 4.1a and Table 4.1 was 10 in. and 12 in. for 0.6-in. and 0.7-in. strand, respectively. These are the values required for standard reinforcing bar hooks and ensure that the straight portion of the tail exceeds $12d_b$. The smaller bend diameter used for the strand is not believed to be a concern since the standard bend diameter is prescribed to ensure that there is no cracking of a solid bar when bent. The individual wires of a seven-wire strand will slip past each other, and thus each wire is bent individually – this permits a smaller diameter to be used without affecting cracking of the wires.

Table 4.1 Beam end test matrix and specimen identification.

Strand	concrete	straight strand embedment length and specimen labels			90° hook embedment and specimen labels			
		$l_e = 40d_b$	$l_e = 30d_b$	$l_e = 20d_b$	$l_h = 30d_b$	$l_h = 20d_b$	$l_h = 10d_b$	**A**
0.7-in.	NWC 1	l_e = 28 in.[a] 7-40-A/B	l_e = 21 in. 7-30-A/B	l_e = 14 in. 7-20-A/B	l_h = 21 in.[a] H7-30	l_h = 14 in. H7-20	l_h = 7 in. H7-10	12 in.
	NWC 2	-	7-30-C/D	-	-	-	-	-
	LWC	-	L7-30-E/F	-	-	-	-	-
0.6-in.	NWC 1	l_e = 24 in.[a] 6-40-A/B	l_e = 18 in. 6-30-A/B	l_e = 12 in. 6-20-A/B	l_h = 18 in. H6-30	l_h = 12 in. H6-20	l_h = 6 in. H6-10	10 in.
	NWC 2	-	6-30-C/D	-	-	-	-	-
	LWC	-	L6-30-E/F	-	-	-	-	-
0.5 in.	NWC 1	-	-	l_e = 10 in. 5-20-A/B	-	-	-	
3/8 in.	NWC 1	-	-	l_e = 7.5 in. 3-20-A/B	-	-	-	
[a] requires nonstandard 31 in. long specimen								

All strand samples were placed in the concrete in their as-received conditions. All strands appeared clean, free of laitance, oil, residue, and corrosion. While samples were stored in the laboratory prior to testing in a controlled environment, there is no history or chain of custody available for the samples before their receipt. Due to the relatively lower bond stress observed for

the 0.6-in. strand in NWC1 (see Table 4.3) the strand used in NWC2 and LWC specimens was wiped clean with a commercial degreasing agent prior to use. Although the 0.6-in. strand is identical in all tests, the improvement in results (Table 4.3), despite the lower concrete strength suggests that this strand may have been contaminated to some degree when used in NWC1.

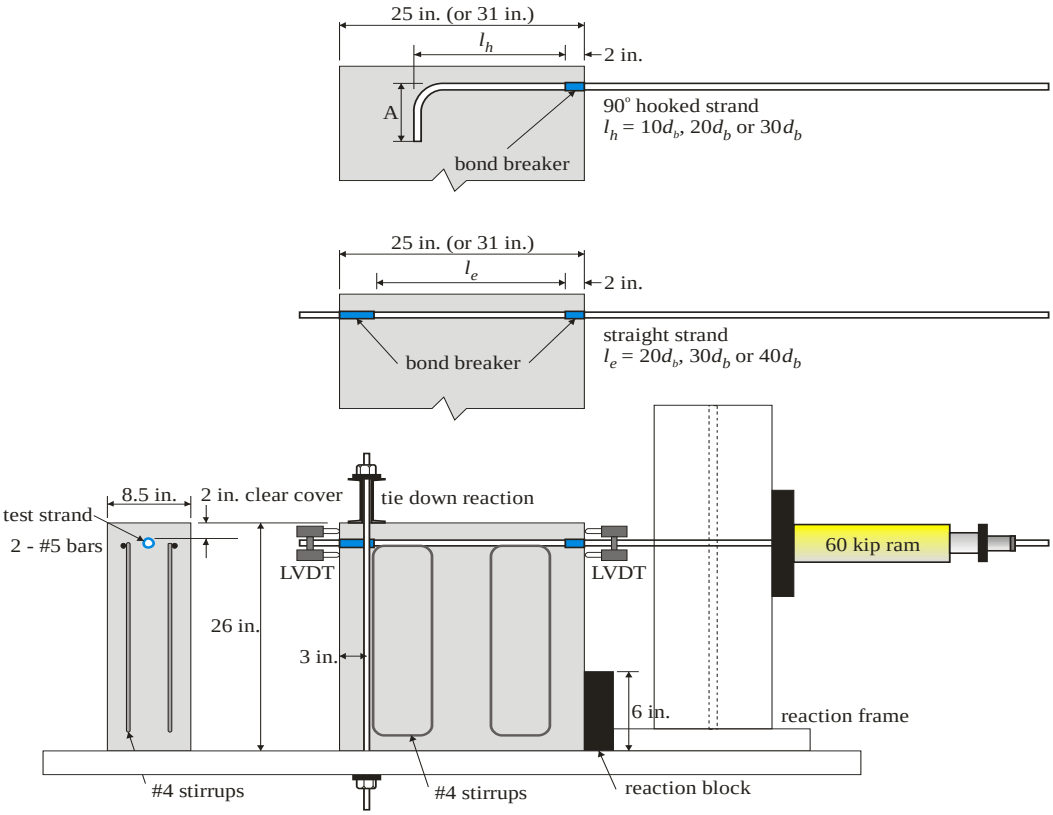

a) test arrangement and specimen details

b) test set up showing single 60 kip (left) and two ram (120 kip) arrangement used for three high force tests (right)

c) free end of strand showing slip transducer

Figure 4.1 Beam End Test

The testing frame (Figure 4.1) was designed around a large self-contained reaction frame. Load is applied concentrically to the strand using a 60-kip hollow-core hydraulic ram (two rams in parallel are required for specimens 7-40, 6-40 and H7-30). Hydraulic pressure is used to calculate the applied load with a precision of 70 lb. Bond breakers (Figure 4.1a) consist of 0.75 in. ID pultruded glass fiber reinforced tubes for the 0.6 and 0.7-in. strand, and plastic strand debonding tube (sheathing) for the 0.5 in. and 3/8 in. strands. LVDT collars (Figure 4.1c) are located at the loaded and free ends of the embedded strands to measure slip. For straight strand beam end test, slip is measured using an LVDT collar having a stroke of 0.5 in. and precision of 0.00005 in., far in excess of that required by ASTM A944 (0.001 in.). For the hook tests, the rear LVDT cannot be used. For these tests, a longer stroke transducer (1.5 in.) is used at the loaded end of the hook, resulting in a resolution of 0.00015 in. for these tests.

4.1.1 Concrete Material Properties

Three concrete mixes were used – two normal weight (NWC) and one lightweight (LWC). All mixes were specified as 5 ksi ready mix concrete having ¾ in. aggregate top size. The NWC mix designs were nominally identical although cast 19 months apart; the second NWC2 batch was required for additional control specimens for the LWC tests. The LWC – using expanded shale coarse aggregate – was otherwise intentionally maintained as close to the companion NWC2 mix design as possible. Mix design and material properties of each batch are given in Table 4.2. Material properties – compressive strength and split cylinder strength – were determined from three standard cylinder tests in each case. NWC1, from which most specimens were cast (see Table 4.1), was a 4 cy batch. NWC2 and LWC were cast from 1 cy batches – although the latter batches were larger than was necessary, the larger batch better assures consistency at the ready-mix plant.

All specimens were cured in ambient laboratory conditions. As seen in Table 4.2, NWC2 did not achieve its specified strength. Figure 4.2 shows some views of the specimens prior to concrete placement. Specimens are cast (Figure 4.2) inverted to the manner in which they are tested (Figure 4.1) – the strand is located at the bottom of the cast and has 24 in. concrete placed above it.

Table 4.2 Concrete mix designs and material properties.

Mix Design	**NWC 1**	**NWC 2**	**LWC**
Type I/II cement (ASTM C150)	574 lb/cy		574 lb/cy
fine aggregate (ASTM C33)	1205 lb/cy		1285 lb/cy
#67 coarse aggregate (ASTM C33)	1700 lb/cy		900 lb/cy (expanded shale)
GGBFS (ASTM C989)	101 lb/cy		101 lb/cy
AE: Sika Air 260 (ASTM C260)	4 oz/cwt		3.5 oz/cwt
water	270 lb/cy (w/c = 0.40)		270 lb/cy (w/c = 0.40)
slump	5.5 in.		5.75 in.
air content	6.7%		6.5%
unit weight	142.8 pcf		116.0 pcf
measured unit weight	not measured	132.5 pcf (COV = 0.007)	115.0 pcf (COV = 0.013)
Material Properties			
28 day compressive strength (ASTM C39)	f_c' = 6895 psi (COV = 0.03)	f_c' = 3369 psi (COV = 0.08)	f_c' = 5196 psi (COV = 0.01)
56 day compressive strength (ASTM C39)	f_c = 7553 psi	f_c = 4075 (COV = 0.04) obtained from cores	f_c' = 5750 psi (COV = 0.06)
84 day compressive strength (ASTM C39)	f_c = 7862 psi (COV = 0.02)	n.a.	n.a.
28 day split cylinder strength (ASTM C496)	595 psi = $7.16\sqrt{f_c'}$ (COV = 0.16)	413 psi = $7.12\sqrt{f_c'}$ (COV = 0.03)	449 psi = $6.23\sqrt{f_c'}$ (COV = 0.09)
56 day split cylinder strength (ASTM C496)	613 psi = $7.05\sqrt{f_c'}$ (COV = 0.26)	not determined due to need for cores	671 psi = $8.85\sqrt{f_c'}$ (COV = 0.08)

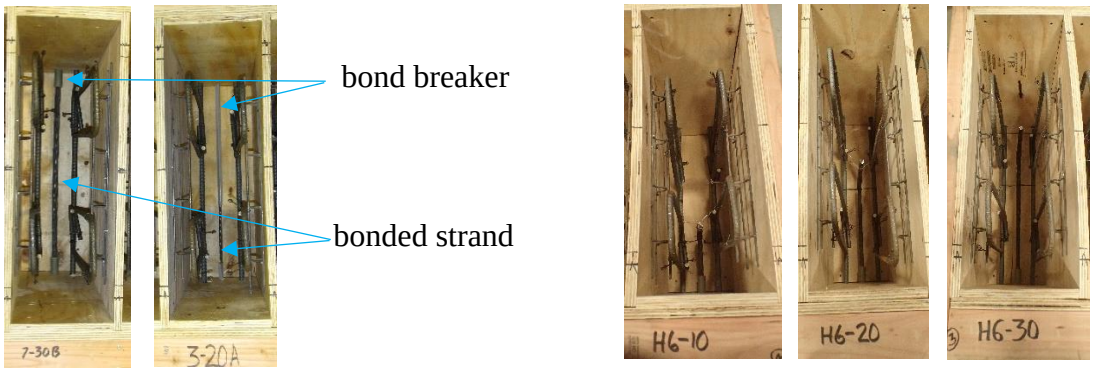

a) specimens 7-30B and 3-20A showing strand embedment and debonding

b) series of 90° bent 0.6-in. strand specimens having embedments of l_{dh} = 10d_b, 20d_b and 30d_b

Figure 4.2 Beam end specimens prior to concrete placement (loaded end at bottom of all images).

4.2 Straight Strand Beam End Test Results

All straight strand beam-end tests were compliant with the method of ASTM A944. Load is applied to the strand slowly (at a rate to result in slip failure between 1 and 3 minutes) until slip is recorded. Due to the sensitivity of the instrument, initial slip was defined as a relative movement of the free end of the strand in excess of 0.0001 in. Once slip is observed, load and slip data are recorded. Specimen cracking, if observed, is also reported. Data from all specimens is reported in Appendix B.

Figure 4.3 shows the strand stress versus free-end slip recorded for each test having NWC1 concrete. Due to the nature of the test set up, slip at the free end represents the ultimate capacity of the embedded strand. It is not possible to reliably obtain the ascending branch of the stress-slip curves.

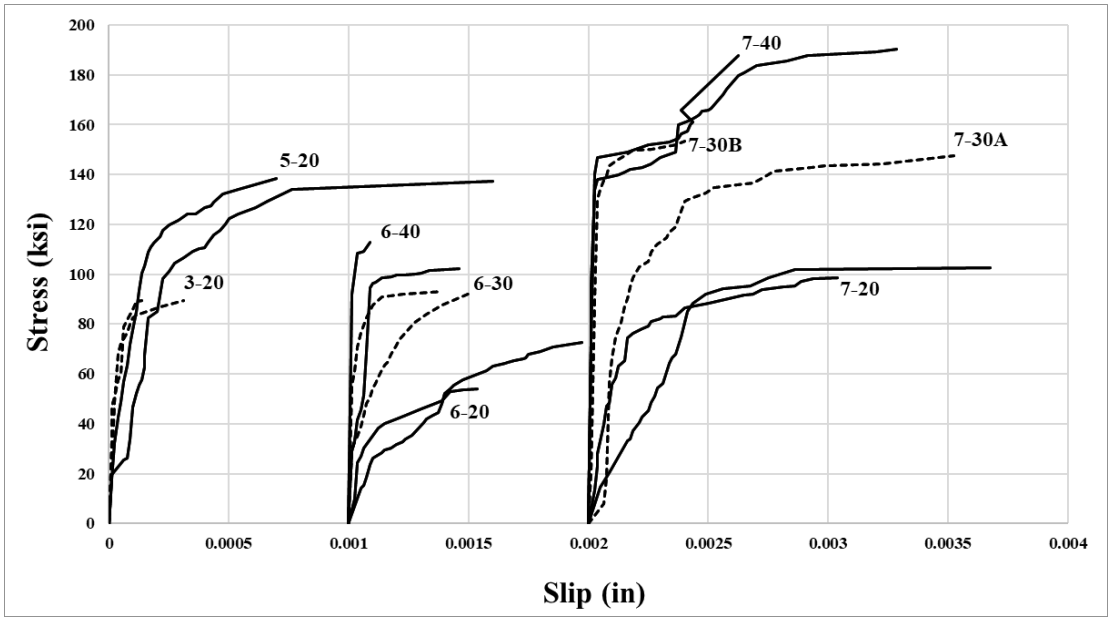

a) NWC1 specimens (data offset 0.001 in. increments horizontally for clarity)

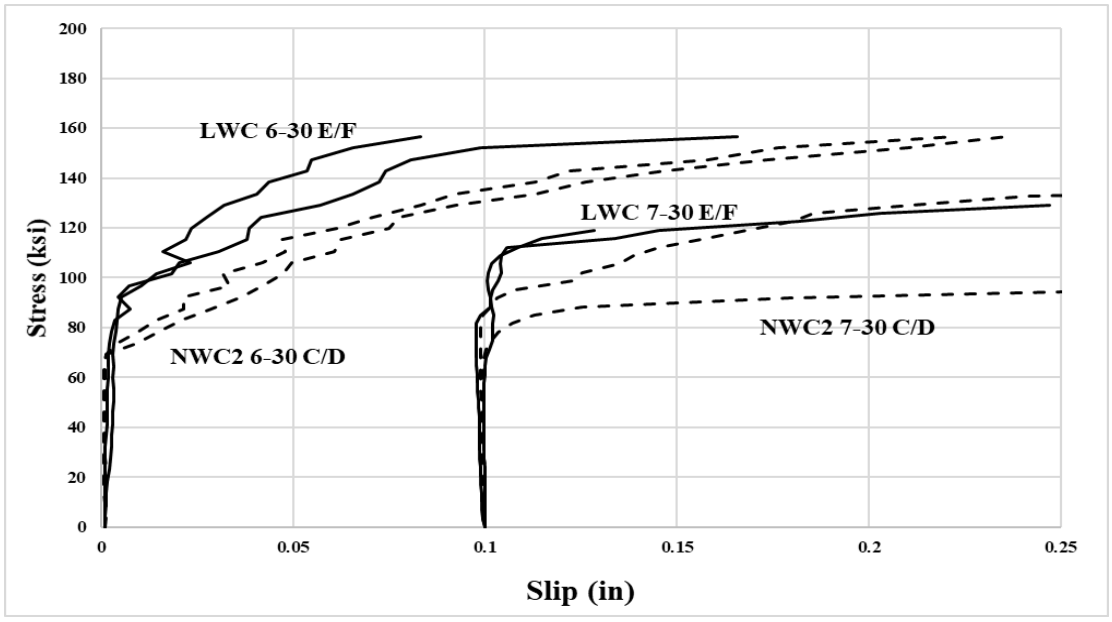

b) NWC2 and LWC specimens (data offset 0.10 in. increments horizontally for clarity)

Figure 4.3 Strand stress versus free end slip (data offset 0.001 in. increments horizontally for clarity)

Failure of all straight strand specimens in NWC1 concrete (Figure 4.3a) is by pullout failure. In this case, the applied load remains constant or drops marginally as the slip continues (i.e. load-slip stiffness is negligible). The test is stopped once slip exceeds 0.5 in. (so as to not damage the slip transducer). None of the NWC1 specimens exhibited any distress to the concrete (indicating a pull-out failure). In these cases, the slip behaviour is 'brittle' with low ultimate slip displacements and brittle pull-out failure closely followed initial slip. Hairline flexural cracks were observed in both 6-40 and 7-40 specimens at loads exceeding the initiation of slip. These are an artefact of using a longer, 31 in., test specimen and the small degree of flexure that is induced in the specimen over this larger span.

NWC2 was a relatively poor concrete mix exhibiting a 'softer' slip behaviour; that is, once slip initiated, a relatively ductile response ensued resulting in larger slip measurements (Figure 4.3b).

LWC, having a strength falling between NWC1 and NWC2 and having a lightweight expanded shale coarse aggregate, also exhibited a more ductile response. In these specimens, concrete splitting failure was observed as shown in Figure 4.4. Splitting results from excessive slip generating greater radial forces as the strand deformations 'move' through the concrete. Splitting initiates at the loaded end of the strand and propagates to the free end as the bond resistance is redistributed. LWC exhibited a higher split tensile capacity than NWC1 (Table 4.3); thus the splitting behaviour observed is attributable to the nature of the LWC – likely the relatively brittle nature of the LWC expanded shale aggregate – rather than to the cylinder-derived strength. Bond capacities resulting from tests exhibiting a splitting failure must be interpreted as being lower-bound bond capacities (making resulting extrapolation of development length upper bound).

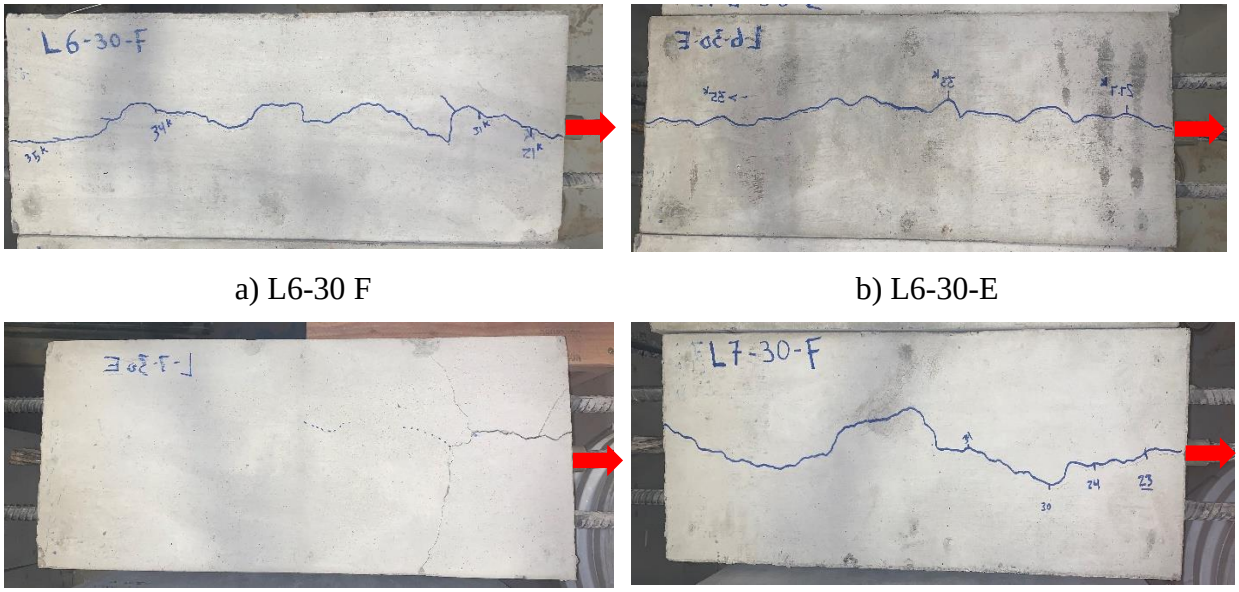

a) L6-30 F b) L6-30-E

c) L7-30-E c) L7-30-F

Figure 4.4 LWC beam end specimens showing splitting behavior (pull-out to right)

The average bond stress, τ, was calculated from Eq.(4–1) and is summarised in Table 4.3 for the first instance of slip and the ultimate capacity of each specimen. Applied load, P, is normalised by strand area to give strand stress: $f_s = P/A_{ps}$.

$$\tau = P/\pi d_b l_e = f_s A_{ps}/\pi d_b l_e \quad (4–1)$$

Finally, assuming a linear relationship between bar stress and development length, the embedment length required to develop the 270 ksi strand capacity, l_d, can be extrapolated using Eq.(4–2); this is also reported in Table 4.3.

$$l_d = l_e(f_{pu}/f_{max}) \quad (4–2)$$

Table 4.3 Straight strand slip results.

Specimen	concrete	d_b	A_{ps}	l_e	slip > 0.0001 in.			initial splitting			maximum load			$l_d = l_e(f_{pu}/f_{max})$ (splitting if applicable)
					P_{slip}	f_{slip}	τ_{slip}	P_{slip}	f_{slip}	τ_{slip}	P_{max}	f_{max}	τ_{max}	
		in.	in^2	in	kips	ksi	ksi	kips	ksi	ksi	kips	ksi	ksi	in.
7-40-A	NWC 1 7.9 ksi	0.7	0.294	28	21.8	74.1	0.35	n.o.	n.o.	n.o.	55.2	187.8	0.90	40.2 = 57.5d_b
7-40-B					21.2	72.1	0.34	n.o.	n.o.	n.o.	56.0	190.5	0.91	39.7 = 56.7d_b
7-30-A				21	5.5	18.7	0.12	n.o.	n.o.	n.o.	43.4	148.6	0.94	38.2 = 54.5d_b
7-30-B					6.2	21.1	0.13	n.o.	n.o.	n.o.	45.1	153.4	0.98	37.0 = 52.8d_b
7-30-C	NWC 2 4.1 ksi				16.0	54.4	0.35	n.o.	n.o.	n.o.	29.0	98.6	0.63	57.5 = 82.2d_b
7-30-D					18.0	61.2	0.39	n.o.	n.o.	n.o.	41.0	139.5	0.89	40.6 = 58.1d_b
L7-30-E	LWC 5.8 ksi				22.0	74.8	0.48	36.0	122.4	0.78	36.0	122.4	0.78	46.3 = 66.2d_b
L7-30-F					15.0	51.0	0.32	23.0	78.2	0.50	39.0	132.7	0.84	42.7 = 61.0d_b (72.5=103.5d_b)
7-20-A	NWC 1 7.9 ksi			14	6.0	20.4	0.19	n.o.	n.o.	n.o.	30.2	102.7	0.98	36.8 = 52.6d_b
7-20-B					4.0	13.6	0.13	n.o.	n.o.	n.o.	29.0	98.6	0.94	38.3 = 54.8d_b
6-40-A		0.6	0.217	24	20.0	92.2	0.44	n.o.	n.o.	n.o.	24.5	112.9	0.54	57.4 = 95.7d_b
6-40-B					7.2	33.2	0.16	n.o.	n.o.	n.o.	22.2	102.3	0.49	63.3 = 105.5d_b
6-30-A				18	12.1	55.8	0.36	n.o.	n.o.	n.o.	20.2	93.1	0.60	52.2 = 87.0d_b
6-30-B					6.4	29.5	0.19	n.o.	n.o.	n.o.	20.1	92.7	0.59	52.4 = 87.4d_b
6-30-C	NWC 2 4.1 ksi				14.0	64.5	0.41	n.o.	n.o.	n.o.	35.0	161.3	1.03	30.1 = 50.2d_b
6-30-D					15.0	69.1	0.44	n.o.	n.o.	n.o.	35.0	161.3	1.03	30.1 = 50.2d_b
L6-30-E	LWC 5.8 ksi				2.0	9.2	0.06	21.0	96.8	0.62	35.0	161.3	1.03	30.1 = 50.2d_b (50.2= 83.7d_b)
L6-30-F					7.0	32.3	0.21	27.7	127.6	0.82	35.0	161.3	1.03	30.1 = 50.2d_b (38.1= 63.5d_b)
6-20-A	NWC 1 7.9 ksi			12	3.1	14.3	0.14	n.o.	n.o.	n.o.	15.8	72.8	0.70	44.5 = 74.2d_b
6-20-B					5.9	27.2	0.26	n.o.	n.o.	n.o.	11.8	54.4	0.52	59.6 = 99.3d_b
5-20-A		0.5	0.153	10	4.0	26.1	0.25	n.o.	n.o.	n.o.	21.0	137.3	1.34	19.7 = 39.4d_b
5-20-B					4.9	32.0	0.32	n.o.	n.o.	n.o.	20.5	134.0	1.31	20.1 = 40.3d_b
3-20-A		3/8	0.085	7.5	2.8	32.9	0.32	n.o.	n.o.	n.o.	7.6	89.4	0.86	22.7 = 60.4d_b
3-20-B					2.0	23.5	0.23	n.o.	n.o.	n.o.	7.6	89.4	0.86	22.7 = 60.4d_b
n.o. = not observed														

4.3 Discussion of Straight Strand Beam End Test Results

4.3.1 Strands Embedded in Normal Weight Concrete (NWC)

Considering only the specimens fabricated of NWC, a primary conclusion observed from the data presented in Table 4.3 and summarised in Table 4.4 is that, although performance of a given strand size was quite consistent, quite different performance was observed for different strand sizes. The variation in bond behaviour is not attributed to the strand size itself since there is no size dependent trend evident. Similarly, the variation is not attributed to the mechanical interlock of the strand since the relative rib areas are similar for each strand (Table 2.1). There appears to be some impact of concrete quality (strength) although the data in insufficient to quantify this.

Based on the results of NWC1 and NWC2, it is hypothesized, that the condition of the strand has affected both the relatively high bond results for the 0.5 in. strand and the low results for the 0.6 in. strands in NWC1. For the NWC2 and LWC tests, both the 0.6-in. and 0.7-in. strands were degreased in advance. This process has apparently improved the bond of the 0.6-in. strands in NWC2, despite the poorer concrete quality.

Table 4.4 Summary of straight strand test results (COV in brackets were applicable).

nominal strand diameter, d_b	in.	**0.7**	**0.7**	**0.7**	**0.6**	**0.6**	**0.6**	**0.5**	**3/8**
concrete		NWC 1	NWC 2	LWC	NWC 1	NWC 2	LWC	NWC 1	NWC 1
bond stress at initial slip, τ_{slip}	ksi	0.21 (0.52)	0.37	0.40	0.30 (0.38)	0.42	0.13	0.28	0.28
bond stress at maximum load, τ_{max}	ksi	0.94 (0.04)	0.76	0.81	0.57 (0.13)	1.03	1.03	1.32	0.86
extrapolated development length, l_d	in.	38.4 (0.04)	49.0	59.4[a]	54.9 (0.12)	30.1	44.2[a]	19.9	22.7
		$55d_b$	$70d_b$	$85d_b$	$92d_b$	$50d_b$	$74d_b$	$40d_b$	$60d_b$
[a] controlled by splitting failure; interpret as lower bound value.									

4.3.2 Strands Embedded in Lightweight Concrete (LWC)

According to Greene and Graybeal (2019) (see Section 1.8), LWC is most likely will have longer transfer length than normal weight concrete. In accordance with this study, Table 4.4 shows 0.7-in. strands with LWC as having longer development length than all other NWC strands. Similarly, 0.6-in. strands show the same trend except for NWC1 in which the conditions of the strands (as mentioned previously) could have affected the results.

4.3.3 Summary of Straight Strand Beam End Tests

These tests were intended to be "proof tests" of current AASHTO provisions. The results suggest that current development equations are conservative for NWC and LWC. Nevertheless, the degree of conservativeness cannot be adequately assessed. AASHTO prescriptive requirements necessarily include many factors not addressed in this study (or others) including: creep, shrinkage, long-term losses such as friction between steel and concrete and so on.

AASHTO LRFD §5.9.4.3.2 specifies the development length of bonded strand to be:

$$l_d = \kappa(f_{ps} - 0.66f_{pe})d_b = 170d_b \quad (4\text{–}3)$$

ACI 318-14 §25.4.8.1 specifies an essentially identical equation with $\kappa = 1$. Taking $\kappa = 1$ and $f_{pe} = 0.56f_{pu}$, the length required to develop f_{pu} is $169d_b$. In this study, no extrapolated value of l_d exceeded $106d_b$. The 0.5 in. strand exhibited apparent values of l_d as low as $40d_b$. Both 0.6-in. and 0.7-in. strands embedded in LWC resulted in splitting failures at bond stresses lower than observed in comparable NWC, although concrete strengths were relatively low.

4.4 90-degree Strand Beam End Test Results

An identical test arrangement using only concrete mix NWC1 is used for the hooked strands. As mentioned in Section 4.1, an LVDT collar is located on the loaded end of the strand. This transducer measures elongation of the unbonded portion of the strand plus the effect of bond deformation and eventually slip. Slip at the loaded end of the strand, however, begins at the initiation of load and will be gradual; thus it is not possible to identify a true initial slip. Applied load versus elongation plots are shown in Figure 4.5. A summary of results for the hook specimens is given in Table 4.5.

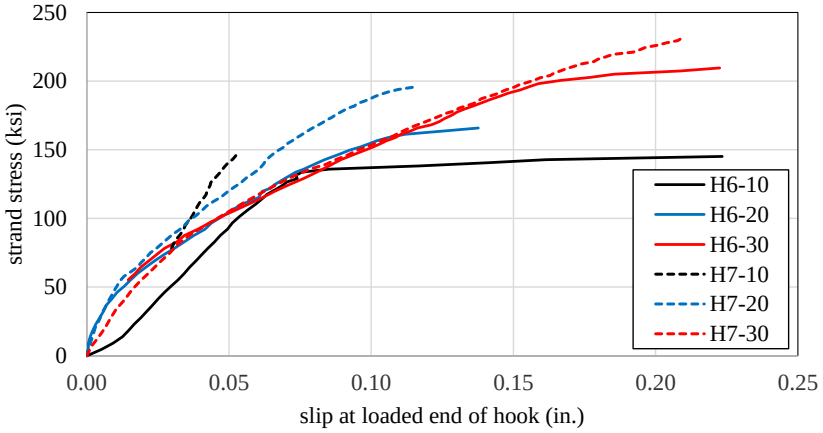

Figure 4.5 Elongation at loaded end of hooked strands.

Table 4.5 Hooked strand test results.

Specimen	d_b	A_{ps}	l_{dh}	occurrence of transverse crack		maximum load		
				P_{crack}	f_{crack}	P_{max}	f_{max}	failure mode
	in.	in^2	in	kips	ksi	kips	ksi	
H7-30	0.7	0.294	21	60.0	204	69.0	235	splitting (Figure 4.12d)
H7-20			14	39.0	133	57.5	196	splitting (Figure 4.12d) following initial formation of shear crack
H7-10			7	43.5	148	43.5	148	shear (Figure 4.12c)
H6-30	0.6	0.217	18	not observed		45.5	210	splitting (Figure 4.12d)
H6-20			12	32.0	147	36.5	168	splitting (Figure 4.12d)
H6-10			6	28.0	129	32.5	150	shear (Figure 4.12c)

4.4.1 Hooked Embedment Failure Modes

Each test progresses as shown schematically in Figure 4.6. Load is applied and the strand bond increases and then begins to deteriorate at the loaded end (Figure 4.6a). As the loading continues, the region of deteriorated bond progresses toward the hook and the hook becomes engaged in sharing the strand pull-out force. At some point, the entire straight portion of the strand is essentially debonded at which point the strand is anchored only by the hooked embedment (Figure 4.6b). Shortly after this, a tension crack occurs at the top of the specimen at the location of the hook. This crack is an artefact of the test arrangement and results from the small degree of flexure at the 'beam end' modelled by the beam end test. Once this crack appears, the behaviour is no longer a 'pull-out' behaviour but rather a strut developing between the hook anchorage and the horizontal reaction (Figure 4.6b). The strut angle and the number of #4 stirrups (see Figure 4.1a) it engages is a function of the embedment, l_{dh}, provided. Specimen behaviour then takes one of two forms:

1. For short embedment (H6-10 and H7-10), a steep strut engaging only two stirrup legs is engaged (Figure 4.6c). The block of concrete engaged by the hooked bar fails in shear along the inclined strut and rotates away from the specimen (Figure 4.6c).
2. For longer embedment in which the strut is shallower and engages more stirrup legs, the shear resistance is increased. In this case, a splitting failure occurs (Figure 4.6d) including the typical 'wishbone' crack at the end of the hook. This failure is initiated by a combination of the hook being unable to fully anchor the tapered strut that develops (shown in the plan view of Figure 4.6b) and the vertical force that results as the hook is 'unbent' (see Figure 4.8g). Side or back splitting of the specimen is mitigated by the greater concrete cover in both these dimensions.

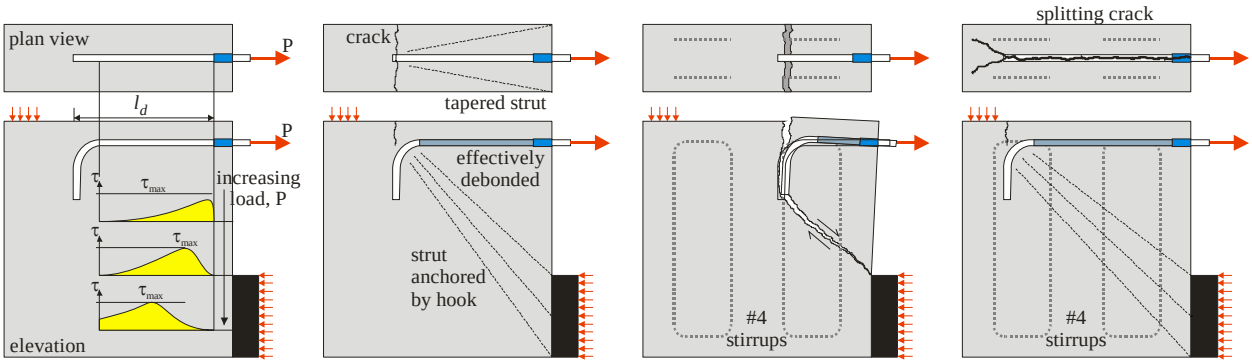

a) increasing load

b) straight portion of bar effectively debonded

c) failure of short embedment length

d) splitting failure of long embedment length

Figure 4.6 Schematic representation of beam-end specimen loading and failure modes.

The behaviour observed is the same as that described for reinforcing bar hooks by Joh and Goto (2000). The behaviours described above correspond to failure modes RO and SS reported by Joh and Goto shown in Figure 4.7. Other possible hooked strand failure modes not observed in this test are shown in Figure 4.7 (Joh and Goto 2000):

3. Fracture of the strand (FR). The specimen size and hook embedment in the present tests were insufficient to achieve the high stress required to fracture a strand. It is noted, however, that the stresses achieved in the hooked strand tests were more than sufficient to facture conventional mild reinforcing bars.

4. Crushing at the horizontal reaction (JS). The specimen dimensions were chosen intentionally to mitigate this failure mode.

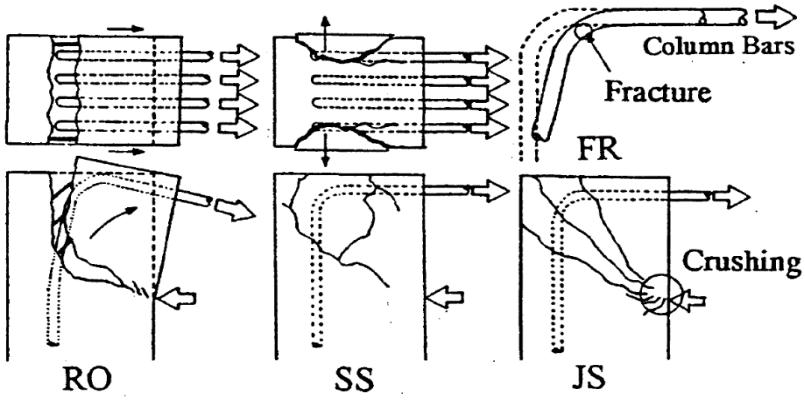

Figure 4.7 Four beam-end failure modes by (Jon and Goto 2000)

Figure 4.8 shows the hooked embedment strand tests following testing. The shear failure of H6-10 and H7-10 are clearly evident as is the shear crack that developed prior to splitting failure of H7-20. Splitting failures of H6-20, H6-30 and H7-30 were not accompanied by any cracking on the sides of the specimen.

Figure 4.8g shows evidence of the hook beginning to unbend (compare the hook with its imprint in the concrete). The effect of pulling the hook out of its embedment is a vertical force that helps to drive the top face splitting. The result of this is evident in H7-30 in which the entire top cover of the specimen spalled as a result of the failure (the concrete cover shown in Figure 4.8f was simply lifted away by hand). Figure 4.8h shows the strand imprint in the concrete illustrating excellent consolidation and well-defined helical deformations.

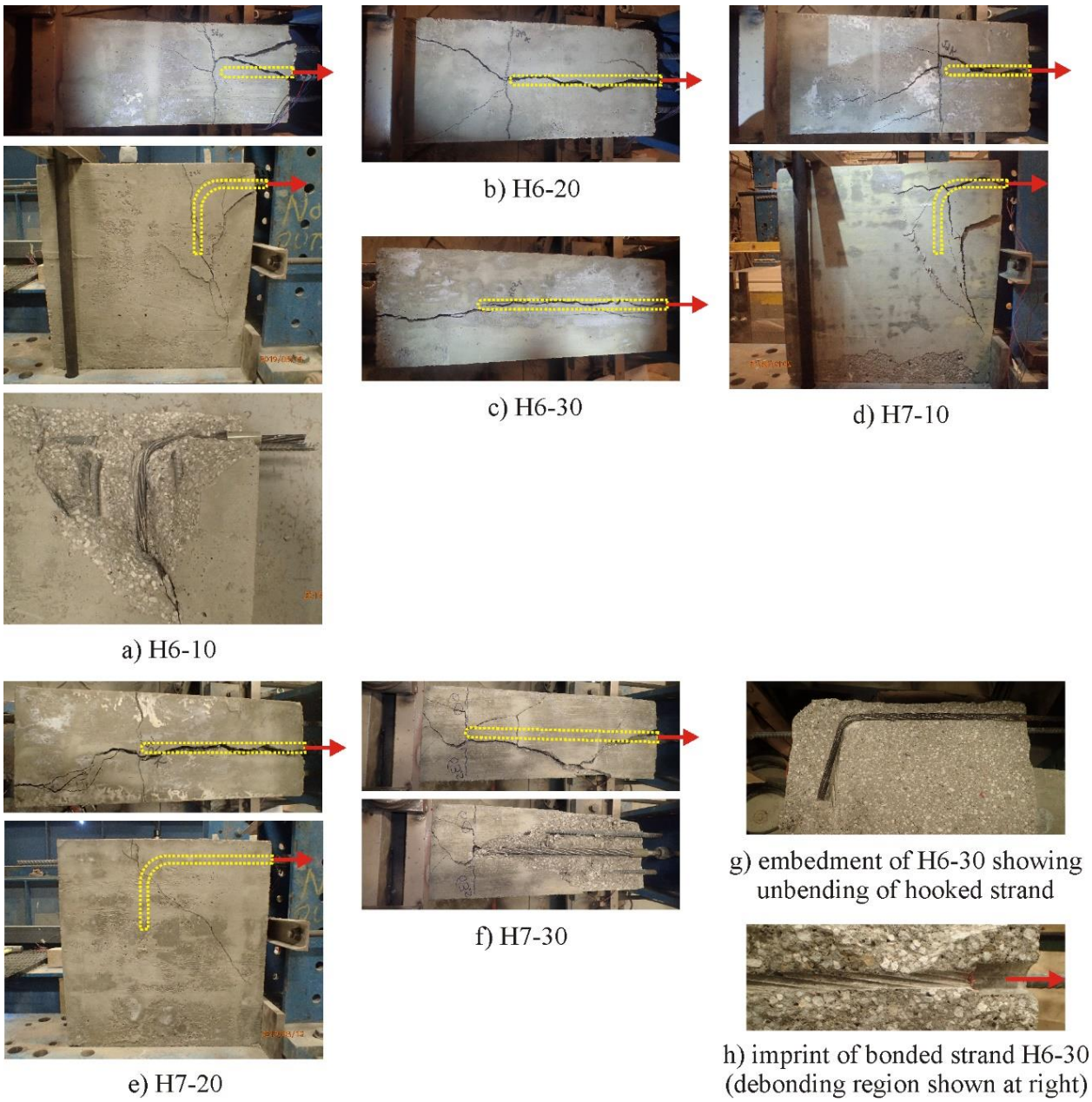

Figure 4.8 Images of hook embedment specimens following testing illustration failure modes.

4.5 Discussion of Hooked Strand Beam End Test Results

As expected and shown in Figure 4.9, the capacity of the hooked strands increases with increased embedment length. Table 4.6 summarizes the observed relationships for the 0.6-in. and 0.7-in. strand tested. As an approximation, the intercept (capacity at zero embedment) – 106 ksi and 116 ksi for 0.7-in. and 0.6-in. strand, respectively – represents the contribution of the hook geometry, while the l_{dh}/d_b term represents the bonded straight portion of the strand. The results reflect the better bond of the 0.7-in. strand seen in the straight strand tests (Table 4.4).

Extrapolating the relationships given in Table 4.6 to determine the hook embedment required to develop f_{pu}, it is clear the presence of the hook reduces the theoretical development length from that determined for a straight strand embedment. The reduction is on the order 31% and 45% for the 0.7-in. and 0.6-in. strands respectively. By comparison, similar reductions are implied when considered deformed reinforcing bars. The ratio of hooked bar to straight bar development length prescribed by AASHTO LRFD is $l_{dh} = 0.26l_d$ and that prescribed by ACI 318-14 is $l_{dh} = 0.50l_d$ (#6 bars and smaller).

As seen in Figure 4.8g evidence that the hooks were being pulled out of their embedment resulting in them being 'unbent' – is seen in the fact that the hook angle following testing is greater than 90 degrees. Although this effect likely contributes to the forces causing splitting, in no case was the hook observed to pull-out. The length of the tail, A, (Figure 4.1 and Table 4.1) contributes to the resistance to hook unbending. In these tests, A was based on the detail of a standard reinforcing bar hook; this value could be made longer in strands to resist hook unbending. Making dimension A longer may improve the performance described in Table 4.6 marginally.

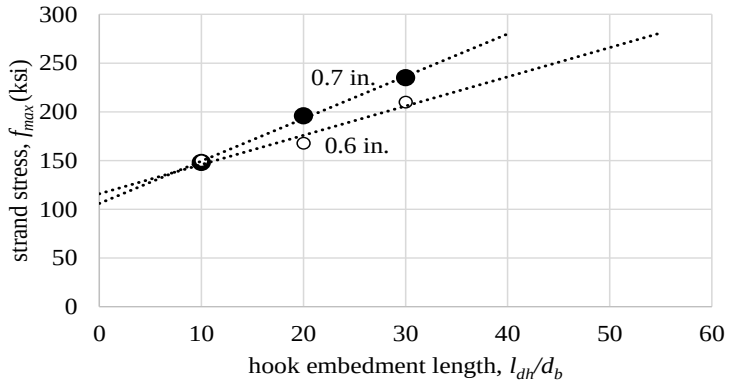

Figure 4.9 Hook embedment versus beam end pull-out capacity.

Table 4.6 Observed relationships for hooked strands

nominal strand diameter, d_b	**0.7**	**0.6**
observed relationship (Figure 4.9)	$f_{max} = 4.35 l_{dh}/d_b + 106$ ($R^2 = 0.99$)	$f_{max} = 3 l_{dh}/d_b + 116$ ($R^2 = 0.95$)
extrapolated hook embedment required to develop f_{pu} = 270 ksi	l_{dh} = 26.4 in. = $38 d_b$	l_{dh} = 30.8 in. = $51.3 d_b$
	$l_{dh} = 0.69 l_d$	$l_{dh} = 0.55 l_d$

4.6 Potential Utility of 90-degree Strand Anchorage

Due to the expected high stresses in the beam-end region, girders constructed with 0.7-in diameter prestressing strand may be more susceptible to anchorage shear failure. When a crack initiates near the beam end, a tension force, *T*, is developed in the prestressing strand, as shown in Figure 4.10. If there is inadequate restraining force coming from the steel crossing the crack, a series of diagonal shear cracks crossing the longitudinal steel forms resulting in virtual complete loss of bond. Eventually, this results in an anchorage shear failure.

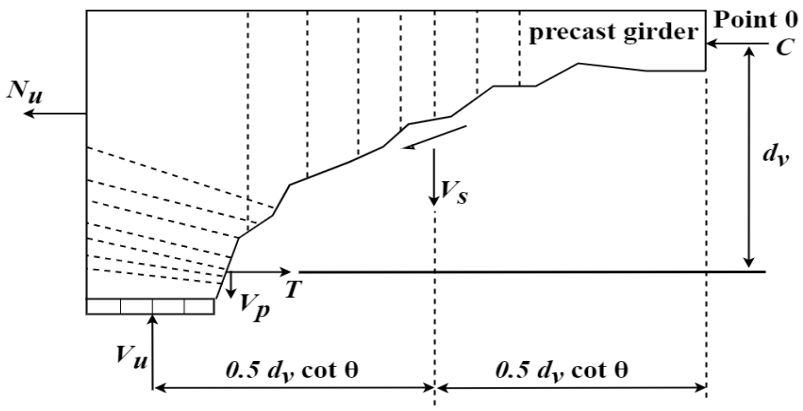

Figure 4.10 Anchorage free body diagram (after AASHTO, 2017a).

This anchorage failure mode is taken into consideration in AASHTO LRFD (2017a) Article 5.8.3.5. Eq.(4–4) prescribes the longitudinal reinforcement needed to develop the required tension force T as a combination of the moment, shear and axial force acting at the critical section.

$$T = \Sigma A_s f_y + \Sigma A_{ps} f_{ps} \geq \frac{|M_u|}{d_v \phi_f} + 0.5\,\frac{N_u}{\phi_c} + \left(\left|\frac{V_u}{\phi_v} - V_p\right| - 0.5 V_s\right)\cot\theta \qquad (4\text{–}4)$$

Where (see Figure 4.10): ΣA_s = area of non-prestressed steel on the flexural tension side of the member at the section under consideration; f_y = specified yield strength of the non-prestressed steel; ΣA_{ps} = area of prestressing steel on the flexural tension side of the member; f_{ps} = stress that may be developed in the prestressed reinforcement based on development at the critical section; M_u = factored moment, not to be taken less than $|V_u - V_p| d_v$; d_v = effective shear depth; ϕ_f = resistance factor for flexure; N_u = factored axial force, taken as positive if tensile and negative if compressive; ϕ_c = resistance factor for axial force; V_u = factored shear force at section; ϕ_v = resistance factor for shear and torsion; V_p = component in the direction of the applied shear of the effective prestressing force (positive if resisting the applied shear; V_p = 0 when only straight strand is present); V_s = shear resistance provided by the transverse reinforcement at the section under

investigation limited to a value of V_u/ϕ_v; θ = angle of inclination of diagonal compressive stresses used in determining the nominal shear resistance of the section under investigation.

It is desirable to provide the force T with only the $\Sigma A_{ps} f_{ps}$ term – this mitigates the need to add additional longitudinal steel in the already congested end region. However:

1. Due to the need to debond strand to mitigate end region cracking, the number of bonded strands (ΣA_{ps}) at the critical section is reduced. Greater debonding will be required for the larger forces inherent in using 0.7-in. strands (Ball 2019 and Shahrooz et al. 2017); and,
2. Due to the proximity to the end of the girder and the larger strand diameter, the strand is only able to develop limited stress, f_{ps}, at the critical section. For larger strands, f_{ps} will be lower due to longer development lengths.

Together this leads to limited tension capacity, T. A parametric study (Shahrooz et al., 2017) concluded that increasing the prestressing force in a girder (and therefore increasing the debonding ratio) also increases the possibility for potential shear anchorage failure. Because debonding is necessary to control cracking at prestess transfer, A_{ps} cannot be increased and will likely be reduced using 0.7-in. strands. Therefore, only increasing f_{ps} is available to mitigate the need for additional reinforcing steel, $\Sigma A_s f_y$ in Eq.(4–4).

It is proposed that the presence of the strand extension beyond the girder end can be used to: a) provide some degree of development to partially debonded strand (giving these strands a value of $f_{ps} > 0$); and, b) improve the development of bonded strand (increasing the available f_{ps} for these strands); this is shown schematically in Figure 4.11. It is unlikely that a short straight strand extension will provide much effect but providing a hook on this strand may be significant. Both cases are considered in the testing program of this chapter.

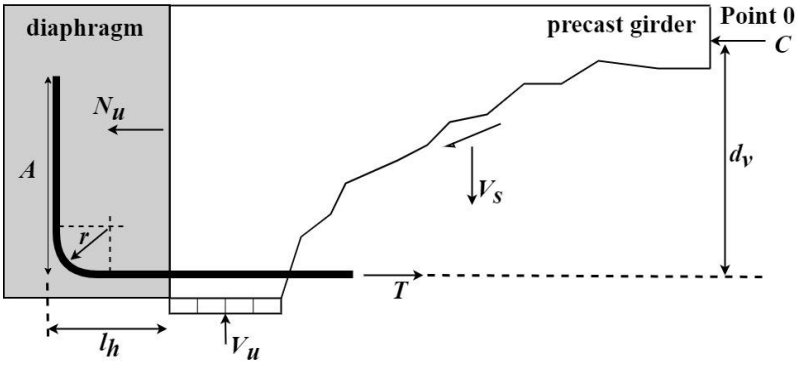

Figure 4.11 90-degree strand anchorage free body diagram (after AASHTO, 2017a)

Shahrooz et al. (2017) reported an extensive finite element-based study of 39 girders having either 0.6 or 0.7-in. strands. The intent of the study was to investigate effects of large amounts of strand debonding. As a result, the examples have large prestress forces and relatively large amounts of strand debonding. When checked for tension capacity Eq.(4–4) at the critical section for shear ($d_v/2$ from the end of the cast girder), seven examples were found to require additional non-prestressed reinforcement. The seven cases are shown in Table 4.7. The inadequate longitudinal reinforcement is indicated in the far right-hand column as a ratio less than 1. Maintaining the initial beam designs, there are two approaches to satisfying Eq.(4–4).

1. Add more mild steel ($\Sigma A_s f_y$); this is Case A in each instance reported in Table 4.7 and is reported by Shahrooz et al. (2017).
2. Increase f_{ps} by providing hooked anchorage; this is Case B and is described further below.

Table 4.7 Summary of stress checks (after Shahrooz et al. 2017)

Model Parameters								A_{ps} at $d_v/2$		A_s at $d_v/2$	f_{ps} at $d_v/2$		$\sum A_{ps} f_{ps}/T$
Case	d_b	N	d_r	$f_{c'}$	L	l_d	l_{dh}	straight	hooked l_{hook} =10 in.	-	straight	hooked l_{hook} =10 in.	-
-	in.	-	-	ksi	ft	in.	in.	in^2	in^2	in^2	ksi	ksi	-
Nebraska DOT NU-900 girders spaced at 8 feet ($d_v/2$ = 28.2 in.)													
8	0.6	14	0.14	6	55	102	-	2.604	-	-	118.4	-	0.89
8A	Case 8 w/ additional A_s= 0.88in.^{2}						-	2.604	-	0.88	118.4	-	0.98
8B	Case 8 with 7 hooked strands having l_{hook} =10 in.						71.4	1.085	1.519	-	118.4	144.4	1.00
9	0.7	14	0.43	6	65	119	-	2.352	-	-	101.52	-	0.82
9A	Case 9 w/ additional A_s= 1.32in.^{2}						-	2.352	-	1.32	101.52	-	0.99
9B	Case 9 with 8 hooked strands having l_{hook} =10 in.						83.3	-	2.352	-	101.52	123.82	1.00
11	0.6	14	0.00	8	55	102	-	3.038	-	-	118.44	-	0.93
11A	Case 11 w/ additional A_s= 0.62in.^{2}						-	3.038	-	0.62	118.44	-	0.99
11B	Case 11 with 5 hooked strands having l_{hook} =10 in.						71.4	1.953	1.085	-	118.44	144.45	1.00
12	0.7	14	0.29	8	65	119	-	2.94	-	-	101.52	-	0.81
12A	Case 12 w/ additional A_s= 1.32in.^{2}						-	2.94	-	1.32	101.52	-	1.01
12B	Case 12 with 10 hooked strands having l_{hook} =10 in.						83.3	-	2.94	-	101.52	123.82	0.99
AASHTO BIV-48 adjacent box girders spaced at 4 feet ($d_v/2$ = 33.6 in.)													
29	0.7	46	0.7	12	165	119	-	4.116	-	-	120.96	-	0.90
29A	Case 29 w/ additional A_s= 1.32in.^{2}						-	4.116	-	1.32	120.96	-	1.01
29B	Case 29 with 10 hooked strands having l_{hook} =10 in.						83.3	1.176	2.94	-	120.96	141.32	1.01
31	0.6	46	0.52	15	145	102	-	4.774	-	-	141.12	-	0.98
31A	Case 31 w/ additional A_s= 0.44in.^{2}						-	4.774	-	0.44	141.12	-	1.00
31B	Case 32 with 12 hooked strands having l_{hook} =10 in.						71.4	4.123	0.651	-	141.12	164.87	1.00
32	0.7	46	0.65	15	165	119	-	4.704	-	-	120.96	-	0.89
32A	Case 32 w/ additional A_s= 1.32in.^{2}						-	4.704	-	1.32	120.96	-	1.00
32B	Case 32 with 12 hooked strands having l_{hook} =10 in.						83.3	1.176	3.528	-	120.96	141.32	1.00

Without a hooked embedment, the value of $f_{ps,straight}$ = design stress in straight pretensioned strand at nominal flexural strength at section of member under consideration (ksi), is given by AASHTO Equations 5.9.4.3.2-2 and 5.9.4.3.2-1 respectively as:

From the point where bonding commences to the end of transfer length:

$$f_{ps,straight} = \frac{f_{pe} l_{px}}{60 d_b} \quad (4–5)$$

From the end of the transfer length and to the end of the development of the strand:

$$f_{ps,straight} = f_{pe} + \frac{l_{px} - 60d_b}{l_d - 60d_b}(f_{ps} - f_{pe}) \quad (4–6)$$

Where: ℓ_{px} = distance from free end of pretensioned strand to section of member under consideration (in.).

Providing a hooked embedment allows $f_{ps,hook}$ to be taken as:

$$f_{ps,hook} = f_{hook} + (f_{pu} - f_{hook})(x + l_{hook})/l_{dh} \quad (4–7)$$

Where: f_{hook} = constant stress that is attributed to the hook (see Table 4.6); may be conservatively taken as $f_{hook} = 0$; f_{pu} = specified tensile strength of prestressing steel, taken as = *270* ksi; l_{hook} = embedment length of hooked strand into diaphragm; l_{dh} = hooked strand development length, proposed as $0.7l_d$; l_d = straight strand development length, $l_d = 170d_b$; x = length along girder measured from end of girder; hook embedment is negative values of x.

4.6.1 Illustrative Example - Case 11- From (Table 4.7):

Case 11 reported in Table 4.7 is an NU 900 girder having geometry reported in Table 4.8; this case had no strand debonding. As shown in Table 4.7, Case 11 had only 93% of the required tensile capacity T (Eq. (4–4)) from the available strand ($\Sigma A_{ps}f_{ps}$).

Table 4.8 Case 11 geometric details

Girder properties							Strands along girder			
Case	*H (in)*	d_v *(in)*	d_b *(in)*	A_{ps} *(in²)*	l_t *(in)*	l_d *(in)*	*0-36 (in)*	*36-72 (in)*	*72-108 (in)*	*108+ (in)*
11	36	32.4	0.6	0.217	36	102	14	14	14	14

The following steps are taken to calculate the required:

1. embedment length of hooked strand into diaphragm, l_h, taken as 10-in. in all cases (Figure 4.11); f_{hook} is conservatively assumed to be zero.

2. critical section*: dv/2 =(support+dv)/2 = (12+32.4)/2 = 28.2 in.*

3. hooked strand development length*: $l_{dh} = 0.7l_d = 0.7(170\ d_b) = 119d_b = 119 \times 0.6 = 71.4$ in.*

4. stress in pretensioned strand at nominal flexural strength at section of member under consideration: since *dv/2* is less than transfer length, l_t, Eq.(4–5) is used.

$$f_{ps,straight} = \frac{f_{pe} l_{px}}{60 d_b} = \frac{0.56(f_{pu})(28.2)}{60(0.6)} = 118.4\ ksi$$

5. For hooked strand: $f_{ps} = f_{hook} + (f_{pu} - f_{hook})(x + l_{hook})/l_{dh}$

Thus, $f_{ps,hook} = 270(ksi)\ \frac{[28.2(in.)+10(in.)]}{71.4(in.)} = 144.4\ ksi$

6. $A_{psstraight}$ *= (No. of strands – No. of hooked strands)* A_{ps}

Thus, $A_{ps,straight}$ *= [14 (total strands) – 5(hooked strands)] X 0.217 = 1.953 in.*^{2}

7. $A_{ps,hook}$ *= No. of hooked strands x Aps = 5 x 0.217 = 1.085 in.*^{2}

8. $\frac{\sum A_{ps} f_{ps}}{T} = \frac{(A_{ps} f_{ps,straight} + A_{ps} f_{ps,hooked})}{T} = \frac{(231.3+156.7)}{387.7} = 1.0008 > 1.00$

Therefore, by providing 90^o hooks the improved capacity of the now-anchored straight strands is adequate to resist the tension force T and anchorage failure is prevented.

4.6.2 Possible Effect of Hooked Strand Embedment on AASHTO LRFD Equations 5.8.3.5-1 and 5.8.3.5-2

To show the effect of hooked strand embedment, two similar Cases, 11 and 12, are shown in Figure 4.12 with two options for each case. Case 11 has 14-0.6-in. strands and Case 12 has 14-0.7-in. strands. The first option shown in Figure 4.12, **I**, assumes the hooked bar to have zero stress developed by the tail of the hook ($f_{hook} = 0$); the second option, **II**, assumes the tail is able to provide a capacity ($0.37f_{pu} = 100$ ksi). The second option reflects the results shown in Table 4.6. In both options the development length of the hooked strand is assumed to be $l_{dh} = 0.7l_d$.

The increase in available f_{ps} varies. For Case 11 (Figure 4.12a), considering option **I** ($f_{hook} = 0$), there is an increase in f_{ps} of about 27% at the critical section $d_v/2$. This increase doesn't affect the overall stress check. Therefore, f_{hook} can be conservatively taken equal to zero. From Case 12 (Table 4.7 and Figure 4.12b) the increase is less than that of Case 11 due to the debonding present. Hooked anchorages are not believed to provide additional capacity (i.e., effectively anchor) partially debonded strands. While they do so in theory, the strand stress must be accompanied by a strain over the partially debonded regions of the strand – this would result in unacceptable levels of concrete cracking.

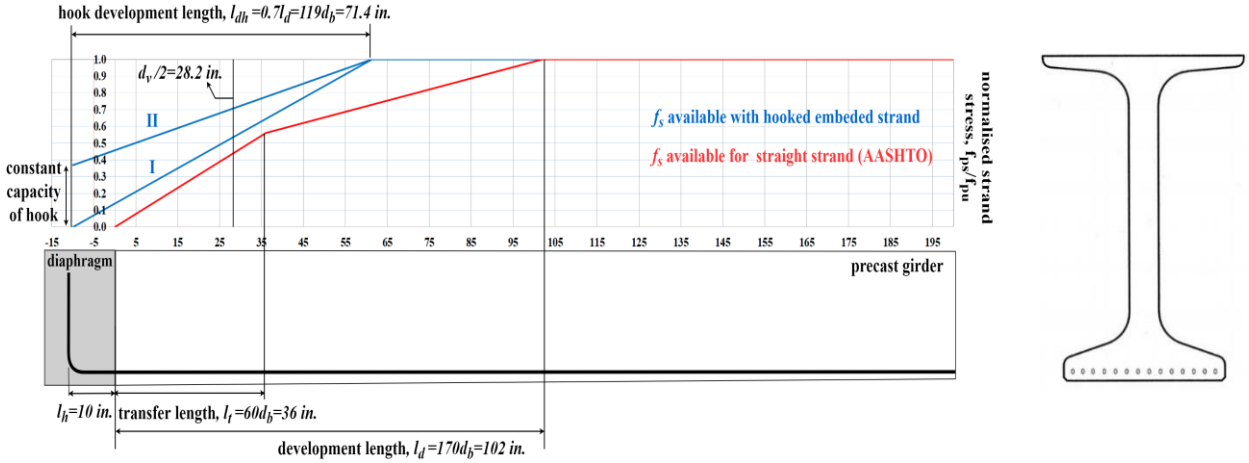

a) Case 11 NU-900 girder having 14 0.6-in. strands and no partial debonding

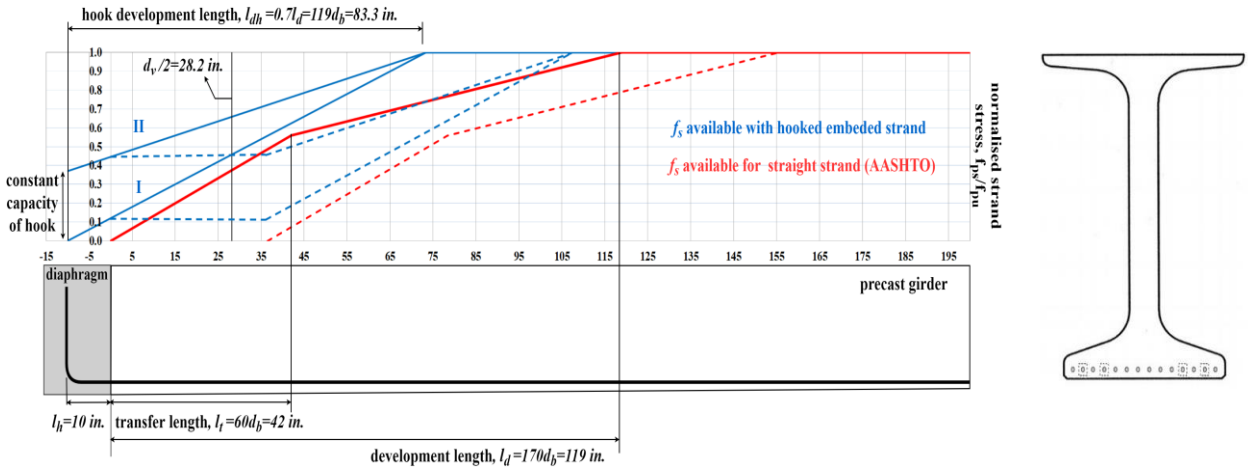

b) Case 12 NU-900 girder having 14 0.7-in. strands and partial debonding ratio, d_r = 0.29 (dotted lines are debonded strands from 0 to 36 in)

Figure 4.12 Schematic development of strand stress of full bonded strands with and without hooked anchors.

5.0 Finite Element Modelling (FEM) of Effects of Prestress Transfer

5.1 Background and Modeling Assumptions

In order to better understand the effects of prestress transfer at the interface between the strand and concrete, a series of finite element analyses was conducted using ABAQUS. Single-strand and four strands models of different sizes of strands are used. Recognizing that behavior is highly dependent on concrete, the models have been developed and used to obtain data trends, and should not be interpreted as providing absolute values.

Two prismatic models were developed and analyzed using ABAQUS (version 6.10EF). Shown in Figure 5.1, square sections having either a single strand or four strands are used. the single strand models are 6-in. square while the 4-strand models have a square dimension equal to 3 times the strand spacing (3*s*) being investigated. All prisms are 50 in. long, exceeding the longest transfer length assumed in this study ($60d_b$ = 60 x 0.7 = 42 in.). Concrete strength is assumed to be f_c' = 15 ksi; the strength at prestress transfer used in this study is $f_{ci} = 0.6f'_c$ = 9 ksi, consistent with previous related work (Shahrooz et al. 2017).

In this study, two values of transfer length are used: $60d_b$, consistent with ASSHTO LRFD (see Eq.(1–1) and $30d_b$. The latter is considered a 'realistic' value of *in situ* transfer length supported by a number of experimental studies and adopted by Shahrooz et al. (2017).

Prism boundary conditions were modeled as a cantilever; with elements fixed in all three principle directons at one end and free elsewhere. Strand dilation was modeled using a temperature field as described in Section 5.1.1. No other forces were included.

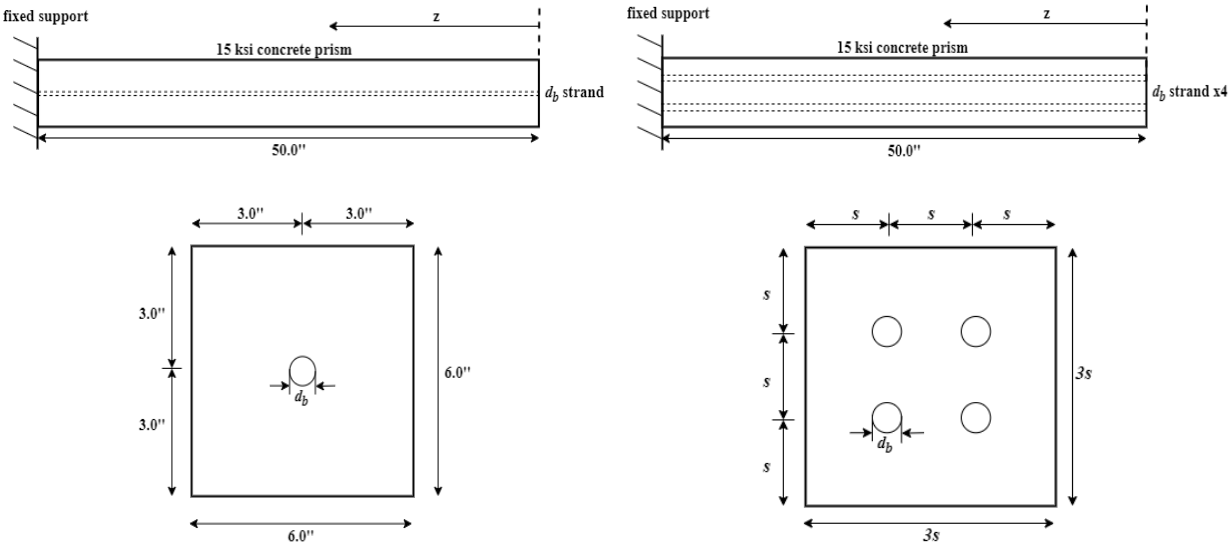

a) single strand prism model dimensions

b) four strand prism model dimensions; 2 in. spacing is shown.

Figure 5.1 FEM prism model dimensions

The single strand models (Table 5.1), comprising a single 0.6-in. or 0.7-in. strand in a 6-in. square prism, are used to validate and better illustrate the Hoyer effect described in Sections 1.5 and Chapter 3. The four-strand (Table 5.2) models are intended to investigate effects of strand spacing. Single-strand cases are labelled X-YY-ZZ as follows:

X = 6 → d_b = 0.6-in. strand
X = 7 → d_b = 0.7-in. strand

YY = 30 → 30d_b transfer length
YY = 60 → 60d_b transfer length

ZZ = 20 → v_p = 0.20
ZZ = 25 → v_p = 0.25
ZZ = 30 → v_p = 0.30
ZZ = 35 → v_p = 0.35
ZZ = 40 → v_p = 0.40

Where v_p is the assume dilation ratio of the strand.

Table 5.1 Single-strand models

0.6- in. strand (r_0 = 0.30 in.)			0.7-in. strand (r_0 = 0.35 in.)		
Case	v_p	L_t (in.)	Case	v_p	L_t (in.)
6-30-20	0.20	18 ($30d_b$)	7-30-20	0.20	21 ($30d_b$)
6-30-25	0.25		7-30-25	0.25	
6-30-30	0.30		7-30-30	0.30	
6-30-35	0.35		7-30-35	0.35	
6-30-40	0.40		7-30-40	0.40	
6-60-20	0.20	36 ($60d_b$)	7-60-20	0.20	42 ($60d_b$)
6-60-25	0.25		7-60-25	0.25	
6-60-30	0.30		7-60-30	0.30	
6-60-35	0.35		7-60-35	0.35	
6-60-40	0.40		7-60-40	0.40	

Table 5.2 Four-strands models

Case	d_b (in)	s(in)	Prism dimension. 3s (in)
4S-5-1.75	0.5	1.75	5.25
4S-5-2	0.5	2.00	6.00
4S-6-2	0.6	2.00	6.00
4S-6-2.25	0.6	2.25	6.75
4S-7-2	0.7	2.00	6.00
4S-7-2.25	0.7	2.25	6.75

5.1.1 Elastic Model Properties

Because of the complexity of the model and desire to verify that the method of affecting strand transfer forces appeared valid, an initial isotropic elastic model was developed. For this, only modulus of elasticity and Poisson's ratio is required. Poisson's ratio of concrete was taken as v_c = 0.2. Concrete modulus of elasticity is determined based on *AASHTO LRFD* Article 5.4.2.4:

$$E_c = 120{,}000\, w_c^2 f'^{0.33}_c \qquad (5\text{–}1)$$

$$E_c = 120000 \times 1.0 \times 0.155^2 \times 15^{0.33} = 7050 \text{ ksi}$$

$$E_{ci} = 120000 \times 1.0 \times 0.155^2 \times 9^{0.33} = 5950 \text{ ksi}$$

where w_c = 0.145 + 0.001f'_c – 0.005 = 0.155 kcf. Strand modulus (E_p) was taken as 29000 ksi and dilation (v_p) is varied in this analysis.

5.1.2 Modeling Strand Dilation at Prestress Transfer

Strand dilation is affected by applying a temperature field along the transfer length of the strand, L_t, varying from a maximum, ΔT, at the free end (z = 0) linearly to zero at the transfer length ($z = L_t$). Assumed strand dilation is shown schematically in Figure 1.4a; geometry and notation is consistent with that presented in Section 1.5. The dilation strain of a prestressing strand due to initial prestress force, f_{pi} = 202.5 ksi, is (Figure 1.3 and Eq. (1–7)):

$$\varepsilon_{pH} = (r_0 - r_s)/r_0 = [r_0 - r_o(1 - v_p f_{pi}/E_p)]/r_0 = v_p f_{pi}/E_p = 0.007 v_p \quad (5–2)$$

ABAQUS C3D8R (8-node linear brick, reduced integration, hourglass control) elements were used to model the concrete and strand – this method makes the model consistent with the simple analytic approach described in Section 1.5. The strand was modeled as a cylinder having a diameter equal to the strand diameter. A temperature field was applied to the strand to produce dilation and thereby model the Hoyer effect. The temperature, ΔT, required to produce the desired dilation strain is:

$$\Delta T = \frac{f_{pi}}{E}\frac{v_p}{\alpha_s} \quad (5–3)$$

Where f_{pi} = initial prestress force = 0.75f_{pu} = 0.75 x 270 = 202.5 (ksi); E = modulus of elasticity for steel; v_p = desired dilation ratio; α_s = The coefficient of thermal expansion (CTE) of the strand taken as 12 x 10^{-6} m/m^{o}K. Values of ΔT used for each analysis are given with the results in Table 5.3.

For simplicity (and consistency with Section 1.5), the analyses neglect the transfer of longitudinal prestress to the concrete; this assumption is believed to be acceptable since the focus of these analyses is on the high stresses at the free end of the prism.

5.1.3 Mesh Size and Material Interface

Due to the focus of this study being on the relatively small strains and stresses in the immediate vicinity of the strand-concrete interface, the following relatively fine mesh size was adopted:

The strand was divided circumferentially into 100 equal radial segments, each segment was divided of multiple elements through the radius – resulting in 1280 elements in a strand section. Thus, the circumferential mesh dimension at the strand-concrete interface is 0.019 in. for the 0.6-in. strand and 0.022 in. for the 0.7-in. strand.

Near the strand, the concrete was similarly modeled with a fine, radially generated mesh having 128 segments around the strand circumference and a radial mesh size of 0.05 in. out to a distance 1 in. from the strand-concrete interface. Further from the strand, the concrete mesh size is increased to 0.3 in. by 0.3 in. for 6 in. prisms and marginally smaller or larger for smaller or larger prisms (Table 5.2); i.e., the number of elements was kept constant.

Along the length of the prism, the mesh dimension for both strand and concrete were 0.5 in. The resulting meshes are seen in Figure 5.5.

Interface between the thermally stressed strand and surrounding concrete was modelled as a tie-type constraint, where the strand is the master surface and concrete is the slave surface.

5.1.4 Smeared Crack (SC) Concrete Model

Following validation of the elastic model (Section 5.1.1), a more realistic plastic modeling of the concrete is adopted. Particularly due to the high elastic stresses predicted, the concrete is anticipated to have cracked locally. Such cracking will permit stress redistribution resulting in significantly different (and more realistic) behavior than assumed using elastic analysis inherent in the approach described in Section 1.4.

The ABAQUS ‘smeared crack’ concrete model is adopted (ABAQUS 2011):

"The smeared crack concrete model in ABAQUS provides a general capability for modeling concrete in all types of structures. As a ‘smeared’ model, it does not track individual 'macro' cracks. Constitutive calculations are performed independently at each integration point of the finite element model. The presence of cracks enters into these calculations by the way in which the cracks affect the stress and material stiffness associated with the integration point. Cracking is assumed to occur when the stress of the element reaches the 'crack detection surface' which is a linear relationship between the equivalent pressure stress and the Mises equivalent deviatoric stress. As soon as the crack detection surface has been activated, the crack direction is taken to be the direction of that part of the maximum principal plastic strain. Following the crack detection, the crack affects the response of the model because a damage elasticity model is used."

In order to affect a smeared crack model, nonlinear compression and tension constitutive models and a failure surface interaction are defined (Wahalathantri et al., 2011) as described in the following sections.

5.1.4.1 Concrete Compression

The complete stress-strain curve for concrete under compression is derived using the experimentally verified numerical model proposed by Hsu and Hsu (1994). Shown in Figure 5.2a, this model can be used to develop the stress-strain relationship under uni-axial compression through $0.3\sigma_{cu}$ in the descending portion using only the maximum compressive strength (σ_{cu}).

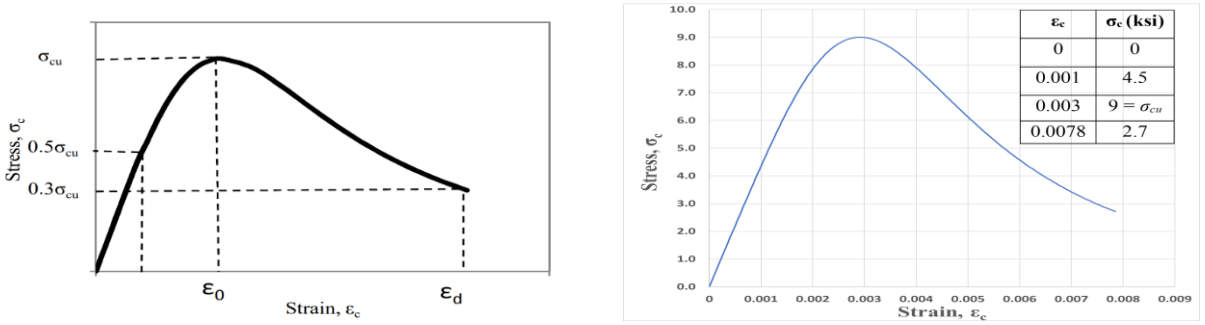

a) generic constitutive curve b) relationship adopted in present study

Figure 5.2 Compressive Stress-Strain Relationship for ABAQUS (after Hsu and Hsu 1994)

The model assumes linear behavior having stiffness E_c through $0.5\sigma_{cu}$. Beyond $0.5\sigma_{cu}$, the stress-strain relationship through $0.3\sigma_{cu}$ (at ε_d) is defined as:

$$\sigma_c = \left(\frac{\bar{\beta}\left(\frac{\varepsilon_c}{\varepsilon_0}\right)}{\bar{\beta} - 1 + \left(\frac{\varepsilon_c}{\varepsilon_0}\right)^{\bar{\beta}}} \right) \sigma_{cu} \qquad (5\text{–}4)$$

Where, the parameter $\bar{\beta}$, which depends on the shape of the stress-strain diagram, is calculated from Eq.(5–5) and the strain at peak stress, ε_0, is given by Eq.(5–6):

$$\bar{\beta} = \frac{1}{1 - \left[\frac{\sigma_{cu}}{\varepsilon_0 E_0}\right]} \qquad (5\text{–}5)$$

$$\varepsilon_0 = 8.9x10^{-5}\sigma_{cu} + 2.114x10^{-3} \text{ [ksi units]} \qquad (5\text{–}6)$$

Concrete strength and modulus are taken as those at transfer: $f_{ci} = 0.6f_c' = 9$ ksi and $E_{ci} = 5950$ ksi (Eq.(5–1)). The resulting compression stress-strain relationship used in this study is shown in Figure 5.2b.

5.1.4.2 Concrete Tension

Tension stiffening is the ability of concrete to carry tension between cracks in reinforced concrete members, and is known to control deformation calculation particularly at serviceability stress levels (Bischoff 2003). The concrete tensile stress-strain model proposed by Nayal and Rasheed (2006) is integrated into ABAQUS (Figure 5.3). Like compression, this is essentially a two-parameter model, requiring cracking stress, σ_{to} and concrete elastic modulus. AASHTO LRFD (Commentary C5.4.2.7) recommends a concrete cracking stress of $\sigma_{t0} = 0.23\sqrt{f_{ci}} = 0.69$ ksi. Using $E_{ci} = 5950$ ksi (Eq. (5–1)), the corresponding cracking strain is $\varepsilon_{t0} = 0.69/5950 = 0.000116$. All other control parameters for the tension stiffening stress-strain model are shown in Figure 5.3.

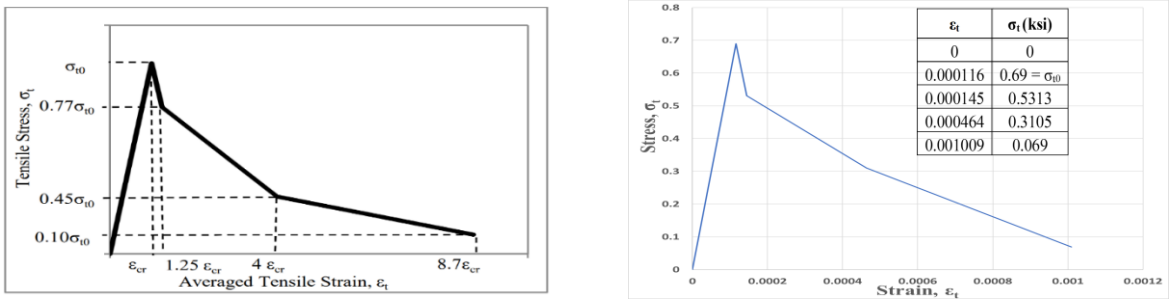

a) generic constitutive curve b) relationship adopted in present study

Figure 5.3 Modified Tension Stiffening Model for ABAQUS (After Nayal and Rasheed, 2006)

5.1.4.3 Failure Surface

The plane stress smeared crack concrete failure surface adopted in ABAQUS is that described by Kupfer and Gerstle (1973) and is shown in Figure 5.4. Four failure ratios are required:

1. The ratio of the ultimate biaxial compressive stress to the ultimate uniaxial compressive stress, f_2/f_{ci} = 1.16 [ABAQUS default value].

2. The absolute value of the ratio of the uniaxial tensile stress at failure to the ultimate uniaxial compressive stress, f_{t0}/f_{ci} = 0.69/9 = 0.077 [calculations shown above].

3. The ratio of the magnitude of a principal component of plastic strain at ultimate stress in biaxial compression to the plastic strain at ultimate stress in uniaxial compression; the ABAQUS default value is 1.28.

4. The ratio of the tensile principal stress at cracking, in plane stress, when the other principal stress is at the ultimate compressive value, to the tensile cracking stress under uniaxial tension; the ABAQUS default value is 0.33.

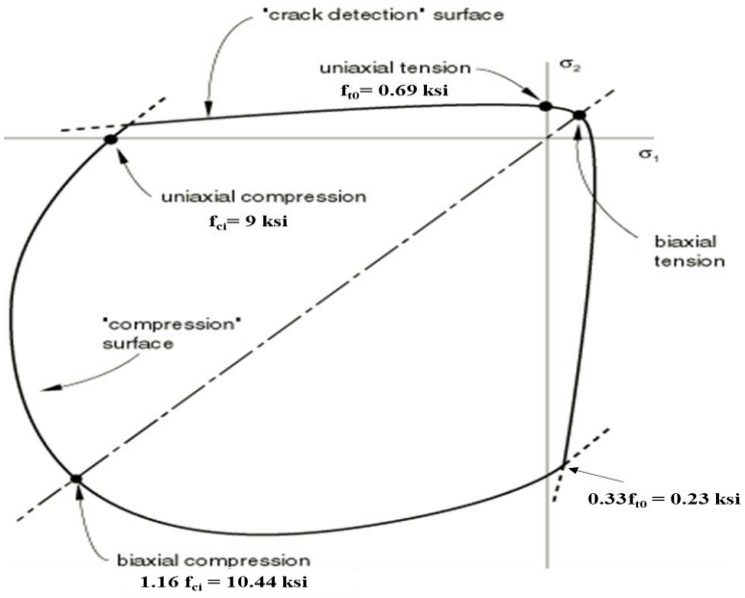

Figure 5.4 ABAQUS smeared crack concrete failure surface (after Kupfer and Gerstle 1973)

5.1.4.4 Shear Retention

The ABAQUS smeared crack model also permits shear retention – that is the degree of shear capacity retained in the cracked concrete model. In this study, full shear retention (ABAQUS default) is assumed. This assumption should not impact results of this study in any way.

5.1.5 Application of Elastic and Smeared Crack Models:

Figure 5.5 shows representative examples of the implementation of both the elastic (left side of figure) and smeared crack models (right side).

Model geometry and the effects of applying the temperature-induced transverse strand strains on elastic isotropic models are shown in Figure 5.5a and c. Both figures show the stresses at the interface of the strand/concrete; clearly showing the correct linear application of the [temperature-induced] dilation. The very local effects of this stress validate the use of the prism size adopted. Elastic stresses will be compared with those derived from the theory presented in Section 1.5 in order to validate the model; this is presented in Section 0. The significantly lower stresses and nonlinearity in the smeared crack model (Figure 5.5b and d) dramatically illustrate the effects of softening and cracking behavior.

elastic concrete properties
Stress range shown is -5.63 to 6.32 ksi.

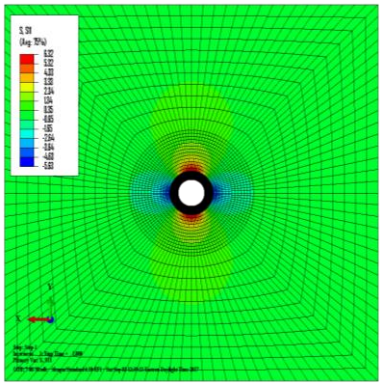

a) Cross section at z = 0 showing distribution of horizontally oriented stress (σ_x); circumferential stress, σ_θ, is therefore at 12 and 6 o'clock around the strand

smeared crack concrete model
Stress range shown is -4.21 to 1.58 ksi.

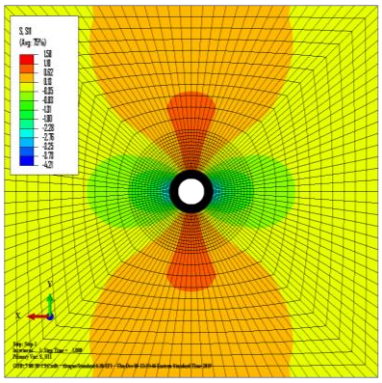

b) Cross section at z = 0 showing distribution of horizontally oriented stress (σ_x); circumferential stress, σ_θ, is therefore at 12 and 6 o'clock around the strand.

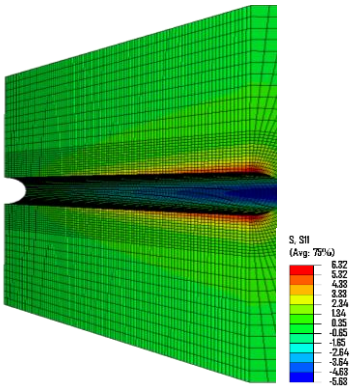

c) Elastic longitudinal section along interface of strand and concrete (free end on right) showing distribution of horizontally oriented stress (σ_x)

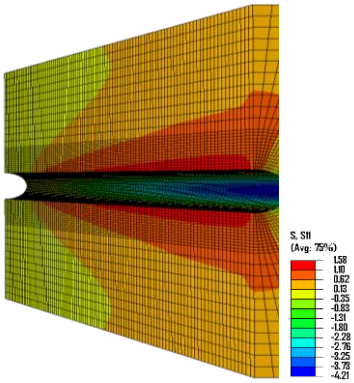

d) Smeared crack longitudinal section along interface of strand and concrete (free end on right) showing distribution of horizontally oriented stress (σ_x).

Figure 5.5 Representative FEM results of single strand model 7-60-30 having elastic and smeared crack concrete models.

5.2 Results of Elastic Modeling

The isotropic elastic concrete model was used to validate the FEM against the theoretical solution presented in Section 1.5. Although limited based on elastic behavior, the model permits behavior trends to be established and permits a direct comparison between 0.6-in. and 0.7-in. strand behavior.

5.2.1 Single-strand Models Results

Circumferential stresses determined from the FEM study and determined analytically using Eq.(1–10) are shown in Table 5.3. Stresses are reported at longitudinal distances, $z = 0$ and $z = 4$ in. from the free end of the prism. At each location, stresses are reported at the surface of the strand ($r = r_0$) and at a radial distance from the center of the strand of $r = 1$ in. As expected, the trends are identical and the FEM-predicted values are uniformly lower than the simple analytical model.

Table 5.3. Predicted circumferential tensile stresses resulting from Hoyer effect for single-strand elastic concrete model

Case	v_p	L_t (in.)	σ_θ (ksi), Eq. (1–10)				σ_θ (ksi), (FEM)					
			z = 0		z = 4 in.		ε_{pH}	ΔT (°K)	z = 0		z = 4 in.	
			$r = r_0$	r = 1.0 in.	$r = r_0$	r = 1.0 in.			$r = r_0$	r = 1.0 in.	$r = r_0$	r = 1.0 in.
0.6- in. strand (r_0 = 0.30 in.)												
6-30-20	0.20	18 ($30d_b$)	6.15	0.61	4.85	0.48	0.0014	117	4.45	0.48	3.38	0.36
6-30-25	0.25		7.74	0.77	6.09	0.60	0.0018	150	5.84	0.62	4.36	0.47
6-30-30	0.30		9.36	0.93	7.35	0.73	0.0021	175	7.00	0.74	5.21	0.56
6-30-35	0.35		11.01	1.09	8.63	0.86	0.0025	208	8.54	0.90	6.26	0.67
6-30-40	0.40		12.69	1.26	9.94	0.98	0.0028	233	9.88	1.04	7.20	0.77
6-60-20	0.20	36 ($60d_b$)	6.15	0.61	5.50	0.54	0.0014	117	4.48	0.48	3.82	0.41
6-60-25	0.25		7.74	0.77	6.92	0.68	0.0018	150	5.88	0.63	4.95	0.53
6-60-30	0.30		9.36	0.93	8.36	0.83	0.0021	175	7.06	0.75	5.96	0.64
6-60-35	0.35		11.01	1.09	9.82	0.97	0.0025	208	8.61	0.91	7.17	0.77
6-60-40	0.40		12.69	1.26	11.31	1.12	0.0028	233	9.91	1.05	8.13	0.87
0.7-in. strand (r_0 = 0.35 in.)												
7-30-20	0.20	21 ($30d_b$)	6.16	0.83	5.06	0.68	0.0014	117	3.97	0.56	3.12	0.44
7-30-25	0.25		7.76	1.04	6.36	0.85	0.0018	150	5.23	0.73	3.97	0.57
7-30-30	0.30		9.38	1.26	7.67	1.03	0.0021	175	6.28	0.87	4.73	0.67
7-30-35	0.35		11.03	1.48	9.01	1.21	0.0025	208	7.69	1.06	5.79	0.82
7-30-40	0.40		12.71	1.71	10.37	1.39	0.0028	233	8.86	1.21	6.48	0.92
7-60-20	0.20	42 ($60d_b$)	6.16	0.83	5.61	0.75	0.0014	117	4.00	0.56	3.50	0.50
7-60-25	0.25		7.76	1.04	7.06	0.95	0.0018	150	5.27	0.73	4.50	0.64
7-60-30	0.30		9.38	1.26	8.53	1.14	0.0021	175	6.32	0.88	5.26	0.75
7-60-35	0.35		11.03	1.48	10.02	1.35	0.0025	208	7.74	1.07	6.46	0.92
7-60-40	0.40		12.71	1.71	11.54	1.55	0.0028	233	8.93	1.23	7.31	1.04

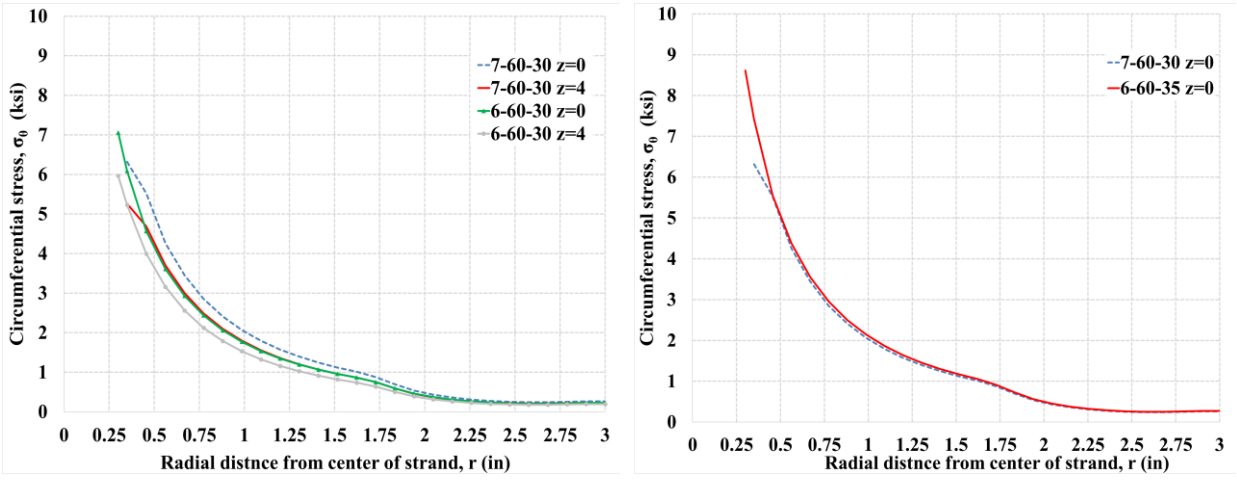

(a) 6-60-30 and 7-60-30 (b) 6-60-35 and 7-60-30

Figure 5.6. Distribution of σ_θ in comparable single-strand models

Figure 5.6 shows examples of the FEM-predicted distribution of circumferential tension stress. Figure 5.6(a) shows the distribution of circumferential tension stress for comparable FEM models 7-60-30 and 6-60-30. The stress at the strand-concrete interface ($r = r_0$) for the 0.7-in. strand is 89% of that for the 0.6-in. strand. This difference reflects the greater contact area (circumference x length) between strand and concrete for the 0.7-in. strand – a parameter not captured in the analytical solution given by Eq.(1–10). At r = 1 in. (theoretically midway between adjacent strands spaced at 2 in.) the stress resulting from dilation of the 0.7-in. strand is 117% of that for the 0.6-in. strand although for the larger strand, r = 1 in. is proportionally closer to the strand surface.

Figure 5.6(b) compares 7-60-30 and 6-60-35. This comparison, based on dilation results reported by Briere et al. (2013), is closer to being comparable since the dilation ratio of the 0.7-in. strand is lower than that of the 0.6-in. strand. In this case, the stress at $r = r_0$ for the 0.7-in. strand is only 73% of that for the 0.6-in. strand; the additional reduction resulting from the smaller dilation ratio. At r = 1 in. the stress resulting from dilation of the 0.7-in. strand is 96% of that for the 0.6-in. strand. Because of the assumption of linear variation of dilation along the transfer length, the model also reflects a linear variation of circumferential stresses from those shown at z = 0 to zero at $z = L_t$.

Based on the Hoyer test results presented in Chapter 3, the relationship between dilation ratio and strand size is not established. In this study (Table 3.2), the dilation ratio generally increases with strand diameter whereas Briere et al (2013) reported the opposite trend (Table 3.1). Nevertheless, it is clear from Table 5.3 that dilation has a significant impact on predicted concrete

stress proportional to the dilation ratio selected. However, more research is necessary to better establish the dilation effects with diameter.

In conclusion, the single strand FEM models predict that – as a result of the greater contact area, the circumferential stresses resulting from the Hoyer effect, will be proportionally lower for the larger strand diameter. The behavior is also affected by the dilation ratio. A lower dilation ratio also results in proportionally lower stresses. Combining these effects in the case were the dilation ratio for the larger strand is lower (Briere et al. 2013), the circumferential stresses resulting from the Hoyer effect are, in fact, marginally lower for the larger strand diameter.

5.2.2 Four-strand Models Results

Results of the four-strand cases are shown in Table 5.4. In each analysis, $v_p = 0.30$ and $L_t = 30d_b$. Results are shown at the free end of the prism ($z = 0$) at the strand surface ($r = r_o$) and midway between adjacent strands ($r = s/2$) as shown in Figure 5.7a.

Table 5.4. Interaction analyses

Case	d_b (in)	s(in)	Prism dimension, 3s (in)	σ_θ (ksi) at $z = 0$			
				Four-strand FEM		Single-strand FEM (see Table 5.3)	
				$r = r_0$	$r = s/2$	$r = r_0$	$r = s/2 = 1.0$
4S-5-1.75	0.5	1.75	5.25	8.14	1.62	-	-
4S-5-2	0.5	2.00	6.00	8.04	1.22	-	-
4S-6-2	0.6	2.00	6.00	7.13	1.49	7.00	0.74
4S-6-2.25	0.6	2.25	6.75	6.65	1.20	-	-
4S-7-2	0.7	2.00	6.00	6.44	1.74	6.28	0.87
4S-7-2.25	0.7	2.25	6.75	6.38	1.39	-	-

Figure 5.7b shows the distributions of circumferential stresses along a section through the center of two strands (see Figure 5.7a). Maximum observed stresses along this section are reported in Table 5.4. Maximum stresses occur at the interface of the strand and concrete and are marginally higher (less than 1% greater in all cases) on the side of the strand facing the adjacent strand indicating some degree of interaction. The minimum stress between the strands (at r = s/2) is also reported in Table 5.4.

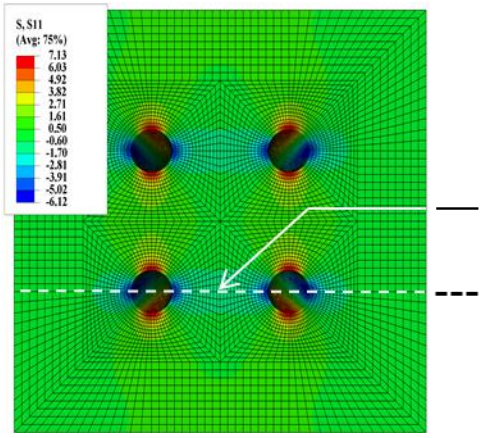

a) Cross section at $z = 0$ showing distribution of horizontally oriented stress (σ_x); horizontal line is line across which stresses are plotted

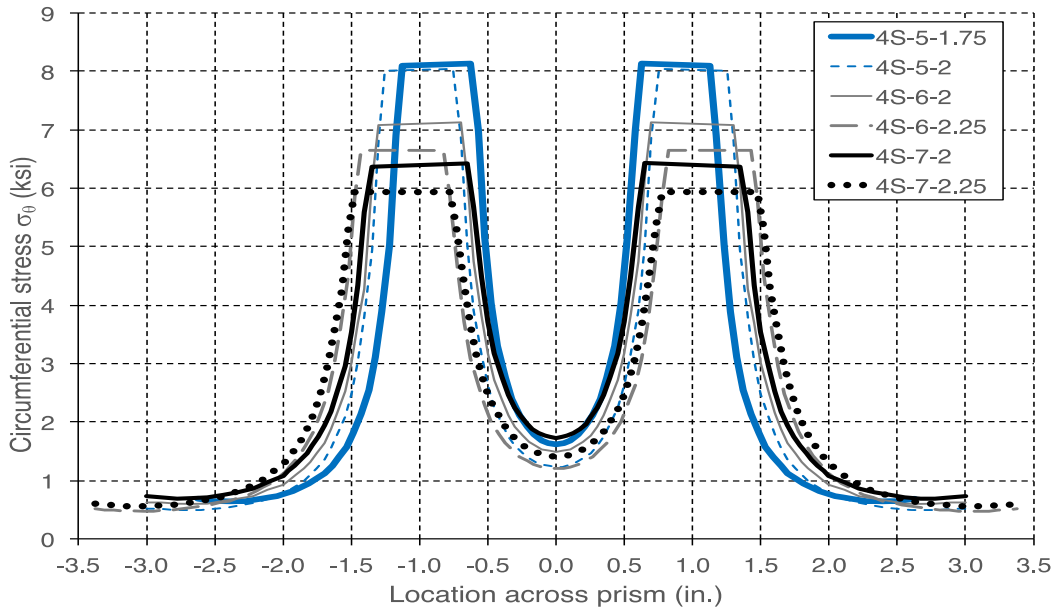

b) stress distribution across section shown in part a of figure

Figure 5.7. Distribution of σ_θ in four-strand models

The results from the four-strand models confirm the findings of the single-strand models: peak circumferential stress falls with increasing strand diameter for the same dilation ratio. This result may be more or less pronounced than is shown in Figure 5.7 since dilation ratio varies with strand diameter. Based on the inverse relationship of dilation and strand diameter reported by

Briere et al. (2013), the peak circumferential stress is expected to be even lower for the larger strand diameter. Overall, peak circumferential stress is only marginally greater in the four-strand model than the single-strand model (Table 5.4); only two comparable cases are available), indicating interaction between adjacent strands.

At the midpoint between strands ($r = s/2$), the stresses are essentially superimposed from the effects of adjacent strands. As should be expected, stresses fall with increased strand spacing although the decrease is not proportional with spacing. The interaction of strand diameter (stress decreasing with diameter) and spacing (stress decreasing with increased spacing) results in similar stresses at $r = s/2$ regardless of the case considered. These findings are consistent with those discussed previously in Section 1.7.

5.3 Results of Smeared Crack Modeling

By capturing the nonlinear effects of material softening and cracking and the resulting redistribution of stress, the smeared crack model is believed to provide a much more realistic estimate of the behavior of concrete affected by the transfer of prestress forces.

5.3.1 SC Single-strand Models Results

Results of all single strand smeared crack models are given in Table 5.3. Comparing these to the elastic model values in Table 5.5, it is clear that stresses are reduced in the presence of cracking. This is due to the softer response and redistribution of stress accompanying cracking. Additionally, due to what is interpreted as extensive predicted cracking at the very end of the prism, the peak stresses occur in the vicinity of z = 1 to 4.5 in. (Table 5.5).

Table 5.5 Predicted circumferential tensile stresses resulting from Hoyer effect for single-strand smeared crack concrete model.

Case	v_p	L_t (in.)	ε_{pH}	ΔT (°K)	σ_θ (FEM) (ksi)				
					z = 0		z *(in)* at $\sigma_{\theta,max}$	$r = r_0$	r = 1 *in.*
					$r = r_0$	r = 1 *in.*			
	0.6- in. strand (r_0 = 0.30 in.)								
6-30-20	0.20	18 ($30d_b$)	0.0014	117	1.04	0.66	1	1.45	0.57
6-30-25	0.25		0.0018	150	1.02	0.73	1	1.56	0.68
6-30-30	0.30		0.0021	175	0.96	0.73	1	1.61	0.69
6-30-35	0.35		0.0025	208	0.90	0.73	1	1.68	0.69
6-30-40	0.40		0.0028	233	0.81	0.73	1	1.73	0.69
6-60-20	0.20	36 ($60d_b$)	0.0014	117	1.04	0.66	1	1.48	059
6-60-25	0.25		0.0018	150	1.02	0.73	1	1.57	0.68
6-60-30	0.30		0.0021	175	0.97	0.73	4	1.63	0.74
6-60-35	0.35		0.0025	208	0.91	0.73	4	1.72	0.77
6-60-40	0.40		0.0028	233	0.82	0.73	4	1.78	0.79
	0.7-in. strand (r_0 = 0.35 in.)								
7-30-20	0.20	21 ($30d_b$)	0.0014	117	0.94	0.70	1	1.38	0.63
7-30-25	0.25		0.0018	150	0.89	0.73	2	1.50	0.72
7-30-30	0.30		0.0021	175	0.81	0.73	1	1.56	0.70
7-30-35	0.35		0.0025	208	0.72	0.73	1	1.62	0.71
7-30-40	0.40		0.0028	233	0.61	0.73	3	1.66	0.79
7-60-20	0.20	42 ($60d_b$)	0.0014	117	0.94	0.71	1	1.40	0.65
7-60-25	0.25		0.0018	150	0.89	0.73	4.5	1.54	0.74
7-60-30	0.30		0.0021	175	0.82	0.73	4.5	1.58	0.77
7-60-35	0.35		0.0025	208	0.73	0.73	4.5	1.66	0.81
7-60-40	0.40		0.0028	233	0.62	0.73	4.5	1.71	0.83

As expected, the smeared crack results (Table 5.5) show the same trends as the elastic analysis and analytical approaches (Table 5.3). The larger strand results in lower circumferential stresses at the interface between the strand and concrete and the dilation ratio affects the interface stresses in a proportional manner.

5.3.1.1 Stress and Cracking Distribution Along the Transfer Length

Figure 5.8 shows the circumferential stress in Case 7-60-30. This is the same data shown in Figure 5.5d except that the grey region in Figure 5.8 indicates the region in which predicted tensile strains exceed those expected to cause cracking (σ_{t0} > 0.69 ksi). This is the region over which smeared cracking is calculated to occur.

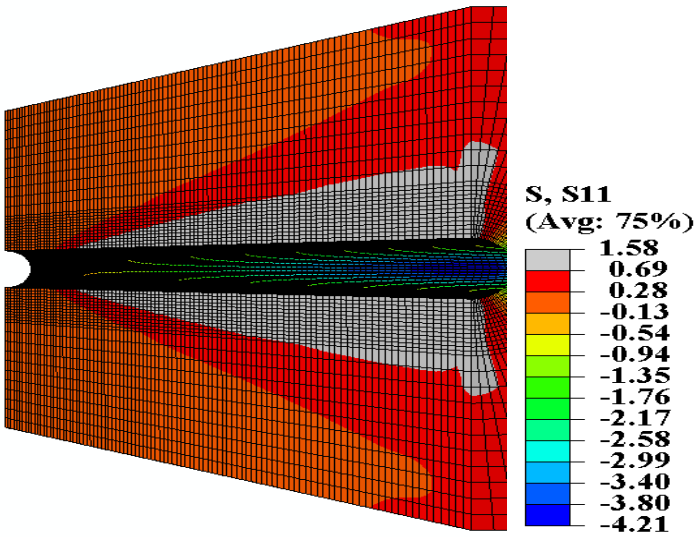

Figure 5.8 Longitudinal section along interface of strand and concrete of 7-60-30 (free end on right) showing distribution of horizontally oriented stress (σ_x).

Unsurprisingly, cracking is predicted at the region of highest dilation, at the free end of the prism. Figure 5.8, however, shows a thin region of smeared cracking extending along the strand almost to the full transfer length ($60d_b$ = 42 in., in the case shown in Figure 5.8). In order to investigate this effect, the model was re-run with lower values of initial prestress force as shown in Table 5.6. The resulting longitudinal distributions of circumferential stress are shown in Figure 5.9.

Table 5.6 effect of different prestress force on circumferential stress on case 7-60-30

Case	Initial force, f_{pi} (ksi)	ΔT (°K)	σ_θ (FEM) (ksi) @ (z = 0, $r = r_0$)
1	$1.00f_{pi}$ = 202.5	175	1.58
2	$0.75f_{pi}$ = 151.9	131	1.47
3	$0.50f_{pi}$ = 101.2	87	1.22
4	$0.25f_{pi}$ = 50.6	44	0.91
5	$0.15f_{pi}$ = 30.4	26	0.78
6	$0.10f_{pi}$ = 20.2	18	0.61

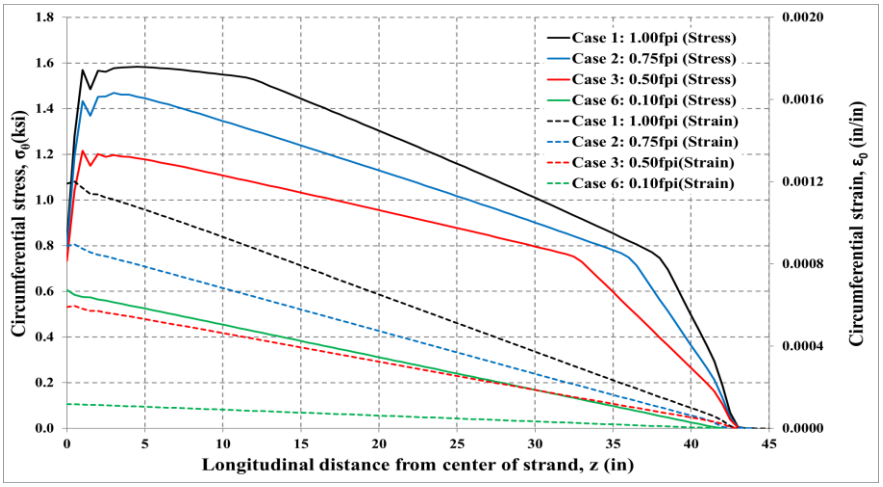

a) effect of different initial prestress force, f_{pi}

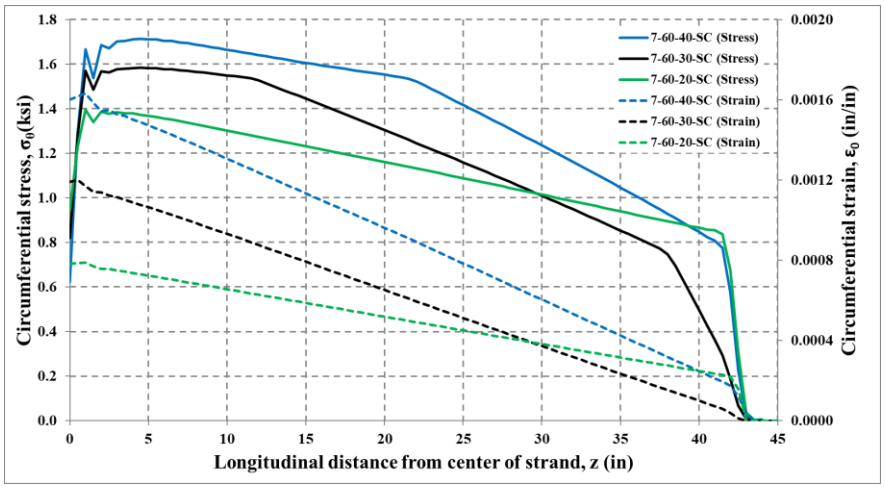

b) effect of different dilation, υ_p

Figure 5.9 Distribution of σ_0 for case 7-60

The behavior shown in Figure 5.9a reveals a distinctly three-part response. From right to left: The end of the transfer length remains uncracked; this uncracked region is represented as the initial "straight" section of the stress distribution. A softened, cracked but still well confined region follows. Finally, at the free end, there is evidence of significant stress redistribution due to local cracking. This behavior is consistent for all initial stress conditions except $0.10f_{pi}$ (Case 6 in Table

5.6) which does not exceed the cracking tensile stress of 0.69 ksi. The sensitivity of this behavior to the assumed dilation of the strand is seen in Figure 5.9b in which three representative cases, 7-60-40, 7-60-30 and 7-60-20, each stressed to f_{pi}, are shown. As described previously, lower dilation results in lower circumferential stress and therefore a reduced region of softened behavior.

5.3.2 Four-strands Models Results

The results of four-strand smeared crack models confirm the findings of the single-strand models.Table 5.7 show the same trends as the elastic analysis and analytical approaches (Table 5.4). Figure 5.10 shows the circumferential stresses through the same section as shown in Figure 5.7 at z = 1 in. and near the end of the development length at z = 25d_b (15 in. for 0.6-in. strand and 17.5 in. for 0.7-in. strand). As reported previously, the larger strand results in lower circumferential stresses at the interface between the strand and concrete (Figure 5.10).

Between adjacent strands, stresses fall with increased strand spacing although the decrease is not proportional to the increase in spacing (Figure 5.10). At z = 1 in., the tensile stresses exceed the cracking threshold of 0.69 ksi and the effect is apparent in the relatively nonuniform circumferential stress adjacent to and moving away from the strands. At z = 1 in. concrete damage is apparent between adjacent strands. Damage between strands is more pronounced at a) smaller spacing; and b) for the larger 0.7 in. strands.

Near the end of the transfer length, at 25d_b, the stress results show the same trends although at lower stresses. Less damage in the concrete is apparent as evidenced by smooth stress transitions between and around strands.

Table 5.7 The effect of applying SC on circumferential tensile stresses for four-strands

Case	d_b (in.)	s (in.)	Prism dimension (in.)	σ_θ (ksi) at z = 0				σ_θ (ksi) at z = 1 in	
				Four-strand FEM		**Four-strand FEM with SC**			
				$r = r_0$	$r = s/2$	$r = r_0$	$r = s/2$ = 1.0	$r = r_0$	$r = s/2$ = 1.0
1	0.5	1.75	5.25	8.14	1.62	0.75	0.79	1.01	0.81
2	0.5	2.00	6.00	8.04	1.22	0.78	0.77	1.00	0.73
3	0.6	2.00	6.00	7.13	1.49	0.71	0.78	0.94	0.78
4	0.6	2.25	6.75	6.65	1.20	0.91	0.76	0.93	0.71
5	0.7	2.00	6.00	6.44	1.74	0.66	0.78	0.91	0.76
6	0.7	2.25	6.75	6.38	1.39	0.66	0.73	0.91	0.66

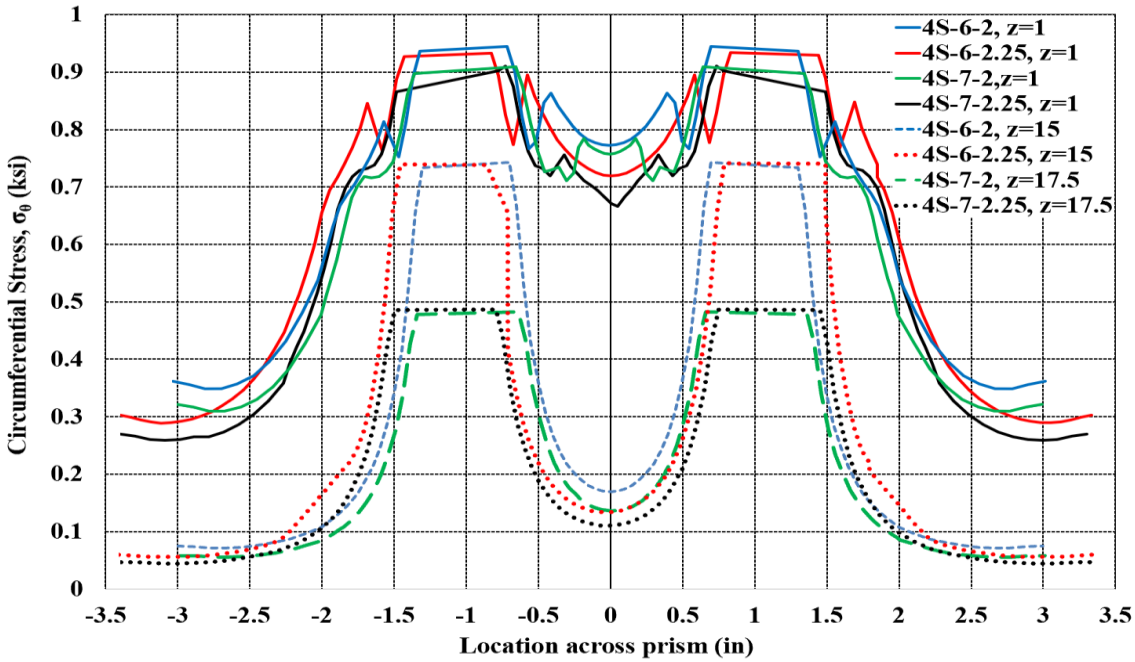

Figure 5.10 Distribution of σ_θ in comparable four-strand models showing the effect of strand size and spacing

5.4 Summary of FEM Findings

5.4.1 Key Observations of This Analytical Study Include:

1. The Hoyer effect is expected to result in circumferential stresses at the strand-concrete interface to exceed the concrete stress tensile strength. The following observations are made in relation to the circumferential stresses:

Dilation ratio: A **lower** dilation ratio results in **lower** circumferential stresses at the interface between the strand and concrete.

Strand diameter: The **larger** strand results in **lower** circumferential stresses.

Spacing: The **greater** spacing between adjacent strands results in **lower** circumferential stresses in a proportional manner.

2. Adopting a smeared crack model of the concrete illustrates the extent of the region of concrete whose stress exceeds the concrete cracking stress. Especially at the free end of the strand, localized damaged associated with only partially-restrained Hoyer effect is evident (Figure 5.9 and Figure 5.10

3. In light of the discussion in Section 1.7, the effect of strand spacing is less clear. Although the concrete stress is not significantly affected (using the smeared crack approach as seen in Table 5.7), the physical extent of ‘cracked’ concrete is greater for smaller spacings and larger strand sizes.

5.4.2 Limitations of the FEM Study

The analytic study presented focused in the effects of dilation only. The inclined radial stresses associated with anchorage (Figure 1.2) are not included. Similarly, the concrete prism was not subject to longitudinal compression and associated lateral Poisson effects. Finally, the prisms modelled lack the transverse confinement of a) transverse reinforcement which would be present along the strand transfer length; and b) the inherent confinement provided by greater amounts of surrounding concrete.

6.0 Long-span Girder Stability

Currently, the largest strand diameter used in prestressed bridge girders is 0.6-in. diameter strand; with the use of 0.7-in. diameter strand, span lengths of existing girder shapes could be increased up to 20% (Ball, 2019). As girders become longer, lifting and handling become more difficult and challenging. Stability during lifting and handling can often control aspects of design. Stability of prestressed concrete girders is considered in terms of the potential for rollover and the susceptibility to excessive deformations causing stress limits to be exceeded.

Rollover is the rigid body rotation of the girder off its seat. Bracing at the girder supports restrains this. Rollover is checked when the girder is seated on cribbing, during transport and during erection. Rollover will typically control long girder design (Zureick et al. 2009). However, mitigating rollover by providing bracing is relatively straight forward at all handling, transportation and erection stages and is commonly done (and is good practice).

Excessive lateral displacement – similar in shape/pattern to lateral torsional buckling (LTB) – causes biaxial bending of the girder leading to cracking and stresses exceeding those permitted in design. Although the mechanism is the same as LTB, the allowable stress limits for prestressed concrete against which section stresses are checked are lower than those at which a true buckling instability would occur. Essentially, no practical prestressed concrete section will exhibit LTB without first cracking and exceeding allowable stress limits. Thus satisfying stress checks *de facto* mitigates LTB. Concrete tension and compression stress limits are those prescribed in AASHTO LRFD *Design Specifications* (2017a; § 5.9.2.3.1a). Excessive lateral deflections must be checked for the girder in its seated or hanging conditions. Effects of lateral forces due to wind and centrifugal forces (during road transportation) are included in these checks.

Zureick et al. (2009) determine girder stability limits for AASHTO Type girders (Table 6.1). They include calculation of LTB and rollover stability for simply supported AASHTO Type I through Type VI girders with a minimum concrete compressive strength of 6 ksi. The LTB calculations do not consider AASHTO stress limits and assume that the girder ends are restrained against roll-over. As a point of reference, Ball (2019) reports the maximum achievable length of a Type VI girder prestressed with 0.6-in. strands having 15 ksi concrete and girder spacing of 6 feet as 184 feet. Using 0.7-in. strands, the maximum achievable length is 202 feet. In either case, the cracking and failure stress limits are likely exceeded before theoretical LTB reported in Table 6.1. The rollover limits in Table 6.1 reinforce the need to provide appropriate bracing at girder supports.

Table 6.1 AASHTO Concrete Girder Stability Limits (FHWA, 2015)

AASHTO Girder Type	Unsupported simple span length below which lateral torsional buckling does not occur (feet)	Simple span length above which rollover support is required (feet)
I	127	75
II	133	80
III	155	100
IV	175	110
V	197	135
VI	193	140

Using the PCI approach described in the following section, similar calculations for a range of single-web sections having 0.6-in. and 0.7-in. strands are developed in order to a) assess the effects of using the larger 0.7-in. strand; and b) investigate mitigating strategies when stability becomes a critical limit state. In addition to potentially longer girder spans, the use of 0.7-in. strand may also result in larger initial prestress forces and greater initial cambers which may exacerbate issues of girder stability.

6.1 PCI Method of Stability Analysis

The prestressed girder stability analysis approach prescribed by PCI (2015) is followed in this Chapter. The fundamental steps of a stability analysis are as follows:

1. Determine girder geometry (Figure 6.1a) and concrete material properties at each erection stage; typically these will be early-age properties.
2. Consider all other factors affecting stability analysis including camber, prestress force, lateral wind pressure, centrifugal force during transport, etc. (PCI 2015).
3. Determine the factor of safety for stability for conditions causing cracking, failure and rollover:

$$FS = \frac{M_r}{M_a} \tag{6–1}$$

Where: M_r= resisting moment; M_a= acting moment.

The PCI procedure is programmed on an Excel spreadsheet (PCI 2019). The version of the spreadsheet used in this study has been revised by the NCHRP 12-109 research team to address a number of programming errors found in the original.

6.1.1 Hanging Girders

The hanging girder condition corresponds to that in which a girder is supported (by a crane) from above by cables attached to the girder's web or top flange. Support is provided near each girder end (Figure 6.1b). For long span girders, lift cables are always vertical (as opposed to inclined as when using a basket or bridle arrangement). The critical lift condition will be when the girder is supported at only two locations (as opposed to when multiple spreaders are used to affect a multi-point lift). Only these conditions are considered here.

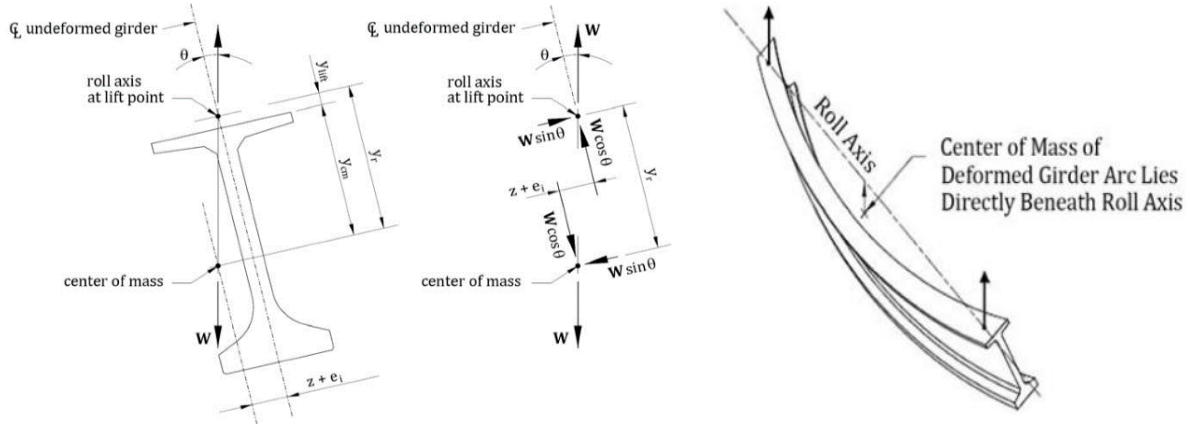

a) Free body diagram of rotated girder

b) Perspective view of a hanging girder

Figure 6.1 Equilibrium position of hanging concrete precast beam (PCI, 2015).

Two factors of safety are calculated when evaluating stability of a hanging girder:

The factor of safety against cracking, which must exceed 1.0, is calculated as:

$$FS_{cr} = \frac{y_r \theta_{max}}{z_0 \theta_{max} + z_{wind} - e_{wind} + e_i} \tag{6–2}$$

The factor of safety against failure, which must exceed 1.5, is calculated as:

$$FS' = \frac{y_r \theta'_{max}}{(z_0 \theta'_{max} + z_{wind})(1 + 2.5\theta'_{max}) - e_{wind} + e_i} \tag{6–3}$$

Where (in reference to Figure 6.1a): y_r = distance of center of gravity of girder from roll axis; θ = rotation angle of the girder from vertical; z_0 = theoretical lateral deflection of the center of gravity of the beam with full dead weight applied laterally; z_{wind} = lateral deflection due to wind force; e_{wind} = eccentricity of girder weight due to wind force; e_i = lateral eccentricity due to sweep and eccentricity due to lifting device from the center line.

The rotation at which a girder cracks is given as:

$$\theta_{max} = \frac{M_{y,crack}}{M_z} \tag{6–4}$$

Where: $M_{y,crack}$ = lateral moment applied to the girder that causes tensile cracking in the most critical flange, and M_z = gravity moment of the girder.

For a cracked section, the lateral stiffness of the girder is reduced, so it will deflect more under the same load. Mast (1993) defines the maximum tilt angle for the cracked section, θ'_{max} as:

$$\theta'_{max} = \sqrt{\frac{e_i}{2.5\ z_0}} \tag{6–5}$$

6.1.2 Seated Girders

The seated girder condition corresponds that in which a girder is supported from below during transportation, storage, or on site (see Figure 6.2).

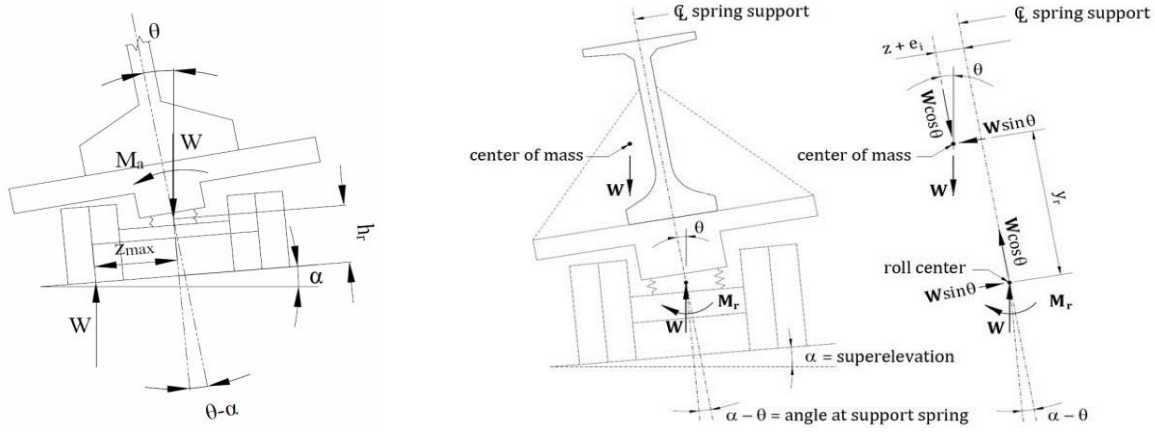

a) Geometric Condition and Free Body Diagram of Transport Vehicle Rollover

b) Geometric Condition and Free Body Diagram of Rotated Girder on Transport Vehicle.

Figure 6.2 Equilibrium of seated girders on transport (PCI, 2015)

Three factors of safety are calculated for analyzing stability of a seated girder:

The factor of safety against cracking, which must exceed 1.0, is calculated as:

$$FS_{cr} = \frac{K_\theta(\theta_{max} - \alpha)}{W\left((\bar{z_0} + y_r)\theta_{max} + z_{wind} + e_i - z_{CE}\right) + M_{ot}} \tag{6–6}$$

The factor of safety against failure, which must exceed 1.5, is calculated as:

$$FS' = \frac{K_\theta(\theta'_{max} - \alpha)}{W\left((\bar{z_0}\theta'_{max} + z_{wind} - z_{CE})(1 + 2.5\theta'_{max}) + e_i + y_r\theta'_{max}\right) + M_{ot}} \tag{6–7}$$

The factor of safety against rollover, which must exceed 1.5, is calculated as:

$$FS_{roll} = \frac{K_\theta(\theta''_{max} - \alpha)}{W\left((\bar{z_0}\theta''_{max} + z_{wind} - z_{CE})(1 + 2.5\theta''_{max}) + e_i + y_r\theta''_{max}\right) + M_{ot}} \tag{6–8}$$

Where (in reference to Figure 6.2): K_θ= rotational constant of the transport rig or support condition; α = maximum roadway super elevation or cross slope of the support condition; W =

weight of girder; $\bar{z_0}$ = lateral deflection of centroid of the cross section; z_{CE} = deflection of girder due to centrifugal force (when present; see below).

The rotation angles θ_{max} and θ'_{max} are those given by in Eqs (6–4) and (6–5). The critical rotation angle is calculated as:

$$\theta''_{max} = \frac{W(z_{max} - h_r\,\alpha) - (WS - CE)(h_r + z_{max}\,\alpha)}{K_\theta} + \alpha \qquad (6\text{–}9)$$

Where: WS = wind force.

6.1.2.1 Additional Lateral Forces During Transportation

PCI (2015) describes the superposition of wind (WS) and centrifugal force (CE) on a girder during the transportation stage. However, in a conventional arrangement of a vehicle traveling around a curve, the CE component is counteracting the effect of the superelevation (in Figure 6.2b, CE would act to push the girder to the right). Notes provided related to PCI (2019) indicate that two cases should be checked:

a) A transport vehicle stopped on a superelevated curve. In this case CE = 0 since the design speed and curvature radius are not applicable.

b) A transport vehicle travelling around a curve with adverse superelevation such as making a left turn. In this case, for the very long girders considered in this study, one would anticipate speed to be very low and controllable and therefore, once again CE ≈ 0.

Therefore, in this study of very long girders, only wind (WS) loads are applied in the transportation stage analysis.

6.1.3 Interpreting and Revising Stability Analyses

In the conduct of this study, a number of issues arose while interpreting the results of stability analyses and considering measures to mitigate unstable girder conditions.

In some preliminary analyses, negative factor of safety values were obtained in some instances. Such results appear to indicate cases in which the girder being analyzed is exceeding stress limits with only the non-stability-related loads applied. Essentially, such girders are not meeting their design requirements prior to checking for stability.

As will be demonstrated in the following sections, there are many interacting parameters affecting stability. Some are easily revised in the field and it is these parameters that can be more easily (and rationally) varied to meet factor of safety requirements:

Girder support locations are described by parameter *a* (distance from end of girder as shown in Figure 6.3d). In place, a girder is intended to be supported at its ends ($a \approx 6$ in.) and is designed accordingly. However, when supported on dunnage or by a crane, support locations may be varied to improve the stability of the girder – reducing internal stresses and mitigating rollover. For example, a girder that fails to meet requirements for rollover will be braced when placed on its support. Using a shorter span, however, ***may*** permit the girder to be supported on dunnage without the need for bracing. In this study, with very long girders, the support locations are found to be crucial in ensuring adequate stability. Following an initial assumption, the value of *a* is revised until adequate factors of safety are achieved.

It should be noted that the value of *a* may be limited by the interaction of vehicle and roadway geometry. Specifically, the arc 'swept' out by the overhanging end of the girder. Even for very long girders, the value of *a* during the transportation stage is likely limited to about 20 feet.

Transverse support stiffness is also a critical parameter, especially during the transportation phase: the so called "hauling rig stiffness", $K_{q,\,trans}$ parameter (PCI 2015 and 2019). This parameter can be schematically represented by the springs shown beneath the girder support in Figure 6.2. There is little guidance for calculating the transverse support stiffness provided by a transport vehicle. For more conventional girders, using conventional flat-bed trucks, $K_{q,trans} \approx 40000$ kip-in/rad. For the very large girders considered in this study, a special transport would be required. This will inevitably have a greater rotational stiffness since both the girder bearing width and vehicle wheel base will be wider. Upon consultation with practitioners, a value of $K_{q,trans} \approx 82000$ kip-in/rad was selected as an initial value. In some analyses of very long (and heavy) girders, $K_{q,trans}$ had to be increased further to ensure stability.

6.2 Stability Case Study – 223 ft Long WF100G

In order to illustrate and validate the PCI (2015 and 2019) stability analysis procedure, an analysis was conducted of the 223 ft long WF100G described by West (2019). This unique girder design permits the investigation of the PCI approach using an extreme, although documented case. The impact of redesigning this girder – built with 0.6-in. strand – using 0.7-in. strand is also explored.

To achieve the record 223 ft span, West reports the need to modify the WF100G girder section by widening the top flange to improve stability during handling: "*Special consideration was given to girder stability and stresses during plant handling, hauling, and erection. This analysis resulted in the selection of a modified WSDOT WF100G girder cross section, where the top flange was widened from 4 ft-1 in. to 5 ft-1 in. for this project to increase the weak-axis stiffness."*

The present study leverages this knowledge, conducting stability analyses on four variations of the WG100G reported by West. Each variation considers the 223 ft span girder reported.

1. WF100G with 0.6 strand – this, as reported by West, apparently had issues with stability, ultimately requiring Case 2.
2. As built WF100G-MOD with 0.6 strand – this is the modified section reported by West (2019) having a 12 in. wider compression flange.
3. WF100G with 0.7 strand – same as Case 1 but with 0.7 strands providing the same total prestress force.
4. WF100G-MOD with 0.7 strand – same as Case 3 but with the wider top flange of Case 2.

The analyses conducted considered the following conditions for each girder (PCI 2015):

1. Initial crane lift from prestressing bed
2. Girder supported on dunnage
3. Transportation of girder to site
4. Crane lift in field
5. Girder in place in final position with top (temporary strands still active)
6. Girder in place following cutting top strands

Although the following cases are calculated, due to the length of the girders, it is expected that bracing would be installed at each girder end immediately upon setting in place and that required bracing would be installed as soon after multiple girders were in place and absolutely before deck construction began.

7. Multiple seated girders at inactive construction
8. Active deck construction

6.2.1 Cross Section Geometry

Figure 6.3 shows the geometry of the WF100G section. The only difference between WF100G and WF100G-MOD is that the top flange width of the latter is 12 in. wider. Table 6.2 summarizes the section geometries of WF100G and WF100G-MOD. Importantly, it is seen that while the 12 in. wider flange is only a 3% increase in section area (weight), it results in a 40% increase in the weak axis moment of inertia, I_y.

As reported by West (2019), the lightweight concrete used had a unit weight, $\rho_{concrete}$ = 0.125 kip/ft^3, making the unit weight of the girder with reinforcement, $\rho_{reinforced}$ = 0.138 kip/ft^3. The modulus of elasticity of concrete is taken as: $E_c = 120{,}000 w_c^2 f'^{0.33}_c$ (i.e. Eq. (5–1)).

6.2.1.1 Strand Arrangement in WF100G and WF100G-MOD with 0.6-in. Strand

The following strand arrangement is reported by West (2019) and confirmed from available drawings of WF girders (WSDOT 2019).

46 straight 0.6-in. strands:	cgs[1] = 4.08 in. (E in Figure 6.3b)
35 harped 0.6-in. strands:	cgs at midspan = 6.7 in. (F in Figure 6.3c)
	cgs at the end of the girder = 79.5 in. (F_0 in. Figure 6.3b)
	harp point, *b* = 87.5 ft (Figure 6.3d)
10 temporary top 0.6-in. strands:	cgs = 98.5 in. (T in Figure 6.3c)

6.2.1.2 Strand Arrangement in WF100G and WF100G-MOD with 0.7-in. Strand

The WF100G girder was redesigned using 0.7-in. strands. The criteria for the substitution of 0.6-in. with 0.7-in. strand was that total prestress force in both straight and harped strands remained essentially the same and that the girder moment capacity – as described by the prestress force multiplied by the depth to the cgs – remained the same. The resulting design uses fewer strands and, as a result, has lower cgs values at midspan:

32 straight 0.7-in. strands:	cgs = 3.00 in.
28 harped 0.7-in. strands:	cgs at midspan = 5.4 in.
	cgs at the end of the girder = 83.5 in.
	harp point, *b* = 87.5 ft (Figure 6.3d)
10 temporary top 0.6-in. strands:	cgs = 98.5 in. (unchanged from West, 2019)

[1] center of gravity of steel in cross section measured relative to the girder soffit

6.2.1.3 Assumed Prestress Loss

Initial prestress is $f_{pi} = 0.75 f_{pu} = 0.75 \times 270 = 202.5$ ksi. Prestress losses are assumed to be 10% upon release and 50% of total long term losses at 28 days (Martin and Pellow 1983). The effective stress, f_{peff}, is assumed to be the same for top and bottom strands. Therefore:

at release: $f_{peff} = 0.90 f_{pi} = 182$ ksi

at stages after initial storage: $f_{peff} = 0.62 f_{pu} = 167$ ksi

long term: $f_{peff} = 0.56 f_{pu} = 151$ ksi (not required for stability analysis)

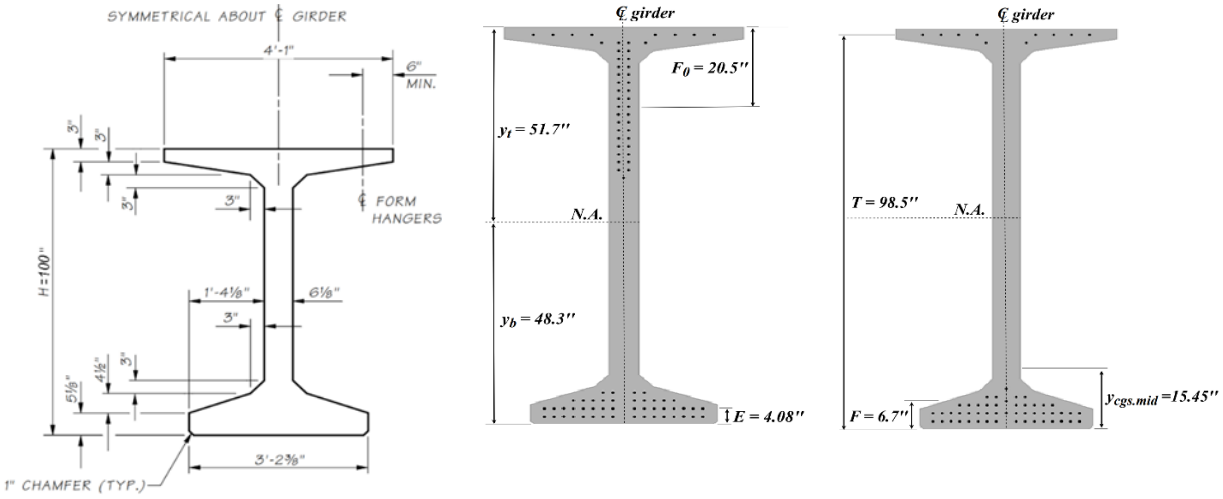

a) WF100G dimensions (WSDOT 2019) top flange = 5 ft-1 in. for WG100G-MOD

b) 0.6-in. strand layout at girder end

c) 0.6-in. strand layout at midspan

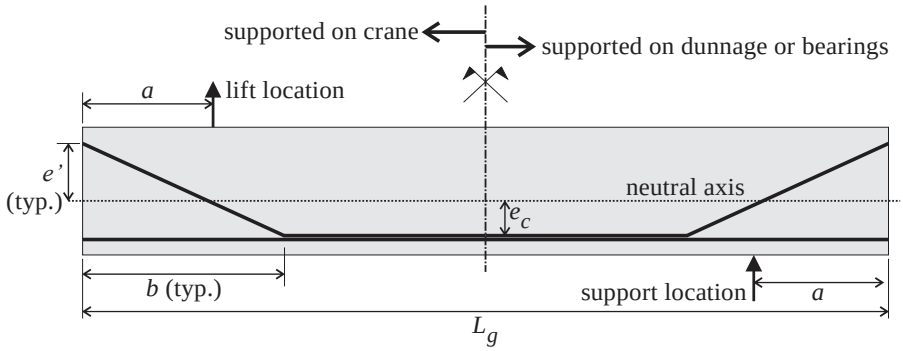

d) longitudinal strand layout and dimensions required for stability analysis
a = lifting and/or dunnage location

Figure 6.3 Geometry of WF100G girder.

Table 6.2 WF100G vs. WF100G-MOD geometric properties.

	WF100G	WF100G-MOD	WF100G-MOD / WF100G
$b_{top\ flange}$	49 in.	61 in.	1.24
A	1084 in^2	1120 in^2	1.03
$A_{top\ flange}$	266 in^2	302 in^2	1.14
$A_{bottom\ flange}$	338 in^2	338 in^2	1.00
I_x	1,526,584 in^4	1,614,640 in^4	1.06
I_y	68,602 in^4	95,935 in^4	1.40
J	8552 in^4	8660 in^4	1.01
I_y/I_x	0.045	0.059	1.32
$I_{y\ top\ flange}$	36,739 in^4	64,072 in^4	1.74
$I_{y\ bottom\ flange}$	30,362 in^4	30,362 in^4	1.00
$I_{y\ web}$	1501 in^4 = 0.022I_y	1501 in^4 = 0.016I_y	1.00
$I_{y\ top}$ / $I_{y\ bottom}$	1.21	2.11	1.74
r_x	37.5 in.	38.0 in.	1.01
r_y	7.96 in.	9.26 in.	1.16
$r_{y\ top\ flange}$	11.75 in.	14.57 in.	1.24
y_{bot}	48.3 in.	50.6 in.	1.05
w	1.039 (kip/ft)	1.070 (kip/ft)	1.03

6.2.1.4 Calculation of Camber

Camber (positive value is upward deflection) is calculated as:

$$\Delta = \Delta_{self} + \Delta_{ps} + \Delta_{ohang} \tag{6–10}$$

Δ_{self} is the [downward] deflection due to girder self-weight calculated over the distance between supports:

$$\Delta_{self} = \frac{-5w\left(L_g - 2a\right)^4}{384EI_g} \tag{6–11}$$

Where a = distance from end of girder to support.

Δ_{ps} is the [net upward] deflection due to prestress, comprised of three components:

straight (temporary top strands): $\Delta_{ps,st} = \frac{p_{eff,st}\, e_{c,st}\, {L_g}^2}{8EI_g}$ (6–12)

straight bottom strands: $\Delta_{ps,sb} = \frac{p_{eff,sb}\, e_{c,sb}\, {L_g}^2}{8EI_g}$ (6–13)

harped strands: $$\Delta_{ps,h} = \frac{p_{eff,h}}{EI_g}\left(\frac{e_{c,h}L^2}{8} - \frac{e'_h b^2}{6}\right) \quad (6\text{–}14)$$

Δ_{ohang} is the [upward] deflection resulting from the girder overhang beyond locations of support:

$$\Delta_{ohang} = \frac{wa^2(L_g - 2a)^2}{16EI_g} \quad (6\text{–}15)$$

Note that in Eqs (6–12) to (6–14), eccentricity is measured from the centroid of the cross section (Figure 6.3d) with strand below the centroid having positive eccentricity. Thus Eq. (6–12) should have a negative [downward] result while Eqs (6–13) and (6–14) are positive [upward].

6.2.1.5 Sweep Tolerance

As recommended by PCI (2015) sweep eccentricity is taken as 1/8 in. per 10 ft length of girder: $e_i = \frac{L_g}{10ft} \times \frac{1}{8}\ in.$ = 2.8 in.

For the transport stability check, 1 in. is added to sweep: $e_{i,trans}$ = 3.8 in. For the initial lift from the prestressing bed, experience from practice indicates that sweep is about one half that recommended: $e_{i,bed}$ = 1.4 in.

6.2.1.6 Bearing Rotational Stiffness, K_q

Bearing stiffness in all cases was calculated based on the recommendations of NCHRP Report 596 (2008):

$$K_q = \frac{EI}{t}(A_r + B_r S^2) \quad (6\text{–}16)$$

Where, *E* and *t* are Young's modulus and thickness of the bearing material; and,

moment of inertia: $$I = L_{brg}W_{brg}^3/12 \quad (6\text{–}17)$$

shape factor: $$S = \frac{L_{brg} W_{brg}}{2t(L_{brg} + W_{brg})} \quad (6\text{–}18)$$

L_{brg} = plan dimension of the bearing parallel to the axis of rotation (length along beam)

W_{brg} = plan dimension of the bearing perpendicular to the axis of the rotation (width across beam section)

A_r is a dimensionless constant taken as 1.0 for rectangular bearing pads.

B_r is a dimensionless constant calculated as follows:

$$B_r \approx (0.24 - 0.024\lambda_{brg}) + (1.15 - 0.89\lambda_{brg})\left(1 - \exp\left(-\frac{0.64 L_{brg}}{W_{brg}}\right)\right) \quad (6\text{–}19)$$

Where the compressibility index is: $\lambda_{brg} = S\sqrt{\frac{3G}{K}}$ (6–20)

G = shear modulus of bearing

K = bulk modulus of bearing

For the WF100G bearings, elastomeric bearings having E = 1.04 ksi, G = 0.1275 ksi, K = 450 ksi, t = 2 in., bearing length, L_{brg} = 12 in. and width, W_{brg} = width of bottom flange – 2 in. =

36 in. With these parameters, K_q = 79303 kip-in/rad.

6.2.1.7 Hauling Rig Stiffness, $K_{q,trans}$

Upon consultation with practitioners, an initial value of $K_{q,trans} \approx$ 82000 kip-in/rad was selected. As described previously, this value may be revised to address transportation stability issues.

6.2.1.8 Stability Analysis Input Parameters

Table 6.3 summarizes girder geometry- and prestressing-related input parameters for the stability analysis. It is noted that material properties vary with the presumed age of the girder at each step. Table 6.4 summarizes the remainder of assumed parameters which do not vary from case to case. In the analyses, an initial value of $a = 0.1L_g = 23$ ft was assumed. This was revised to the values shown in Table 6.3 in order to maximize the factors of safety calculated. A maximum value of $a = 20$ ft was used for the transportation stage. The value of $a = 0.5$ ft is used for all analyses of girders on their bearings and cannot be revised.

Table 6.3 Girder geometry- and prestressing-related input parameters for the stability analysis.

Condition	Lift from bed		Dunnage		Transport		Lift in field		In place		In place (top strands cut)	
Assumed age	Immediately after release		Immediately after release		> 28 days		> 28 days		> 28 days		> 28 days	
strand (in.)	**0.6**	**0.7**	**0.6**	**0.7**	**0.6**	**0.7**	**0.6**	**0.7**	**0.6**	**0.7**	**0.6**	**0.7**
f_c (ksi)	8.4		8.4		10.0		10.0		10.0		10.0	
prestress losses	10%		10%		50%		50%		50%		50%	
f_{peff} (ksi)	182		182		167		167		167		167	
p_{eff} (kips)	3594	3605	3594	3605	3298	3308	3298	3308	3298	3308	2935	2946
$y_{cgs,mid}$ (in)	15.45	14.46	15.45	14.46	15.45	14.46	15.45	14.46	15.45	14.46	5.31	4.12
$e_{i.total}$ (in)	1.4		2.8		3.8		2.8		2.8		2.8	
a (ft)	29		26		20		29		0.5		0.5	
	WF100G											
Δ (in) (L_g/Δ)	14.03 (191)	14.79 (181)	13.60 (197)	14.36 (186)	10.66 (251)	11.32 (236)	11.99 (223)	12.65 (212)	6.36 (421)	7.02 (381)	8.54 (313)	9.20 (291)
Δ_{self} (in)	-2.46	-2.46	-2.84	-2.84	-3.51	-3.51	-2.32	-2.32	-7.61	-7.61	-7.61	-7.61
Δ_{ps} (in)	16.13	16.89	16.13	16.89	13.97	14.63	13.97	14.63	13.97	14.63	16.15	16.81
Δ_{ohang} (in)	0.36	0.36	0.31	0.31	0.20	0.20	0.34	0.34	0.00	0.00	0.00	0.00
	WF100G-MOD											
Δ (in) (L_g/Δ)	14.12 (190)	14.83 (180)	13.70 (195)	14.41 (186)	10.76 (249)	11.38 (235)	12.07 (222)	12.69 (211)	6.57 (408)	7.18 (372)	8.54 (314)	9.15 (292)
Δ_{self} (in)	-2.40	-2.40	-2.77	-2.77	-3.43	-3.43	-2.27	-2.27	-7.44	-7.44	-7.44	-7.44
Δ_{ps} (in)	16.16	16.88	16.16	16.88	14.00	14.62	14.00	14.62	14.00	14.62	15.97	16.59
Δ_{ohang} (in)	0.36	0.36	0.31	0.31	0.20	0.20	0.34	0.34	0.00	0.00	0.00	0.00

Table 6.4 Other input parameters for stability analysis (PCI 2015)

Lifting	
rigid extension of lift device above top of girder, y_{lift}	0.000 in.
lateral tolerance of lift device from centerline of girder, e_{conn}	0.250 in.
lateral wind force at lifting from bed, $w_{wind.lift1} = w_{wind.lift1i}$	0.015 klf
lateral wind force at lifting in field, $w_{wind.lift2} = w_{wind.lift2i}$	0.015 klf
Seating on Dunnage	
plan dimension of the bearing parallel to the axis of the rotation, $W_{brg.seat1}$	width of bottom flange – 2 in. = 36 in.
height from roll center to bottom of girder, $y_{brg.seat1}$	2.000 in.
height of roll center from bearing seat, $h_{roll.seat1}$	2.000 in.
bearing tolerance from CL girder to CL support, $e_{brg.seat1}$	0.250 in.
bearing rotational stiffness, K_{qseat1}	Eq.(6–16)
transverse seating tolerance from level, a_{seat1}	0.005 ft/ft
lateral wind force, $w_{wind.seat1}$	0.055 klf
Transportation	
bunking tolerance from CL girder to CL support, $e_{bunk.trans}$	1.000 in.
hauling rig stiffness, $K_{g.trans}$	82000 kip-in/rad
superelevation, a_{trans} =	0.020 ft/ft
turn radius for adverse cross slope, $Radius_{trans}$	120.00 ft
hauling rig velocity in turn, Vel_{trans}	10.000 mph
height from roll center to bottom of girder, $y_{seat.trans}$	12.000 in.
horiz. dist. from roll axis to center of tire group, $z_{max.trans}$	36.000 in.
height of roll center above roadway, $h_{roll.trans}$	48.000 in.
lateral wind force, $w_{wind.trans}$	0.055 klf
Single Girder on Bearings	
plan dimension of the bearing parallel to the axis of the rotation, $W_{brg.seat1}$	width of bottom flange – 2 in. = 36 in.
height of bearing, $h_{brg.seat2}$	2.000 in.
height from roll center to bottom of girder, $y_{brg.seat2} = h_{brg.seat2}/2$	1.000 in.
height of roll center from bearing seat, $h_{roll.seat2} = y_{brg.seat2}$	1.000 in.
bearing tolerance from CL girder to CL support, $e_{brg.seat2}$	0.250 in.
bearing rotational stiffness, $K_{g.seat2}$	Eq.(6–16)
transverse seating tolerance from level, a_{seat2} =	0.005 ft/ft
lateral wind force, $w_{wind.seat2}$ =	0.015 klf

6.2.1.9 Stability Analysis Results

Results of the stability analyses are given in Table 6.5 in terms of the three Factors of Safety prescribed by PCI (2015) and described in Section 6.1:

$FS_{cr} \geq 1.0$ factor of safety against girder cracking

$FS' \geq 1.5$ factor of safety against girder failure

$FS_{roll} \geq 1.5$ factor of safety against girder rolling off supports

Table 6.5 Summary of stability analysis

	WF100G 0.6-in. strands			WF100G-MOD 0.6-in. strands			WF100G 0.7-in. strands			WF100G-MOD 0.7-in. strands		
	FS_{cr}	FS'	FS_{roll}	FS_{cr}	FS'	FS_{roll}	FS_{cr}	FS'	FS_{roll}	FS_{cr}	FS'	FS_{roll}
acceptance criteria	1.0	1.5	1.5	1.0	1.5	1.5	1.0	1.5	1.5	1.0	1.5	1.5
lift from bed	1.57	1.57	-	1.83	1.83	-	1.53	1.53	-	1.76	1.76	-
on dunnage	1.43	2.63	1.79	1.65	2.87	1.93	1.18	2.63	1.78	1.42	2.86	1.93
transportation	**0.78**	1.90	1.55	**0.95**	2.11	1.70	**0.64**	1.89	1.55	**0.81**	2.11	1.70
lift in field	1.55	1.55	-	1.78	1.78	-	1.51	1.51	-	1.72	1.72	-
place on bearings	1.32	**1.21**	**0.65**	1.53	**1.43**	**0.76**	1.29	**1.21**	**0.65**	1.50	**1.43**	**0.76**

The analyses conducted in this study suggest that the girder is susceptible to cracking during transportation ($FS_{cr} < 1$). The low FS values for the transportation stage result from the imposed practical limit $a < 20$ ft. Using $a = 37$ ft, for instance, all four analyses presented result in $FS_{cr} > 1.0$. It must be understood that many assumptions (Table 6.4) go into these analyses and results are quite sensitive, in some cases, to these. Regardless of the analysis, however, it is clear that this extra-long girder requires immediate shoring to resist rollover when placed on its bearings.

The dramatic improvement in stability by simply increasing the compression flange width 12 in. resulting in a 40% increase in Iy (Table 6.2) is clearly evident. Given the extreme dimensions of the case study girder, it is felt that this is a reasonable and efficient approach to improving stability when required.

When using larger strands the stability factors of safety fall marginally in some cases (Table 6.5). This is due primarily to the larger camber in each case (Table 6.3). The stability can be improved by adjusting some of the analysis parameters such as: crane hook locations (a), increasing bearing rotational stiffness (K_q), increasing hauling rig stiffness ($K_{q,trans}$), decreasing the hauling rig velocity ($V_{el,trans}$), increasing dimension of bearing (W_{brg}, L_{brg}) where possible, and so on. If revision of these parameters does not improved stability sufficiently, the girder requires intermediate bracing which is only practical once erected.

6.3 Evaluation of Cases From Ball (2019)

The objective of Ball (2019) was to maximize girder spans for different cross section shapes using 0.6-in. and 0.7-in. strand. Typically, the larger strand allowed longer lengths to be achieved due to the greater prestress force available using the same – already maximized – strand pattern. Ball considered all AASHTO design limits in order to maximize the span lengths but did not verify girder stability limitations.

In the present study, those cross section and span combinations resulting in the greatest achievable increases in span length when replacing 0.6-in. with 0.7-in. strands are selected for stability analysis. These potentially represent the most efficient use of 0.7-in. strands but also introduce the greatest potential impacts on stability. Table 6.6 summarizes the cases reported by Ball (2019) selected for stability analysis in this study. Only the longer 0.7-in. strand-reinforced girders are analyzed.

Table 6.6 Critical cases selected from Ball (2019)

Case	f'_c (ksi)	girder spacing (ft)	L_g (ft) with 0.6-in. strands	L_g (ft) with 0.7-in. strands	potential increase in span length using 0.7-in. strand
WF100G	15	10	170	207	21.8%
WF74G	18	10	150	181	20.7%
BT-72	18	12	113	135	19.5%
OHWF-72	10	8	164	185	12.8%
FIB-96	18	8	207	223	12.6%
NU-2000	18	6	196	220	12.2%

Similar to the case study presented in Section 6.2, girder and analysis parameters are assembled from Ball (2019) or assumed as in Section 6.2. Strand arrangement, geometric, and prestressing-related input parameters are shown in Table 6.7 through Table 6.9. Girder unit weight is assumed to be 0.150 kips/ft^3 in all cases. Other analysis parameters not indicated are the same as those given in Table 6.4. The girder support location, *a* was the primary parameter used to

maximize the calculated factors of safety. In all analyses, an initial assumption of $a = 0.1L_g$ was made and the analyses revised until adequate (or maximum) factors of safety were achieved. the resulting values of a used are reported in Table 6.9. A complete set of example calculations for the NU-2000 girder are provided in Appendix C.

Table 6.7 Strand arrangement (Ball 2019)

WF100G and WF74G	
46 straight 0.7-in. strands;	cgs = 4.08 in.
11 harped 0.7-in. strands;	cgs at midspan = 8.5 in.
	cgs at the end of the girder = 91.5 in.
BT-72	
32 straight 0.7-in. strands;	cgs = 3.875 in.
2 harped 0.7-in. strands;	cgs at midspan = 6 in.
	cgs at the end of the girder = 70 in.
4 debonded 0.7-in. strands;	2@5', 2@10'
OHWF-72	
57 straight 0.7-in. strands;	cgs = 7.6 in.
2 harped 0.7-in. strands;	cgs at midspan = 10 in.
	cgs at the end of the girder = 69.5 in.
14 debonded 0.7-in. strands;	4@5', 2@10', 2@15', 4@25', 2@30
FIB-96	
66 straight 0.7-in. strands;	cgs = 5.91 in.
5 harped 0.7-in. strands;	cgs at midspan = 14.2 in.
	cgs at the end of the girder = 91.5 in.
NU-2000	
52 straight 0.7-in. strands;	cgs = 4.08 in.
8 harped 0.7-in. strands;	cgs at midspan = 11.00 in.
	cgs at the end of the girder = 70.7-in.

Table 6.8 Geometric properties used in stability analysis (calculations based on Ball (2019))

	WF100G	**WF74G**	**BT-72**	**OHWF-72**	**FIB-96**	**NU-2000**
L_g (ft)	207	181	135	185	223	220
$b_{top\ flange}$ (in)	49	49	42	49	48	48.25
$b_{bot\ flange}$ (in.)	38.375	38	26	40	38	38.375
A (in^2)	1,084	825	767	1,163	1,176	904
I_x (in^4)	1,524,912	734,356	545,894	844,069	1,464,296	790,592
I_y (in^4)	68,602	72,018	41,083	104,334	77,066	60,817
I_y/I_x	0.045	0.098	0.075	0.124	0.055	0.077
J (in^4)	8552	6560	6178	11,414	11,043	7224
y_{bot} (in)	48.3	35.6	36.6	35.8	42.8	35.7
w (kip/ft)	1.128	0.859	0.799	1.212	1.278	0.942

Table 6.9 Girder geometry-and prestressing-related input parameters for the stability analysis (Ball 2019)

Girder	Condition	Lift from bed	Dunnage	Transport	Lift in field	In place
	Assumed age	**Immediately after release**	**Immediately after release**	**> 28 days**	**> 28 days**	**> 28 days**
	prestress losses	10%	10%	50%	50%	50%
	f_{peff} (ksi)	182	182	167	167	167
WF100G (207 ft)	f_c (ksi)	12.5	12.5	15	15	15
	p_{eff} (kips)	3050	3050	2799	2799	2799
	$y_{cgs,mid}$ (in)	4.06	4.06	4.06	4.06	4.06
	$e_{i.total}$ (in)	1.3	2.6	3.6	2.6	2.6
	a (ft)	22	0.5	0.5	22	0.5
	Δ *(in)*	9.70	6.6	5.32	8.24	5.32
	(L_g/Δ)	256	377	467	301	467
WF100G (207 ft) - (+12 inches to top flange width)	*a (ft)*	19	6	4	19	0.5
	Δ *(in)*	8.78	7.02	5.47	7.43	4.89
	(L_g/Δ)	283	354	454	334	508
WF100G (207 ft) - (+18 inches to top flange width)	*a (ft)*	16	4	4	16	0.5
	Δ *(in)*	8.21	6.48	5.28	6.91	4.71
	(L_g/Δ)	303	383	470	360	528
WF74G	f_c (ksi)	15	15	18	18	18
	p_{eff} (kips)	3050	3050	2799	2799	2799
	$y_{cgs,mid}$ (in)	4.06	4.06	4.06	4.06	4.06
	$e_{i.total}$ (in)	1.1	2.3	3.3	2.3	2.3
	a (ft)	12	1	1	12	0.5
	Δ *(in)*	9.81	8.07	6.66	8.29	6.57
	(L_g/Δ)	221	269	326	262	331
BT-72	f_c (ksi)	15	15	18	18	18
	p_{eff} (kips)	1605	1605	1472	1472	1472
	$y_{cgs,mid}$ (in)	4.00	4.00	4.00	4.00	4.00
	$e_{i.total}$ (in)	0.8	1.7	2.7	1.7	1.7
	a (ft)	4	1	1	4	0.5
	Δ *(in)*	3.54	3.27	2.71	2.96	2.66
	(L_g/Δ)	458	495	599	548	609
OHWF-72	f_c (ksi)	8.4	8.4	10	10	10
	p_{eff} (kips)	2408	2408	2209	2209	2209
	$y_{cgs,mid}$ (in)	7.68	7.68	7.68	7.68	7.68
	$e_{i.total}$ (in)	1.2	2.3	3.3	2.3	2.3
	a (ft)	15	1	1	15	0.5
	Δ *(in)*	5.89	2.52	1.66	4.85	1.52
	(L_g/Δ)	377	882	1335	457	1457
FIB-96	f_c (ksi)	15	15	18	18	18
	p_{eff} (kips)	3799	3799	3486	3486	3486
	$y_{cgs,mid}$ (in)	6.49	6.49	6.49	6.49	6.49
	$e_{i.total}$ (in)	1.4	2.8	3.8	2.8	2.8
	a (ft)	25	15	15	25	0.5
	Δ *(in)*	10.38	8.89	7.39	8.80	4.59
	(L_g/Δ)	258	301	362	304	584
FIB-96 - (+12 inches to top flange width)	*a (ft)*	21	11	17	21	0.5
	Δ *(in)*	9.42	7.75	7.34	7.92	4.21
	(L_g/Δ)	284	345	364	338	635
NU-2000	f_c (ksi)	15	15	18	18	18
	p_{eff} (kips)	3210	3210	2946	2946	2946
	$y_{cgs,mid}$ (in)	5.00	5.00	5.00	5.00	5.00
	$e_{i.total}$ (in)	1.4	2.8	3.8	2.8	2.8
	a (ft)	26	10	13	26	0.5
	Δ *(in)*	14.13	10.57	9.38	11.99	5.89
	(L_g/Δ)	187	250	281	220	448

Results of stability analyses are given in Table 6.10 in terms of the three Factors of Safety prescribed by PCI (2015) and described in Section 6.1.

Table 6.10 summary of stability analysis

Girder		acceptance criteria	lift from bed	dunnage	transportation	lift in field	Place on bearings
WF100G (207 ft)	FS_{cr}	1	1.20	**0.25**	**0.02**	1.23	1.60
	FS'	1.5	1.58	1.55	**1.44**	1.54	1.86
	FS_{roll}	1.5	-	**1.15**	**1.23**	-	**0.95**
WF100G (207 ft) (+12 inches to top flange width)	FS_{cr}	1	1.44	**0.58**	**0.31**	1.38	1.90
	FS'	1.5	1.63	2.15	1.85	1.59	2.15
	FS_{roll}	1.5	-	1.53	1.53	-	**1.06**
WF100G (207 ft) (+18 inches to top flange width)	FS_{cr}	1	1.51	1.01	1.00	1.42	2.13
	FS'	1.5	1.58	2.41	2.89	1.52	2.34
	FS_{roll}	1.5	-	1.64	2.05	-	**1.12**
	Changes to parameters in order to stabilize the girder: K_{qseat1} = 87000 kip-in/rad for dunnage support $K_{q.trans}$ = 117000 kip-in/rad and $w_{wind.trans}$ = 0.050 klf for transportation						
WF74G	FS_{cr}	1	1.61	2.72	2.08	1.52	5.06
	FS'	1.5	1.61	4.24	3.80	1.52	4.95
	FS_{roll}	1.5	-	2.09	2.33	-	1.52
BT-72	FS_{cr}	1	1.59	1.00	1.82	1.48	2.37
	FS'	1.5	1.59	3.66	7.35	1.51	2.76
	FS_{roll}	1.5	-	1.80	3.26	-	**1.14**
	Changes to parameters in order to stabilize the girder: $K_{q.seat2}$ = 34000 kip-in/rad for dunnage support						
OHWF-72	FS_{cr}	1	1.84	2.74	2.12	1.58	3.63
	FS'	1.5	1.84	2.81	2.49	1.58	3.20
	FS_{roll}	1.5	-	1.91	1.98	-	**1.37**
FIB-96	FS_{cr}	1	1.53	**0.90**	**0.60**	1.50	1.50
	FS'	1.5	1.53	1.97	1.79	1.50	**1.45**
	FS_{roll}	1.5	-	1.52	1.56	-	**0.83**
FIB-96 (+12 inches to top flange width)	FS_{cr}	1	1.63	1.25	1.01	1.55	1.77
	FS'	1.5	1.63	1.97	2.28	1.55	1.69
	FS_{roll}	1.5	-	1.52	1.89	-	**0.93**
	Changes to parameters in order to stabilize the girder: $K_{q.trans}$ = 88000 kip-in/rad for transportation						
NU-2000	FS_{cr}	1	1.54	1.34	1.00	1.51	2.27
	FS'	1.5	1.54	2.34	2.37	1.51	2.08
	FS_{roll}	1.5	-	1.52	1.82	-	**0.93**

As seen in Table 6.10, despite the long spans, adequate stability could be achieved with all cross sections. Sections having the lowest ratio I_y/I_x – WF100G and FIB-96 – required additional flange width, similar to that described in Section 6.2, in order to achieve stability at all stages. These girders also tended to require stiffer supports as described in Sections 6.1.3 and 6.2.1.9. For example, The WF100G with an 18 in. wider top flange described in Table 6.10 fails the cracking

check in the transportation stage. Increasing the hauling rig stiffness from $K_{q,trans}$ = 82,000 kip-in/rad to $K_{q,trans}$ = 117,000 kip-in/rad brings FS_{cr} = 1.0 for this case. The question then becomes, *is this required rig stiffness achievable?*

The BT-72 section has a thinner bottom flange width, $b_{bot\ flange}$ = 26 inches, than the other sections. This results in a significantly lower bearing rotational stiffness, $K_{q.seat2}$ = 22700 kip-in/rad (Eq.(6–16)). When placed on dunnage, this stiffness is inadequate. Increasing the stiffness to 34000 kip-in/rad is sufficient to mitigate this instability.

It should not be surprising that the factor of safety against rollover when the girders are placed on bearings cannot be achieved. Such long girders would require immediate installation of braces at their ends.

The effect of increasing top width flange on girder stability is shown in Table 6.11 and Figure 6.4. As I_y/I_x increases, the factors of safety against cracking and rollover at the girder placement stage improve. Figure 6.4 shows the effects of increasing the top flange width in 6 in. increments to 24 in. Increasing the ratio I_y/I_x is seen to have considerable effect although typically not enough to achieve an adequate safety against rollover. Rollover must be mitigated by the immediate installation of braces in any event.

Table 6.11 Effect of of I_y/I_x on stability

added flange width	WF100G			BT-72			OHWF-72		
	I_y/I_x	FS_{cr}	FS_{roll}	I_y/I_x	FS_{cr}	FS_{roll}	I_y/I_x	FS_{cr}	FS_{roll}
as built	0.045	1.60	0.95	0.075	2.37	1.14	0.124	3.73	1.37
+12 in.	0.059	1.9	1.06	0.105	2.63	1.19	0.165	4.12	1.47
+18 in.	0.072	2.13	1.12	0.129	2.79	1.21	0.192	4.32	1.52
+24 in.	0.083	2.29	1.17	0.158	2.93	1.23	0.224	4.51	1.56
	FIB-96			NU-2000			WF100G (case study)		
	I_y/I_x	FS_{cr}	FS_{roll}	I_y/I_x	FS_{cr}	FS_{roll}	I_y/I_x	FS_{cr}	FS_{roll}
as built	0.053	1.5	0.83	0.076	2.27	0.93	0.045	1.29	0.65
+12 in.	0.069	1.77	0.93	0.098	2.61	1.04	0.059	1.50	0.76
+18 in.	0.08	1.93	0.99	0.112	2.82	1.10	0.072	1.71	0.83
+24 in.	0.092	2.09	1.04	0.129	3.06	1.16	0.083	1.87	0.89

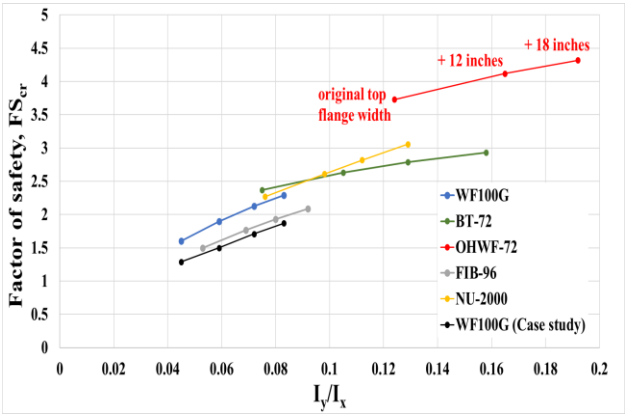

a) Effect of top flange width on FS_{cr}

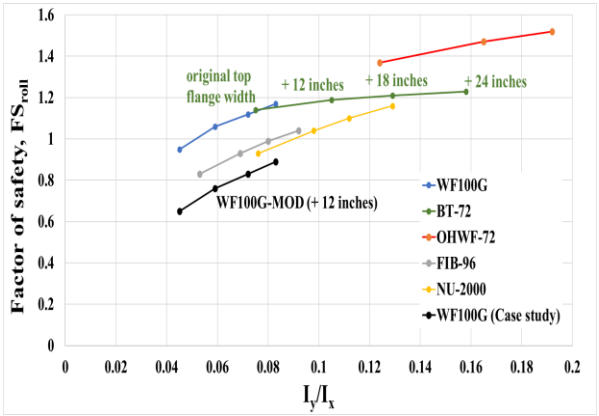

b) Effect of top flange width on FS_{roll}

Figure 6.4 Effect of I_y/I_x on stability

In conclusion, the use of 0.7-in. strand, resulting in longer spans, will surely increase the susceptibility of girders to instabilities. However, this can be mitigated as follows:

1. immediately installing end braces as the girder is set on its bearings;
2. providing stiffer transportation support – assuming this is possible;
3. increasing the width of the top flange since I_y/I_x has the pronounced effect on improving stability; and,

4. Girders having relatively thin bottom flanges are more susceptible to overturning while supported on dunnage or in transportation; such girders are not as well suited to being extended to long spans by privinding addional prestressing force.

7.0 Conclusions and Recommendations

7.1 Conclusions

This thesis presents investigations of bond behavior and girder stability related to the use of 0.7-in. diameter strand in highway bridge girders. Samples of 0.5, 0.6, and 0.7-in. diameter strand were tested to assess their mechanical properties (Chapter 2) and dilation (Hoyer effect) properties (Chapter 3). Data from the dilation tests were used in finite element simulations to investigate the radial stresses that develop at the interface between strand and concrete (Chapter 5); these stresses improve strand bond but only to the point at which they lead to local cracking. In addition, thirty beam-end tests are reported in Chapter 4) to assess the bond capacity of the strands. In a departure from bond, Chapter 6 investigates the effect of using 0.7-in. diameter strand on the stability of long prestressed girders. The main conclusions of this study are as follows.

7.1.1 Geometric and Material Characterization of Seven Wire Prestressing Strand

All strands tested met the requirments of ASTM A416 for minimum breaking strength. The 0.7-in. strands, however, only barely met the '$0.90f_{pu}$ = 243 ksi at 1% elongation' requirement. Based on the formulation presented in Eq. (2–2), the relative rib ratio for the 0.7-in. diameter strand was found to be less than the 0.5 and 0.6-in. strands considered. This could indicate that the mechanical interlock component of bond for the 0.7in. strand was poorer than the others.

7.1.2 Characterization of Strand Dilation (Hoyer Effect)

From the results reported in Table 3.2, it can be seen that the dilation ratio is not only affected by the Poisson effect. As explained in Section 1.5, the tightening and bearing between the wires will play a part in the dilation of the strand. The Poisson's ratio for steel is conventionally given as 0.27 to 0.30. From Table 3.2, and especially with bigger diameter 0.6-in. and 0.7-in. strands, it is clear that the dilation ratio exceeds Poisson ratio.

The trend of decreasing dilation ratio effect with increasing strand diameter reported by Briere et al. (2013) and seen in Table 3.1 was not evident in the present data. Indeed, dilation was relatively uniform in the present study with the 0.7-in. strand, if anything, exhibiting greater dilation. The reason for this divergence from previous data is unknown although the source and manufacture of the strands is different in each study.

The effect of dilation on radial stresses was simulated through a finite element method-based parametric investigation. The Hoyer effect is expected to result in circumferential stresses at the strand-concrete interface to exceed the concrete stress tensile strength. The following observations were made in relation to the circumferential stresses:

1. A **lower** dilation ratio results in **lower** circumferential stresses at the interface between the strand and concrete.
2. The **larger** strand results in **lower** circumferential stresses.
3. The **greater** spacing between adjacent strands results in **lower** circumferential stresses in a proportional manner.

Adopting a smeared crack model of the concrete illustrated the extent of the region of concrete whose stress exceeded the concrete cracking stress. Especially at the free end of the strand, localized damaged associated with only partially-restrained Hoyer effect was evident (Figure 5.9 and Figure 5.10).

In light of the discussion in Section 1.7, the effect of strand spacing was less clear. Although the concrete stress was not significantly affected (using the smeared crack approach as seen in Table 5.7), the physical extent of 'cracked' concrete was greater for smaller spacings and larger strand sizes.

7.1.3 Characterization of Bond (Beam End Tests)

The variation in bond behaviour was not attributed to strand size since there is no size dependent trend evident. Similarly, the variation observed was not attributed to the mechanical interlock of the strand since the relative rib areas were sufficiently similar for each strand (Table 2.1). There appeared to be some impact of concrete quality (strength) although the data was insufficient to quantify this.

Based on the results of normal-weight concrete batches NWC1 and NWC2, it was hypothesized that the condition of the strand affected both the relatively high bond results for the 0.5 in. strand and the low results for the 0.6 in. strands in NWC1. For the NWC2 and LWC tests, both the 0.6-in. and 0.7-in. strands were degreased in advance. This process apparently improved the bond of the 0.6-in. strands in NWC2, despite the poorer concrete quality.

7.1.3.1 Straight Strands in Light Weight Concrete (LWC)

According to Greene and Graybeal (2019) (see Section 1.8), LWC most likely will have longer transfer lengths than normal weight concrete. “Proof tests” of current AASHTO provisions were conducted. The results suggest that current development equations are conservative for both NWC and LWC.

From Eq.(4–3), the length required to develop f_{pu} is $l_d > 169d_b$. In this study, no extrapolated value of l_d exceeded $106d_b$. The 0.5 in. strand exhibited apparent values of l_d as low as $40d_b$. Both 0.6-in. and 0.7-in. strands embedded in LWC resulted in splitting failures at bond stresses lower than observed in comparable NWC, although concrete strengths were relatively low.

7.1.3.2 Hooked Strand Development

As expected and shown in Figure 4.9, the capacity of hooked strands increases with increased embedment length. Table 4.6 summarizes the observed relationships for the 0.6-in. and 0.7-in. strand tested. The contribution of the hook geometry was observed to be approximately 106 ksi and 116 ksi for 0.7-in. and 0.6-in. strand, respectively. Extrapolating the relationships given in Table 4.6 to determine the hook embedment required to develop f_{pu}, it is clear the presence of the hook reduces the theoretical development length from that determined for a straight strand embedment. The reduction is on the order 31% and 45% for the 0.7-in. and 0.6-in. strands, respectively.

Due to the expected high stresses in the beam-end region, girders constructed with 0.7-in diameter prestressing strand may be more susceptible to shear-bond failure. Eq.(4–4) prescribes the longitudinal reinforcement needed to develop the required tension force to resist this failure mode. Using hooked strands embedded into a cast-in-place end diaphragm.

1. permits a larger strand force, f_{ps} to be developed increasing the tension force resisting shear-bond failure.
2. permits some capacity of the unbonded strand to be developed near the end of the girder, adding an additional $A_{ps}f_{ps}$ component to the tension force resisting shear-bond failure.

7.1.4 Chapter 6: Long-span Girder Stability

The use of 0.7-in. strand, resulting in longer spans, will surely increase the susceptibility of girders to instabilities. However, this can be mitigated as follows:

1. immediately installing end braces as the girder is set on its bearings;
2. providing stiffer transportation support – assuming this is possible; and,
3. increasing the width of the top flange since I_y/I_x has the pronounced effect on improving stability.
4. Girders having relatively thin bottom flanges are more susceptible to overturning while supported on dunnage or in transportation; such girders are not as well suited to being extended to long spans by privinding addional prestressing force.

7.2 Recommendations for Future Work

There are only two known studies which have attempted to quantify the Hoyer effect, this study and Briere et al. (2013). It is necessary to conduct more testing to confirm the findings and to explain the apparent divergence in the results of the two studies. Although Chapter 5 provides a better understanding of the effects of prestress transfer at the interface between strand and

concrete, there are limitations in this study as mentioned in Section 5.4.2. Additionally, accurate predictive results rely on the experimental Hoyer effect data. Extending this study to address these limitations should give more reliable predictions. One of the ways to study and develop more understanding about strand behavior is using digital image correlation (DIC). This method was attempted as part of this study and it is explained further in the following section.

Many of the parameters forming the stability analysis of Chapter 6 are assumed with little basis despite having a large impact on the results. Better definition of these parameters and experimental verification of their effects is necessary to improve the reliability of these analyses.

7.2.1 Visualization of Strand Behavior (DIC)

As described in Chapter 3, the implications of which are described in Chapter 5, the dilation behavior of the seven-wire strand tested in this study was contrary to the behavior observed in previous research. As these are the only two known studies of their kind, further research into strand dilation and the Hoyer effect is necessary.

In the present study digital image correlation (DIC) was used in an attempt to map the complex deformation and distortion inherent as a seven-wire strand is stressed. This visualization – it was hoped – would be able to confirm the behavior assumed in this study and those upon which it is built, especially Briere et al. (2013), Oh et al. (2006) and Machida and Durelli (1973). Confirming the dilation behavior of seven-wire strand would also reinforce the extension of Hoyer's (1939) work to multiple wire strand.

A VIC 3D DIC system was used to image seven wire strand subject to tension and release. Rather than individual strain data (as collected in the experimental tests described in Figure 2.4

and 3.1), full field three-dimensional displacement fields are obtained as seen in Figure 7.1. The processing power and field of view of the VIC 3D system used proved inappropriate to establish decisive data. The DIC was able to accurately determine strain-related properties such as Young's modulus (Figure 7.1a). However, three-dimensional displacement trajectories were less clear (Figure 7.1b and c). This is believed to be partially because the complex trajectory of a point on a wire involves twisting of the wire itself. Furthermore, the DIC has an essentially square field of view. In order to capture even a partial twist of a single wire, the field of view is large (those in Figure 7.1 are approximately 3 in. square) resulting in relatively coarse precision. Despite this, the pilot tests show promise for confirming the behavior of seven-wire strand under stress and it is recommended to continue this investigation.

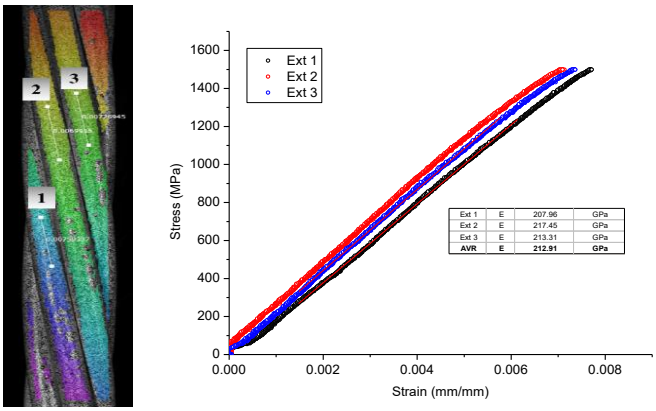

a) validation of axial stress-strain behavior of individual wires

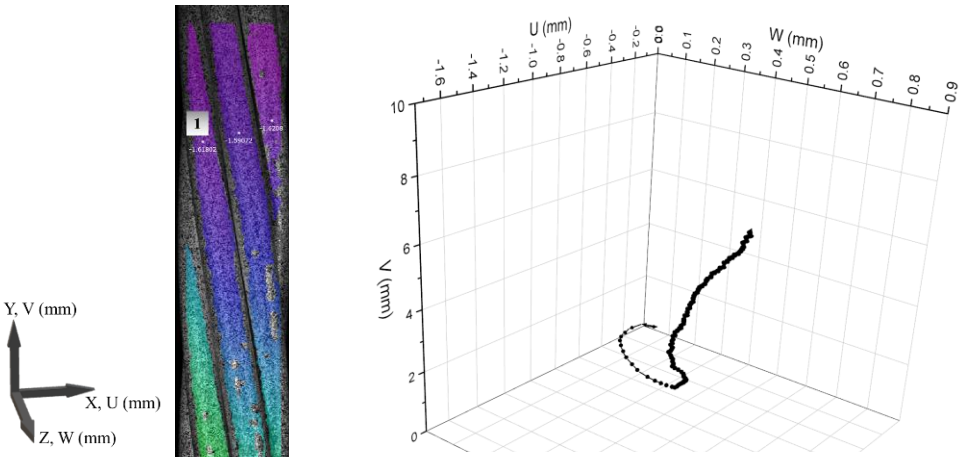

a) point trajectory in a wire under tension

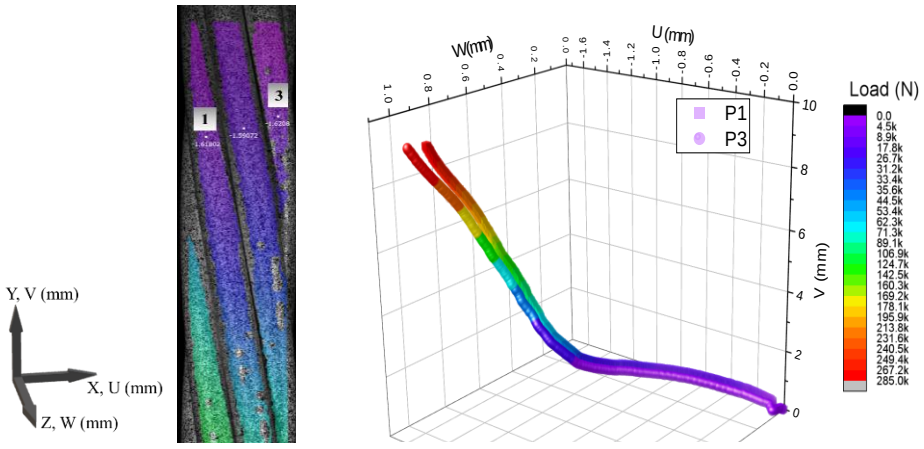

b) point trajectories of two helical wires

Figure 7.1 Full field displacement behavior of seven-wire strand.

Appendix A Hoyer Effect Summary Results

An example calculation of strain and dilation are provided. The example is for 0.7-in. strand #1; raw data is given in Table A1. Each strand is stressed to $0.8f_{pu}$ and released while measuring both axial strain (strain gauge) and transverse dilation (clip gage) as shown in Figure 3.1. The clip gage is factory calibrated to output strain over a 2 in. gage length. For this experimental set up, it was recalibrated to provide displacement directly. The gage has a calibration factor 2.876 mV/V and a stroke of 0.2 in. making the calibration slope (at 5V excitation):

2.876 mV x 5V / 0.2 in. = 72 mV/in.

Dilation data was recorded using a precision voltmeter in units of 0.01 mV. Thus, each unit represents 0.000143 in. Dilation strain over the range $0.8f_{pu}$ to $0.1f_{pu}$ is therefore calculated as:

ε_t = (dilation reading at $0.1f_{pu}$ – dilation reading at $0.8f_{pu}$) x $0.000143/d_b$

Longitudinal strain was recorded directly as strain thus only the correction for lay angle given by Eq.(3–1) is required:

$$\varepsilon_c = (\varepsilon_h \text{ at } 0.8f_{pu} - \varepsilon_h \text{ at } 0.1f_{pu}) / \cos^2\beta \quad \text{(A-1)}$$

Finally, the dilation ratio is $\varepsilon_t/\varepsilon_c$

Modulus of elasticity was calculated between $0.2f_{pu}$ and $0.5f_{pu}$ as follows:

$$E\ (ksi) = \frac{stress_{@0.5} - stress_{@0.2}}{(\mu\varepsilon_{c@0.5} - \mu\varepsilon_{c@0.2})/1000000} \quad \text{(A-2)}$$

Residual strains are calculated as the differences of subsequent axial strains (ε_c) at $0.1f_{pu}$.

Data for all Hoyer tests reported in the following tables.

Table A1: Raw data for 0.7-in. Strand number 1

d_b (in)	A_p (in^2)	$1/\cos(\beta)^2$	RAW DATA (input)									
0.7	0.294	1.024	Cycle-1		Cycle-2		Cycle-3		Cycle-4		Cycle-5	
%	stress	Load	$\mu\varepsilon_h$	dilation	$\mu\varepsilon_h$	dilation	$\mu\varepsilon_h$	dilation	$\mu\varepsilon_h$	dilation	$\mu\varepsilon_h$	dilation
pre	ksi	kips	2313									
0	0	0	(+)	(+)	(+)	(+)	(+)	(+)	(+)	(+)	(+)	(+)
0.1	27	7.9	3015		3432	111.6	3454	111.2	3475	111.1	3465	111
0.2	54	15.9	3815		4037	110.4	4047	110.1	4060	109.9	4074	109.7
0.3	81	23.8	4662		4822	108.9	4824	108.6	4815	108.4	4810	108.3
0.4	108	31.8	5528		5684	107.2	5688	106.9	5681	106.8	5668	106.6
0.5	135	39.7	6367		6549	105.6	6551	105.3	6566	105.1	6567	104.9
0.6	162	47.6	7292		7402	104	7400	103.8	7436	103.5	7387	103.4
0.7	189	55.6	8203		8306	102.4	8322	102.2	8300	102	8292	101.8
0.8	216	63.5	9222	101.2	9222	100.6	9212	100.5	9208	100.2	9280	99.98
0.7	189	55.6	8809	101.5	8839	101.1	8838	100.9	8731	100.9	8848	100.5
0.6	162	47.6	7977	103	8003	102.6	8010	102.4	8019	102.2	8031	102
0.5	135	39.7	7067	104.6	7076	104.3	7101	104	7119	103.9	7145	103.7
0.4	108	31.8	6154	106.3	6161	106	6200	105.7	6218	105.5	6176	105.5
0.3	81	23.8	5264	108	5292	107.6	5314	107.3	5188	107.5	5257	107.2
0.2	54	15.9	4355	109.7	4351	109.4	4348	109.3	4333	109.1	4412	108.9
0.1	27	7.9	3432	111.6	3454	111.2	3475	111.1	3465	111	3477	110.8
post											2552	

Table A2: Corrected data for 0.7-in. Strand number 1

			CORRECTED DATA									
			Cycle-1		Cycle-2		Cycle-3		Cycle-4		Cycle-5	
%	stress	Load	$\mu\varepsilon_c$	$\mu\varepsilon_t$	$\mu\varepsilon_c$	$\mu\varepsilon_t$	$\mu\varepsilon_c$	$\mu\varepsilon_t$	$\mu\varepsilon_c$	$\mu\varepsilon_t$	$\mu\varepsilon_c$	$\mu\varepsilon_t$
pre	ksi	kips	(+)	(+)	(+)	(+)	(+)	(+)	(+)	(+)	(+)	(+)
0.1	27	7.9	-6356		-5929		-5906		-5885		-5895	
0.2	54	15.9	-5537		-5309		-5299		-5286		-5271	
0.3	81	23.8	-4669		-4505		-4503		-4513		-4518	
0.4	108	31.8	-3783		-3623		-3619		-3626		-3639	
0.5	135	39.7	-2923		-2737		-2735		-2720		-2719	
0.6	162	47.6	-1976		-1864		-1866		-1829		-1879	
0.7	189	55.6	-1043		-938		-922		-944		-952	
0.8	216	63.5	0	0	0	-124.3	-10	-145.1	-14	-207.2	59	-252.8
0.7	189	55.6	-423	62.2	-392	-20.7	-393	-62.2	-503	-62.2	-383	-145.1
0.6	162	47.6	-1275	373.0	-1248	290.1	-1241	248.7	-1232	207.2	-1220	165.8
0.5	135	39.7	-2207	704.6	-2197	642.5	-2172	580.3	-2153	559.6	-2127	518.1
0.4	108	31.8	-3142	1057.0	-3134	994.8	-3094	932.6	-3076	891.2	-3119	891.2
0.3	81	23.8	-4053	1409.3	-4024	1326.4	-4002	1264.2	-4131	1305.7	-4060	1243.5
0.2	54	15.9	-4984	1761.6	-4988	1699.4	-4991	1678.7	-5006	1637.3	-4925	1595.8
0.1	27	7.9	-5929	2155.4	-5906	2072.5	-5885	2051.8	-5895	2031.0	-5883	1989.6

Table A3: Raw data for 0.7-in. Strand number 2

d_b (in)	A_p (in^2)	$1/\cos(\beta)^2$	RAW DATA (input)									
0.7	0.294	1.024	Cycle-1		Cycle-2		Cycle-3		Cycle-4		Cycle-5	
%	stress	Load	$\mu\varepsilon_h$	dilation	$\mu\varepsilon_h$	dilation	$\mu\varepsilon_h$	dilation	$\mu\varepsilon_h$	dilation	$\mu\varepsilon_h$	dilation
pre	ksi	kips	2486									
0	0	0	(+)	(+)	(+)	(+)	(+)	(+)	(+)	(+)	(+)	(+)
0.1	27	7.9	2849		3443	138.9	3500	137.2	3653	135.8	3793	134.8
0.2	54	15.9	3690		4032	137.8	4046	136	4292	134.7	4343	133.6
0.3	81	23.8	4732		4839	136	4850	134.3	5086	133.1	5093	132
0.4	108	31.8	5442		5700	134.2	5722	132.5	6109	131.1	6052	130.1
0.5	135	39.7	6278		6561	132.3	6555	130.7	6966	129.3	6815	128.5
0.6	162	47.6	7135		7437	130.4	7401	129	7742	127.8	7770	126.5
0.7	189	55.6	8155		8353	128.6	8367	127.1	8644	126	8655	124.8
0.8	216	63.5	9135	128.7	9296	126.7	9241	125.3	9532	124.3	9540	122.9
0.7	189	55.6	8808	129.3	8910	127.3	8887	126	9227	124.7	9246	123.4
0.6	162	47.6	7860	130.9	8028	129	8108	127.5	8325	126.4	8334	125
0.5	135	39.7	7037	132.5	7113	130.5	7130	129.2	7440	127.9	7435	126.7
0.4	108	31.8	6158	134	6228	132.1	6243	130.8	6479	129.6	6539	128.3
0.3	81	23.8	5261	135.5	5303	133.7	5407	132.3	5493	131.5	5631	129.9
0.2	54	15.9	4373	137.1	4442	135.3	4510	134	4725	132.9	4712	131.7
0.1	27	7.9	3443	138.9	3500	137.2	3653	135.8	3793	134.8	3786	133.6
post											2801	

Table A4: Corrected data for 0.7-in. Strand number 2

			CORRECTED DATA									
			Cycle-1		Cycle-2		Cycle-3		Cycle-4		Cycle-5	
%	stress	Load	$\mu\varepsilon_c$	$\mu\varepsilon_t$	$\mu\varepsilon_c$	$\mu\varepsilon_t$	$\mu\varepsilon_c$	$\mu\varepsilon_t$	$\mu\varepsilon_c$	$\mu\varepsilon_t$	$\mu\varepsilon_c$	$\mu\varepsilon_t$
pre	ksi	kips	(+)	(+)	(+)	(+)	(+)	(+)	(+)	(+)	(+)	(+)
0.1	27	7.9	-6437		-5828		-5770		-5613		-5470	
0.2	54	15.9	-5575		-5225		-5211		-4959		-4907	
0.3	81	23.8	-4509		-4399		-4388		-4146		-4139	
0.4	108	31.8	-3782		-3517		-3495		-3099		-3157	
0.5	135	39.7	-2925		-2636		-2642		-2221		-2376	
0.6	162	47.6	-2048		-1739		-1776		-1426		-1398	
0.7	189	55.6	-1003		-801		-786		-503		-492	
0.8	216	63.5	0	0	165	-414.5	109	-704.6	407	-911.9	415	-1202.0
0.7	189	55.6	-335	124.3	-230	-290.1	-254	-559.6	94	-829.0	114	-1098.4
0.6	162	47.6	-1306	455.9	-1134	62.2	-1052	-248.7	-829	-476.7	-820	-766.8
0.5	135	39.7	-2148	787.5	-2070	373.0	-2053	103.6	-1736	-165.8	-1741	-414.5
0.4	108	31.8	-3048	1098.4	-2977	704.6	-2961	435.2	-2720	186.5	-2658	-82.9
0.3	81	23.8	-3967	1409.3	-3924	1036.2	-3817	746.1	-3729	580.3	-3588	248.7
0.2	54	15.9	-4876	1740.9	-4805	1367.8	-4736	1098.4	-4516	870.4	-4529	621.7
0.1	27	7.9	-5828	2113.9	-5770	1761.6	-5613	1471.5	-5470	1264.2	-5477	1015.5

Table A5: Raw data for 0.7-in. Strand number 3

d_b (in)	A_p (in^2)	$1/\cos(\beta)^2$	RAW DATA (input)									
0.7	0.294	1.024	Cycle-1		Cycle-2		Cycle-3		Cycle-4		Cycle-5	
%	stress	Load	$\mu\varepsilon_h$	dilation	$\mu\varepsilon_h$	dilation	$\mu\varepsilon_h$	dilation	$\mu\varepsilon_h$	dilation	$\mu\varepsilon_h$	dilation
pre	ksi	kips	2149									
0	0	0	(+)	(+)	(+)	(+)	(+)	(+)	(+)	(+)	(+)	(+)
0.1	27	7.9	2840		3349	124.9	3383	124.8	3394	124.7	3414	124.6
0.2	54	15.9	3663		3925	123.7	4009	123.5	3943	123.6	4145	123.1
0.3	81	23.8	4484		4805	121.8	4722	122.3	4802	121.8	4741	121.9
0.4	108	31.8	5360		5622	120.2	5676	120	5611	120.1	5647	120
0.5	135	39.7	6267		6438	118.6	6448	118.5	6608	118.2	6450	118.5
0.6	162	47.6	7290		7337	116.9	7356	116.8	7345	116.8	7539	116.4
0.7	189	55.6	8091		8225	115.3	8311	115.1	8342	115	8238	115.2
0.8	216	63.5	9116	113.5	9123	113.6	9171	113.5	9140	113.5	9211	113.3
0.7	189	55.6	8793	114	8816	114	8828	113.9	8787	114	8819	113.9
0.6	162	47.6	7917	115.6	7911	115.7	7915	115.6	7962	115.5	7973	115.5
0.5	135	39.7	7003	117.4	7030	117.4	7028	117.4	7013	117.4	6943	117.5
0.4	108	31.8	5942	119.6	5906	119.6	6103	119.2	6182	119.6	5998	119.3
0.3	81	23.8	5204	121	5140	121.1	5265	120.8	5077	121.1	5284	120.7
0.2	54	15.9	4286	122.8	4333	122.7	4147	123	4366	122.6	4372	122.5
0.1	27	7.9	3349	124.9	3383	124.8	3394	124.7	3414	124.6	3424	124.6
Post											2377	

Table A6: Corrected data for 0.7-in. Strand number 3

			CORRECTED DATA									
			Cycle-1		Cycle-2		Cycle-3		Cycle-4		Cycle-5	
%	stress	Load	$\mu\varepsilon_c$	$\mu\varepsilon_t$	$\mu\varepsilon_c$	$\mu\varepsilon_t$	$\mu\varepsilon_c$	$\mu\varepsilon_t$	$\mu\varepsilon_c$	$\mu\varepsilon_t$	$\mu\varepsilon_c$	$\mu\varepsilon_t$
pre	ksi	kips	(+)	(+)	(+)	(+)	(+)	(+)	(+)	(+)	(+)	(+)
0.1	27	7.9	-6426		-5905		-5870		-5859		-5839	
0.2	54	15.9	-5584		-5315		-5229		-5297		-5090	
0.3	81	23.8	-4743		-4414		-4499		-4417		-4480	
0.4	108	31.8	-3846		-3578		-3522		-3589		-3552	
0.5	135	39.7	-2917		-2742		-2732		-2568		-2730	
0.6	162	47.6	-1870		-1822		-1802		-1813		-1615	
0.7	189	55.6	-1050		-912		-824		-793		-899	
0.8	216	63.5	0	0.0	7	20.7	56	0.0	25	0.0	97	-41.4
0.7	189	55.6	-331	103.6	-307	103.6	-295	82.9	-337	103.6	-304	82.9
0.6	162	47.6	-1228	435.2	-1234	455.9	-1230	435.2	-1182	414.5	-1170	414.5
0.5	135	39.7	-2164	808.3	-2136	808.3	-2138	808.3	-2153	808.3	-2225	829.0
0.4	108	31.8	-3250	1264.2	-3287	1264.2	-3085	1181.3	-3004	1264.2	-3193	1202.0
0.3	81	23.8	-4006	1554.4	-4071	1575.1	-3943	1512.9	-4136	1575.1	-3924	1492.2
0.2	54	15.9	-4946	1927.4	-4898	1906.7	-5088	1968.9	-4864	1886.0	-4858	1865.2
0.1	27	7.9	-5905	2362.6	-5870	2341.9	-5859	2321.2	-5839	2300.5	-5828	2300.5

Table A7: Raw data for 0.7-in. Strand number 4

d_b (in)	A_p (in^2)	$1/\cos(\beta)^2$	RAW DATA (input)									
0.7	0.294	1.024	Cycle-1		Cycle-2		Cycle-3		Cycle-4		Cycle-5	
%	stress	Load	$\mu\varepsilon_h$	dilation	$\mu\varepsilon_h$	dilation	$\mu\varepsilon_h$	dilation	$\mu\varepsilon_h$	dilation	$\mu\varepsilon_h$	dilation
pre	ksi	kips	2792									
0	0	0	(+)	(+)	(+)	(+)	(+)	(+)	(+)	(+)	(+)	(+)
0.1	27	7.9	3406		3154	145.8	3166	144.6	3194	143.5	3185	142.6
0.2	54	15.9	4282		3679	144.5	3918	142.7	3717	142.5	3750	141.1
0.3	81	23.8	5130		4487	142.7	4493	141.5	4502	140.5	4617	139.4
0.4	108	31.8	5259		5370	140.9	5384	139.7	5362	138.8	5380	137.9
0.5	135	39.7	6083		6269	139.1	6253	138	6299	136.9	6253	136.1
0.6	162	47.6	6964		7140	137.4	7146	136.3	7176	135.2	7361	134
0.7	189	55.6	7924		8053	135.6	8044	134.6	8038	135.5	8153	132.4
0.8	216	63.5	8956	135.4	8945	133.9	8958	132.8	9057	131.5	8975	130.9
0.7	189	55.6	8613	135.9	8598	134.4	8601	133.3	8611	132.2	8632	131.4
0.6	162	47.6	7721	137.4	7766	136	7779	134.9	7790	133.8	7713	133.1
0.5	135	39.7	6721	139.2	6808	137.8	6862	136.6	6798	135.8	6665	135.2
0.4	108	31.8	5907	140.7	5788	139.7	5922	138.4	5851	137.6	5615	137.3
0.3	81	23.8	4968	142.4	4990	141.1	4987	140.1	5060	139	5015	138.3
0.2	54	15.9	3823	144.6	3954	143.1	4085	141.9	4088	140.9	4070	140.1
0.1	27	7.9	3154	145.8	3166	144.6	3194	143.5	3185	142.6	3181	141.8
post											2226	

Table A8: Corrected data for 0.7-in. Strand number 4

			CORRECTED DATA									
			Cycle-1		Cycle-2		Cycle-3		Cycle-4		Cycle-5	
%	stress	Load	$\mu\varepsilon_c$	$\mu\varepsilon_t$	$\mu\varepsilon_c$	$\mu\varepsilon_t$	$\mu\varepsilon_c$	$\mu\varepsilon_t$	$\mu\varepsilon_c$	$\mu\varepsilon_t$	$\mu\varepsilon_c$	$\mu\varepsilon_t$
pre	ksi	kips	(+)	(+)	(+)	(+)	(+)	(+)	(+)	(+)	(+)	(+)
0.1	27	7.9	-5683		-5941		-5929		-5900		-5909	
0.2	54	15.9	-4786		-5403		-5159		-5365		-5331	
0.3	81	23.8	-3918		-4576		-4570		-4561		-4443	
0.4	108	31.8	-3786		-3672		-3658		-3680		-3662	
0.5	135	39.7	-2942		-2751		-2768		-2721		-2768	
0.6	162	47.6	-2040		-1860		-1853		-1823		-1633	
0.7	189	55.6	-1057		-925		-934		-940		-822	
0.8	216	63.5	0	0.0	-11	-310.9	2	-538.8	103	-808.3	19	-932.6
0.7	189	55.6	-351	103.6	-367	-207.2	-364	-435.2	-353	-663.2	-332	-829.0
0.6	162	47.6	-1265	414.5	-1219	124.3	-1205	-103.6	-1194	-331.6	-1273	-476.7
0.5	135	39.7	-2289	787.5	-2199	497.4	-2144	248.7	-2210	82.9	-2346	-41.4
0.4	108	31.8	-3122	1098.4	-3244	891.2	-3107	621.7	-3179	455.9	-3421	393.8
0.3	81	23.8	-4084	1450.7	-4061	1181.3	-4064	974.1	-3989	746.1	-4035	601.0
0.2	54	15.9	-5256	1906.7	-5122	1595.8	-4988	1347.1	-4985	1139.9	-5003	974.1
0.1	27	7.9	-5941	2155.4	-5929	1906.7	-5900	1678.7	-5909	1492.2	-5913	1326.4

Table A9: Raw data for 0.7-in. Strand number 5

d_b (in)	A_p (in^2)	$1/\cos(\beta)^2$	RAW DATA (input)									
0.7	0.294	1.024	Cycle-1		Cycle-2		Cycle-3		Cycle-4		Cycle-5	
%	stress	Load	$\mu\varepsilon_h$	dilation	$\mu\varepsilon_h$	dilation	$\mu\varepsilon_h$	dilation	$\mu\varepsilon_h$	dilation	$\mu\varepsilon_h$	dilation
pre	ksi	kips	2015									
0	0	0	(+)	(+)	(+)	(+)	(+)	(+)	(+)	(+)	(+)	(+)
0.1	27	7.9	2830		3353	127.4	3466	126.8	3599	126.3	3853	126.1
0.2	54	15.9	3591		4059	126.2	4042	125.8	4177	125.5	4407	125.3
0.3	81	23.8	4439		4667	125	4770	124.5	4941	124.1	5160	123.9
0.4	108	31.8	5282		5497	123.2	5603	122.8	5818	122.5	6020	122.3
0.5	135	39.7	6104		6348	121.4	6438	121.1	6651	120.7	6902	120.4
0.6	162	47.6	6952		7242	119.7	7300	119.3	7552	119	7769	118.7
0.7	189	55.6	7858		8082	118.1	8213	117.6	8420	117.3	8720	116.9
0.8	216	63.5	8845	117.3	9030	116.1	9245	115.6	9460	115.4	9548	115.4
0.7	189	55.6	8515	117.8	8570	117.1	8621	116.8	9132	116.1	9223	116
0.6	162	47.6	7729	119.1	7827	118.4	7995	118	8262	117.7	8294	117.7
0.5	135	39.7	6863	120.8	6995	120.2	7081	119.8	7445	119.4	7481	119.3
0.4	108	31.8	5997	122.5	5990	122.2	6240	121.6	6543	121.3	6611	121.2
0.3	81	23.8	5122	124.2	5220	123.7	5337	123.4	5668	123	5694	123
0.2	54	15.9	4208	126	4369	125.3	4426	125.1	4765	124.7	4801	124.7
0.1	27	7.9	3353	127.4	3466	126.8	3599	126.3	3853	126.1	4000	125.9
post											2995	

Table A10: Corrected data for 0.7-in. Strand number 5

			CORRECTED DATA									
			Cycle-1		Cycle-2		Cycle-3		Cycle-4		Cycle-5	
%	stress	Load	$\mu\varepsilon_c$	$\mu\varepsilon_t$	$\mu\varepsilon_c$	$\mu\varepsilon_t$	$\mu\varepsilon_c$	$\mu\varepsilon_t$	$\mu\varepsilon_c$	$\mu\varepsilon_t$	$\mu\varepsilon_c$	$\mu\varepsilon_t$
pre	ksi	kips	(+)	(+)	(+)	(+)	(+)	(+)	(+)	(+)	(+)	(+)
0.1	27	7.9	-6159		-5624		-5508		-5372		-5112	
0.2	54	15.9	-5380		-4901		-4918		-4780		-4544	
0.3	81	23.8	-4512		-4278		-4173		-3998		-3773	
0.4	108	31.8	-3648		-3428		-3320		-3100		-2893	
0.5	135	39.7	-2807		-2557		-2465		-2247		-1990	
0.6	162	47.6	-1938		-1641		-1582		-1324		-1102	
0.7	189	55.6	-1011		-781		-647		-435		-128	
0.8	216	63.5	0	0.0	189	-248.7	410	-352.3	630	-393.8	720	-393.8
0.7	189	55.6	-338	103.6	-282	-41.4	-229	-103.6	294	-248.7	387	-269.4
0.6	162	47.6	-1143	373.0	-1042	228.0	-870	145.1	-597	82.9	-564	82.9
0.5	135	39.7	-2029	725.4	-1894	601.0	-1806	518.1	-1434	435.2	-1397	414.5
0.4	108	31.8	-2916	1077.7	-2923	1015.5	-2667	891.2	-2357	829.0	-2288	808.3
0.3	81	23.8	-3812	1430.0	-3712	1326.4	-3592	1264.2	-3253	1181.3	-3227	1181.3
0.2	54	15.9	-4748	1803.1	-4583	1658.0	-4525	1616.5	-4178	1533.6	-4141	1533.6
0.1	27	7.9	-5624	2093.2	-5508	1968.9	-5372	1865.2	-5112	1823.8	-4961	1782.3

Table A11: Raw data for 0.6-in. Strand number 1

d_b (in)	A_p (in^2)	$1/\cos(\beta)^2$	RAW DATA (input)									
0.6	0.217	1.024	Cycle-1		Cycle-2		Cycle-3		Cycle-4		Cycle-5	
%	stress	Load	$\mu\varepsilon_h$	dilation	$\mu\varepsilon_h$	dilation	$\mu\varepsilon_h$	dilation	$\mu\varepsilon_h$	dilation	$\mu\varepsilon_h$	dilation
pre	ksi	kips	2854									
0	0	0	(+)	(+)	(+)	(+)	(+)	(+)	(+)	(+)	(+)	(+)
0.1	27	5.9	3603		3841	649.8	3836	649	3855	649	3849	649
0.2	54	11.7	4399		4439	650.4	4420	649.4	4400	649.6	4397	649.5
0.3	81	17.6	5249		5248	651.7	5227	650.7	5218	650.9	5212	651
0.4	108	23.4	6068		6157	653.2	6098	652.1	6092	652.5	6114	652.6
0.5	135	29.3	6947		6977	654.6	6967	653.8	6964	654.1	6945	654.1
0.6	162	35.2	7848		7872	655.9	7826	655.1	7828	655.4	7823	655.4
0.7	189	41.0	8698		8730	657	8722	656.4	8745	656.7	8703	656.6
0.8	216	46.9	9657	659	9618	658.4	9591	657.9	9606	657.9	9587	658
0.7	189	41.0	9251	658	9233	657.4	9250	657	9252	657	9267	657.2
0.6	162	35.2	8399	656.3	8403	656	8371	655.5	8420	655.6	8416	655.7
0.5	135	29.3	7477	654.7	7476	654.4	7478	654.1	7490	654.1	7500	654.2
0.4	108	23.4	6557	653.1	6556	652.8	6563	652.5	6474	652.4	6585	652.7
0.3	81	17.6	5670	651.9	5672	651.5	5683	651.3	5668	651.1	5708	651.5
0.2	54	11.7	4732	650.7	4702	650.1	4755	649.9	4771	649.9	4770	650.1
0.1	27	5.9	3841	649.8	3836	649	3855	649	3849	649	3841	649.2
post											2911	

Table A12: Corrected data for 0.6-in. Strand number 1

			CORRECTED DATA									
			Cycle-1		Cycle-2		Cycle-3		Cycle-4		Cycle-5	
%	stress	Load	$\mu\varepsilon_c$	$\mu\varepsilon_t$	$\mu\varepsilon_c$	$\mu\varepsilon_t$	$\mu\varepsilon_c$	$\mu\varepsilon_t$	$\mu\varepsilon_c$	$\mu\varepsilon_t$	$\mu\varepsilon_c$	$\mu\varepsilon_t$
pre	ksi	kips	(+)	(+)	(+)	(+)	(+)	(+)	(+)	(+)	(+)	(+)
0.1	27	5.9	-6199		-5955		-5961		-5941		-5947	
0.2	54	11.7	-5384		-5343		-5363		-5383		-5386	
0.3	81	17.6	-4514		-4515		-4536		-4545		-4552	
0.4	108	23.4	-3675		-3584		-3644		-3650		-3628	
0.5	135	29.3	-2775		-2744		-2754		-2758		-2777	
0.6	162	35.2	-1852		-1828		-1875		-1873		-1878	
0.7	189	41.0	-982		-949		-957		-934		-977	
0.8	216	46.9	0	0.0	-40	-143.3	-68	-262.7	-52	-262.7	-72	-238.9
0.7	189	41.0	-416	-238.9	-434	-382.2	-417	-477.7	-415	-477.7	-399	-429.9
0.6	162	35.2	-1288	-644.9	-1284	-716.6	-1317	-836.0	-1267	-812.1	-1271	-788.2
0.5	135	29.3	-2232	-1027.1	-2233	-1098.7	-2231	-1170.4	-2219	-1170.4	-2209	-1146.5
0.4	108	23.4	-3174	-1409.2	-3175	-1480.9	-3168	-1552.5	-3259	-1576.4	-3146	-1504.8
0.3	81	17.6	-4083	-1695.8	-4081	-1791.4	-4069	-1839.2	-4085	-1886.9	-4044	-1791.4
0.2	54	11.7	-5043	-1982.5	-5074	-2125.8	-5019	-2173.5	-5003	-2173.5	-5004	-2125.8
0.1	27	5.9	-5955	-2197.4	-5961	-2388.5	-5941	-2388.5	-5947	-2388.5	-5955	-2340.7

Table A13: Raw data for 0.6-in. Strand number 2

d_b (in)	A_p (in^2)	$1/\cos(\beta)^2$	RAW DATA (input)									
0.6	0.217	1.024	Cycle-1		Cycle-2		Cycle-3		Cycle-4		Cycle-5	
%	stress	Load	$\mu\varepsilon_h$	dilation	$\mu\varepsilon_h$	dilation	$\mu\varepsilon_h$	dilation	$\mu\varepsilon_h$	dilation	$\mu\varepsilon_h$	dilation
pre	ksi	kips	1725									
0	0	0	(+)	(+)	(+)	(+)	(+)	(+)	(+)	(+)	(+)	(+)
0.1	27	5.9	2415		2700	10684	2703	10692	2700	10694	2703	10694
0.2	54	11.7	3180		3231	10667	3232	10675	3234	10677	3272	10681
0.3	81	17.6	3967		4018	10694	3980	10698	3949	10698	3955	10700
0.4	108	23.4	4777		4799	10720	4803	10725	4789	10725	4789	10726
0.5	135	29.3	5582		5613	10746	5683	10750	5600	10750	5579	10748
0.6	162	35.2	6434		6430	10769	6453	10771	6425	10770	6450	10771
0.7	189	41.0	7259		7269	10789	7271	10792	7263	10793	7244	10791
0.8	216	46.9	8133	10806	8108	10810	8107	10812	8146	10813	8071	10812
0.7	189	41.0	7854	10794	7840	10803	7783	10804	7774	10803	7812	10804
0.6	162	35.2	7067	10773	7050	10785	7039	10788	7072	10794	7022	10792
0.5	135	29.3	6135	10751	6170	10766	6176	10768	6082	10770	6193	10772
0.4	108	23.4	5316	10730	5317	10743	5321	10746	5328	10751	5346	10751
0.3	81	17.6	4459	10712	4468	10722	4472	10727	4464	10729	4440	10730
0.2	54	11.7	3585	10697	3591	10702	3531	10703	3572	10703	3585	10706
0.1	27	5.9	2700	10684	2703	10692	2700	10694	2703	10694	2704	10693
post											1761	

Table A14: Corrected data for 0.6-in. Strand number 2

			CORRECTED DATA									
			Cycle-1		Cycle-2		Cycle-3		Cycle-4		Cycle-5	
%	stress	Load	$\mu\varepsilon_c$	$\mu\varepsilon_t$	$\mu\varepsilon_c$	$\mu\varepsilon_t$	$\mu\varepsilon_c$	$\mu\varepsilon_t$	$\mu\varepsilon_c$	$\mu\varepsilon_t$	$\mu\varepsilon_c$	$\mu\varepsilon_t$
pre	ksi	kips	(+)	(+)	(+)	(+)	(+)	(+)	(+)	(+)	(+)	(+)
0.1	27	5.9	-6069		-5767		-5764		-5767		-5764	
0.2	54	11.7	-5257		-5203		-5202		-5200		-5160	
0.3	81	17.6	-4422		-4368		-4408		-4441		-4435	
0.4	108	23.4	-3562		-3539		-3535		-3549		-3549	
0.5	135	29.3	-2708		-2675		-2600		-2689		-2711	
0.6	162	35.2	-1803		-1808		-1783		-1813		-1786	
0.7	189	41.0	-928		-917		-915		-923		-944	
0.8	216	46.9	0	0.0	-27	53.1	-28	79.7	14	92.9	-66	79.7
0.7	189	41.0	-296	-159.3	-311	-39.8	-371	-26.6	-381	-39.8	-341	-26.6
0.6	162	35.2	-1131	-438.2	-1150	-278.8	-1161	-239.0	-1126	-159.3	-1179	-185.9
0.5	135	29.3	-2121	-730.3	-2084	-531.1	-2077	-504.6	-2177	-478.0	-2059	-451.5
0.4	108	23.4	-2990	-1009.1	-2989	-836.5	-2985	-796.7	-2977	-730.3	-2958	-730.3
0.3	81	17.6	-3900	-1248.1	-3890	-1115.4	-3886	-1049.0	-3894	-1022.4	-3920	-1009.1
0.2	54	11.7	-4827	-1447.3	-4821	-1380.9	-4885	-1367.6	-4841	-1367.6	-4827	-1327.8
0.1	27	5.9	-5767	-1619.9	-5764	-1513.7	-5767	-1487.1	-5764	-1487.1	-5762	-1500.4

Table A15: Raw data for 0.6-in. Strand number 3

d_b (in)	A_p (in^2)	$1/\cos(\beta)^2$	RAW DATA (input)									
0.6	0.217	1.024	Cycle-1		Cycle-2		Cycle-3		Cycle-4		Cycle-5	
%	stress	Load	$\mu\varepsilon_h$	dilation	$\mu\varepsilon_h$	dilation	$\mu\varepsilon_h$	dilation	$\mu\varepsilon_h$	dilation	$\mu\varepsilon_h$	dilation
pre	ksi	kips	2868									
0	0	0	(+)	(+)	(+)	(+)	(+)	(+)	(+)	(+)	(+)	(+)
0.1	27	5.9	3801		3861	624.4	3882	624.3	3896	624.3	3905	624.3
0.2	54	11.7	4347		4400	624.7	4420	624.6	4419	624.6	4430	624.7
0.3	81	17.6	5192		5230	625.9	5240	625.8	5258	625.8	5316	625.9
0.4	108	23.4	6035		6066	627.2	6070	627.1	6055	627	6044	627
0.5	135	29.3	6893		6979	626.7	6961	628.5	7052	623.6	6994	628.5
0.6	162	35.2	7781		7832	630	7804	629.8	7837	625.8	7900	629.8
0.7	189	41.0	8658		8707	631.1	8689	631.1	8656	631	8660	631
0.8	216	46.9	9577	631.1	9592	632.2	9585	632.2	9586	632.2	9573	632.2
0.7	189	41.0	9312	631.1	9310	632.1	9339	632.1	9355	632.1	9343	632.1
0.6	162	35.2	8446	630	8463	631.2	8410	631.1	8500	631.3	8497	631.4
0.5	135	29.3	7531	629	7467	629.6	7553	629.8	7476	629.8	7584	630
0.4	108	23.4	6611	627.9	6541	628.2	6616	628.3	6681	628.5	6678	628.6
0.3	81	17.6	5723	626.8	5754	627	5583	626.7	5788	627.1	5788	627.2
0.2	54	11.7	4791	625.6	4764	625.5	4856	625.6	4818	625.6	4813	625.7
0.1	27	5.9	3861	624.4	3882	624.3	3896	624.3	3905	624.3	3902	624.2
post											2970	

Table A16: Corrected data for 0.6-in. Strand number 3

			CORRECTED DATA									
			Cycle-1		Cycle-2		Cycle-3		Cycle-4		Cycle-5	
%	stress	Load	$\mu\varepsilon_c$	$\mu\varepsilon_t$	$\mu\varepsilon_c$	$\mu\varepsilon_t$	$\mu\varepsilon_c$	$\mu\varepsilon_t$	$\mu\varepsilon_c$	$\mu\varepsilon_t$	$\mu\varepsilon_c$	$\mu\varepsilon_t$
pre	ksi	kips	(+)	(+)	(+)	(+)	(+)	(+)	(+)	(+)	(+)	(+)
0.1	27	5.9	-5914		-5853		-5831		-5817		-5808	
0.2	54	11.7	-5355		-5301		-5281		-5282		-5270	
0.3	81	17.6	-4490		-4451		-4441		-4423		-4363	
0.4	108	23.4	-3627		-3595		-3591		-3606		-3618	
0.5	135	29.3	-2748		-2660		-2679		-2586		-2645	
0.6	162	35.2	-1839		-1787		-1815		-1782		-1717	
0.7	189	41.0	-941		-891		-909		-943		-939	
0.8	216	46.9	0	0.0	15	262.7	8	262.7	9	262.7	-4	262.7
0.7	189	41.0	-271	0.0	-273	238.9	-244	238.9	-227	238.9	-240	238.9
0.6	162	35.2	-1158	-262.7	-1141	23.9	-1195	0.0	-1103	47.8	-1106	71.7
0.5	135	29.3	-2095	-501.6	-2161	-358.3	-2073	-310.5	-2151	-310.5	-2041	-262.7
0.4	108	23.4	-3037	-764.3	-3109	-692.7	-3032	-668.8	-2965	-621.0	-2968	-597.1
0.3	81	17.6	-3946	-1027.1	-3915	-979.3	-4090	-1050.9	-3880	-955.4	-3880	-931.5
0.2	54	11.7	-4901	-1313.7	-4928	-1337.6	-4834	-1313.7	-4873	-1313.7	-4878	-1289.8
0.1	27	5.9	-5853	-1600.3	-5831	-1624.2	-5817	-1624.2	-5808	-1624.2	-5811	-1648.1

Table A17: Raw data for 0.6-in. Strand number 4

d_b (in)	A_p (in^2)	$1/\cos(\beta)^2$	RAW DATA (input)									
0.6	0.217	1.024	Cycle-1		Cycle-2		Cycle-3		Cycle-4		Cycle-5	
%	stress	Load	$\mu\varepsilon_h$	dilation	$\mu\varepsilon_h$	dilation	$\mu\varepsilon_h$	dilation	$\mu\varepsilon_h$	dilation	$\mu\varepsilon_h$	dilation
pre	ksi	kips	2906									
0	0	0	(+)	(+)	(+)	(+)	(+)	(+)	(+)	(+)	(+)	(+)
0.1	27	5.9	3193		3526	589.3	3508	589.8	3460	590.2	3513	590.7
0.2	54	11.7	4018		4088	590.4	4076	590.9	4068	591.4	4284	592.2
0.3	81	17.6	4873		4891	591.6	4884	592.2	4948	592.8	4880	593.2
0.4	108	23.4	5699		5729	592.9	5719	593.4	5762	594.1	5710	594.5
0.5	135	29.3	6577		6647	594.3	6618	594.8	6562	595.3	6812	596.3
0.6	162	35.2	7455		7476	595.5	7480	596	7496	596.7	7475	597.2
0.7	189	41.0	8332		8370	596.7	8342	597.3	8361	597.8	8380	598.5
0.8	216	46.9	9282	596.9	9260	598	9268	598.5	9240	599.1	9247	599.6
0.7	189	41.0	8966	596.6	8981	597.6	8952	598.2	8992	598.8	8940	599.2
0.6	162	35.2	8106	595.4	8116	596.3	8127	596.9	8136	597.6	8129	598.1
0.5	135	29.3	7211	594.2	7207	595	7178	595.6	7190	596.2	7222	596.7
0.4	108	23.4	6266	592.9	6283	593.6	6095	594	6314	594.8	6284	595.3
0.3	81	17.6	5378	591.7	5399	592.4	5413	593	5394	593.5	5394	594
0.2	54	11.7	4384	590.4	4414	591	4455	591.6	4465	592.1	4480	592.6
0.1	27	5.9	3526	589.3	3508	589.8	3460	590.2	3513	590.7	3504	591.1
post											2581	

Table A18: Corrected data for 0.6-in. Strand number 4

			CORRECTED DATA									
			Cycle-1		Cycle-2		Cycle-3		Cycle-4		Cycle-5	
%	stress	Load	$\mu\varepsilon_c$	$\mu\varepsilon_t$	$\mu\varepsilon_c$	$\mu\varepsilon_t$	$\mu\varepsilon_c$	$\mu\varepsilon_t$	$\mu\varepsilon_c$	$\mu\varepsilon_t$	$\mu\varepsilon_c$	$\mu\varepsilon_t$
pre	ksi	kips	(+)	(+)	(+)	(+)	(+)	(+)	(+)	(+)	(+)	(+)
0.1	27	5.9	-6235		-5894		-5912		-5962		-5907	
0.2	54	11.7	-5390		-5318		-5331		-5339		-5118	
0.3	81	17.6	-4515		-4496		-4503		-4438		-4507	
0.4	108	23.4	-3669		-3638		-3648		-3604		-3658	
0.5	135	29.3	-2770		-2698		-2728		-2785		-2529	
0.6	162	35.2	-1871		-1849		-1845		-1829		-1850	
0.7	189	41.0	-973		-934		-963		-943		-924	
0.8	216	46.9	0	0.0	-23	262.7	-14	382.2	-43	525.5	-36	644.9
0.7	189	41.0	-324	-71.7	-308	167.2	-338	310.5	-297	453.8	-350	549.4
0.6	162	35.2	-1204	-358.3	-1194	-143.3	-1183	0.0	-1173	167.2	-1181	286.6
0.5	135	29.3	-2121	-644.9	-2125	-453.8	-2154	-310.5	-2142	-167.2	-2109	-47.8
0.4	108	23.4	-3088	-955.4	-3071	-788.2	-3263	-692.7	-3039	-501.6	-3070	-382.2
0.3	81	17.6	-3998	-1242.0	-3976	-1074.8	-3962	-931.5	-3981	-812.1	-3981	-692.7
0.2	54	11.7	-5015	-1552.5	-4985	-1409.2	-4943	-1265.9	-4932	-1146.5	-4917	-1027.1
0.1	27	5.9	-5894	-1815.3	-5912	-1695.8	-5962	-1600.3	-5907	-1480.9	-5916	-1385.3

Table A19: Raw data for 0.6-in. Strand number 5

d_b (in)	A_p (in^2)	$1/\cos(\beta)^2$	RAW DATA (input)									
0.6	0.217	1.024	Cycle-1		Cycle-2		Cycle-3		Cycle-4		Cycle-5	
%	stress	Load	$\mu\varepsilon_h$	dilation	$\mu\varepsilon_h$	dilation	$\mu\varepsilon_h$	dilation	$\mu\varepsilon_h$	dilation	$\mu\varepsilon_h$	dilation
pre	ksi	kips	2390									
0	0	0	(+)	(+)	(+)	(+)	(+)	(+)	(+)	(+)	(+)	(+)
0.1	27	5.9	2953		3323	594.4	3324	594.8	3327	595	3333	595.2
0.2	54	11.7	3773		3831	595.3	3841	595.6	3831	595.7	3830	596
0.3	81	17.6	4605		4644	596.8	4623	597.1	4614	597.2	4620	597.4
0.4	108	23.4	5442		5467	598.3	5458	598.6	5480	598.8	5437	599
0.5	135	29.3	6309		6375	599.9	6353	600.1	6360	600.3	6295	600.4
0.6	162	35.2	7166		7558	601.4	7211	601.3	7221	601.4	7171	601.5
0.7	189	41.0	8052		8106	602.2	8133	602.4	8088	602.5	8062	602.7
0.8	216	46.9	8974	602.4	8974	603.3	8969	603.5	8948	603.6	8949	603.9
0.7	189	41.0	8700	601.9	8650	602.6	8710	602.9	8717	603.2	8720	603.4
0.6	162	35.2	7891	600.5	7828	601	7890	601.3	7878	601.5	7896	601.8
0.5	135	29.3	6958	599.1	6974	599.6	6985	599.9	6971	600.1	7002	600.3
0.4	108	23.4	5960	597.8	6066	598.4	6088	598.7	5977	598.8	6058	599
0.3	81	17.6	5172	596.8	5177	597.3	5141	597.5	5203	597.6	5213	597.9
0.2	54	11.7	4223	595.5	4238	596	4154	596.1	4264	596.4	4211	596.5
0.1	27	5.9	3323	594.4	3324	594.8	3327	595	3333	595.2	3318	595.4
post											2393	

Table A20: Corrected data for 0.6-in. Strand number 5

			CORRECTED DATA									
			Cycle-1		Cycle-2		Cycle-3		Cycle-4		Cycle-5	
%	stress	Load	$\mu\varepsilon_c$	$\mu\varepsilon_t$	$\mu\varepsilon_c$	$\mu\varepsilon_t$	$\mu\varepsilon_c$	$\mu\varepsilon_t$	$\mu\varepsilon_c$	$\mu\varepsilon_t$	$\mu\varepsilon_c$	$\mu\varepsilon_t$
pre	ksi	kips	(+)	(+)	(+)	(+)	(+)	(+)	(+)	(+)	(+)	(+)
0.1	27	5.9	-6165		-5786		-5785		-5782		-5776	
0.2	54	11.7	-5326		-5266		-5256		-5266		-5267	
0.3	81	17.6	-4474		-4434		-4455		-4464		-4458	
0.4	108	23.4	-3617		-3591		-3600		-3578		-3622	
0.5	135	29.3	-2729		-2661		-2684		-2677		-2743	
0.6	162	35.2	-1851		-1450		-1805		-1795		-1846	
0.7	189	41.0	-944		-889		-861		-907		-934	
0.8	216	46.9	0	0.0	0	215.0	-5	262.7	-27	286.6	-26	358.3
0.7	189	41.0	-281	-119.4	-332	47.8	-270	119.4	-263	191.1	-260	238.9
0.6	162	35.2	-1109	-453.8	-1173	-334.4	-1110	-262.7	-1122	-215.0	-1104	-143.3
0.5	135	29.3	-2064	-788.2	-2048	-668.8	-2037	-597.1	-2051	-549.4	-2019	-501.6
0.4	108	23.4	-3086	-1098.7	-2978	-955.4	-2955	-883.8	-3069	-859.9	-2986	-812.1
0.3	81	17.6	-3893	-1337.6	-3888	-1218.1	-3925	-1170.4	-3861	-1146.5	-3851	-1074.8
0.2	54	11.7	-4865	-1648.1	-4850	-1528.7	-4936	-1504.8	-4823	-1433.1	-4877	-1409.2
0.1	27	5.9	-5786	-1910.8	-5785	-1815.3	-5782	-1767.5	-5776	-1719.7	-5792	-1672.0

Table A21: Raw data for 0.5-in. Strand number 1

d_b (in)	A_p (in^2)	$1/\cos(\beta)^2$	RAW DATA (input)									
0.5	0.153	1.024	Cycle-1		Cycle-2		Cycle-3		Cycle-4		Cycle-5	
%	stress	Load	$\mu\varepsilon_h$	dilation	$\mu\varepsilon_h$	dilation	$\mu\varepsilon_h$	dilation	$\mu\varepsilon_h$	dilation	$\mu\varepsilon_h$	dilation
pre	ksi	kips	1350									
0	0	0	(+)	(+)	(+)	(+)	(+)	(+)	(+)	(+)	(+)	(+)
0.1	27	4.1	1988		2303	1443	2306	1442	2327	1442	2329	1442
0.2	54	8.3	2755		2788	1443	2752	1443	2750	1442	2749	1442
0.3	81	12.4	3544		3502	1444	3525	1443	3497	1443	3436	1443
0.4	108	16.5	4340		4339	1445	4321	1444	4323	1444	4314	1444
0.5	135	20.7	5190		5195	1446	5200	1445	5150	1445	5215	1445
0.6	162	24.8	6041		6067	1447	6041	1446	6037	1446	6031	1446
0.7	189	28.9	6926		6956	1448	6958	1447	6927	1447	6907	1447
0.8	216	33.0	7846	1449	7830	1449	7799	1448	7811	1448	7788	1448
0.7	189	28.9	7745	1449	7767	1449	7729	1448	7740	1448	7591	1448
0.6	162	24.8	6940	1448	6817	1448	6957	1448	6947	1448	6950	1447
0.5	135	20.7	6014	1447	5906	1447	5996	1447	5995	1447	6039	1447
0.4	108	16.5	5108	1446	5135	1446	5135	1446	5110	1446	5092	1445
0.3	81	12.4	4191	1445	4211	1446	4202	1445	4090	1444	4237	1445
0.2	54	8.3	3328	1444	3316	1444	3315	1443	3317	1443	3318	1443
0.1	27	4.1	2303	1443	2306	1442	2327	1442	2329	1442	2327	1442
post											1332	

Table A22: Corrected data for 0.5-in. Strand number 1

			CORRECTED DATA									
			Cycle-1		Cycle-2		Cycle-3		Cycle-4		Cycle-5	
%	stress	Load	$\mu\varepsilon_c$	$\mu\varepsilon_t$	$\mu\varepsilon_c$	$\mu\varepsilon_t$	$\mu\varepsilon_c$	$\mu\varepsilon_t$	$\mu\varepsilon_c$	$\mu\varepsilon_t$	$\mu\varepsilon_c$	$\mu\varepsilon_t$
pre	ksi	kips	(+)	(+)	(+)	(+)	(+)	(+)	(+)	(+)	(+)	(+)
0.1	27	4.1	-5998		-5676		-5673		-5651		-5649	
0.2	54	8.3	-5213		-5179		-5216		-5218		-5219	
0.3	81	12.4	-4405		-4448		-4425		-4453		-4516	
0.4	108	16.5	-3590		-3591		-3609		-3607		-3617	
0.5	135	20.7	-2720		-2715		-2709		-2761		-2694	
0.6	162	24.8	-1848		-1822		-1848		-1852		-1858	
0.7	189	28.9	-942		-911		-909		-941		-962	
0.8	216	33.0	0	0.0	-16	0.0	-48	-295.0	-36	-295.0	-59	-295.0
0.7	189	28.9	-103	0.0	-81	0.0	-120	-295.0	-109	-295.0	-261	-295.0
0.6	162	24.8	-928	-295.0	-1054	-295.0	-910	-295.0	-921	-295.0	-917	-590.0
0.5	135	20.7	-1876	-590.0	-1986	-590.0	-1894	-590.0	-1895	-590.0	-1850	-590.0
0.4	108	16.5	-2804	-884.9	-2776	-884.9	-2776	-884.9	-2802	-884.9	-2820	-1179.9
0.3	81	12.4	-3743	-1179.9	-3722	-884.9	-3731	-1179.9	-3846	-1474.9	-3695	-1179.9
0.2	54	8.3	-4626	-1474.9	-4639	-1474.9	-4640	-1769.9	-4638	-1769.9	-4637	-1769.9
0.1	27	4.1	-5676	-1769.9	-5673	-2064.8	-5651	-2064.8	-5649	-2064.8	-5651	-2064.8

Table A23: Raw data for 0.5-in. Strand number 2

d_b (in)	A_p (in^2)	$1/\cos(\beta)^2$	RAW DATA (input)									
0.7	0.294	1.024	Cycle-1		Cycle-2		Cycle-3		Cycle-4		Cycle-5	
%	stress	Load	$\mu\varepsilon_h$	dilation	$\mu\varepsilon_h$	dilation	$\mu\varepsilon_h$	dilation	$\mu\varepsilon_h$	dilation	$\mu\varepsilon_h$	dilation
pre	ksi	kips	1462									
0	0	0	(+)	(+)	(+)	(+)	(+)	(+)	(+)	(+)	(+)	(+)
0.1	27	4.1	2170		2340	1489	2344	1489	2337	1489	2346	1489
0.2	54	8.3	2819		2847	1489	2850	1490	2936	1490	2856	1490
0.3	81	12.4	3765		3599	1490	3580	1490	4067	1491	3561	1491
0.4	108	16.5	4810		4452	1491	4407	1491	4389	1491	4471	1492
0.5	135	20.7	5364		5264	1492	5245	1492	5305	1493	5307	1493
0.6	162	24.8	6150		6132	1493	6086	1493	6072	1493	6056	1493
0.7	189	28.9	7046		7268	1495	7041	1494	7030	1494	6944	1494
0.8	216	33.0	7960	1495	7909	1495	7917	1495	8011	1495	7855	1495
0.7	189	28.9	7810	1495	7792	1495	7743	1495	7786	1495	7748	1495
0.6	162	24.8	7021	1494	7001	1494	6822	1494	7042	1494	7040	1494
0.5	135	20.7	6102	1493	6089	1493	6136	1493	5910	1493	6177	1494
0.4	108	16.5	5188	1492	5191	1492	5211	1492	5180	1492	5245	1493
0.3	81	12.4	4236	1491	4285	1491	4140	1491	4287	1491	4280	1492
0.2	54	8.3	3327	1490	3340	1490	3335	1490	3353	1490	3353	1490
0.1	27	4.1	2340	1489	2344	1489	2337	1489	2346	1489	2343	1489
post											1472	

Table A24: Corrected data for 0.5-in. Strand number 2

			CORRECTED DATA									
			Cycle-1		Cycle-2		Cycle-3		Cycle-4		Cycle-5	
%	stress	Load	$\mu\varepsilon_c$	$\mu\varepsilon_t$	$\mu\varepsilon_c$	$\mu\varepsilon_t$	$\mu\varepsilon_c$	$\mu\varepsilon_t$	$\mu\varepsilon_c$	$\mu\varepsilon_t$	$\mu\varepsilon_c$	$\mu\varepsilon_t$
pre	ksi	kips	(+)	(+)	(+)	(+)	(+)	(+)	(+)	(+)	(+)	(+)
0.1	27	4.1	-5929		-5755		-5751		-5758		-5749	
0.2	54	8.3	-5264		-5236		-5232		-5144		-5226	
0.3	81	12.4	-4296		-4466		-4485		-3986		-4504	
0.4	108	16.5	-3225		-3592		-3638		-3657		-3573	
0.5	135	20.7	-2658		-2761		-2780		-2719		-2717	
0.6	162	24.8	-1853		-1872		-1919		-1933		-1950	
0.7	189	28.9	-936		-709		-941		-952		-1040	
0.8	216	33.0	0	0.0	-52	0.0	-44	0.0	52	0.0	-108	0.0
0.7	189	28.9	-154	0.0	-172	0.0	-222	0.0	-178	0.0	-217	0.0
0.6	162	24.8	-962	-295.0	-982	-295.0	-1165	-295.0	-940	-295.0	-942	-295.0
0.5	135	20.7	-1903	-590.0	-1916	-590.0	-1868	-590.0	-2099	-590.0	-1826	-295.0
0.4	108	16.5	-2838	-884.9	-2835	-884.9	-2815	-884.9	-2847	-884.9	-2780	-590.0
0.3	81	12.4	-3813	-1179.9	-3763	-1179.9	-3912	-1179.9	-3761	-1179.9	-3768	-884.9
0.2	54	8.3	-4744	-1474.9	-4731	-1474.9	-4736	-1474.9	-4717	-1474.9	-4717	-1474.9
0.1	27	4.1	-5755	-1769.9	-5751	-1769.9	-5758	-1769.9	-5749	-1769.9	-5752	-1769.9

Table A25: Raw data for 0.5-in. Strand number 3

d_b (in)	A_p (in^2)	$1/\cos(\beta)^2$	RAW DATA (input)									
0.7	0.294	1.024	Cycle-1		Cycle-2		Cycle-3		Cycle-4		Cycle-5	
%	stress	Load	$\mu\varepsilon_h$	dilation	$\mu\varepsilon_h$	dilation	$\mu\varepsilon_h$	dilation	$\mu\varepsilon_h$	dilation	$\mu\varepsilon_h$	dilation
pre	ksi	kips	2096									
0	0	0	(+)	(+)	(+)	(+)	(+)	(+)	(+)	(+)	(+)	(+)
0.1	27	4.1	2928		3048	1526	3082	1527	3092	1527	3091	1527
0.2	54	8.3	3555		3669	1527	3640	1527	3612	1527	3608	1528
0.3	81	12.4	4391		4405	1528	4359	1528	4376	1528	4343	1529
0.4	108	16.5	5216		5358	1529	5453	1530	5258	1530	5182	1530
0.5	135	20.7	6084		6098	1530	6079	1530	6061	1531	6036	1531
0.6	162	24.8	6944		6957	1531	6904	1531	6883	1531	6876	1532
0.7	189	28.9	7749		7777	1532	7791	1532	7749	1533	7728	1533
0.8	216	33.0	8632	1532	8657	1533	8610	1533	8614	1534	8570	1534
0.7	189	28.9	8403	1531	8330	1532	8379	1533	8274	1533	8399	1533
0.6	162	24.8	7650	1531	7640	1532	7658	1532	7704	1532	7700	1533
0.5	135	20.7	6794	1531	6778	1531	6780	1532	6738	1532	6777	1532
0.4	108	16.5	5849	1530	5843	1530	5883	1530	5650	1530	6881	1531
0.3	81	12.4	4961	1529	4940	1529	4933	1529	4994	1530	4987	1530
0.2	54	8.3	4050	1528	4053	1528	4078	1529	4088	1529	4098	1529
0.1	27	4.1	3048	1526	3082	1527	3092	1527	3091	1527	3099	1528
post											2089	

Table A26: Corrected data for 0.5-in. Strand number 3

			CORRECTED DATA									
			Cycle-1		Cycle-2		Cycle-3		Cycle-4		Cycle-5	
%	stress	Load	$\mu\varepsilon_c$	$\mu\varepsilon_t$	$\mu\varepsilon_c$	$\mu\varepsilon_t$	$\mu\varepsilon_c$	$\mu\varepsilon_t$	$\mu\varepsilon_c$	$\mu\varepsilon_t$	$\mu\varepsilon_c$	$\mu\varepsilon_t$
pre	ksi	kips	(+)	(+)	(+)	(+)	(+)	(+)	(+)	(+)	(+)	(+)
0.1	27	4.1	-5841		-5718		-5683		-5673		-5674	
0.2	54	8.3	-5199		-5082		-5112		-5140		-5144	
0.3	81	12.4	-4343		-4328		-4375		-4358		-4392	
0.4	108	16.5	-3498		-3352		-3255		-3455		-3533	
0.5	135	20.7	-2609		-2595		-2614		-2633		-2658	
0.6	162	24.8	-1728		-1715		-1769		-1791		-1798	
0.7	189	28.9	-904		-875		-861		-904		-926	
0.8	216	33.0	0	0.0	26	295.0	-23	295.0	-18	590.0	-63	590.0
0.7	189	28.9	-234	-295.0	-309	0.0	-259	295.0	-367	295.0	-239	295.0
0.6	162	24.8	-1006	-295.0	-1016	0.0	-997	0.0	-950	0.0	-954	295.0
0.5	135	20.7	-1882	-295.0	-1898	-295.0	-1896	0.0	-1939	0.0	-1899	0.0
0.4	108	16.5	-2850	-590.0	-2856	-590.0	-2815	-590.0	-3053	-590.0	-1793	-295.0
0.3	81	12.4	-3759	-884.9	-3780	-884.9	-3788	-884.9	-3725	-590.0	-3732	-590.0
0.2	54	8.3	-4692	-1179.9	-4689	-1179.9	-4663	-884.9	-4653	-884.9	-4643	-884.9
0.1	27	4.1	-5718	-1769.9	-5683	-1474.9	-5673	-1474.9	-5674	-1474.9	-5666	-1179.9

Table A27: Raw data for 0.5-in. Strand number 4

d_b (in)	A_p (in^2)	$1/\cos(\beta)^2$	RAW DATA (input)									
0.7	0.294	1.024	Cycle-1		Cycle-2		Cycle-3		Cycle-4		Cycle-5	
%	stress	Load	$\mu\varepsilon_h$	dilation	$\mu\varepsilon_h$	dilation	$\mu\varepsilon_h$	dilation	$\mu\varepsilon_h$	dilation	$\mu\varepsilon_h$	dilation
pre	ksi	kips	-500									
0	0	0	(+)	(+)	(+)	(+)	(+)	(+)	(+)	(+)	(+)	(+)
0.1	27	4.1	397		530	1566	542	1568	536	1569	537	1570
0.2	54	8.3	975		1055	1567	1051	1569	1036	1570	1034	1571
0.3	81	12.4	1754		1732	1569	1718	1570	1701	1571	1767	1572
0.4	108	16.5	2745		2552	1570	2519	1572	2629	1573	2598	1574
0.5	135	20.7	3329		3316	1572	3288	1573	3279	1574	3257	1575
0.6	162	24.8	4112		4140	1573	4154	1575	4041	1575	4020	1576
0.7	189	28.9	4938		4927	1574	4880	1576	4903	1576	4869	1577
0.8	216	33.0	5732	1573	5685	1576	5654	1577	5675	1578	5597	1579
0.7	189	28.9	5412	1572	5523	1575	5521	1576	5578	1577	5537	1579
0.6	162	24.8	4838	1572	4900	1574	4866	1576	4884	1577	4800	1577
0.5	135	20.7	3956	1570	3995	1573	4024	1574	4077	1575	4044	1576
0.4	108	16.5	3150	1570	3029	1572	3144	1573	3143	1574	3142	1575
0.3	81	12.4	2202	1568	2037	1570	2225	1572	2327	1573	2323	1574
0.2	54	8.3	1442	1567	1455	1569	1460	1570	1475	1571	1457	1572
0.1	27	4.1	530	1566	542	1568	536	1569	537	1570	532	1571
post											-385	

Table A28: Corrected data for 0.5-in. Strand number 4

			CORRECTED DATA									
			Cycle-1		Cycle-2		Cycle-3		Cycle-4		Cycle-5	
%	stress	Load	$\mu\varepsilon_c$	$\mu\varepsilon_t$	$\mu\varepsilon_c$	$\mu\varepsilon_t$	$\mu\varepsilon_c$	$\mu\varepsilon_t$	$\mu\varepsilon_c$	$\mu\varepsilon_t$	$\mu\varepsilon_c$	$\mu\varepsilon_t$
pre	ksi	kips	(+)	(+)	(+)	(+)	(+)	(+)	(+)	(+)	(+)	(+)
0.1	27	4.1	-5463		-5327		-5314		-5321		-5320	
0.2	54	8.3	-4871		-4789		-4793		-4809		-4811	
0.3	81	12.4	-4073		-4096		-4110		-4128		-4060	
0.4	108	16.5	-3059		-3256		-3290		-3177		-3209	
0.5	135	20.7	-2461		-2474		-2503		-2512		-2534	
0.6	162	24.8	-1659		-1630		-1616		-1732		-1753	
0.7	189	28.9	-813		-824		-872		-849		-884	
0.8	216	33.0	0	0.0	-48	884.9	-80	1179.9	-58	1474.9	-138	1769.9
0.7	189	28.9	-328	-295.0	-214	590.0	-216	884.9	-158	1179.9	-200	1769.9
0.6	162	24.8	-915	-295.0	-852	295.0	-887	884.9	-868	1179.9	-954	1179.9
0.5	135	20.7	-1819	-884.9	-1779	0.0	-1749	295.0	-1695	590.0	-1728	884.9
0.4	108	16.5	-2644	-884.9	-2768	-295.0	-2650	0.0	-2651	295.0	-2652	590.0
0.3	81	12.4	-3615	-1474.9	-3784	-884.9	-3591	-295.0	-3487	0.0	-3491	295.0
0.2	54	8.3	-4393	-1769.9	-4380	-1179.9	-4374	-884.9	-4359	-590.0	-4377	-295.0
0.1	27	4.1	-5327	-2064.8	-5314	-1474.9	-5321	-1179.9	-5320	-884.9	-5325	-590.0

Table A29: Raw data for 0.5-in. Strand number 5

d_b (in)	A_p (in^2)	$1/\cos(\beta)^2$	RAW DATA (input)									
0.7	0.294	1.024	Cycle-1		Cycle-2		Cycle-3		Cycle-4		Cycle-5	
%	stress	Load	$\mu\varepsilon_h$	dilation	$\mu\varepsilon_h$	dilation	$\mu\varepsilon_h$	dilation	$\mu\varepsilon_h$	dilation	$\mu\varepsilon_h$	dilation
pre	ksi	kips	3033									
0	0	0	(+)	(+)	(+)	(+)	(+)	(+)	(+)	(+)	(+)	(+)
0.1	27	4.1	3718		3961	1587	3975	1589	3956	1589	3994	1589
0.2	54	8.3	4456		4472	1588	4461	1589	4459	1589	4483	1590
0.3	81	12.4	5235		5818	1589	5203	1590	5199	1590	5199	1591
0.4	108	16.5	6189		6068	1591	6077	1591	6219	1592	6030	1592
0.5	135	20.7	6919		6923	1592	6944	1592	6887	1593	6881	1593
0.6	162	24.8	7761		7810	1593	7755	1594	7744	1594	7786	1595
0.7	189	28.9	8664		8692	1595	8697	1595	8784	1595	8627	1595
0.8	216	33.0	9560	1595	9570	1595	9572	1595	9561	1595	9517	1595
0.7	189	28.9	9427	1595	9436	1595	9462	1595	9490	1595	9459	1595
0.6	162	24.8	8603	1595	8628	1595	8636	1595	8641	1595	8665	1595
0.5	135	20.7	7723	1594	7524	1594	7788	1594	7805	1595	7679	1595
0.4	108	16.5	6789	1592	6689	1593	6748	1593	6847	1594	6838	1594
0.3	81	12.4	5884	1591	5821	1591	5600	1591	5934	1592	5496	1592
0.2	54	8.3	4936	1589	4965	1590	4975	1590	4979	1591	4994	1591
0.1	27	4.1	3961	1587	3975	1589	3956	1589	3994	1589	3989	1589
post											3141	

Table A30: Corrected data for 0.5-in. Strand number 5

			CORRECTED DATA									
			Cycle-1		Cycle-2		Cycle-3		Cycle-4		Cycle-5	
%	stress	Load	$\mu\varepsilon_c$	$\mu\varepsilon_t$	$\mu\varepsilon_c$	$\mu\varepsilon_t$	$\mu\varepsilon_c$	$\mu\varepsilon_t$	$\mu\varepsilon_c$	$\mu\varepsilon_t$	$\mu\varepsilon_c$	$\mu\varepsilon_t$
pre	ksi	kips	(+)	(+)	(+)	(+)	(+)	(+)	(+)	(+)	(+)	(+)
0.1	27	4.1	-5982		-5733		-5719		-5738		-5699	
0.2	54	8.3	-5226		-5210		-5221		-5223		-5199	
0.3	81	12.4	-4429		-3832		-4461		-4466		-4466	
0.4	108	16.5	-3452		-3576		-3566		-3421		-3615	
0.5	135	20.7	-2704		-2700		-2679		-2737		-2743	
0.6	162	24.8	-1842		-1792		-1848		-1860		-1817	
0.7	189	28.9	-917		-889		-884		-795		-955	
0.8	216	33.0	0	0.0	10	0.0	12	0.0	1	0.0	-44	0.0
0.7	189	28.9	-136	0.0	-127	0.0	-100	0.0	-72	0.0	-103	0.0
0.6	162	24.8	-980	0.0	-954	0.0	-946	0.0	-941	0.0	-916	0.0
0.5	135	20.7	-1881	-295.0	-2085	-295.0	-1814	-295.0	-1797	0.0	-1926	0.0
0.4	108	16.5	-2837	-884.9	-2940	-590.0	-2879	-590.0	-2778	-295.0	-2787	-295.0
0.3	81	12.4	-3764	-1179.9	-3829	-1179.9	-4055	-1179.9	-3713	-884.9	-4161	-884.9
0.2	54	8.3	-4735	-1769.9	-4705	-1474.9	-4695	-1474.9	-4691	-1179.9	-4675	-1179.9
0.1	27	4.1	-5733	-2359.8	-5719	-1769.9	-5738	-1769.9	-5699	-1769.9	-5705	-1769.9

Table A31: Raw data for 0.375-in. Strand number 1

d_b (in)	A_p (in^2)	$1/\cos(\beta)^2$	RAW DATA (input)									
0.375	0.085	1.024	Cycle-1		Cycle-2[a]		Cycle-3		Cycle-4[b]		Cycle-5	
%	stress	Load	$\mu\varepsilon_h$	dilation	$\mu\varepsilon_h$	dilation	$\mu\varepsilon_h$	dilation	$\mu\varepsilon_h$	dilation	$\mu\varepsilon_h$	dilation
pre	ksi	kips	4200									
0	0	0	(+)	(+)	(+)	(+)	(+)	(+)	(+)	(+)	(+)	(+)
0.2	54	4.6	4705		4077	171	4576	169.1	4099	106.6	4058	102.4
0.3	81	6.9	5010		4838	170.9	4963	169	4883	106	4795	101.8
0.4	108	9.2	5627		5628	170.6	5630	168.9	5650	105.4	5598	101.2
0.5	135	11.5	6384		6470	170	6337	168.8	6477	104.6	6433	100.4
0.6	162	13.8	7239		7305	169.3	7351	168.5	7275	103.8	7264	99.68
0.7	189	16.1	8191		8225	168.4	8150	168.2	8191	102.8	8100	98.92
0.8	216	18.4	9000	24.82	9297	167.4	9045	167.6	9100	101.8	8951	98.13
0.7	189	16.1	8966	24.48	9051	167.4	8974	167.5	9004	101.8	8657	98.33
0.6	162	13.8	8404	24.65	8277	167.5	8067	167.6	8119	102.4	8292	98.56
0.5	135	11.5	7633	25.29	7249	167.8	7103	167.9	7379	102.9	7491	99.14
0.4	108	9.2	6713	25.31	6463	168	6451	168.1	6557	103.4	6587	99.61
0.3	81	6.9	5713	26.17	5512	168.4	5470	168.4	5585	103.9	5202	100.2
0.2	54	4.6	4682	27	4576	169.1	4563	169	4623	104.3	4640	100.4
post											4150	

[a] New dilation reading started here
[b] New dilation reading started here

Table A32: Corrected data for 0.375-in. Strand number 1

			CORRECTED DATA									
			Cycle-1		Cycle-2		Cycle-3		Cycle-4		Cycle-5	
%	stress	Load	$\mu\varepsilon_c$	$\mu\varepsilon_t$	$\mu\varepsilon_c$	$\mu\varepsilon_t$	$\mu\varepsilon_c$	$\mu\varepsilon_t$	$\mu\varepsilon_c$	$\mu\varepsilon_t$	$\mu\varepsilon_c$	$\mu\varepsilon_t$
pre	ksi	kips	(+)	(+)	(+)	(+)	(+)	(+)	(+)	(+)	(+)	(+)
0.2	54	4.6	-4398		-5345		-4834		-5121		-5010	
0.3	81	6.9	-4086		-4566		-4438		-4318		-4256	
0.4	108	9.2	-3454		-3757		-3755		-3533		-3433	
0.5	135	11.5	-2679		-2895		-3031		-2686		-2578	
0.6	162	13.8	-1803		-2040		-1993		-1869		-1727	
0.7	189	16.1	-828		-1098		-1174		-931		-871	
0.8	216	18.4	0	0.0	0	0.0	-258	76.5	0	0.0	0	0.0
0.7	189	16.1	-35	-130.0	-252	0.0	-331	38.2	-98	0.0	-301	76.5
0.6	162	13.8	-610	-65.0	-1044	38.2	-1259	76.5	-1005	229.4	-675	164.4
0.5	135	11.5	-1400	179.7	-2097	153.0	-2247	191.2	-1762	420.6	-1495	386.2
0.4	108	9.2	-2342	187.4	-2902	229.4	-2914	267.7	-2604	611.8	-2421	565.9
0.3	81	6.9	-3366	516.2	-3876	382.4	-3919	382.4	-3599	803.0	-3839	791.5
0.2	54	4.6	-4421	833.6	-4834	650.0	-4847	611.8	-4584	955.9	-4414	868.0

Table A33: Raw data for 0.375-in. Strand number 2

d_b (in)	A_p (in^2)	$1/\cos(\beta)^2$	RAW DATA (input)									
0.375	0.085	1.024	Cycle-1		Cycle-2		Cycle-3[a]		Cycle-4		Cycle-5	
%	stress	Load	$\mu\varepsilon_h$	dilation	$\mu\varepsilon_h$	dilation	$\mu\varepsilon_h$	dilation	$\mu\varepsilon_h$	dilation	$\mu\varepsilon_h$	dilation
pre	ksi	kips	1779									
0	0	0	(+)	(+)	(+)	(+)	(+)	(+)	(+)	(+)	(+)	(+)
0.2	54	4.6	3125		3627	62.16	3144	752	3722	751.8	3080	750.6
0.3	81	6.9	3850		4037	62.16	3894	752.7	4029	751.8	3800	751.3
0.4	108	9.2	4625		4623	62.2	4609	753.1	4675	752.1	5130	753.2
0.5	135	11.5	5528		5357	62.55	5477	753.6	5377	752.6	5603	753.5
0.6	162	13.8	6290		6303	63.19	6316	754.1	6284	753.6	6244	753.8
0.7	189	16.1	7280		7175	63.88	7377	755.1	7186	754.5	7277	754.8
0.8	216	18.4	7904	75.54	8055	64.48	8125	755.5	7979	755.2	8011	755.3
0.7	189	16.1	7866	75.66	8004	64.55	8055	755.4	7937	755.2	7948	755.4
0.6	162	13.8	7250	75.78	7197	64.7	7454	755	7209	754.8	7424	755.1
0.5	135	11.5	6476	75.77	6392	64.53	6592	754.3	6656	754.3	6569	754.5
0.4	108	9.2	5616	75.43	5617	64.45	5650	753.5	5677	753.5	5707	753.6
0.3	81	6.9	4646	74.9	4637	64.2	4690	752.6	4733	752.6	4715	752.8
0.2	54	4.6	3638	74.26	3671	63.79	3722	751.8	3766	751.8	3790	752.1
post											1900	

[a] New dilation reading started here

Table A34: Corrected data for 0.375-in. Strand number 2

			CORRECTED DATA									
			Cycle-1		Cycle-2		Cycle-3		Cycle-4		Cycle-5	
%	stress	Load	$\mu\varepsilon_c$	$\mu\varepsilon_t$	$\mu\varepsilon_c$	$\mu\varepsilon_t$	$\mu\varepsilon_c$	$\mu\varepsilon_t$	$\mu\varepsilon_c$	$\mu\varepsilon_t$	$\mu\varepsilon_c$	$\mu\varepsilon_t$
pre	ksi	kips	(+)	(+)	(+)	(+)	(+)	(+)	(+)	(+)	(+)	(+)
0.1	27	2.3	-8093		-8248		-8320		-8320		-8320	
0.2	54	4.6	-4894		-4534		-5100		-4509		-5166	
0.3	81	6.9	-4151		-4114		-4332		-4194		-4429	
0.4	108	9.2	-3358		-3514		-3600		-3533		-3067	
0.5	135	11.5	-2433		-2763		-2711		-2814		-2582	
0.6	162	13.8	-1653		-1794		-1852		-1885		-1926	
0.7	189	16.1	-639		-901		-766		-962		-868	
0.8	216	18.4	0	0.0	0	0.0	0	0.0	-149	-114.7	-117	-76.5
0.7	189	16.1	-39	45.9	-52	26.8	-72	-38.2	-193	-114.7	-181	-38.2
0.6	162	13.8	-670	91.8	-879	84.1	-687	-191.2	-938	-267.7	-718	-153.0
0.5	135	11.5	-1462	87.9	-1703	19.1	-1570	-458.9	-1504	-458.9	-1593	-382.4
0.4	108	9.2	-2343	-42.1	-2496	-11.5	-2534	-764.8	-2507	-764.8	-2476	-726.5
0.3	81	6.9	-3336	-244.7	-3500	-107.1	-3517	-1108.9	-3473	-1108.9	-3492	-1032.4
0.2	54	4.6	-4368	-489.4	-4489	-263.8	-4509	-1414.8	-4463	-1414.8	-4439	-1300.1

Table A35: Raw data for 0.375-in. Strand number 3

d_b (in)	A_p (in^2)	$1/\cos(\beta)^2$	RAW DATA (input)									
0.375	0.085	1.024	Cycle-1		Cycle-2		Cycle-3		Cycle-4		Cycle-5	
%	stress	Load	$\mu\varepsilon_h$	dilation	$\mu\varepsilon_h$	dilation	$\mu\varepsilon_h$	dilation	$\mu\varepsilon_h$	dilation	$\mu\varepsilon_h$	dilation
pre	ksi	kips	2096									
0	0	0	(+)	(+)	(+)	(+)	(+)	(+)	(+)	(+)	(+)	(+)
0.1	27	2.3	2928		3048	1526	3082	1527	3092	1527	3091	1527
0.2	54	4.6	2928		3048	1526	3082	1527	3092	1527	3091	1527
0.3	81	6.9	3555		3669	1527	3640	1527	3612	1527	3608	1528
0.4	108	9.2	4391		4405	1528	4359	1528	4376	1528	4343	1529
0.5	135	11.5	5216		5358	1529	5453	1530	5258	1530	5182	1530
0.6	162	13.8	6084		6098	1530	6079	1530	6061	1531	6036	1531
0.7	189	16.1	6944		6957	1531	6904	1531	6883	1531	6876	1532
0.8	216	18.4	7749		7777	1532	7791	1532	7749	1533	7728	1533
0.7	189	16.1	8632	1532	8657	1533	8610	1533	8614	1534	8570	1534
0.6	162	13.8	8403	1531	8330	1532	8379	1533	8274	1533	8399	1533
0.5	135	11.5	7650	1531	7640	1532	7658	1532	7704	1532	7700	1533
0.4	108	9.2	6794	1531	6778	1531	6780	1532	6738	1532	6777	1532
0.3	81	6.9	5849	1530	5843	1530	5883	1530	5650	1530	6881	1531
0.2	54	4.6	4961	1529	4940	1529	4933	1529	4994	1530	4987	1530
0.1	27	2.3	3048	1526	3082	1527	3092	1527	3091	1527	3099	1528
post											2089	

Table A36: Corrected data for 0.375-in. Strand number 3

			CORRECTED DATA									
			Cycle-1		Cycle-2		Cycle-3		Cycle-4		Cycle-5	
%	stress	Load	$\mu\varepsilon_c$	$\mu\varepsilon_t$	$\mu\varepsilon_c$	$\mu\varepsilon_t$	$\mu\varepsilon_c$	$\mu\varepsilon_t$	$\mu\varepsilon_c$	$\mu\varepsilon_t$	$\mu\varepsilon_c$	$\mu\varepsilon_t$
pre	ksi	kips	(+)	(+)	(+)	(+)	(+)	(+)	(+)	(+)	(+)	(+)
0.1	27	2.3	-5841		-5718		-5683		-5673		-5674	
0.2	54	4.6	-5199		-5082		-5112		-5140		-5144	
0.3	81	6.9	-4343		-4328		-4375		-4358		-4392	
0.4	108	9.2	-3498		-3352		-3255		-3455		-3533	
0.5	135	11.5	-2609		-2595		-2614		-2633		-2658	
0.6	162	13.8	-1728		-1715		-1769		-1791		-1798	
0.7	189	16.1	-904		-875		-861		-904		-926	
0.8	216	18.4	0	0.0	26	382.4	-23	382.4	-18	764.8	-63	764.8
0.7	189	16.1	-234	-382.4	-309	0.0	-259	382.4	-367	382.4	-239	382.4
0.6	162	13.8	-1006	-382.4	-1016	0.0	-997	0.0	-950	0.0	-954	382.4
0.5	135	11.5	-1882	-382.4	-1898	-382.4	-1896	0.0	-1939	0.0	-1899	0.0
0.4	108	9.2	-2850	-764.8	-2856	-764.8	-2815	-764.8	-3053	-764.8	-1793	-382.4
0.3	81	6.9	-3759	-1147.1	-3780	-1147.1	-3788	-1147.1	-3725	-764.8	-3732	-764.8
0.2	54	4.6	-4692	-1529.5	-4689	-1529.5	-4663	-1147.1	-4653	-1147.1	-4643	-1147.1
0.1	27	2.3	-5718	-2294.3	-5683	-1911.9	-5673	-1911.9	-5674	-1911.9	-5666	-1529.5

Table A37: Raw data for 0.375-in. Strand number 4

d_b (in)	A_p (in^2)	$1/\cos(\beta)^2$	RAW DATA (input)									
0.375	0.085	1.024	Cycle-1		Cycle-2		Cycle-3		Cycle-4		Cycle-5	
%	stress	Load	$\mu\varepsilon_h$	dilation	$\mu\varepsilon_h$	dilation	$\mu\varepsilon_h$	dilation	$\mu\varepsilon_h$	dilation	$\mu\varepsilon_h$	dilation
pre	ksi	kips	2760									
0	0	0	(+)	(+)	(+)	(+)	(+)	(+)	(+)	(+)	(+)	(+)
0.1	27	2.3	3592		3685	758.2	3731	758.3	3692	758.6	3735	759
0.2	54	4.6	4047		4193	758.7	4209	758.7	4187	759.1	4187	759.3
0.3	81	6.9	4885		4848	759.4	4857	759.5	4848	759.8	4852	760
0.4	108	9.2	5662		5505	760	5495	760.1	5487	760.4	5480	760.5
0.5	135	11.5	6488		6485	761.1	6461	761.3	6450	761.6	6602	761.8
0.6	162	13.8	7316		7277	761.7	7270	762.1	7204	762.3	7277	762.3
0.7	189	16.1	8250		8184	762.4	8214	762.9	8212	763.2	8155	763.1
0.8	216	18.4	9028	761.9	9170	763.2	9145	763.7	9070	763.9	8955	763.8
0.7	189	16.1	8973	762.1	9115	763.2	9093	763.7	9023	763.9	8912	763.8
0.6	162	13.8	8587	762	8584	762.8	8616	763.4	8562	763.6	8404	763.4
0.5	135	11.5	7630	761.4	7626	762.1	7478	762.5	7563	762.9	7660	763
0.4	108	9.2	6718	760.7	6744	761.3	6745	761.8	6737	762	6662	762
0.3	81	6.9	5738	760	5747	760.4	5726	760.8	5710	761	5712	761.2
0.2	54	4.6	4750	759.2	4760	759.4	4774	759.9	4750	760.1	4767	760.2
0.1	27	2.3	3685	758.2	3731	758.3	3692	758.6	3735	759	3777	759.1
post											2777	

Table A38: Corrected data for 0.375-in. Strand number 4

			CORRECTED DATA									
			Cycle-1		Cycle-2		Cycle-3		Cycle-4		Cycle-5	
%	stress	Load	$\mu\varepsilon_c$	$\mu\varepsilon_t$	$\mu\varepsilon_c$	$\mu\varepsilon_t$	$\mu\varepsilon_c$	$\mu\varepsilon_t$	$\mu\varepsilon_c$	$\mu\varepsilon_t$	$\mu\varepsilon_c$	$\mu\varepsilon_t$
pre	ksi	kips	(+)	(+)	(+)	(+)	(+)	(+)	(+)	(+)	(+)	(+)
0.1	27	2.3	-5566		-5471		-5424		-5464		-5420	
0.2	54	4.6	-5100		-4951		-4934		-4957		-4957	
0.3	81	6.9	-4242		-4280		-4271		-4280		-4276	
0.4	108	9.2	-3447		-3607		-3618		-3626		-3633	
0.5	135	11.5	-2601		-2604		-2629		-2640		-2484	
0.6	162	13.8	-1753		-1793		-1800		-1868		-1793	
0.7	189	16.1	-797		-864		-834		-836		-894	
0.8	216	18.4	0	0.0	145	497.1	120	688.3	43	764.8	-75	726.5
0.7	189	16.1	-56	76.5	89	497.1	67	688.3	-5	764.8	-119	726.5
0.6	162	13.8	-452	38.2	-455	344.1	-422	573.6	-477	650.0	-639	573.6
0.5	135	11.5	-1432	-191.2	-1436	76.5	-1587	229.4	-1500	382.4	-1401	420.6
0.4	108	9.2	-2365	-458.9	-2339	-229.4	-2338	-38.2	-2346	38.2	-2423	38.2
0.3	81	6.9	-3369	-726.5	-3360	-573.6	-3381	-420.6	-3398	-344.1	-3395	-267.7
0.2	54	4.6	-4381	-1032.4	-4370	-955.9	-4356	-764.8	-4381	-688.3	-4363	-650.0
0.1	27	2.3	-5471	-1414.8	-5424	-1376.6	-5464	-1261.9	-5420	-1108.9	-5377	-1070.7

Table A39: Raw data for 0.375-in. Strand number 5

d_b (in)	A_p (in^2)	$1/\cos(\beta)^2$	RAW DATA (input)									
0.375	0.085	1.024	Cycle-1		Cycle-2		Cycle-3		Cycle-4		Cycle-5	
%	stress	Load	$\mu\varepsilon_h$	dilation	$\mu\varepsilon_h$	dilation	$\mu\varepsilon_h$	dilation	$\mu\varepsilon_h$	dilation	$\mu\varepsilon_h$	dilation
pre	ksi	kips	3545									
0	0	0	(+)	(+)	(+)	(+)	(+)	(+)	(+)	(+)	(+)	(+)
0.1	27	2.3	4373		4566	744.4	4618	743.7	4643	743.4	4573	743.2
0.2	54	4.6	5055		5144	744.8	5153	744	5152	743.7	5131	743.6
0.3	81	6.9	5850		5810	745.2	5825	744.5	5833	744.2	5804	744.1
0.4	108	9.2	6660		6613	745.8	6490	745	6496	744.8	6471	744.7
0.5	135	11.5	7583		7490	746.5	7497	746.2	7472	745.9	7530	745.9
0.6	162	13.8	8471		8377	747.1	8313	746.9	8500	746.8	8280	746.6
0.7	189	16.1	9266		9423	747.8	9278	747.6	9355	747.6	9330	747.6
0.8	216	18.4	10081	748	10465	748.5	10119	748.2	10235	748.2	10145	748.2
0.7	189	16.1	10045	748.1	10380	748.4	10344	748.4	10174	748.2	10091	748.1
0.6	162	13.8	9478	747.9	9757	748	9740	748	9489	747.7	9483	747.8
0.5	135	11.5	8758	747.5	8787	747.2	8825	747.2	8736	747.1	8787	747.3
0.4	108	9.2	7814	746.9	7830	746.4	7839	746.2	7827	746.3	7834	746.3
0.3	81	6.9	6772	746	6777	745.4	6713	745.3	6777	745.3	6758	745.3
0.2	54	4.6	5707	745.2	5720	744.5	5738	744.4	5666	744.3	5724	744.4
0.1	27	2.3	4566	744.4	4618	743.7	4643	743.4	4573	743.2	4606	743.3
post											3607	

Table A40: Corrected data for 0.375-in. Strand number 5

			CORRECTED DATA									
			Cycle-1		Cycle-2		Cycle-3		Cycle-4		Cycle-5	
%	stress	Load	$\mu\varepsilon_c$	$\mu\varepsilon_t$	$\mu\varepsilon_c$	$\mu\varepsilon_t$	$\mu\varepsilon_c$	$\mu\varepsilon_t$	$\mu\varepsilon_c$	$\mu\varepsilon_t$	$\mu\varepsilon_c$	$\mu\varepsilon_t$
pre	ksi	kips	(+)	(+)	(+)	(+)	(+)	(+)	(+)	(+)	(+)	(+)
0.1	27	2.3	-5845		-5647		-5594		-5568		-5640	
0.2	54	4.6	-5146		-5055		-5046		-5047		-5069	
0.3	81	6.9	-4332		-4373		-4358		-4350		-4380	
0.4	108	9.2	-3503		-3551		-3677		-3671		-3697	
0.5	135	11.5	-2558		-2653		-2646		-2672		-2612	
0.6	162	13.8	-1649		-1745		-1810		-1619		-1844	
0.7	189	16.1	-835		-674		-822		-743		-769	
0.8	216	18.4	0	0.0	393	191.2	39	76.5	158	76.5	66	76.5
0.7	189	16.1	-37	38.2	306	153.0	269	153.0	95	76.5	10	38.2
0.6	162	13.8	-617	-38.2	-332	0.0	-349	0.0	-606	-114.7	-612	-76.5
0.5	135	11.5	-1355	-191.2	-1325	-305.9	-1286	-305.9	-1377	-344.1	-1325	-267.7
0.4	108	9.2	-2321	-420.6	-2305	-611.8	-2296	-688.3	-2308	-650.0	-2301	-650.0
0.3	81	6.9	-3388	-764.8	-3383	-994.2	-3449	-1032.4	-3383	-1032.4	-3403	-1032.4
0.2	54	4.6	-4479	-1070.7	-4466	-1338.3	-4447	-1376.6	-4521	-1414.8	-4461	-1376.6
0.1	27	2.3	-5647	-1376.6	-5594	-1644.2	-5568	-1758.9	-5640	-1835.4	-5606	-1797.2

Table A41: Hoyer test results summary for all cases

				με$_t$/με$_c$					residual (με$_c$)				
d_b (in)	Strand	E (ksi)	COV of E	1	2	3	4	5	1	2	3	4	5
0.7	1	31773	0.009	-0.364	-0.351	-0.349	-0.345	-0.338	427	23	22	-10	12
0.7	2	32292	0.031	-0.363	-0.305	-0.262	-0.231	-0.185	608	58	157	143	-7
0.7	3	31670	0.056	-0.400	-0.399	-0.396	-0.394	-0.395	521	35	11	20	10
0.7	4	29862	0.140	-0.363	-0.322	-0.285	-0.253	-0.224	-258	12	29	-9	-4
0.7	5	30762	0.038	-0.372	-0.357	-0.347	-0.357	-0.359	536	116	136	260	151
0.6	1	32223	0.004	0.369	0.401	0.402	0.402	0.393	244	-5	19	-6	-8
0.6	2	31209	0.022	0.281	0.263	0.258	0.258	0.260	303	3	-3	3	1
0.6	3	32522	0.014	0.273	0.279	0.279	0.280	0.284	61	22	14	9	-3
0.6	4	32064	0.011	0.308	0.287	0.268	0.251	0.234	341	-18	-49	54	-9
0.6	5	31821	0.013	0.330	0.314	0.306	0.298	0.289	379	1	3	6	-15
0.5	1	30734	0.011	0.312	0.364	0.365	0.366	0.365	323	3	22	2	-2
0.5	2	30787	0.028	0.308	0.308	0.307	0.308	0.308	174	4	-7	9	-3
0.5	3	31032	0.017	0.310	0.260	0.260	0.260	0.208	123	35	10	-1	8
0.5	4	28615	0.023	0.388	0.278	0.222	0.166	0.111	136	12	-6	1	-5
0.5	5	30904	0.013	0.412	0.309	0.308	0.311	0.310	249	14	-19	39	-5
3/8	1	26765	0.172	-0.189	-0.134	-0.126	-0.209	-0.197	-24	511	-13	537	596
3/8	2	26911	0.190	0.112	0.059	0.314	0.317	0.293	525	45	592	45	727
3/8	3	31032	0.017	0.401	0.336	0.337	0.337	0.270	123	35	10	-1	8
3/8	4	29488	0.038	0.259	0.254	0.231	0.205	0.199	95	47	-40	44	43
3/8	5	30180	0.035	0.244	0.294	0.316	0.325	0.321	198	53	26	-72	34

Appendix B Beam-end Test Data

In all beam-end test data, the slip is measured using and LVDT which provides a linear mV/V/in output units; the slip is calculated in inches based on the resolution of the data acquitition used. The following tables provide data from each beam end test conducted.

Table B1: Beam-end test data for 3-20

3-20 A				**3-20 B**			
Strand area, A_p = 0.085 in^2							
Load (Kips)	Stress (ksi)	Slip (V)	Slip (in)	Load (Kips)	Stress (ksi)	Slip (V)	Slip (in)
0	0	3.3215	0	0	0.00	3.4302	0
2.85	33.53	3.3214	1.2E-05	2	23.53	3.4301	1.3E-05
4	47.06	3.3214	1.2E-05	4.15	48.82	3.43	2.5E-05
4.3	50.59	3.3213	2.5E-05	5.8	68.24	3.4299	3.8E-05
4.9	57.65	3.3212	3.7E-05	6.13	72.12	3.4298	5.0E-05
5.13	60.35	3.3211	5.0E-05	6.3	74.12	3.4297	6.3E-05
6.7	78.82	3.321	6.2E-05	6.5	76.47	3.4296	7.5E-05
6.96	81.88	3.3209	7.5E-05	6.8	80.00	3.4295	8.8E-05
7.3	85.88	3.3207	1.0E-04	7	82.35	3.4294	1.0E-04
7.56	88.94	3.3206	1.1E-04	7.1	83.53	3.4293	1.1E-04
7.6	89.41	3.3204	1.4E-04	7.4	87.06	3.4285	2.1E-04
7.6	89.41	0	4.2E-01	7.6	89.41	3.4277	3.1E-04
				7.6	89.41	0	4.3E-01

Table B2: Beam-end test data for 5-20

5-20 A				5-20 B			
Strand area, A_p = 0.153 in^2							
Load (Kips)	Stress (ksi)	Slip (V)	Slip (in)	Load (Kips)	Stress (ksi)	Slip (V)	Slip (in)
0	0	3.6483	0	0	0.00	3.7244	0
3	19.61	3.6482	1.2E-05	2.8	18.30	3.7243	1.3E-05
3.9	25.49	3.6478	6.2E-05	4.94	32.29	3.7242	2.5E-05
4	26.14	3.6477	7.5E-05	6.52	42.61	3.7241	3.8E-05
5.2	33.99	3.6476	8.7E-05	7.5	49.02	3.724	5.0E-05
7.17	46.86	3.6475	1.0E-04	8.7	56.86	3.7239	6.3E-05
8	52.29	3.6474	1.1E-04	9.7	63.40	3.7238	7.5E-05
8.5	55.56	3.6473	1.2E-04	11	71.90	3.7237	8.8E-05
8.8	57.52	3.6472	1.4E-04	11.9	77.78	3.7236	1.0E-04
9.6	62.75	3.6471	1.5E-04	13	84.97	3.7235	1.1E-04
10.33	67.52	3.6471	1.5E-04	14.3	93.46	3.7234	1.3E-04
12.6	82.35	3.647	1.6E-04	15.35	100.33	3.7233	1.4E-04
13	84.97	3.6467	2.0E-04	15.8	103.27	3.7232	1.5E-04
15	98.04	3.6465	2.2E-04	16.65	108.82	3.7231	1.6E-04
15.5	101.31	3.6463	2.5E-04	17	111.11	3.723	1.8E-04
16	104.58	3.6461	2.7E-04	17.2	112.42	3.7229	1.9E-04
16.33	106.73	3.6458	3.1E-04	17.6	115.03	3.7227	2.1E-04
16.7	109.15	3.6455	3.5E-04	18	117.65	3.7226	2.3E-04
16.88	110.33	3.6453	3.7E-04	18.3	119.61	3.7224	2.5E-04
16.9	110.46	3.6451	4.0E-04	18.6	121.57	3.7221	2.9E-04
17.24	112.68	3.645	4.1E-04	19	124.18	3.7218	3.3E-04
17.7	115.69	3.6448	4.4E-04	19	124.18	3.7215	3.6E-04
18	117.65	3.6446	4.6E-04	19.4	126.80	3.7212	4.0E-04
18.4	120.26	3.6444	4.9E-04	19.5	127.45	3.721	4.3E-04
18.7	122.22	3.6443	5.0E-04	19.7	128.76	3.7209	4.4E-04
19	124.18	3.644	5.4E-04	20.2	132.03	3.7206	4.8E-04
19.4	126.80	3.6434	6.1E-04	20.5	133.99	3.7201	5.4E-04
19.8	129.41	3.643	6.6E-04	21.15	138.24	3.7188	7.0E-04
20.5	133.99	3.6422	7.6E-04				
21	137.25	3.6355	1.6E-03				

Table B3: Beam-end test data for 6-20

6-20 A				6-20 B			
Strand area, A_p = 0.217 in^2							
Load (Kips)	Stress (ksi)	Slip (V)	Slip (in)	Load (Kips)	Stress (ksi)	Slip (V)	Slip (in)
0	0	3.3481	0	0	0	3.5913	0
3.1	14.29	3.3477	5.0E-05	2.15	9.91	3.5911	2.5E-05
3.35	15.44	3.3476	6.3E-05	5.3	24.42	3.591	3.7E-05
4	18.43	3.3475	7.5E-05	5.87	27.05	3.5909	5.0E-05
5.16	23.78	3.3474	8.8E-05	6.59	30.37	3.5908	6.2E-05
5.7	26.27	3.3473	1.0E-04	8.27	38.11	3.5903	1.2E-04
6.13	28.25	3.347	1.4E-04	8.7	40.09	3.5901	1.5E-04
6.4	29.49	3.3469	1.5E-04	9.1	41.94	3.5897	2.0E-04
6.6	30.41	3.3467	1.8E-04	9.4	43.32	3.5894	2.4E-04
6.84	31.52	3.3465	2.0E-04	10	46.08	3.5889	3.0E-04
7.14	32.90	3.3463	2.3E-04	10.37	47.79	3.5885	3.5E-04
7.35	33.87	3.3462	2.4E-04	10.67	49.17	3.5882	3.9E-04
7.67	35.35	3.346	2.6E-04	11.5	53.00	3.5879	4.3E-04
8.8	40.55	3.3456	3.1E-04	11.6	53.46	3.5875	4.8E-04
9.13	42.07	3.3455	3.3E-04	11.75	54.15	3.587	5.4E-04
9.4	43.32	3.3453	3.5E-04	11.75	54.15	0	4.5E-01
9.66	44.52	3.3451	3.8E-04				
10.44	48.11	3.345	3.9E-04				
11.32	52.17	3.3449	4.0E-04				
11.75	54.15	3.3447	4.3E-04				
12	55.30	3.3446	4.4E-04				
12.5	57.60	3.3443	4.8E-04				
13.3	61.29	3.3435	5.7E-04				
13.7	63.13	3.3433	6.0E-04				
13.9	64.06	3.3429	6.5E-04				
14	64.52	3.3428	6.6E-04				
14.2	65.44	3.3426	6.9E-04				
14.3	65.90	3.3423	7.3E-04				
14.4	66.36	3.3422	7.4E-04				
14.7	67.74	3.3421	7.5E-04				
15	69.12	3.3417	8.0E-04				
15.4	70.97	3.3413	8.5E-04				
15.6	71.89	3.3407	9.3E-04				
15.8	72.81	3.3403	9.8E-04				
15.8	72.81	0	4.2E-01				

Table B4: Beam-end test data for 7-20

7-20 A				7-20 B			
Strand area, A_p = 0.294 in^2							
Load (Kips)	Stress (ksi)	Slip (V)	Slip (in)	Load (Kips)	Stress (ksi)	Slip (V)	Slip (in)
0	0	3.3915	0	0	0	3.386	0
4.32	14.69	3.3911	5.0E-05	4	13.61	3.3858	2.5E-05
6	20.41	3.3908	8.8E-05	6.9	23.47	3.3857	3.8E-05
9.78	33.27	3.3902	1.6E-04	8.2	27.89	3.3857	3.8E-05
10	34.01	3.3901	1.8E-04	11.7	39.80	3.3855	6.3E-05
10.9	37.07	3.39	1.9E-04	13.8	46.94	3.3854	7.5E-05
11.9	40.48	3.3898	2.1E-04	14.2	48.30	3.3853	8.8E-05
12.5	42.52	3.3897	2.3E-04	16.4	55.78	3.3852	1.0E-04
13.25	45.07	3.3895	2.5E-04	17.2	58.50	3.3851	1.1E-04
14.3	48.64	3.3894	2.6E-04	18.6	63.27	3.385	1.3E-04
15	51.02	3.3893	2.8E-04	19.2	65.31	3.3848	1.5E-04
16	54.42	3.3892	2.9E-04	21.9	74.49	3.3847	1.6E-04
16.5	56.12	3.389	3.1E-04	22.4	76.19	3.3845	1.9E-04
18.9	64.29	3.3888	3.4E-04	23	78.23	3.3842	2.3E-04
19.5	66.33	3.3887	3.5E-04	23.3	79.25	3.384	2.5E-04
20	68.03	3.3886	3.6E-04	23.8	80.95	3.3839	2.6E-04
22	74.83	3.3884	3.9E-04	24.2	82.31	3.3836	3.0E-04
25	85.03	3.3882	4.1E-04	24.4	82.99	3.3835	3.1E-04
26	88.44	3.388	4.4E-04	24.5	83.33	3.3831	3.6E-04
27	91.84	3.3876	4.9E-04	25.4	86.39	3.3828	4.0E-04
27.7	94.22	3.387	5.6E-04	26	88.44	3.382	5.0E-04
28	95.24	3.3861	6.8E-04	26.3	89.46	3.3816	5.5E-04
29	98.64	3.3855	7.5E-04	26.9	91.50	3.3808	6.5E-04
30	102.04	3.3846	8.6E-04	27	91.84	3.3805	6.9E-04
30.2	102.72	3.3781	1.7E-03	27.6	93.88	3.3802	7.3E-04
				27.9	94.90	3.3795	8.1E-04
				28	95.24	3.3791	8.6E-04
				28.5	96.94	3.3789	8.9E-04
				28.9	98.30	3.3785	9.4E-04
				29	98.64	3.3777	1.0E-03

Table B5: Beam-end test data for 6-30 A-B

6-30 A				6-30 B			
Strand area, A_p = 0.217 in^2							
Load (Kips)	Stress (ksi)	Slip (V)	Slip (in)	Load (Kips)	Stress (ksi)	Slip (V)	Slip (in)
0	0	3.4579	0	0	0	3.1165	0
12.07	55.62	3.4578	1.2E-05	6.38	29.40	3.1164	1.2E-05
13.28	61.20	3.4577	2.5E-05	7.12	32.81	3.1163	2.5E-05
15.33	70.65	3.4576	3.8E-05	7.62	35.12	3.1162	3.7E-05
16.6	76.50	3.4575	5.0E-05	8.44	38.89	3.1161	5.0E-05
17.3	79.72	3.4574	6.3E-05	9.43	43.46	3.116	6.2E-05
17.9	82.49	3.4573	7.5E-05	10.45	48.16	3.1159	7.5E-05
18.52	85.35	3.4572	8.8E-05	11	50.69	3.1158	8.7E-05
19.02	87.65	3.4571	1.0E-04	11.8	54.38	3.1157	1.0E-04
19.7	90.78	3.4568	1.4E-04	12.23	56.36	3.1156	1.1E-04
20	92.17	3.4561	2.2E-04	12.72	58.62	3.1155	1.2E-04
20.21	93.13	3.4548	3.9E-04	13.42	61.84	3.1154	1.4E-04
20.21	93.13	0	4.3E-01	13.75	63.36	3.1153	1.5E-04
				14	64.52	3.1152	1.6E-04
				14.7	67.74	3.1151	1.7E-04
				15.54	71.61	3.1149	2.0E-04
				16	73.73	3.1148	2.1E-04
				17.47	80.51	3.1143	2.7E-04
				18.2	83.87	3.1139	3.2E-04
				19	87.56	3.1134	3.9E-04
				20.1	92.63	3.1124	5.1E-04
				20.1	92.63	0	3.9E-01

Table B6: Beam-end test data for 6-30 C-D

6-30 C				6-30 D			
Strand area, A_p = 0.217 in^2							
Load (Kips)	Stress (ksi)	Slip (V)	Slip (in)	Load (Kips)	Stress (ksi)	Slip (V)	Slip (in)
0	0.00	3.379	0.00	0	0.00	3.4354	0.00
1	4.61	3.3771	0.00024	1	4.61	3.4363	-0.000113
2	9.22	3.3769	0.00026	2	9.22	3.4366	-0.000150
3	13.82	3.3769	0.00026	3	13.82	3.4371	-0.000213
4	18.43	3.3772	0.00022	4	18.43	3.4375	-0.000262
5	23.04	3.378	0.00012	5	23.04	3.4376	-0.000275
6	27.65	3.3782	0.00010	6	27.65	3.4378	-0.000300
7	32.26	3.3787	0.00004	7	32.26	3.4379	-0.000312
8	36.87	3.3787	0.00004	8	36.87	3.438	-0.000325
9	41.47	3.3789	0.00001	9	41.47	3.4381	-0.000337
10	46.08	3.3792	-0.00002	10	46.08	3.4384	-0.000375
11	50.69	3.3794	-0.00005	11	50.69	3.4386	-0.000400
12	55.30	3.3796	-0.00007	12	55.30	3.4386	-0.000400
13	59.91	3.38	-0.00012	13	59.91	3.4387	-0.000412
14	64.52	3.3802	-0.00015	14	64.52	3.4384	-0.000375
15	69.12	3.3775	0.00019	15	69.12	3.4342	0.000150
16	73.73	3.3122	0.00835	16	73.73	3.4112	0.003025
17	78.34	3.266	0.01413	17	78.34	3.3645	0.008863
18	82.95	3.2192	0.01998	18	82.95	3.3282	0.013400
19	87.56	3.1588	0.02753	19	87.56	3.2727	0.020338
20	92.17	3.0937	0.03566	20	92.17	3.2711	0.020538
21	96.77	3.0511	0.04099	21	96.77	3.1766	0.032350
22	101.38	3.009	0.04625	22	101.38	3.1888	0.030825
23	105.99	2.9905	0.04856	23	105.99	3.1082	0.040900
24	110.60	2.9021	0.05961	24	110.60	3.059	0.047050
25	115.21	2.888	0.06138	25	115.21	3.0666	0.046100
26	119.82	2.788	0.07388	26	119.82	2.952	0.060425
27	124.42	2.7668	0.07653	27	124.42	2.8777	0.069713
28	129.03	2.6481	0.09136	28	129.03	2.7766	0.082350
29	133.64	2.4818	0.11215	29	133.64	2.7076	0.090975
30	138.25	2.3781	0.12511	30	138.25	2.538	0.112175
31	142.86	2.2147	0.14554	31	142.86	2.4689	0.120813
32	147.47	2	0.17238	32	147.47	2.18	0.156925
33	152.07	1.7066	0.20905	33	152.07	2.0323	0.175388
34	156.68	1.5	0.23488	34	156.68	1.6676	0.220975
35	161.29	0	0.42238	35	161.29	0	0.429425

Table B7: Beam-end test data for L6-30 E-F

L6-30 E				L6-30 F			
Strand area, A_p = 0.217 in^2							
Load (Kips)	Stress (ksi)	Slip (V)	Slip (in)	Load (Kips)	Stress (ksi)	Slip (V)	Slip (in)
0	0.00	3.5894	0.00	0	0.00	3.5159	0.00
1	4.61	3.5893	0.00001	1	4.61	3.5163	-0.00005
2	9.22	3.5884	0.00012	2	9.22	3.5154	0.00006
3	13.82	3.587	0.00030	3	13.82	3.5165	-0.00008
4	18.43	3.5849	0.00056	4	18.43	3.5165	-0.00008
5	23.04	3.5809	0.00106	5	23.04	3.5165	-0.00008
6	27.65	3.5789	0.00131	6	27.65	3.5164	-0.00006
7	32.26	3.5761	0.00166	7	32.26	3.5156	0.00004
8	36.87	3.5751	0.00179	8	36.87	3.5133	0.00032
9	41.47	3.5743	0.00189	9	41.47	3.5119	0.00050
10	46.08	3.5742	0.00190	10	46.08	3.5111	0.00060
11	50.69	3.5724	0.00212	11	50.69	3.5124	0.00044
12	55.30	3.5715	0.00224	12	55.30	3.5108	0.00064
13	59.91	3.5728	0.00207	13	59.91	3.51	0.00074
14	64.52	3.572	0.00217	14	64.52	3.5091	0.00085
15	69.12	3.5732	0.00203	15	69.12	3.5086	0.00091
16	73.73	3.5717	0.00221	16	73.73	3.5059	0.00125
17	78.34	3.5662	0.00290	17	78.34	3.5028	0.00164
18	82.95	3.5651	0.00304	18	82.95	3.4962	0.00246
19	87.56	3.5634	0.00325	19	87.56	3.4632	0.00659
20	92.17	3.5555	0.00424	20	92.17	3.4894	0.00331
21	96.77	3.5151	0.00929	21	96.77	3.4668	0.00614
22	101.38	3.4822	0.01340	22	101.38	3.3762	0.01746
23	105.99	3.4131	0.02204	23	105.99	3.3621	0.01923
24	110.60	3.4691	0.01504	24	110.60	3.28	0.02949
25	115.21	3.4211	0.02104	25	115.21	3.22	0.03699
26	119.82	3.4101	0.02241	26	119.82	3.2154	0.03756
27	124.42	3.3781	0.02641	27	124.42	3.1908	0.04064
28	129.03	3.3414	0.03100	28	129.03	3.0687	0.05590
29	133.64	3.273	0.03955	29	133.64	2.9986	0.06466
30	138.25	3.2472	0.04278	30	138.25	2.9449	0.07138
31	142.86	3.1688	0.05258	31	142.86	2.9306	0.07316
32	147.47	3.1595	0.05374	32	147.47	2.8787	0.07965
33	152.07	3.0718	0.06470	33	152.07	2.7324	0.09794
34	156.68	2.9311	0.08229	34	156.68	2.1985	0.16468
35	161.29	0	0.44868	35	161.29	0	0.43949

Table B8: Beam-end test data for 7-30 A-B

7-30 A				7-30 B			
Strand area, A_p = 0.294 in^2							
Load (Kips)	Stress (ksi)	Slip (V)	Slip (in)	Load (Kips)	Stress (ksi)	Slip (V)	Slip (in)
0	0	3.7499	0	0	0	3.3456	0
2.38	8.10	3.7494	6.2E-05	6.19	21.05	3.3455	1.3E-05
5.48	18.64	3.7493	7.5E-05	26.65	90.65	3.3454	2.5E-05
16.5	56.12	3.7492	8.7E-05	38.25	130.10	3.3453	3.8E-05
19.48	66.26	3.7491	1.0E-04	39.39	133.98	3.3452	5.0E-05
21.98	74.76	3.749	1.1E-04	40.46	137.62	3.3451	6.3E-05
22.89	77.86	3.7489	1.2E-04	40.99	139.42	3.345	7.5E-05
23.7	80.61	3.7488	1.4E-04	42.2	143.54	3.3449	8.8E-05
25.6	87.07	3.7487	1.5E-04	42.7	145.24	3.3447	1.1E-04
26.56	90.34	3.7486	1.6E-04	43	146.26	3.3446	1.3E-04
27.92	94.97	3.7485	1.7E-04	43.4	147.62	3.3444	1.5E-04
29	98.64	3.7484	1.9E-04	44	149.66	3.3441	1.9E-04
29.7	101.02	3.7483	2.0E-04	44.15	150.17	3.3435	2.6E-04
30.3	103.06	3.7482	2.1E-04	44.7	152.04	3.3427	3.6E-04
30.93	105.20	3.7479	2.5E-04	45.1	153.40	3.3424	4.0E-04
32	108.84	3.7478	2.6E-04				
32.65	111.05	3.7477	2.7E-04				
33	112.24	3.7476	2.9E-04				
33.2	112.93	3.7475	3.0E-04				
33.7	114.63	3.7473	3.2E-04				
34.4	117.01	3.7472	3.4E-04				
35	119.05	3.747	3.6E-04				
36	122.45	3.7469	3.7E-04				
38	129.25	3.7467	4.0E-04				
38.3	130.27	3.7465	4.2E-04				
39	132.65	3.746	4.9E-04				
39.6	134.69	3.7457	5.2E-04				
40.1	136.39	3.7447	6.5E-04				
40.2	136.73	3.7444	6.9E-04				
40.4	137.41	3.7443	7.0E-04				
40.9	139.12	3.744	7.4E-04				
41.5	141.16	3.7437	7.7E-04				
41.8	142.18	3.7431	8.5E-04				
42	142.86	3.7425	9.2E-04				
42.2	143.54	3.742	9.9E-04				
42.4	144.22	3.7401	1.2E-03				
43.4	147.62	3.7377	1.5E-03				

Table B9: Beam-end test data for 7-30 C-D

7-30 C				7-30 D			
Strand area, A_p = 0.294 in^2							
Load (Kips)	Stress (ksi)	Slip (V)	Slip (in)	Load (Kips)	Stress (ksi)	Slip (V)	Slip (in)
0	0.00	3.2139	0	0	0.00	3.3604	0
1	3.40	3.2144	-0.00006	1	3.40	3.364	-0.00045
2	6.80	3.2147	-0.00010	2	6.80	3.365	-0.00058
3	10.20	3.2148	-0.00011	3	10.20	3.3655	-0.00064
4	13.61	3.2147	-0.00010	4	13.61	3.3656	-0.00065
5	17.01	3.2147	-0.00010	5	17.01	3.3661	-0.00071
6	20.41	3.2148	-0.00011	6	20.41	3.3664	-0.00075
7	23.81	3.2148	-0.00011	7	23.81	3.3665	-0.00076
8	27.21	3.2151	-0.00015	8	27.21	3.3669	-0.00081
9	30.61	3.2154	-0.00019	9	30.61	3.3672	-0.00085
10	34.01	3.2157	-0.00022	10	34.01	3.3672	-0.00085
11	37.41	3.2159	-0.00025	11	37.41	3.3677	-0.00091
12	40.82	3.2161	-0.00027	12	40.82	3.3678	-0.00093
13	44.22	3.2163	-0.00030	13	44.22	3.368	-0.00095
14	47.62	3.2166	-0.00034	14	47.62	3.3681	-0.00096
15	51.02	3.2169	-0.00037	15	51.02	3.3682	-0.00098
16	54.42	3.2172	-0.00041	16	54.42	3.3684	-0.00100
17	57.82	3.2172	-0.00041	17	57.82	3.3689	-0.00106
18	61.22	3.2171	-0.00040	18	61.22	3.3691	-0.00109
19	64.63	3.2168	-0.00036	19	64.63	3.3692	-0.00110
20	68.03	3.2161	-0.00027	20	68.03	3.3692	-0.00110
21	71.43	3.2112	0.00034	21	71.43	3.3692	-0.00110
22	74.83	3.2008	0.00164	22	74.83	3.3692	-0.00110
23	78.23	3.186	0.00349	23	78.23	3.3693	-0.00111
24	81.63	3.1562	0.00721	24	81.63	3.3689	-0.00106
25	85.03	3.1108	0.01289	25	85.03	3.3652	-0.00060
26	88.44	3.0109	0.02538	26	88.44	3.3485	0.00149
27	91.84	2.58	0.07924	27	91.84	3.3356	0.00310
28	95.24	1.833	0.17261	28	95.24	3.2999	0.00756
29	98.64	0	0.40174	29	98.64	3.1788	0.02270
				30	102.04	3.1588	0.02520
				31	105.44	3.0812	0.03490
				32	108.84	3.0511	0.03866
				33	112.24	2.999	0.04518
				34	115.65	2.9	0.05755
				35	119.05	2.8153	0.06814
				36	122.45	2.7187	0.08021
				37	125.85	2.675	0.08568
				38	129.25	2.472	0.11105
				39	132.65	2.2287	0.14146
				40	136.05	1.4809	0.23494
				41	139.46	0	0.42005

Table B10: Beam-end test data for L7-30 E-F

L7-30 E				L7-30 F			
Strand area, A_p = 0.217 in^2							
Load (Kips)	Stress (ksi)	Slip (V)	Slip (in)	Load (Kips)	Stress (ksi)	Slip (V)	Slip (in)
0	0.00	3.4455	0	0	0.00	3.3108	0
1	3.40	3.4456	-0.000013	1	3.40	3.315	-0.00052
2	6.80	3.4458	-0.000038	2	6.80	3.3165	-0.00071
3	10.20	3.4466	-0.000138	3	10.20	3.3181	-0.00091
4	13.61	3.4461	-0.000075	4	13.61	3.3165	-0.00071
5	17.01	3.4463	-0.000100	5	17.01	3.3188	-0.00100
6	20.41	3.4463	-0.000100	6	20.41	3.3197	-0.00111
7	23.81	3.4465	-0.000125	7	23.81	3.3205	-0.00121
8	27.21	3.4467	-0.000150	8	27.21	3.3212	-0.00130
9	30.61	3.4467	-0.000150	9	30.61	3.3215	-0.00134
10	34.01	3.447	-0.000188	10	34.01	3.322	-0.00140
11	37.41	3.447	-0.000188	11	37.41	3.3223	-0.00144
12	40.82	3.447	-0.000188	12	40.82	3.3227	-0.00149
13	44.22	3.4468	-0.000163	13	44.22	3.3232	-0.00155
14	47.62	3.4468	-0.000163	14	47.62	3.3236	-0.00160
15	51.02	3.4469	-0.000175	15	51.02	3.324	-0.00165
16	54.42	3.4468	-0.000163	16	54.42	3.327	-0.00203
17	57.82	3.4467	-0.000150	17	57.82	3.3275	-0.00209
18	61.22	3.4465	-0.000125	18	61.22	3.3277	-0.00211
19	64.63	3.4452	0.000038	19	64.63	3.328	-0.00215
20	68.03	3.444	0.000188	20	68.03	3.3282	-0.00217
21	71.43	3.4353	0.001275	21	71.43	3.3282	-0.00217
22	74.83	3.43	0.001937	22	74.83	3.3287	-0.00224
23	78.23	3.43	0.001937	23	78.23	3.3289	-0.00226
24	81.63	3.4298	0.001962	24	81.63	3.3283	-0.00219
25	85.03	3.4275	0.002250	25	85.03	3.3197	-0.00111
26	88.44	3.4315	0.001750	26	88.44	3.3	0.00135
27	91.84	3.435	0.001312	27	91.84	3.2988	0.00150
28	95.24	3.4379	0.000950	28	95.24	3.2956	0.00190
29	98.64	3.4398	0.000713	29	98.64	3.2838	0.00338
30	102.04	3.4395	0.000750	30	102.04	3.277	0.00422
31	105.44	3.432	0.001688	31	105.44	3.2795	0.00391
32	108.84	3.4137	0.003975	32	108.84	3.2777	0.00414
33	112.24	3.3776	0.008487	33	112.24	3.2644	0.00580
34	115.65	3.3261	0.014925	34	115.65	3.0393	0.03394
35	119.05	3.2172	0.028538	35	119.05	2.9495	0.04516
36	122.45	0	0.430688	36	122.45	2.6585	0.08154
				37	125.85	2.4864	0.10305
				38	129.25	2.1336	0.14715
				39	132.65	0	0.41385

Table B11: Beam-end test data for 6-40

6-40 A				6-40 B			
Strand area, A_p = 0.217 in^2							
Load (Kips)	Stress (ksi)	Slip (V)	Slip (in)	Load (Kips)	Stress (ksi)	Slip (V)	Slip (in)
0	0	3.7438	0	0	0	3.629	0
20	92.17	3.7437	1.2E-05	6.3	29.03	3.6289	1.3E-05
23.5	108.29	3.7435	3.7E-05	7.2	33.18	3.6288	2.5E-05
23.6	108.76	3.7434	5.0E-05	9	41.47	3.6287	3.8E-05
23.7	109.22	3.7433	6.2E-05	9.89	45.58	3.6286	5.0E-05
24.5	112.90	3.7431	8.7E-05	11.2	51.61	3.6285	6.3E-05
24.5	112.90	0	4.7E-01	15	69.12	3.6284	7.5E-05
				20.5	94.47	3.6283	8.8E-05
				20.9	96.31	3.6282	1.0E-04
				21	96.77	3.6281	1.1E-04
				21.4	98.62	3.6279	1.4E-04
				21.5	99.08	3.6276	1.7E-04
				21.6	99.54	3.6274	2.0E-04
				21.66	99.82	3.6272	2.2E-04
				21.71	100.05	3.6268	2.8E-04
				21.8	100.46	3.6266	3.0E-04
				22	101.38	3.6263	3.4E-04
				22.22	102.40	3.6253	4.6E-04
				22.22	102.40	0	4.5E-01

Table B12: Beam-end test data for 7-40

7-40 A				7-40 B			
Strand area, A_p = 0.294 in^2							
Load (Kips)	Stress (ksi)	Slip (V)	Slip (in)	Load (Kips)	Stress (ksi)	Slip (V)	Slip (in)
0	0	2.8686	0	0	0	3.5407	0
21.78	74.08	2.8685	1.2E-05	21.14	71.90	3.5406	1.3E-05
41.28	140.41	2.8684	2.5E-05	28	95.24	3.5406	1.3E-05
43.2	146.94	2.8683	3.7E-05	39.36	133.88	3.5405	2.5E-05
43.8	148.98	2.8673	1.6E-04	40.58	138.03	3.5404	3.8E-05
44.68	151.97	2.8666	2.5E-04	40.8	138.78	3.5401	7.5E-05
45.04	153.20	2.8659	3.4E-04	41.16	140.00	3.5397	1.3E-04
45.4	154.42	2.8656	3.7E-04	41.4	140.82	3.5395	1.5E-04
46	156.46	2.8655	3.9E-04	41.8	142.18	3.5393	1.8E-04
46.3	157.48	2.8653	4.1E-04	42	142.86	3.5389	2.3E-04
47	159.86	2.8652	4.2E-04	42.4	144.22	3.5386	2.6E-04
47.4	161.22	2.8651	4.4E-04	43.2	146.94	3.5383	3.0E-04
48.72	165.71	2.8655	3.9E-04	43.8	148.98	3.5378	3.6E-04
55.2	187.76	2.8636	6.2E-04	47	159.86	3.5377	3.8E-04
				47.6	161.90	3.5373	4.3E-04
				48	163.27	3.5371	4.5E-04
				48.2	163.95	3.537	4.6E-04
				48.6	165.31	3.5369	4.8E-04
				48.8	165.99	3.5367	5.0E-04
				49	166.67	3.5366	5.1E-04
				50.6	172.11	3.5362	5.6E-04
				51.2	174.15	3.5361	5.8E-04
				52	176.87	3.5359	6.0E-04
				52.8	179.59	3.5357	6.3E-04
				53.2	180.95	3.5355	6.5E-04
				54	183.67	3.5351	7.0E-04
				54.2	184.35	3.5347	7.5E-04
				54.6	185.71	3.5341	8.3E-04
				55.2	187.76	3.5334	9.1E-04
				55.6	189.12	3.5311	1.2E-03
				56	190.48	3.5304	1.3E-03

Table B13: Beam-end test data for H6-10

H6-10			
Strand area, A_p = 0.217 in^2			
Load (Kips)	Stress (ksi)	Slip (mV)	Slip (in)
0	0	179.02	0.000
1	4.61	192.88	0.005
2	9.22	203.8	0.009
3	13.82	212.65	0.013
4	18.43	218.35	0.015
5	23.04	223.48	0.017
6	27.65	229.84	0.019
7	32.26	235.17	0.021
8	36.87	240.84	0.023
9	41.47	246.13	0.025
10	46.08	251.66	0.027
11	50.69	258.15	0.030
12	55.30	264.7	0.032
13	59.91	270.3	0.034
14	64.52	275.58	0.036
15	69.12	281.34	0.038
16	73.73	286.98	0.040
17	78.34	292.61	0.043
18	82.95	298.71	0.045
19	87.56	304.16	0.047
20	92.17	310.89	0.049
21	96.77	315.42	0.051
22	101.38	322.29	0.054
23	105.99	329.61	0.056
24	110.60	337.82	0.060
25	115.21	344.72	0.062
25.5	117.51	347.96	0.063
26	119.82	352.92	0.065
26.5	122.12	358.32	0.067
27	124.42	363.09	0.069
27.5	126.73	366.77	0.070
28	129.03	376.34	0.074
28.5	131.34	374.87	0.073
29	133.64	380.75	0.076
29.5	135.94	406.36	0.085
30	138.25	491.28	0.117
30.5	140.55	556	0.141
31	142.86	609.6	0.161
31.5	145.16	774.8	0.223
32	147.47	965.8	0.295

Table B14: Beam-end test data for H7-10

H7-10							
Strand area, A_p = 0.294 in^2							
Load (Kips)	Stress (ksi)	Slip (mV)	Slip (in)	Load (Kips)	Stress (ksi)	Slip (mV)	Slip (in)
0	0	222.15	0.000	37	125.85	258.4	0.014
1	3.40	219.45	-0.001	37.5	127.55	259.64	0.014
2	6.80	213.72	-0.003	38	129.25	262.22	0.015
3	10.20	210.34	-0.004	38.5	130.95	264.22	0.016
4	13.61	207.56	-0.005	39	132.65	266.12	0.016
5	17.01	205.24	-0.006	39.5	134.35	268.25	0.017
6	20.41	203	-0.007	40	136.05	269.66	0.018
7	23.81	201.73	-0.008	40.5	137.76	271.42	0.018
8	27.21	201.2	-0.008	41	139.46	273.59	0.019
9	30.61	200.93	-0.008	41.5	141.16	275.58	0.020
10	34.01	200.93	-0.008	42	142.86	278.65	0.021
11	37.41	201.11	-0.008	42.5	144.56	280.65	0.022
12	40.82	201.61	-0.008	43	146.26	282.36	0.023
13	44.22	202.84	-0.007	43.5	147.96	283	0.023
14	47.62	204.16	-0.007				
15	51.02	206.16	-0.006				
16	54.42	207.68	-0.005				
17	57.82	208.86	-0.005				
18	61.22	211.08	-0.004				
19	64.63	212.94	-0.003				
20	68.03	215.86	-0.002				
21	71.43	217.52	-0.002				
22	74.83	219.72	-0.001				
23	78.23	221.69	0.000				
24	81.63	223.65	0.001				
25	85.03	226.22	0.002				
26	88.44	229.88	0.003				
27	91.84	232.82	0.004				
28	95.24	234.65	0.005				
29	98.64	238.25	0.006				
30	102.04	241.24	0.007				
31	105.44	243.54	0.008				
32	108.84	245.97	0.009				
33	112.24	248.64	0.010				
33.5	113.95	250.65	0.011				
34	115.65	252.37	0.011				
34.5	117.35	253.88	0.012				
35	119.05	254.6	0.012				
35.5	120.75	255.72	0.013				
36	122.45	256.83	0.013				
36.5	124.15	257.8	0.013				

Table B15: Beam-end test data for H6-20

H6-20							
Strand area, A_p = 0.217 in^2							
Load (Kips)	Stress (ksi)	Slip (mV)	Slip (in)	Load (Kips)	Stress (ksi)	Slip (mV)	Slip (in)
0	0	231.64	0.000	34.5	158.99	514.2	0.106
1	4.61	233.21	0.001	35	161.29	530.3	0.112
2	9.22	233.22	0.001	35.5	163.59	566.1	0.125
3	13.82	234.82	0.001	36	165.90	598.8	0.138
4	18.43	237.21	0.002				
5	23.04	240	0.003				
6	27.65	243.82	0.005				
7	32.26	247.19	0.006				
8	36.87	250	0.007				
9	41.47	255.18	0.009				
10	46.08	259.79	0.011				
11	50.69	267.05	0.013				
12	55.30	272.85	0.015				
13	59.91	279.22	0.018				
14	64.52	287.22	0.021				
15	69.12	295.11	0.024				
16	73.73	304.26	0.027				
17	78.34	314.05	0.031				
18	82.95	322.92	0.034				
19	87.56	332.06	0.038				
20	92.17	342.41	0.042				
21	96.77	348.63	0.044				
22	101.38	358.55	0.048				
23	105.99	367.48	0.051				
24	110.60	377.81	0.055				
25	115.21	392.84	0.060				
26	119.82	396.1	0.062				
26.5	122.12	404.34	0.065				
27	124.42	407.3	0.066				
27.5	126.73	412.13	0.068				
28	129.03	417.1	0.070				
28.5	131.34	422.26	0.071				
29	133.64	427.49	0.073				
29.5	135.94	435.16	0.076				
30	138.25	441.6	0.079				
30.5	140.55	448.27	0.081				
31	142.86	454.62	0.084				
31.5	145.16	462.78	0.087				
32	147.47	471	0.090				
32.5	149.77	477.96	0.092				
33	152.07	488.1	0.096				
33.5	154.38	496.25	0.099				
34	156.68	503.77	0.102				

Table B16: Beam-end test data for H7-20

H7-20							
Strand area, A_p = 0.294 in^2							
Load (Kips)	Stress (ksi)	Slip (mV)	Slip (in)	Load (Kips)	Stress (ksi)	Slip (mV)	Slip (in)
0	0	313.57	0.000	40	136.05	475.22	0.061
1	3.40	314.33	0.000	41	139.46	479.19	0.062
2	6.80	316	0.001	42	142.86	482	0.063
3	10.20	317.24	0.001	42.5	144.56	484.7	0.064
4	13.61	318.8	0.002	43	146.26	487.17	0.065
5	17.01	320.14	0.002	43.5	147.96	490	0.066
6	20.41	321.53	0.003	44	149.66	493	0.067
7	23.81	323.86	0.004	44.5	151.36	496.9	0.069
8	27.21	326	0.005	45	153.06	500	0.070
9	30.61	327.39	0.005	45.5	154.76	502.19	0.071
10	34.01	329.88	0.006	46	156.46	506	0.072
11	37.41	332.24	0.007	46.5	158.16	509.15	0.073
12	40.82	334.43	0.008	47	159.86	512.8	0.075
13	44.22	337.19	0.009	47.5	161.56	516.2	0.076
14	47.62	339.57	0.010	48	163.27	519.7	0.077
15	51.02	341.98	0.011	48.5	164.97	523.2	0.079
16	54.42	344.41	0.012	49	166.67	527	0.080
17	57.82	348.6	0.013	49.5	168.37	531.2	0.082
18	61.22	355	0.016	50	170.07	535.4	0.083
19	64.63	361.12	0.018	50.5	171.77	538.7	0.084
20	68.03	364.61	0.019	51	173.47	543.1	0.086
21	71.43	369.17	0.021	51.5	175.17	546.4	0.087
22	74.83	373.15	0.022	52	176.87	550.2	0.089
23	78.23	378.99	0.025	52.5	178.57	554.3	0.090
24	81.63	383.95	0.026	53	180.27	558.2	0.092
25	85.03	388.97	0.028	53.5	181.97	564.6	0.094
26	88.44	393.84	0.030	54	183.67	566.7	0.095
27	91.84	400.67	0.033	54.5	185.37	573.4	0.097
28	95.24	405.46	0.034	55	187.07	579.4	0.100
29	98.64	409.3	0.036	55.5	188.78	583.7	0.101
30	102.04	415.88	0.038	56	190.48	589.7	0.104
31	105.44	421.13	0.040	56.5	192.18	596.5	0.106
32	108.84	425.7	0.042	57	193.88	605.2	0.109
33	112.24	432.18	0.044	57.5	195.58	619.3	0.115
34	115.65	439.54	0.047				
35	119.05	445	0.049				
36	122.45	451.25	0.052				
37	125.85	457.97	0.054				
38	129.25	462.74	0.056				
39	132.65	469.29	0.058				

Table B17: Beam-end test data for H6-30

H6-30							
Strand area, A_p = 0.217 in^2							
Load (Kips)	Stress (ksi)	Slip (mV)	Slip (in)	Load (Kips)	Stress (ksi)	Slip (mV)	Slip (in)
0	0	293.21	0.000	36.5	168.20	576.5	0.106
1	4.61	274.84	-0.007	37	170.51	583.8	0.109
2	9.22	271.63	-0.008	37.5	172.81	588.6	0.111
3	13.82	270.88	-0.008	38	175.12	595.4	0.113
4	18.43	270.63	-0.008	38.5	177.42	600.4	0.115
5	23.04	270.65	-0.008	39	179.72	607.3	0.118
6	27.65	270.79	-0.008	39.5	182.03	616	0.121
7	32.26	272.54	-0.008	40	184.33	624	0.124
8	36.87	274.81	-0.007	40.5	186.64	631.3	0.127
9	41.47	278.81	-0.005	41	188.94	640.2	0.130
10	46.08	283	-0.004	41.5	191.24	648.4	0.133
11	50.69	286.41	-0.003	42	193.55	659.7	0.137
12	55.30	292.07	0.000	42.5	195.85	667.6	0.140
13	59.91	298.6	0.002	43	198.16	676.6	0.144
14	64.52	304.05	0.004	43.5	200.46	697.4	0.152
15	69.12	311.35	0.007	44	202.76	724.9	0.162
16	73.73	318.85	0.010	44.5	205.07	747.7	0.170
17	78.34	326.23	0.012	45	207.37	810	0.194
18	82.95	337.47	0.017	45.5	209.68	846.6	0.208
19	87.56	344.69	0.019				
20	92.17	357.3	0.024				
21	96.77	368.2	0.028				
22	101.38	379.49	0.032				
23	105.99	392.48	0.037				
24	110.60	405.43	0.042				
25	115.21	418	0.047				
26	119.82	429.26	0.051				
27	124.42	442.58	0.056				
28	129.03	456.24	0.061				
29	133.64	468.77	0.066				
30	138.25	480.39	0.070				
31	142.86	491.5	0.074				
32	147.47	506.7	0.080				
33	152.07	521.7	0.086				
33.5	154.38	528.5	0.088				
34	156.68	534.3	0.090				
34.5	158.99	542.7	0.094				
35	161.29	547.7	0.095				
35.5	163.59	556.8	0.099				
36	165.90	563.3	0.101				

Table B18: Beam-end test data for H7-30

H7-30							
Strand area, A_p = 0.294 in^2							
Load (Kips)	Stress (ksi)	Slip (mV)	Slip (in)	Load (Kips)	Stress (ksi)	Slip (mV)	Slip (in)
0	0	0.5224	0.000	56.5	192.18	0.9109	0.146
2	6.80	0.5265	0.002	57	193.88	0.9163	0.148
4	13.61	0.5335	0.004	57.5	195.58	0.9229	0.150
6	20.41	0.5396	0.006	58	197.28	0.9275	0.152
8	27.21	0.5446	0.008	58.5	198.98	0.9349	0.155
10	34.01	0.55	0.010	59	200.68	0.9416	0.157
12	40.82	0.5578	0.013	59.5	202.38	0.9475	0.159
14	47.62	0.5644	0.016	60	204.08	0.9569	0.163
16	54.42	0.5724	0.019	60.5	205.78	0.9605	0.164
18	61.22	0.5819	0.022	61	207.48	0.9666	0.167
20	68.03	0.5905	0.026	61.5	209.18	0.9725	0.169
22	74.83	0.6003	0.029	62	210.88	0.9796	0.171
24	81.63	0.6081	0.032	62.5	212.59	0.9864	0.174
26	88.44	0.6198	0.037	63	214.29	0.9978	0.178
28	95.24	0.6345	0.042	63.5	215.99	1.0015	0.180
30	102.04	0.649	0.047	64	217.69	1.0086	0.182
32	108.84	0.6639	0.053	64.5	219.39	1.0154	0.185
34	115.65	0.6792	0.059	65	221.09	1.0348	0.192
36	122.45	0.6951	0.065	65.5	222.79	1.0408	0.194
38	129.25	0.7116	0.071	66	224.49	1.046	0.196
40	136.05	0.7321	0.079	66.5	226.19	1.0575	0.201
41	139.46	0.747	0.084	67	227.89	1.0657	0.204
42	142.86	0.7559	0.088	67.5	229.59	1.0766	0.208
43	146.26	0.7672	0.092	68	231.29	1.08	0.209
44	149.66	0.7756	0.095				
45	153.06	0.7877	0.099				
46	156.46	0.7982	0.103				
47	159.86	0.8093	0.108				
48	163.27	0.8177	0.111				
49	166.67	0.8271	0.114				
50	170.07	0.8391	0.119				
51	173.47	0.8498	0.123				
52	176.87	0.8604	0.127				
52.5	178.57	0.8682	0.130				
53	180.27	0.8711	0.131				
53.5	181.97	0.8776	0.133				
54	183.67	0.8847	0.136				
54.5	185.37	0.8888	0.137				
55	187.07	0.8921	0.139				
55.5	188.78	0.899	0.141				
56	190.48	0.9061	0.144				

Appendix C Example Calculations From Section 6.3: NU-2000 girder:

Appendix C.1 General Information

Table C1 General input and properties for NU-2000 girder

General Input	
Overall Girder Length, L_{girder}	220 ft
Number of Girders in Typical Section, $n_{girders}$	11
Girder Spacing, s_{girder}	6 ft
Girder Properties	
Girder Section Height, h_{girder}	78.7 in
Girder Section Area, A_{girder}	903.8 in^2
Top Flange Width, $b_{topflange}$	48.2 in
Bottom Flange Width, $b_{bottomflange}$	38.4 in
CG of Section to Bottom of Girder, y_b	35.7 in
CG of Section to Bottom of Girder, $y_t = h_{girder} - y_b = 78.7 - 35.7$	43 in
Horizontal Axis Moment of Inertia, I_x	810590 in^4
Horizontal Axis Section Modulus Top Flange, $S_{x.t} = I_x/y_t$	18851 in^3
Horizontal Axis Section Modulus Bottom Flange, $S_{x.b} = I_x/y_b$	22706 in^3
Vertical Axis Moment of Inertia, I_y	61956 in^4
Vertical Axis Section Modulus Top Flange, $S_{y.t} = I_y/(\frac{b_{topflange}}{2})$	2571 in^3
Vertical Axis Section Modulus Bottom Flange, $S_{y.b} = I_y/(\frac{b_{bottomflange}}{2})$	3227 in^3
Torsional Constant, J_{girder}	7224 in^4
Material Properties	
Correction Factor for Modulus of Elasticity, K_1	1.00
Unit Weight of Unreinforced Girder Concrete, w_c	0.150 kcf
Unit Weight of Girder Concrete with Reinforcement, w_{girder}	0.155 kcf
Concrete Density Modification Factor, λ (LRFD 5.4.2.8)	1.00
Unit Weight of Girder, $w_{DC.girder} = \frac{A_{girder}}{w_{girder}}$	0.973 klf
Total Weight of Girder, $W_{girder} = w_{DC.girder} L_{girder}$	214 kips
Prestressing Properties	
Distance from Midspan to Strand Draping Harp Point, L_{harp} = 0.1 L_{girder}	22 ft
Harp Location (from girder end), $a_{harp} = \frac{L_{girder}}{2} - L_{harp}$	88 ft

Lateral Deflection (Sweep) Tolerance, $e_{i.tol} = \frac{L_{girder}}{10ft} \frac{1}{8} in$ = 2.75 in. Unless specified otherwise by the client, $e_{i.total}$ should be taken as one half of $e_{i.tol}$ for cases *lift1*, *lift1i* and *seat1*, and 1 inch plus $e_{i.tol}$ for all other cases. For as-built conditions, field measurements can be utilized.

Appendix C.2 Lifting from Bed – Vertical Cables

Table C2 Concrete and prestress properties

Concrete Properties	
Concrete Compressive Strength, $f_{c.lift1}$	15 ksi
Concrete Modulus of Elasticity, $E_{c.lift1} = 120000\ K_1\ w_c^2\ f_{c.lift1}^{0.33}$	6599 ksi
Modulus of Rupture, $f_{r.lift1} = \quad -0.24\ \lambda\ \sqrt{f_{c.lift1}}$	-0.930 ksi
Prestress Force	
Effective Prestress Force at Lifting, $P_{eff.lift1}$	3210 kips
CG of Strands at Midspan to Bottom of Girder, $y_{cgs.mid.lift1}$	5 in
Camber, $\Delta_{camb.lift1}$	8.250 in
Other Configuration Parameters	
Lift Connection Locations from End of Girder, a_{lift1}	25 ft
Rigid Extension Lift Connection above Top of Girder, y_{lift}	0.00 in
Lift Connection Tolerance from Centerline of Girder, e_{conn}	0.25 in
Other Loading Parameters	
Lateral Wind Force, $w_{wind.lift1}$	0.015 klf
Vertical Wind Uplift Considered Negligible for Lifting Impact Factor, IM_{lift1}	0.00
Unit Weight of Girder, $w_{DC.girder}$	0.973 klf
Effective Unit Weight of Girder, $w_{DC.girder.lift1} = w_{DC.girder}\ (1 + IM_{lift1})$	0.973 klf

Appendix C.2.1 Girder Eccentricities

Table C3 Girder eccentricities

Offset to centroid of a parabolically deflected girder from roll axis (used horizontally and vertically)	
Total Lateral Deflection over Girder Length, $e_{i.total.lift1}$	1.400 in (Assumed Parabolic)
Center of Mass Eccentricity Reduction Factor, $offset_{lift1}$: $L_{1.lift1} = L_{girder} - 2\,a_{lift1}$	168.00 ft
$Offset_{lift1} = \left(\frac{L_{1.lift1}}{L_{girder}}\right)^2 - \frac{1}{3}$ based on MAST 2, with generic variables	0.250
Center of mass eccentricity due to lateral deflection: $e_{i.lift1} = e_{i.total.lift1}\, Offset_{lift1}$	0.350 in
Distance from the Center of Mass of the Cambered Girder below Roll Axis, $y_{r.lift1} = y_t - offset_{lift1}\,\Delta_{camb.lift1} + y_{lift}$	39.470 in
Center of Mass Eccentricity Due to Wind Deflection, $z_{wind.lift1} = \frac{w_{wind.lift1}}{12\,E_{c.lift1}\,I_y\,L_{girder}}\left(\frac{L_{1.lift1}^5}{10} - a_{lift1}^2\,L_{1.lift1}^3 + 3\,a_{lift1}^4\,L_{1.lift1} + \frac{6}{5}\,a_{lift1}^5\right)$	0.250 in
Mid-Height of the Cambered Arc Below Roll Axis, $y_{w.lift1} = \frac{h_{girder}}{2} + y_{lift} - offset_{lift1}\,\Delta_{camber.lift1}$	35.820 in
Center of Mass Eccentricity Due to Girder Weight on Weak Axis, $z_{0.lift1} = \frac{w_{DC.girder.lift1}}{12\,E_{c.lift1}\,I_y\,L_{girder}}\left(\frac{L_{1.lift1}^5}{10} - a_{lift1}^2\,L_{1.lift1}^3 + 3\,a_{lift1}^4\,L_{1.lift1} + \frac{6}{5}\,a_{lift1}^5\right)$	16.232 in
Eccentricity of Girder Dead Load to Equilibrate Wind Load, $e_{wind.lift1} = \frac{w_{wind.lift1}\,y_{w.lift1}}{w_{DC.girder.lift1}}$	0.552 in

Table C4 Checking stresses during lifting from bed

Check Stresses	
Moment Due to Gravity Load, $M_{g.lift1}$ at $x = a_{harp}$ from girder end: $M_{g.lift1} = \frac{w_{DC.girder.lift1}\, L_{girder}}{2}\left(x - a_{lift1}\right) - \frac{w_{DC.girder.lift1}\, x^2}{2}$	34415 kip-in
Lateral Moment Due to Wind, $M_{wind.lift1}$ at $x = a_{harp}$ from girder end: $M_{wind.lift1} = \frac{w_{wind.lift1}\, L_{girder}}{2}\left(x - a_{lift1}\right) - \frac{w_{wind.lift1}\, x^2}{2}$	531 kip-in
Base Concrete Stresses in Girder before Rotation and Wind	
$f_{t.lift1.base} = P_{eff.lift1}\left(\frac{1}{A_{girder}} - \frac{y_b - y_{cgs.mid.lift1}}{S_{x.t}}\right) + \frac{M_{g.lift1}}{S_{x.t}}$	0.150 ksi
$f_{b.lift1.base} = P_{eff.lift1}\left(\frac{1}{A_{girder}} + \frac{y_b - y_{cgs.mid.lift1}}{S_{x.b}}\right) - \frac{M_{g.lift1}}{S_{x.b}}$	6.376 ksi
Check Compressive and Tensile Stresses at Equilibrium Rotation - Wind Right	
$\theta_{eq.lift1.wr} = \frac{\left(e_{i.lift1} + e_{conn} - z_{wind.lift1} + e_{wind.lift1}\right)}{y_{r.lift1} - z_{0.lift1}}$	0.039 rad
Check of Bottom Flange Tips - Wind Right	
$f_{b.lift1.wr.left} = f_{b.lift1.base} - \frac{M_{g.lift1}\ \theta_{eq.lift1.wr}}{S_{y.b}} + \frac{M_{wind.lift1}}{S_{y.b}}$	6.127 ksi
$f_{b.lift1.wr.right} = f_{b.lift1.base} + \frac{M_{g.lift1}\ \theta_{eq.lift1.wr}}{S_{y.b}} - \frac{M_{wind.lift1}}{S_{y.b}}$	6.626 ksi
$f_{b.ck.lift1.wr} = \text{Max}(f_{b.lift1.wr.left}, f_{b.lift1.wr.right})$	6.626 ksi
Check of Top Flange Tips - Wind Right	
$f_{t.lift1.wr.left} = f_{t.lift1.base} - \frac{M_{g.lift1}\ \theta_{eq.lift1.wr}}{S_{y.t}} + \frac{M_{wind.lift1}}{S_{y.t}}$	-0.163 ksi
$f_{t.lift1.wr.right} = f_{t.lift1.base} + \frac{M_{g.lift1}\ \theta_{eq.lift1.wr}}{S_{y.t}} - \frac{M_{wind.lift1}}{S_{y.t}}$	0.463 ksi
$f_{t.ck.lift1.wr} = \text{Min}(f_{t.lift1.wr.left}, f_{t.lift1.wr.right})$	-0.163 ksi
Check Compressive and Tensile Stress to Equilibrium Rotation - Wind Left	
$\theta_{eq.lift1.wl} = \frac{\left(e_{i.lift1} + e_{conn} + z_{wind.lift1} - e_{wind.lift1}\right)}{y_{r.lift1} - z_{0.lift1}}$	0.013 rad
Check of Bottom Flange Tips - Wind Left	
$f_{b.lift1.wl.left} = f_{b.lift1.base} - \frac{M_{g.lift1}\ \theta_{eq.lift1.wl}}{S_{y.b}} - \frac{M_{wind.lift1}}{S_{y.b}}$	6.075 ksi
$f_{b.lift1.wl.right} = f_{b.lift1.base} + \frac{M_{g.lift1}\ \theta_{eq.lift1.wl}}{S_{y.b}} + \frac{M_{wind.lift1}}{S_{y.b}}$	6.677 ksi
$f_{b.ck.lift1.wl} = \text{Max}(f_{b.lift1.wl.left}, f_{b.lift1.wl.right})$	6.677 ksi
Check of Top Flange Tips - Wind Left	
$f_{t.lift1.wl.left} = f_{t.lift1.base} - \frac{M_{g.lift1}\ \theta_{eq.lift1.wl}}{S_{y.t}} - \frac{M_{wind.lift1}}{S_{y.t}}$	-0.228 ksi
$f_{t.lift1.wl.right} = f_{t.lift1.base} + \frac{M_{g.lift1}\ \theta_{eq.lift1.wl}}{S_{y.t}} + \frac{M_{wind.lift1}}{S_{y.t}}$	0.528 ksi
$f_{t.ck.lift1.wl} = \text{Min}(f_{t.lift1.wl.left}, f_{t.lift1.wl.right})$	-0.228 ksi

Table C5 Checking allowable stresses during lifting from bed

Stresses	Critical	Allowable (LRFD 5.9.2.3.1a)	
Compressive	6.677 ksi	0.65 $f_{c.lift1}$= 0.65 (15ksi) = 9.75 ksi	**OK**
Tensile	-0.228 ksi	$f_{r.lift1}$ = -0.930 ksi	**OK**

Analysis assumes $e_{i.lift1}$ is due to form misalignment and not eccentric prestressing.

Table C6 Check factor of safety against cracking and failure during lifting from bed

Check Factor of Safety Against Cracking	
Base Concrete Stresses in Girder with Wind (Left Top Tip)	
$f_{t.lift1.wr} = f_{t.lift1.base} + \frac{M_{wind.lift1}}{S_{y.t}}$	0.356 ksi
$f_{t.lift1.wl} = f_{t.lift1.base} - \frac{M_{wind.lift1}}{S_{y.t}}$	-0.057 ksi
Lateral Moment to Cause Cracking	
Wind Right: $M_{lat.lift1.wr} = \left(f_{t.lift1.wr} - f_{r.lift1}\right) S_{y.t}$	275.4 kip-ft
Wind Left: $M_{lat.lift1.wl} = \left(f_{t.lift1.wl} - f_{r.lift1}\right) S_{y.t}$	187.0 kip-ft
Tilt Angle at Cracking due to Lateral Deflection	
Wind Right: $\theta_{cr.lift1.wr} = \frac{M_{lat.lift1.wr}}{M_{g.lift1}}$	0.096 rad
Wind Left: $\theta_{cr.lift1.wl} = \frac{M_{lat.lift1.wl}}{M_{g.lift1}}$	0.065 rad
Factor of Safety Against Cracking	
Wind Right: $FS_{cr.lift1.wr} = \frac{y_{r.lift1}\,\theta_{cr.lift1.wr}}{z_{0.lift1}\,\theta_{cr.lift1.wr} + e_{conn} - z_{wind.lift1} + e_{wind.lift1} + e_{i.lift1}}$	1.540
Wind Left: $FS_{cr.lift1.wl} = \frac{y_{r.lift1}\,\theta_{cr.lift1.wl}}{z_{0.lift1}\,\theta_{cr.lift1.wl} + e_{conn} + z_{wind.lift1} - e_{wind.lift1} + e_{i.lift1}}$	1.898
Critical Factor of Safety Against Cracking	
$FS_{cr.lift1} = \min(FS_{cr.lift1.wr}, FS_{cr.lift1.wl}) = 1.540 \geq 1.000$	**OK**
Check Factor of Safety Against Failure - Wind Right	
Rotation at Maximum Factor of Safety, $\theta_{max.ult.lift1.wr} = \sqrt{\frac{e_{i.lift1} + e_{conn} - z_{wind.lift1} + e_{wind.lift1}}{2.5\,z_{0.lift1}}}$	0.149 rad
$FS_{ult.lift1.wr}(\theta) = \frac{y_{r.lift1}\,\theta}{(z_{0.lift1}\,\theta - z_{wind.lift1})(1 + 2.5\theta) + e_{wind.lift1} + e_{conn} + e_{i.lift1}}$	1.425
Check Factor of Safety Against Failure - Wind Left	
Rotation at Maximum Factor of Safety: $\theta_{max.ult.lift1.wl} = \sqrt{\frac{e_{i.lift1} + e_{conn} + z_{wind.lift1} - e_{wind.lift1}}{2.5\,z_{0.lift1}}}$	0.086 rad
$FS_{ult.lift1.wl}(\theta) = \frac{y_{r.lift1}\,\theta}{\left(z_{0.lift1}\,\theta + z_{wind.lift1}\right)(1 + 2.5\theta) - e_{wind.lift1} + e_{conn} + e_{i.lift1}}$	1.658
Critical Factor of Safety Against Failure	
$FS_{ult.crit.lift1} = min(FS_{ult.lift1.wr}, FS_{ult.lift1.wl})$	1.425
Check Factor of Safety Against Failure for Critical Case	
$FS_{ult.lift1} = max(FS_{ult.crit.lift1}, FS_{cr.lift1}) = 1.540 \geq 1.500$	**OK**
Lateral Ultimate Moment Capacity Required, $M_{ult.y.lift1} = \frac{1.5}{FS_{ult.lift1}} \left(M_{g.lift1}\ \max\left(\theta_{max.ult.lift1.wr}\ ,\ \theta_{max.ult.lift1.wl}\right)\right)$	416 kip-ft

Appendix C.3 Seated on Dunnage

Table C7 Checking stresses during seated on dunnage

Check Stresses	
Moment Due to Gravity Load, $M_{g.seat1}$ at x = aharp from Girder End: $M_{g.seat1} = \frac{w_{DC.girder}\, L_{girder}}{2}(x - a_{seat1}) - \frac{w_{DC.girder}\, x^2}{2}$	54962 kip-in
Lateral Moment Due to Wind, $M_{wind.seat1}$ at $x = a_{harp}$ from Girder End: $M_{wind.seat1} = \frac{w_{wind.seat1}\, L_{girder}}{2}(x - a_{seat1}) - \frac{w_{wind.seat1}\, x^2}{2}$	3107 kip-in
Overturning Moment Due to Wind, $M_{ot.seat1} = L_{girder}\, w_{wind.seat1}\, y_{mid.seat1}$	563 kip-in
Concrete Stresses in Girder	
$f_{t.seat1} = P_{eff.seat1}\left(\frac{1}{A_{girder}} - \frac{y_b - y_{cgs.mid.seat1}}{S_{x.t}}\right) + \frac{M_{g.seat1}}{S_{x.t}} - \frac{M_{wind.seat1}}{S_{y.t}}$	0.031 ksi
$f_{b.seat1} = P_{eff.seat1}\left(\frac{1}{A_{girder}} + \frac{y_b - y_{cgs.mid.seat1}}{S_{x.b}}\right) - \frac{M_{g.seat1}}{S_{x.b}} + \frac{M_{wind.seat1}}{S_{y.b}}$	6.434 ksi
$\theta_{eq.seat1} = \frac{K_{\theta.seat}\, \alpha_{seat1} + W_{girder}(z_{wind.seat1} + e_{i.seat1} + e_{brg.seat1}) + M_{ot.seat1}}{K_{\theta.seat1} - W_{girder}(y_{r.seat1} + z_{0.seat1})}$	0.031 rad
$f_{eq.t.seat1} = f_{t.seat1} - \frac{M_{g.seat1}\, \theta_{eq.seat1}}{S_{y.t}}$	-0.642 ksi
$f_{eq.b.seat1} = f_{b.seat1} + \frac{M_{g.seat\,1}\, \theta_{eq.seat1}}{S_{y.b}}$	6.970 ksi

Table C8 Checking allowable stresses during seated on dunnage

Stresses	Critical	Allowable (LRFD 5.9.2.3.1a)	
Compressive	6.970 ksi	0.65 $f_{c.lift1}$= 0.65 (15ksi) = 9.75 ksi	**OK**
Tensile	-0.642 ksi	$f_{r.lift1}$ = -0.930 ksi	**OK**

Table C9 Check factor of safety against cracking, failure, and rollover during seated on dunnage

Check Factor of Safety Against Cracking	
Lateral Moment to Cause Cracking : $M_{lat.seat1} = (f_{t.seat1} - f_{r.seat1})S_{y.t}$	563 kip-in
Tilt Angle at Cracking due to Lateral Deflection, $\theta_{cr.seat1} = \frac{M_{lat.seat1}}{M_{g.seat1}}$	0.045 rad
$FS_{cr.seat1} = \frac{K_{\theta.seat1}(\theta_{cr.seat1} - \alpha_{seat1})}{W_{girder}[(y_{r.seat1}+z_{0.seat1})\theta_{cr.seat1}+z_{wind.seat1} + e_{i.seat1} + e_{brg.seat1}]+ M_{ot.seat1}}$	1.342
$FS_{cr.seat1} = 1.342 \geq 1.000$	**OK**
Check Factor of Safety Against Failure	
$FS_{ult.seat1} = \frac{K_{\theta.seat1}(\theta-\alpha_{seat1})}{W_{girder}[(z_{0.seat1}\theta+z_{wind.seat1})(1+2.5\theta)+y_{r.seat1}\theta+e_{i.seat1}+e_{brg.seat1}]+M_{ot.seat1}}$	2.336
Solution for Maximum Factor of Safety, $\theta_{max.ult.seat}$	$0.253 \leq 0.4$ rad
Check Factor of Safety Against Failure for Critical Case	
$FS_{ult.seat1} = max(FS_{ult.seat1}, FS_{cr.seat1}) = 2.336 \geq 1.500$	**OK**
Check Factor of Safety Against Rollover (Cracked)	
Horizontal Distance from Roll Axis to Edge of Girder, $z_{max.seat1} = \frac{W_{brg.seat1}}{2}$	18 in
Overturning Moment from Wind, $M_{roll.seat1} = L_{girder}\, w_{wind.seat1}\, h_{roll.seat1}$	24.2 kip-in
Tilt Angle at Maximum Resisting Moment Arm, $\theta_{max.p.seat1} = \frac{W_{girder}(z_{max.seat1} - y_{r.seat1}\,\alpha_{seat1} - e_{brg.seat1})+ M_{roll.seat1}}{K_{\theta.seat1}} + \alpha_{seat1}$	0.059 rad
Corresponding Center of Mass Eccentricity due to Tilt Angle, $z_{0.p.seat1} = z_{0.seat1}(1 + 2.5\theta_{max.p.seat1})$	55.767 in
$FS_{roll.seat1} = \frac{K_{\theta.seat1}(\theta_{max.p.seat1} - \alpha_{seat1})}{W_{girder}[(z_{0.p.seat1}+y_{r.seat1})\theta_{max.p.seat1}+z_{wind.seat1}(1+2.5\,\theta_{max.p.seat1})+e_{brg.seat1}+e_{i.seat1}]+M_{rollt.seat1}}$	1.524
$FS_{roll.seat1} = 1.524 \geq 1.500$	**OK**
Overturning Moment to be Resisted by Bracing (Service), if needed: $M_{ot.seat1.brace} = \frac{W_{girder}[z_{0.p.seat1}\,\theta_{max.p.seat1}+ y_{r.seat1}\theta_{max.p.seat1}+e_{i.seat1}+e_{brg.seat1}]+M_{ot.seat1}}{2}$	43.6 kip-ft
Concurrent Lateral Force (Service): $F_{ot.seat1.brace} = \frac{L_{girder}\, w_{wind.seat1}}{2}$	6.050 kip, for each brace

Appendix C.4 Seated on Transport

Table C10 Checking stresses during seated on transport

Concrete Properties	
Concrete Compressive Strength, $f_{c.lift1}$	18 ksi
Concrete Modulus of Elasticity, $E_{c.lift1} = \quad 120000\ K_1\ w_c^2\ f_{c.lift1}^{0.33}$	7008 ksi
Modulus of Rupture, $f_{r.lift1} = \quad -0.24\ \lambda \sqrt{f_{c.lift1}}$	-1.018 ksi
Prestress Force	
Effective Prestress Force at Lifting, $P_{eff.lift1}$	2946 kips
CG of Strands at Midspan to Bottom of Girder, $y_{cgs.mid.lift1}$	5 in
Camber, $\Delta_{camb.lift1}$	9.380 in
Check Stresses	
Total Lateral Moment, $M_{total.trans} = \quad M_{wind.trans}$	2889 kip-in
Overturning Moment Due to Wind and $M_{ot.trans} = L_{girder}\ (\ w_{wind.trans}\ y_{wind.trans})$	672 kip-in
Concrete Stresses in Girder	
$f_{t.trans} = \quad P_{eff.trans}\left(\frac{1}{A_{girder}} - \frac{y_b - y_{cgs.mid.trans}}{S_{x.t}}\right) + \frac{M_{g.trans}}{S_{x.t}} - \frac{M_{total.trans}}{S_{y.t}}$	0.049 ksi
$f_{b.trans} = \quad P_{eff.trans}\left(\frac{1}{A_{girder}} + \frac{y_b - y_{cgs.mid.trans}}{S_{x.b}}\right) - \frac{M_{g.trans}}{S_{x.b}} + \frac{M_{total.trans}}{S_{y.b}}$	5.887 ksi
$\theta_{eq.trans} = \frac{K_{\theta.trans}\,\alpha_{trans} + W_{girder.trans}(z_{total.trans} + e_{i.trans}) + M_{ot.trans}}{K_{\theta.trans} - W_{girder.trans}(y_{r.trans} + z_{0.trans})}$	0.053 rad
$f_{eq.t.trans} = \quad f_{t.trans} - \frac{M_{g.trans}\ \theta_{eq.trans}}{S_{y.t}}$	-1.015 ksi
$f_{eq.b.trans} = \quad f_{b.trans} + \frac{M_{g.trans}\ \theta_{eq.trans}}{S_{y.b}}$	6.735 ksi

Table C11 Checking allowable stresses during seated on transport

Stresses	Critical	Allowable (LRFD 5.9.2.3.1a)	
Compressive	6.735 ksi	0.60 $f_{c.lift1}$ = 0.65 (18ksi) = 10.80 ksi	**OK**
Tensile	-1.015 ksi	$f_{r.lift1}$ = -1.018 ksi	**OK**

Table C12 Check factor of safety against cracking, failure, and rollover during seated on transport

Check Factor of Safety Against Cracking	
Lateral Moment to Cause Cracking, $M_{lat.trans} = (f_{t.trans} - f_{r.trans})S_{y.t}$	228.7 kip-ft
Tilt Angle at Cracking due to Lateral Deflection, $\theta_{cr.trans} = \frac{M_{lat.trans}}{M_{g.trans}}$	0.054 rad
$FS_{cr.trans} = \frac{K_{\theta.trans}(\theta_{cr.trans} - \alpha_{trans})}{W_{girder.trans}[(y_{r.trans}+z_{0.trans})\theta_{cr.trans}+z_{total.trans}+e_{i.trans}]+M_{ot.trans}}$	1.004
Critical Factor of Safety Against Cracking: $FS_{cr.trans} = 1.004 \geq 1.000$	**OK**
Check Factor of Safety Against Failure	
$FS_{ult.trans}(\theta) = \frac{K_{\theta.trans}(\theta - \alpha_{trans})}{W_{girder.trans}[(z_{0.trans}\theta+z_{total.trans})(1+2.5\theta)+y_{r.trans}\theta+e_{i.trans}]+M_{ot.trans}}$	2.371
Solution for Maximum Factor of Safety, $\theta_{max.ult.seat}$	$0.342 \leq 0.4$ rad
$FS_{ult.trans} = max(FS_{ult.trans}, FS_{cr.trans}) = 2.371 \geq 1.500$	**OK**
Check Factor of Safety Against Rollover (Cracked)	
Overturning Moment from Wind and CE, $M_{roll.trans} = L_{girder}(w_{wind.trans} + CE_{trans})(h_{roll.trans} + z_{max.trans}\alpha_{trans})$	590 kip-in
Tilt Angle at Maximum Resisting Moment Arm, $\theta_{max.p.trans} = \frac{W_{girder.trans}(z_{max.trans} - h_{roll.trans}\alpha_{trans})+M_{roll.trans}}{K_{\theta.trans}} + \alpha_{trans}$	0.11865 rad
Corresponding Center of Mass Eccentricity due to Tilt Angle, $z_{0.p.trans} = z_{0.trans}(1 + 2.5\theta_{max.p.trans})$	49.939 in
$FS_{roll.trans} = \frac{K_{\theta.trans}(\theta_{max.p.trans} - \alpha_{trans})}{W_{girder.trans}[(z_{0.p.trans}+y_{r.trans})\theta_{max.p.trans}+z_{total.trans}(1+2.5\theta_{max.p.trans})+e_{i.trans}]+M_{ot.trans}}$	1.823
$FS_{roll.trans} = 1.823 \geq 1.500$	**OK**

Appendix C.5 Lift in Field

Table C13 Checking stresses during lift in field

Check stresses	
Moment Due to Gravity Load at $x = a_{harp}$ from girder end: $M_{g.lift2} = \frac{w_{DC.girder.lift2}\, L_{girder}}{2}\left(x - a_{lift2}\right) - \frac{w_{DC.girder.lift2}\, x^2}{2}$	34415 kip-in
Lateral Moment Due to Wind at $x = a_{harp}$ from girder end: $M_{wind.lift2} = \frac{w_{wind.lift2}\, L_{girder}}{2}\left(x - a_{lift2}\right) - \frac{w_{wind.lift2}\, x^2}{2}$	531 kip-in
Base Concrete Stresses in Girder before Rotation and Wind	
$f_{t.lift2.base} = P_{eff.lift2}\left(\frac{1}{A_{girder}} - \frac{y_b - y_{cgs.mid.lift2}}{S_{x.t}}\right) + \frac{M_{g.lift2}}{S_{x.t}}$	0.287 ksi
$f_{b.lift2.base} = P_{eff.lift2}\left(\frac{1}{A_{girder}} + \frac{y_b - y_{cgs.mid.lift2}}{S_{x.b}}\right) - \frac{M_{g.lift2}}{S_{x.b}}$	5.727 ksi
Check Compressive and Tensile Stresses at Equilibrium Rotation - Wind Right $\theta_{eq.lift2.wr} = \frac{\left(e_{i.lift2} + e_{conn} - z_{wind.lift2} + e_{wind.lift2}\right)}{y_{r.lift2} - z_{0.lift2}}$	0.051 rad
Check of Bottom Flange Tips - Wind Right	
$f_{b.lift2.wr.left} = f_{b.lift2.base} - \frac{M_{g.lift2}\,\theta_{eq.lift2.wr}}{S_{y.b}} + \frac{M_{wind.lift2}}{S_{y.b}}$	5.342 ksi
$f_{b.lift2.wr.right} = f_{b.lift2.base} + \frac{M_{g.lift2}\,\theta_{eq.lift2.wr}}{S_{y.b}} - \frac{M_{wind.lift2}}{S_{y.b}}$	6.112 ksi
$f_{b.ck.lift2.wr} =$ Max($f_{b.lift2.wr.left}$, $f_{b.lift2.wr.right}$)	6.112 ksi
Check of Top Flange Tips - Wind Right	
$f_{t.lift2.wr.left} = f_{t.lift2.base} - \frac{M_{g.lift2}\,\theta_{eq.lift2.wr}}{S_{y.t}} + \frac{M_{wind.lift2}}{S_{y.t}}$	-0.196 ksi
$f_{t.lift2.wr.right} = f_{t.lift2.base} + \frac{M_{g.lift2}\,\theta_{eq.lift2.wr}}{S_{y.t}} - \frac{M_{wind.lift2}}{S_{y.t}}$	0.771 ksi
$f_{t.ck.lift2.wr} =$ Min($f_{t.lift2.wr.left}$, $f_{t.lift2.wr.right}$)	-0.163 ksi
Check Compressive and Tensile Stresses at Equilibrium Rotation - Wind Left $\theta_{eq.lift2.wl} = \frac{\left(e_{i.lift2} + e_{conn} + z_{wind.lift2} - e_{wind.lift2}\right)}{y_{r.lift2} - z_{0.lift2}}$	0.025 rad
Check of Bottom Flange Tips - Wind Left	
$f_{b.lift2.wl.left} = f_{b.lift2.base} - \frac{M_{g.lift2}\,\theta_{eq.lift2.wl}}{S_{y.b}} - \frac{M_{wind.lift2}}{S_{y.b}}$	5.293 ksi
$f_{b.lift2.wl.right} = f_{b.lift2.base} + \frac{M_{g.lift2}\,\theta_{eq.lift2.wl}}{S_{y.b}} + \frac{M_{wind.lift2}}{S_{y.b}}$	6.161 ksi
$f_{b.ck.lift2.wl} =$ Max($f_{b.lift2.wl.left}$, $f_{b.lift2.wl.right}$)	6.161 ksi
Check of Top Flange Tips - Wind Left	
$f_{t.lift2.wl.left} = f_{t.lift2.base} - \frac{M_{g.lift2}\,\theta_{eq.lift2.wl}}{S_{y.t}} - \frac{M_{wind.lift2}}{S_{y.t}}$	-0.257 ksi
$f_{t.lift2.wl.right} = f_{t.lift2.base} + \frac{M_{g.lift2}\,\theta_{eq.lift2.wl}}{S_{y.t}} + \frac{M_{wind.lift2}}{S_{y.t}}$	0.832 ksi
$f_{t.ck.lift2.wl} =$ Min($f_{t.lift2.wl.left}$, $f_{t.lift2.wl.right}$)	-0.257 ksi

Table C14 Checking allowable stresses during lift in field

Stresses	Critical	Allowable (LRFD 5.9.2.3.1a)	
Compressive	6.161 ksi	0.60 $f_{c.lift1}$= 0.60 (18 ksi) = 10.80 ksi	**OK**
Tensile	-0.257 ksi	$f_{r.lift1}$ = -1.018 ksi	**OK**

Analysis assumes $e_{i.lift2}$ is due to form misalignment and not eccentric prestressing. Base Concrete Stresses in Girder with Wind (Left Top Tip).

Table C15 Check factor of safety during lift in field

Check Factor of Safety Against Cracking	
Base Concrete Stresses in Girder with Wind (Left Top Tip)	
$f_{t.lift2.wr} = f_{t.lift2.base} + \frac{M_{wind.lift2}}{S_{y.t}}$	0.494 ksi
$f_{t.lift2.wl} = f_{t.lift2.base} - \frac{M_{wind.lift2}}{S_{y.t}}$	0.081 ksi
Lateral Moment to Cause Cracking:	
Wind Right : $M_{lat.lift2.wr} = (f_{t.lift2.wr} - f_{r.lift2})S_{y.t}$	323.9 kip-ft
Wind Left : $M_{lat.lift2.wl} = (f_{t.lift2.wl} - f_{r.lift2})S_{y.t}$	235.5 kip-ft
Tilt Angle at Cracking due to Lateral Deflection	
Wind Right: $\theta_{cr.lift2.wr} = \frac{M_{lat.lift2.wr}}{M_{g.lift2}}$	0.113 rad
Wind Left : $\theta_{cr.lift2.wl} = \frac{M_{lat.lift2.wl}}{M_{g.lift2}}$	0.082 rad
Factor of Safety Against Cracking:	
Wind Right : $FS_{cr.lift2.wr} = \frac{y_{r.lift2}\,\theta_{cr.lift2.wr}}{z_{0.lift2}\,\theta_{cr.lift2.wr} + e_{conn} - z_{wind.lift2} + e_{wind.lift2} + e_{i.lift2}}$	1.506
Wind Left: $FS_{cr.lift2.wl} = \frac{y_{r.lift2}\,\theta_{cr.lift2.wl}}{z_{0.lift2}\,\theta_{cr.lift2.wl} + e_{conn} + z_{wind.lift2} - e_{wind.lift2} + e_{i.lift2}}$	1.748
$FS_{cr.lift2} = \min(FS_{cr.lift2.wr}, FS_{cr.lift2.wl})$ = 1.506 ≥ 1.000	**OK**
Check Factor of Safety Against Failure - Wind Right	
Rotation at Maximum Factor of Safety: $\theta_{max.ult.lift2.wr} = \sqrt{\frac{e_{i.lift2} + e_{conn} - z_{wind.lift2} + e_{wind.lift2}}{2.5\,z_{0.lift2}}}$	0.183 rad
$FS_{ult.lift2.wr} = \frac{y_{r.lift2}\,\theta}{(z_{0.lift2}\,\theta - z_{wind.lift2})(1+2.5\theta) + e_{wind.lift2} + e_{conn} + e_{i.lift2}}$	1.396
Check Factor of Safety Against Failure - Wind Left	
Rotation at Maximum Factor of Safety: $\theta_{max.ult.lift2.wl} = \sqrt{\frac{e_{i.lift2} + e_{conn} + z_{wind.lift2} - e_{wind.lift2}}{2.5\,z_{0.lift2}}}$	0.128 rad
$FS_{ult.lift2.wl} = \frac{y_{r.lift2}\,\theta}{(z_{0.lift2}\,\theta + z_{wind.lift2})(1+2.5\theta) - e_{wind.lift2} + e_{conn} + e_{i.lift2}}$	1.560
$FS_{ult.crit.lift2} = min(FS_{ult.lift2.wr}, FS_{ult.lift2.wl})$	1.396
$FS_{ult.lift2} = \max(FS_{ult.crit.lift2}, FS_{cr.lift2})$ = 1.506 ≥ 1.500	**OK**
Lateral Ultimate Moment Capacity Required: $M_{ult.y.lift2} = \frac{1.5}{FS_{ult.lift2}} (M_{g.lift2}\ \max(\theta_{max.ult.lift2.wr}, \theta_{max.ult.lift2.wl}))$	522 kip-ft

Appendix C.6 First Girder Seated on Bearings

Table C16 Checking stresses during seated on bearings

Check Stresses	
Moment Due to Gravity Load at $x = a_{harp}$ from girder end: $M_{g.seat2} = \frac{w_{DC.girder} L_{girder}}{2} (x - a_{seat2}) - \frac{w_{DC.girder} x^2}{2}$	67161 kip-in
Lateral Moment Due to Wind at $x = a_{harp}$ from girder end: $M_{wind.seat2} = \frac{w_{wind.seat2} L_{girder}}{2} (x - a_{seat2}) - \frac{w_{wind.seat2} x^2}{2}$	1036 kip-in
Overturning Moment Due to Wind, $M_{ot.seat2} = L_{girder}\, w_{wind.seat2}\, y_{mid.seat2}$	149 kip-in
Concrete Stresses in Girder	
$f_{t.seat2} = P_{eff.seat2} \left(\frac{1}{A_{girder}} - \frac{y_b - y_{cgs.mid.seat2}}{S_{x.t}}\right) + \frac{M_{g.seat2}}{S_{x.t}} - \frac{M_{wind.seat2}}{S_{y.t}}$	1.622 ksi
$f_{b.seat2} = P_{eff.seat2} \left(\frac{1}{A_{girder}} + \frac{y_b - y_{cgs.mid.seat2}}{S_{x.b}}\right) - \frac{M_{g.seat2}}{S_{x.b}} + \frac{M_{wind.seat2}}{S_{y.b}}$	4.606 ksi
$\theta_{eq.seat2} = \frac{K_{\theta.seat2}\, \alpha_{seat2} + W_{girder}(z_{wind.seat2} + e_{i.seat2} + e_{brg.seat2}) + M_{ot.seat2}}{K_{\theta.seat2} - W_{girder}(y_{r.seat2} + z_{0.seat2})}$	0.023 rad
$f_{eq.t.seat2} = f_{t.seat2} - \frac{M_{g.seat2}\, \theta_{eq.seat2}}{S_{y.t}}$	1.011 ksi
$f_{eq.b.seat2} = f_{b.seat2} + \frac{M_{g.seat2}\, \theta_{eq.seat2}}{S_{y.b}}$	5.093 ksi

Table C17 Checking allowable stresses during seated on bearings

Stresses	Critical	Allowable (LRFD 5.9.2.3.1a)	
Compressive	5.093 ksi	0.60 $f_{c.lift1}$= 0.60 (18ksi) = 10.80 ksi	**OK**
Tensile	1.011 ksi	$f_{r.lift1}$ = -1.018 ksi	**OK**

Table C18 Check factor of safety against cracking, failure, and rollover during seated on bearings

Check Factor of Safety Against Cracking	
Lateral Moment to Cause Cracking: $M_{lat.seat2} = (f_{t.seat2} - f_{r.seat2})S_{y.t}$	565.6 kip-ft
Tilt Angle at Cracking due to Lateral Deflection: $\theta_{cr.seat2} = \frac{M_{lat.seat2}}{M_{g.seat2}}$	0.10105 rad
$FS_{cr.seat2} = \frac{K_{\theta.seat2}\,(\theta_{cr.seat2} - \alpha_{seat2})}{W_{girder}\,[(y_{r.seat2}+z_{0.seat2})\,\theta_{cr.seat2}+z_{wind.seat2} + e_{i.seat2}+ e_{brg.seat2}\,]+ M_{ot.seat2}}$	2.267
$FS_{cr.seat2}$ = 2.267 ≥ 1.000	**OK**
Check Factor of Safety Against Failure	
$FS_{ult.seat2}(\theta) = \frac{K_{\theta.seat2}\,(\theta - \alpha_{seat2})}{W_{girder}[\,(z_{0.seat2}\,\theta+z_{wind.seat2})(1+2.5\theta)+ y_{r.seat2}\theta+e_{i.seat2} + e_{brg.seat2}]+ M_{ot.seat2}}$	2.083
Solution for Maximum Factor of Safety, $\theta_{max.ult.seat}$	0.166 ≤ 0.4 rad
$FS_{ult.seat2} = max(FS_{ult.seat2}, FS_{cr.seat2})$ = 2.267 ≥ 1.500	**OK**
Check Factor of Safety Against Rollover (Cracked)	
Horizontal Distance from Roll Axis to Kern Point of Pad, $z_{max.seat2} = \frac{W_{brg.seat2}}{6}$	6 in
Overturning Moment from Wind, $M_{roll.seat2} = L_{girder}\,w_{wind.seat2}\,h_{roll.seat2}$	6 kip-in
Tilt Angle at Maximum Resisting Moment Arm: $\theta_{max.p.seat2} = \frac{W_{girder}(z_{max.seat2} - h_{roll.seat2}\,\alpha_{seat2} - e_{brg.seat2})+ M_{roll.seat2}}{K_{\theta.seat2}} + \alpha_{seat2}$	0.020 rad
Corresponding Center of Mass Eccentricity due to Tilt Angle: $z_{0.p.seat2} = z_{0.seat2}\,(1 + 2.5\theta_{max.p.seat2})$	77.525 in
$FS_{roll.seat2} = \frac{K_{\theta.seat2}\,(\theta_{max.p.seat2} - \alpha_{seat2})}{W_{girder}[\,(z_{0.p.seat2}+y_{r.seat2})\theta_{max.p.seat2}+ z_{wind.seat2}(1+2.5\theta_{max.p.seat2})+ e_{i.seat2}+e_{brg.seat2}]+M_{roll.seat2}}$	0.933
$FS_{roll.seat2}$ = 0.933 < 1.500	**N.G.; Add end bracing**
Overturning Moment to be Resisted by Bracing (Service), if needed: $M_{ot.seat2.brace} = \frac{W_{girder}[\,z_{0.p.seat2}\,\theta_{max.p.seat2}+ y_{r.seat2}\theta_{max.p.seat2}+e_{i.seat2}+e_{brg.seat2}]+M_{ot.seat2}}{2}$	43.6 kip-ft for each brace
Concurrent Lateral Force (Service): $F_{ot.seat2.brace} = \frac{L_{girder}\,w_{wind.seat2}}{2}$	1.650 kip for each brace

Bibliography

AASHTO (2017a). *AASHTO LRFD Bridge Design Specifications 8th Edition*, American Association of State Highway and Transportation Officials, Washington, DC.

AASHTO (2017b). *AASHTO LRFD Bridge Construction Specifications 4th Edition*, American Association of State Highway and Transportation Officials, Washington, DC.

AASHTO M 195 (2011). *Standard Specification for Lightweight Aggregates for Structural Concrete*, American Association of State Highway and Transportation Officials, Washington, DC.

Abaqus (2011). Abaqus Analysis User's Manual, Volume III: Materials. 22.6.1-2 pp.

ACI 408.3R-12 (2012). *Splice and Development Length of High Relative Rib Area Reinforcing Bars in Tension*, American Concrete Institute.

ACI Committee 318 (1963). *Building Code Requirements for Reinforced Concrete* (ACI 318R-63), American Concrete Institute, Farmington Hills, Michigan.

ACI Committee 318 (2014). *Building Code Requirements for Reinforced Concrete* (ACI 318-14), American Concrete Institute, Farmington Hills, Michigan.

ACI Committee 408 (2012). *ACI 408.R-03 Bond and Development of Straight Reinforcing Bars in Tension*, American Concrete Institute.

ASTM A1061 / A1061M-20ae1 (2020). *Standard Test Methods for Testing Multi-Wire Steel Prestressing Strand*, ASTM International, West Conshohocken, PA, 2020, www.astm.org.

ASTM A416-06 (2006). *Standard Specification for Steel Strand, Uncoated Seven-Wire for Prestressed Concrete*, ASTM International.

ASTM A944-10 (2010). *Standard Test Method for Comparing Bond Strength of Steel Reinforcing Bars for Concrete Using Beam-End Specimens*, ASTM International.

ASTM C567 / C567M-19 (2019). *Standard Test Method for Determining Density of Structural Lightweight Concrete*, ASTM International, West Conshohocken, PA, 2019, www.astm.org.

Ball, P.D. (2019). *The Use of 0.7-in. Prestressed Strand in Various Bridge Girder Types*, MS Thesis, university of Cincinnati. 80 pp.

Bischoff, P. H. (2003). Tension stiffening and cracking of steel fiber reinforced concrete. *Journal of Materials in Civil Engineering, 15*(2), 174–182 pp.

Briere, V., Harries, K.A., Kasan, J. and Hager, C. (2013). *Dilation Behavior of Seven-Wire Prestressing Strand – The Hoyer Effect*, Construction and Building Materials, *Vol 40*, 650-658 pp.

BSI (2014). *Eurocode 2: Design of Concrete Structures*, British Standards Institution, BS EN 1992-1-1:2004 + A1:2014, London.

Chen, Wai-Fah and Duan, Lian (2014). *Bridge Engineering Handbook: Superstructure Design 2nd edition*, 3 pp.

FHWA (1988). *Federal Highway Administration*, Memorandum dated October 26, 1988.

FHWA (2015). *Engineering for Structural Stability in Bridge Construction*, Federal Highway Administration, Report No. FHWA-NHI-15-044, Washington, DC, 7.46-7.47 pp.

Girgis, A.F. and Tuan, C.Y. (2004). *Bond Strength of Self-Consolidating Concrete for Prestressed Concrete Applications*, NDOR Project Number SPR-P1(04) P571, 14 pp.

Greene, G.G. and Graybeal, B.A. (2019). *Lightweight Concrete: Transfer and Development Length of Prestressing Strands*, FHWA-HIF-19-018.

Hoyer, E. (1939). *Der Stahlsaitenbeton [piano-string-concrete]*, Otto Elsner, Berlin, 136 pp. [in German].

Hoyer, E., and Friedrich, E. (1939). *Beitrag zur Frage der Haftspannung in Eisenbetonbauteilen [Contribution to the issue of detention of iron stress in concrete structures]*, Beton und Eisen, *Vol 38*, No. 6, 107-110 pp. [in German].

Hsu, L.S., and Hsu, C.-T.T. (1994). *Complete stress-strain behaviour of high-strength concrete under compression*, Magazine of Concrete Research, *46*(169), 301-312 pp.

Jiang, X. (2013). *Bond Performance of High-Capacity Strands in High Strength Concrete*, PhD diss, University of Tennessee, 61 pp.

Joh,O., Goto, Y. (2000). *Anchorage behavior of 90-degree hooked beam bars in reinforced concrete knee joints*. Division of Social and Geotechnical Engineering Graduate School of Engineering, Hokkaido University, Japan.

Kupfer, H. B., and K. H. Gerstle (1973). Behavior of Concrete under Biaxial Stresses, *Journal of Engineering Mechanics Division*, ASCE, *vol. 99 853*, 1973.

Lane, S.N. (1998). *A New Development Length Equation for Pretensioning Strands in Bridge Beams and Piles*, FHWA RD *98-116*, 123 pp.

Machida S, and Durelli AJ. (1973). Response of a strand to axial and torsional displacements, *Journal of Mechanical Engineering Science, Vol. 15*, No. 4, 241-251 pp.

Martin, L.D. and Pellow, Donald L. (1983). Low-Relaxation Strand Practical Applications in Precast Prestressed Concrete, *PCI Journal*.

Mast, R.F. (1993). Lateral Stability of Long Prestressed Concrete Beams—Part 2, *PCI Journal*, Precast/Prestressed Concrete Institute, Chicago, IL, *V. 38*, No. 1, (January-February), 70-88 pp.

Morcous, G. (2013). *Implementation of 0.7-in. Diameter Strands in Prestressed Concrete Girders*, Nebraska Department of Roads, Project SPR-P1(13) M333, Lincoln, NE, 32 pp.

Morcous, G., Assad, S., Hatami, A., and Tadros, M.K. (2014). Implementation of 0.7-in. Diameter Strands at 2.0 x 2.0 in. Spacing in Pretensioned Bridge Girder, *PCI Journal*, *59*(3), 145-158 pp.

National Academies of Sciences, Engineering, and Medicine (2008). *NCHRP Report 596 Rotation Limits for Elastomeric Bearings*, Washington, DC: The National Academies Press. https://doi.org/10.17226/23131.

Nayal, R., and Rasheed, H.A. (2006). Tension Stiffening Model for Concrete Beams Reinforced with Steel and FRP Bars, *Journal of Materials in Civil Engineering*, *18*(6), 831-841 pp.

Oh, B.H., Kim, E.S., and and Choi, Y.C. (2006). Theoretical Analysis of Transfer Lengths in Pretensioned Prestressed Concrete Members, *ASCE Journal of Engineering Mechanics*, *Vol. 132*, No. 10, 1057-1066 pp.

PCI (2015). *Lateral Stability of Precast, Prestressed Concrete Bridge Girders,* Precast/Prestressed Concrete Institute, Chicago, IL

PCI (2019). *Girder Stability Analysis v1.0, Excel Spreadsheet*, Precast/Prestressed Concrete Institute.te, Chicago, IL

Ramirez, J.A. and Russell, B.W. (2008). *Transfer, Development, and Splice Length for Strand/Reinforcement in High-Strength Concrete*, NCHRP Report 603, 1-2 pp.

Rehm, G., (1961). *Uber die Grundlagen des Verbundes zwischen Stahl und Beton* [On the basics of bond between steel and concrete], Deutscher Ausschuss für Stahlbeton, Heft 138, Berlin, 59 pp.

Salmons, J.R. and McCrate, T.E. (1973). *Bond of Untensioned Prestress Strand*, Study Number 72-2, Missouri State Highway Department. 121 pp.

Shahawy, M. (1999). *Critical Evaluation of The Design Code Requirements for Development Length of Prestressing Tendons*, FLDot Report.

Shahrooz B.M., Miller R.A., Harries K.A., Castrodale R.W. (2018). *Interim Report 2, Use of 0.7-in. Diameter Strands in Precast Pretensioned Girders,* NCHRP Report 12-109 (revised March 9, 2018).

Shahrooz, B.M., Miller, R.A., Harries, K.A., Yu, Q. and Russell, H.G. (2017). *Strand Debonding in Pretensioned Girders*, NCHRP Report 849, Transportation Research Board.

Unay, I.O, Russell, B., Burns, N. and Kreger, M. (1991). *Measurement of Transfer Length on Prestressing Strands in Prestressed Concrete Specimens*, Research Report 1210-1, University of Texas at Austin, 250 pp.

Utting, W.S. and Jones, N. (1987). The Response of Wire Rope Strands to Axial Tensile Loads – Part I, Experimental Results and Theoretical Predictions, *International Journal of Mechanics Science*, *29* (9), 605-619 pp.

Wahalathantri, B.L., Thambiratnam, D.P., Chan, T.H.T, and Fawzia, S. (2011). A material model for flexural crack simulation in reinforced concrete elements using Abaqus, *In Proceedings of the First International Conference on Engineering*, Designing and Developing the Built Environment for Sustainable Wellbeing, 27-29 April 2011, Qld, Australia.

West, C. (2019). Prestressed Concrete Girders Achieve Record Lengths, *Aspire*, Fall 2019, 56-57.

WSDOT (2019). *Bridge Design Manual (LRFD)*, Washington State Department of Transportation.

Zureick, A.H, Kahn, L. Will, K.M., Kalkan, I., Hurff, J. and Lee, J.H. (2009). *Stability of Precast Prestressed Concrete Bridge Girders Considering Sweep and Thermal Effects*, Georgia Institute of Technology for the Georgia Depart of Transportation.